

FINAL REPORT
Shear Transfer in Thick Walled Reinforced
Concrete Structures Under Seismic Loading
NSF Grant No. ATA73-03178

by

Richard N. White
Peter Gergely

May 1978

Report 78-2

This report was prepared with the support of the National Science Foundation, Grant No. ATA73-03178. However, any opinions, findings, conclusions, or recommendations expressed herein are those of the authors and do not necessarily reflect the views of the National Science Foundation.

W

REPORT DOCUMENTATION PAGE	1. REPORT NO. NSF/RA-780168	2.	3. Recipient's Accession No. PR285970								
4. Title and Subtitle Shear Transfer in Thick Walled Reinforced Concrete Structures Under Seismic Loading, Final Report		5. Report Date May 1978									
7. Author(s) R.N. White, P. Gergely		8. Performing Organization Rept. No. 78-2									
9. Performing Organization Name and Address Cornell University Department of Structural Engineering Ithaca, New York 14850		10. Project/Task/Work Unit No. 11. Contract(C) or Grant(G) No. (C) ATA7303178 (G)									
12. Sponsoring Organization Name and Address Applied Science and Research Applications (ASRA) National Science Foundation Washington, D.C. 20550		13. Type of Report & Period Covered Final									
15. Supplementary Notes											
<p>16. Abstract (Limit: 200 words)</p> <p>The project had three major goals: (1) to understand the mechanism of cyclic shear stress transfer in cracked thick-walled reinforced concrete structures; (2) to incorporate mathematical models of the shear transfer mechanism into computer-based analysis methods for determining structural response to earthquakes; and (3) to provide experimental and analytical background material for formulation of improved design procedures that would result in better and less costly designs without sacrificing safety. Experiments on large specimens of cracked concrete were conducted. Various types of shear transfer were studied for a wide range of variables. It was found that the behavior of concrete and steel in the structure can be predicted with reasonable accuracy. A simplified model of this behavior is being completed. The computer-based analysis program gives reliable predictions of forces, stresses, overall deformations, and displacements of thick-walled concrete structures subjected to earthquake forces. From these studies, it is possible to rely upon some shear transfer capacity from the combination of normal vertical and horizontal steel and the inherent roughness of the crack surface in the concrete in reinforced containment vessels and similar structures. This saves reinforcing steel and permits a more rational design.</p>											
<p>17. Document Analysis a. Descriptors</p> <table border="0"> <tr> <td>Earthquake resistant structures</td> <td>Seismology</td> </tr> <tr> <td>Concrete construction</td> <td>Dynamic structural analysis</td> </tr> <tr> <td>Structural design</td> <td>Shear properties</td> </tr> <tr> <td>Reinforced concrete</td> <td></td> </tr> </table> <p>b. Identifiers/Open-Ended Terms</p> <p style="text-align: center;">REPRODUCED BY NATIONAL TECHNICAL INFORMATION SERVICE U. S. DEPARTMENT OF COMMERCE SPRINGFIELD, VA. 22161</p> <p>c. COSATI Field/Group</p>				Earthquake resistant structures	Seismology	Concrete construction	Dynamic structural analysis	Structural design	Shear properties	Reinforced concrete	
Earthquake resistant structures	Seismology										
Concrete construction	Dynamic structural analysis										
Structural design	Shear properties										
Reinforced concrete											
18. Availability Statement NTIS		19. Security Class (This Report) 20. Security Class (This Page) 22. Price A11-A01									

CAPITAL SYSTEMS GROUP, INC.
6110 EXECUTIVE BOULEVARD
SUITE 250
ROCKVILLE, MARYLAND 20852

SUMMARY

This research project had three major goals: (1) to understand the mechanism of cyclic shear stress transfer in cracked thick-walled reinforced concrete structures, (2) to incorporate mathematical models of the shear transfer mechanism into computer-based analysis methods for determining structural response to earthquakes, and (3) to provide experimental and analytical background material for formulation of improved design procedures that would result in better and less costly designs (without sacrificing safety).

Extensive experiments on large specimens of cracked concrete were conducted. Shear transfer by interface, shear transfer on the rough cracked surfaces, plus shear transfer by dowel action of reinforcing crossing the crack, were studied for a wide range of variables. The degradation of the shear transfer mechanism with continued cycling of shear stress was of particular concern and importance in the experiments. It was found that cyclic shear stresses on the order of 200 psi could be carried quite efficiently by this mechanism. The behavior of both the concrete and steel in the structure can be predicted with reasonable accuracy on the basis of experimental evidence. Final reduction of all data into a comprehensive, simplified model of behavior is being done at the present time under a continuation of this project.

The computer-based analysis program completed during this study gives reliable predictions of forces, stresses, overall deformations, and displacements of thick-walled concrete structures subjected to earthquake forces.

Prior to Cornell University shear transfer studies, diagonally-oriented reinforcing steel was normally required to resist the entire seismic shear stress in reinforced containment vessels and similar structures. Now it is possible to rely upon some shear transfer capacity from the combination of normal vertical and horizontal steel and the inherent roughness of the crack surface in the concrete. This saves reinforcing steel and permits a more rational design.

SCOPE AND ORGANIZATION OF REPORT

This report is divided into the following sections:

A. Reduced Scale Experiments on Combined Interface Shear Transfer and Dowel Action

A summary of the work of Eleiott (Ref. 1) is given for experiments with #4 and #6 reinforcing bars subjected to combined dowel action and interface shear transfer. Behavior was determined for specimens carrying shear by (a) interface shear transfer (IST) alone, (b) dowel action alone, and (c) combined interface shear transfer and dowel action. In addition, the combination of cyclic shear and external tension applied to the bar crossing the crack was studied.

B. Dowel Action: A Mathematical Model for Unidirectional Shear, and Dowel Experiments with Cyclic Shearing Forces

This part of the report is extracted from the research of Stanton (Ref. 2). A mathematical model for dowel action is presented which predicts dowel stiffness and bending stresses in the dowel at an open crack. The analysis is supplemented by experiments on dowel action in #11 reinforcing bars in large specimens that had greased plates at the shear plane normal to the reinforcing bar. Comparisons are given between the analytical model and earlier experiments on specimens reinforced with #11 bars and carrying shear by combined dowel action and interface shear transfer.

Stanton also developed a dynamic analysis capability to account for the nonlinear shear force-shear slip relationship that occurs at the cracks in reinforced concrete subjected to simultaneous tension and seismic shear. The results are reported in Ref. 3. Details of Stanton's analysis program was perfected by Smith (Ref. 4) and is given in Section D of this report.

C. Large-Scale Tests with Combined Axial Tension and Dowel Effects

Two large specimens (225 in² shearing area) reinforced with four #9 reinforcing bars were subjected to combined tension and cyclic shear to study the effect of tension on shear stiffness and strength.

Four additional specimens with the same shearing area, reinforced with a single #14 bar, were loaded with simultaneous tension and reversing shear.

These experiments constitute only a portion of the extensive experimental investigation that is central to this research. Because a definitive resolution of the effects of many variables on shear stiffness and strength will not be reached during the current project, the reader may find this section of the report rather lacking in conclusions. Additional results are given in Section E, and a comprehensive report that systematically explains the effects of each variable will be published in the continuation of this research grant (Ref. 6).

D. The Effects of Cracks on the Semismic Analysis of Reinforced Concrete Nuclear Containment Vessels

A computer program was developed to do seismic analysis of a cracked reinforced concrete containment vessel and other thick-walled reinforced concrete structures (Ref. 4). Since the shear transfer mechanism at the cracks in these structures is highly nonlinear, and degrades with continued shear cycling, the program is non-linear and must be executed with small time steps. A synthetic earthquake generated from response spectra given in NRC 1.60 was used as the base acceleration in all computer runs. Analyses were done for the uncracked structure, for the structure including the effects of cracks, and for several different soil stiffnesses. In addition, a system identification approach was used to develop a linear seismic analysis capability for the highly nonlinear response of the cracked structure.

Results indicate that the shear transfer capabilities of the combination of cracked concrete and reinforcement orthogonal to the cracks can adequately resist the shear forces developed by design earthquakes normally used in reactor containment design. A final recommendation on this important design question can be made only after suitable experiments are conducted on reinforced concrete specimens subjected to combined biaxial tension and cyclic shear (planned as a part of the continuing research program on shear transfer at Cornell University).

E. Ongoing Research

The current project is being continued in two major areas: (a) effect of bar size, specimen geometry, and level of axial tension on shear strength and stiffness, with particular emphasis on determining the relative amount of shear force being transmitted by dowel action and by interface shear transfer, and on the possibility of splitting effects produced by dowel and bond forces in large bars (#11 and larger), and (b) strength and stiffness of orthogonally reinforced concrete specimens subjected to combined biaxial tension and cyclic shear stresses; this research is being conducted under the primary sponsorship of the Nuclear Regulatory Commission but is closely tied into the NSF research on shear transfer.

A major effort is underway by Jiminez on the first area. Early experimental results are given in Section E in a reprint of a paper presented in 1976 (Ref. 5). The entire study (analytical and experimental) will be reported later in Ref. 6.

The second area of concern, biaxial tension effects on shear performance, likewise will be reported separately as the extensive experimental study progresses.

A. REDUCED SCALE EXPERIMENTS ON COMBINED INTERFACE SHEAR TRANSFER (IST) AND DOWEL ACTION

A series of specimens with 3 in. by 5 in. shearing areas, reinforced with two different bar sizes (#4 and #6) were loaded in reversing shear to simulate a seismic shear loading. Behavior was determined for specimens carrying shear by (a) interface shear transfer (IST) alone, (b) dowel action alone, and (c) combined interface shear transfer and dowel action. In addition, the combination of cyclic shear and external tension applied to the bar crossing the crack was studied.

The experiments were conducted on a new form of specimen that presented some difficulties (one of the reasons for the study was to assess the adequacy of the specimen for large-scale tests). The results should be interpreted with this fact in mind; certainly the overall trends are valid but the precise values for some experiments may not be fully reliable.

Specimen Configuration and Loading

The specimen geometry and loading methods are shown in Fig. A1. The crack surfaces were formed in the intersection of the vertical members and the cross members to provide a total of 30 in² of shearing surface at each end of the specimen. Positive and negative shear loads across the two cracks were applied as shown in Figs. Alb, where the forces marked (+) and (-) indicate the loads and reactions for the two loading conditions. Slips and crack openings were measured with dial gages.

Specimens designed to study IST alone had no embedded reinforcing bars. Instead, they had external steel restraint rods across the cracks, as indicated in the upper part of Fig. Alb. With the nuts on the restraint rods in the loose position, the specimen was cracked by jacking metal plates into the V-shaped crack-initiating grooves case into the specimen. The desired initial crack width was then set by adjusting the nuts on the restraining system.

Specimens designed to study dowel action alone, and combined dowel action and IST, had embedded deformed reinforcing bars, one per shearing plane, as illustrated in the lower half of Fig. Alb.

Dowel action alone was achieved by casting greased steel plates in the shear planes with oversize holes at the reinforcing bar locations. No cracking was necessary in this specimen. For combined IST and dowel action, the specimens were cracked by tensioning the reinforcing bar against an independent external tubular steel frame.

In each test two shear planes were loaded simultaneously, and the resulting sets of displacements were averaged.

Interface Shear Transfer

Two tests were made to compare the IST mode behavior of the small scale specimens with that of the large specimens (300 in²) used in all earlier tests. Specimen parameters were:

Concrete: f'_c = 2920 psi with $\frac{1}{2}$ in. maximum aggregate
 Restraint stiffness: = 700 k/in on 15 in² shear surface
 = 46.7 ksi/in
 Initial crack width: = 0.030 in.
 Shear stress: = \pm 150 psi
 Load cycles: = 15 full reversals of shear load

The behavior measured in the two tests was nearly identical and is shown for Test IST1 in Fig. A2. It is basically the same as that exhibited by the large scale specimens. The load-slip relationship is linear for loading in both directions during the first cycle. There is a pronounced "locking effect" during unloading and the neutral slip position can be reached only by reversing the load.

The slip increases with cycling but at a decreasing rate, increasing from 0.0135 in. in cycle 1 to 0.0175 in. in cycle 15. With each cycle, the "free slip" that occurs at low shearing stresses (less than 50 psi) increases, while the shear stiffness during the upper portion of the load cycle (from 50 to 150 psi) increases by a factor of nearly 4 from cycle 1 to cycle 15.

In the first cycle the shear resistance is provided primarily by bearing stresses between the particles projecting across the shear plane from one surface to the other. The loading and unloading action of the first cycle produces marked changes in behavior, and the free slip increases more between the 1st and 2nd

cycles than it does between the 2nd and 15th cycles. Once firm contact is made between the surfaces in the later cycles, the compacted concrete is stiffer and the sharply upward curving load-slip curve results.

Over-riding (and frictional resistance) becomes more prevalent as cycling wears down the surfaces. As the shear displacement increases, the over-riding action causes the crack to widen, thereby increasing the forces in the restraining bar which in turn increases the frictional resistance. Thus the restraint stiffness across the crack has substantially less influence in first cycle slip values than in later cycle slips. The results presented below verify this observation.

The results for large scale specimen J3 (from Laible) are shown in Fig. A2b for comparison. The J3 results are for ± 180 psi shear stress and a restraint stiffness of 7640 k/in on a 300 in² shearing surface; therefore direct comparisons of behavior are not possible.

The restraint stiffness for the small specimen was 83% higher than that for the large specimen. The small scale data are plotted in Fig. A3 along with a series of large scale test results. Specimen IST1 results appear to be consistent with the other data and no appreciable size effect is evident.

A summary of comparisons between specimens IST1 and J3 includes:

	Small scale <u>specimen IST1</u>	Large scale <u>specimen J3</u>
slip, cycle 1	0.016 in.	0.017 in.
slip, cycle 15	0.021 in.	0.031 in.
shear stiffness, cycle 1	11.1 ksi/in	9.9 ksi/in
shear stiffness, cycle 15		
free slip, cycle 1	0.0028 in.	0.0025 in.
free slip, cycle 15	0.014 in.	0.022 in.

Specimen IST1 results are scaled linearly from 150 psi shear up to 180 psi shear in the above comparisons. The higher shear stress level does produce more surface deterioration, however,

and these effects cannot be totally scaled. Thus it is expected that cycle 15 results will not compare as well as cycle 1 results. Also, the difference in restraint stiffness has more effect in the 15th cycle than in the 1st cycle.

Dowel Action

Several experiments were conducted to determine the behavior of specimens transferring cyclic shear by dowel action alone. Transfer of shear by dowel action is dependent upon preventing major dowel cracking along the bar, or by controlling such cracks with transverse reinforcement. Before cracking, slippage along the shear transfer plane is produced by bending of the bar and local deformation of the concrete under the very high local contact stresses. Consequently, the critical physical parameters are the diameter of the reinforcing bar and the concrete strength and stiffness.

The reinforcing across a crack ordinarily carries tension from either flexural action or membrane action. This tensile stress produces high localized bond stresses on each side of the shear plane that may lead to very small yet significant cracks around the bar and thus influence the shear stiffness.

The variables studied were:

1. diameter of reinforcing bar (1/2 and 3/4 in.)
2. axial stress applied to reinforcing bar, $f_t = 0, 25,$ and 50 ksi.
3. level of shear stress - ± 150 psi and ± 180 psi for $f_t = 0$; ± 150 psi for $f_t = 25$ and 50 ksi. These shear stresses are computed on the basis of the concrete area. Actual average shear stresses on the dowel crossing the crack ranged from 5.1 to 13.5 ksi as detailed in Table A1.

In each specimen a single reinforcing bar was embedded at the center of the shearing plane. Interface shear transfer was prevented by casting greased plates in the specimen. Concrete strength varied from 2890 to 3130 psi.

Thirteen tests on four specimens are summarized in Table A1. Each specimen had two ends that were tested independently; they are marked with U (upper) and L (lower) in the table. Five tests (3a, 4a, 5a, 6a, and 8a) were done on specimens that had already been cycled according to the load history values given in Table A1 on the unlettered tests (3, 4, 5, 6, and 8). The number of specimens used to cover these parameters is inadequate, but again it must be realized that this program was designed to be exploratory and as an aid to planning large scale tests.

Dowel Action - Applied Axial Stress $f_t = 0$

Tests 1 and 2 on Specimen D1 resulted in early failure by dowel cracking because of twisting of the central loaded block around the reinforcing bar, and subsequent splitting produced by the wedging action of the deformed bars. The results of these tests are not meaningful and will not be reported here.

Specimen D2, with a #4 bar initially unstressed, was identical to Specimen D1 except the loading was changed to eliminate the twisting effects observed in D1. Discussion here will focus on tests 4 and 4a done on one end of the specimen.

The load-slip behavior for Tests 4 and 4a is summarized in Figure A4 and Table A2. The slip at ± 150 psi shear stress increased from 0.082 in. during cycle 1 to 0.0125 in. in the 15th cycle; the increase was negligible after 10 cycles. After 15 cycles at ± 150 psi shear, the loading was increased to ± 180 psi for 10 more cycles (Test 4a) with the response as shown in Fig. A4. The rate of increase of slip, which had become zero in Test 4, increased again when the shear stress level was raised. It appears that Test 4a behavior was not strongly influenced by the earlier 15 cycles at 150 psi, although the ratio of final maximum slips ($\text{slip}_{25}/\text{slip}_{10} = 1.42$) was greater than the ratio of shear stresses ($180/150 = 1.2$).

These load-slip curves have the same general shape as the curves for interface shear transfer except the first cycle loading in each direction has a slightly decreasing stiffness which must be due to localized concrete crushing from excessive bearing

stresses near the shear plane. There is also less free slip than in the IST mode, however, since the flexural stiffness of the reinforcing bar tends to return the specimen to a neutral slip value as it is unloaded. The free slip increased from 0.0008 in. on cycle 1 to 0.0052 in. in cycle 15, but the rate of increase decreased with cycling. In Test 4a the free slip increased by 35% in the 10 loading cycles, with 3/4 of this increase occurring in the first 5 cycles (16-20). The shear stiffnesses after free slip were essentially identical for cycles 10 and 25 in the two tests, which indicates that the shear stiffness approaches a constant value after a certain amount of cycling. If the shear stress level is then increased, the shear stiffness may initially decrease but subsequent cycling will bring it back to the previous level.

Tests 3 and 3a should have given the same results as 4 and 4a, but instead showed slips about twice as great as in the latter tests. Dowel cracking terminated the test on the 26th load cycle (19 at ± 150 psi and 7 at ± 180 psi shear). Since there is no feasible extraneous mechanism that could have enhanced the shear resistance in Tests 4 and 4a, and since the 3a test led to failure while the 4a test did not, it is concluded that some twisting action must have been present in Tests 3 and 3a to reduce the performance in shear.

Specimen D4 had a #6 reinforcing bar across each shear plane but was identical to D2 in all other respects. Tests 7 and 8 were done at ± 150 psi for 10 cycles and 5 cycles, respectively. The behavior is summarized in Fig. A5 and Table A3 where it is seen that the two tests gave essentially identical results.

The effect of bar size on shear stiffness is difficult to quantify because of the variable results achieved for the two #4 bar tests (3 and 4). The post-free slip stiffnesses at various cycles for the #6 bar tests were about 40 to 60% higher than those of Test 3 (#4 bar with highest slips). This agrees well with Baumann's prediction in Ref. A1 that the dowel shear stiffness varies as the diameter of the bar. On the other hand, Test 4 results for the #4 bar gave higher stiffnesses than measured in Tests 7 and 8 with the #6 bar.

The first cycle shear stiffness of the #6 bar (405 k/in) may be compared with results obtained by Baumann (A1) and Teller and Cashell (A2) on similar size bars. Baumann tested two 0.786 in. diameter bars in a concrete beam with $f'_c = 5200$ psi and obtained $K = 619$ k/in. This result is extrapolated to one 0.75 in. bar with $f'_c = 3130$ by

$$K = \left(\frac{3130}{5200}\right)^{\frac{3}{8}} \left(\frac{1}{2}\right)^{\frac{1}{4}} \left(\frac{0.75}{0.786}\right) (619) = 410 \text{ k/in}$$

This value compares very well with the measured K of 405 k/in.

Teller and Cashell obtained $K = 333$ k/in per 0.75 in. dowel in a specimen with a 3/4 in. crack width. This value becomes $K = 585$ k/in after applying the Teller and Cashell adjustment for the effect of crack width and scaling back from their high concrete modulus of 7120 ksi. With these rather severe adjustments it is not surprising that a 42% difference exists between the two K values (585 vs. 405 k/in).

An approximate analysis of the first cycle shear stiffness was made, modeling the reinforcing bar as a beam on a semi-infinite elastic foundation. This analysis indicates that within the narrow range of bar size studied, the effective foundation modulus K' is nearly independent of bar size and the shear stiffness K is of the form

$$K = \frac{d(K')}{0.23} 0.75$$

where d is the bar diameter and K' is about 1000 k/in^2 .

Second and subsequent cycle behavior differs considerably from that of the first cycle. A large increase in the free slip occurs because of the concrete crushing action of the first cycle. The initial stress concentrations in the concrete are reduced by localized failures; thus after the free slip occurs, the elastic curve of the bar has a better contact with the compacted concrete and the shear stiffness increases. In some tests this behavior held true to the peak shear stress of cycle 2; in others, there was some decrease in shear stiffness near the peak of cycle 2, indicating some further substantial crushing action in the concrete under the bar. In later cycles (say after 10) the bar can firmly bed itself in the concrete without producing any significant new concrete crushing.

Dowel Action with Applied Axial Stress $f_t = 25$ or 50 ksi

The effect of applied external bar tension on shear stiffness was examined with Specimen D3 (Tests 5, 5a, 6, 6a on a #4 bar) and with Specimen D4 (Test 8a on a #6 bar).

A #4 bar tensioned to 25 ksi was cycled at ± 150 psi for 15 cycles in Test 5. The axial stress was then increased to 50 ksi, and a single cycle of shear load (Test 5a) produced a dowel cracking failure. This behavior is summarized in Fig. A6. Tests 6 and 6a were then run on the other end of the specimen, with one cycle at $f_t = 25$ ksi and 4 cycles at $f_t = 50$ ksi before the specimen cracked along the reinforcement (Fig. A7).

The crack widths and slips at several critical cycles are given in Table A4. At $f_t = 25$ ksi, the average crack width doubled during 15 cycles of shear, with nearly all of the increase occurring during the first cycle, and the slip increased by about 50%. On cycle 16 (Test 5a) the crack width again doubled when f_t was doubled from 25 to 50 ksi. In Test 6a, where the tensile stress was doubled on cycle 2, the crack width again doubled (from 0.0038 to 0.0075 in.) and increased to 0.0095 in. during four more cycles with $f_t = 50$ ksi.

Several observations can be made from these tests on #4 bars:

- a. Shear displacements with $f_t = 25$ ksi were about twice those at $f_t = 0$ (compare Figs. A4 and A6.) Shear stiffnesses were correspondingly lower in the axially stressed case. This comparison must be tempered by the fact that the two tests at $f_t = 0$ differed considerably.
- b. When f_t was increased from 25 to 50 ksi, the shear stiffness after free slip decreased by about 30% in the next shear cycle. This decreased stiffness indicates the additional bond-induced cracking produced by increased bar stress, which opens the crack and decreases the integrity and stiffness of the concrete around the bar. The first cycle shear stiffness with $f_t = 50$ ksi decreased substantially in the stress range from 100 to 150 psi, thereby demonstrating the additional damage done to the concrete. Some inelastic action in the reinforcing

may also have occurred under the combined stresses of 50 ksi tension, 11.2 ksi average shear, and the local bending stresses near the shear plane.

- c. The shape of the upper portion of the load-slip curve during the first cycle at $f_t = 50$ ksi was the same in Tests 5a and 6a, even though the earlier cycling history at $f_t = 25$ ksi was considerably different in the two tests (15 and 1 cycles, respectively). The total slip and free slip values were greater in 5a, of course, but the shear stiffness after free slip was nearly identical to that in 6a.
- d. Both ends of the specimen failed from dowel-induced cracks when the axial stress level was 50 ksi; one end carried four cycles of shear and the other only one. The difference in cycle numbers to failure can be attributed to the extra degree of damage done to the concrete by more extensive prior cycling with $f_t = 25$ ksi in Test 5 (15 cycles). The severity of combined high tension and cyclic shear is rather evident from this behavior.

The influence of axial stress on dowel action with a #6 bar was examined with Test 8a, where 10 cycles of shear stress (± 150 psi) were applied with $f_t = 25$ ksi after the specimen was cycled 5 times with $f_t = 0$. The response is shown in Fig. A8 as cycles 6-15. The first cycle with $f_t = 25$ ksi (cycle 6) produced an increase in slip of 15% and a decrease in shear stiffness (after free slip) of about 30%. The slip increased rather sharply in the first 5 cycles (cycles 6-11) but had leveled off by cycle 15. The total increase in slip during the 10 load cycles was the same as that shown in 10 cycles with $f_t = 0$ in Test 7 (compare cycles 1 and 10 in Fig. A5 with cycles 6 and 15 in Fig. A8). The shape of the load-slip curve and the shear stiffness after free slip remained essentially unchanged during cycles 6-15, with only the free slip component increasing because of continuing deterioration of the concrete surfaces adjacent to the bar.

It may be concluded that combined cyclic shear of ± 150 psi (measured in terms of the concrete surface area) and axial stress of 25 ksi on the #6 bar is not substantially more damaging to the

concrete than cyclic shear stress alone. The improved performance of the #6 bar over the #4 bar is at least partially due to the fact that the same shear load was applied to both types of specimens; hence the shear stress and the bending stresses and deformations were substantially lower in the #6 bar. No tests were made with #6 bars stressed higher than 25 ksi tension, and it is not known if the application of 50 ksi would produce as severe as results as were measured with the #4 bar specimen.

In Test 8a a procedure was evolved to establish the axial restraint stiffness of the internally embedded reinforcement and its variation with increased cycling. At various times during a test, when the shear load had been decreased to zero before reversing the load direction, the axial stress in the reinforcement was released. The stress was then reapplied in increments and the crack width was measured after each step. A typical plot of crack width vs. bar stress is given in Fig. A9. The data is approximated with the straight dashed line, and its slope, multiplied by the bar area of 0.44 in^2 , gives the axial stiffness of the combined bar-concrete specimen. In Fig. A9 the stiffness is $K = 30(0.44)/0.00366 = 3600 \text{ k/in}$. This type of stiffness measurement was used mainly in the combined interface shear transfer and dowel action tests that are described in the following section.

Combined Interface Shear Transfer and Dowel Action

Combined interface shear transfer and dowel action was investigated on a double-ended specimen with a single #4 bar passing through each shear plane. The interface shear mode is highly dependent upon the normal restraint stiffness supplied by the reinforcement crossing the shear plane. With internal reinforcement, this restraint stiffness is determined in part by the bond between the steel and surrounding concrete. As the shear cycling progresses, dowel action results in crushing of the concrete around the bars, destroying the bond and changing the restraint stiffness. This process, which was studied for dowel action alone, will be less severe when interface shear transfer is also included because the increased shear stiffness and lower slips will decrease the rate of deterioration of bond.

Cracking of the specimen was achieved by tensioning the reinforcement and, when necessary, forcing wedges into the V-shaped crack initiating grooves at the crack plane. Both ends were cracked on the same day; one end was tested immediately and the other two weeks later. One end of the specimen was subjected to 45 cycles of shear with four different combinations of axial stress and shear stress (Tests 9, 9a, 9b, and 9c in Table A5). The other end was loaded with 28 cycles and three different stress combinations (Tests 10, 10a, and 10b in Table A5).

Axial stress in the reinforcing bar at the peak shear stress is of major importance in these tests. High axial stresses produce slip between the reinforcement and concrete. This damages the concrete, resulting in larger dowel shear displacements. The axial stress in the reinforcement is increased by the overriding of surface irregularities. This not only decreases the dowel stiffness but may also result in yielding of the bars if the initial axial stress is high or the steel ratio is low. When the reinforcement yields, neither dowel resistance nor the frictional component of interface shear transfer can increase further until large shear displacements produce kinking of the reinforcement.

Measurement of the bar stress at the crack was done indirectly by first measuring the effective axial stiffness of the bar at the crack by the procedure described in the earlier section on dowel action. This stiffness, multiplied by the increase in crack width between zero shear load and peak shear load, was used to estimate the change in bar stress at the crack during shear loading. This method of stress measurement was felt to be better than the use of strain gages on the bar that might interfere with bond between concrete and reinforcing.

The load position was adjusted at the end of the first cycle to force the slips on each of the two shear planes to be equal. In some tests the two shear planes still had significantly different stiffnesses because the crack widths became different with cycling.

The two variables in this test series were:

1. axial stress level, f_t - 25 or 50 ksi
2. shear stress level of 150, 250, and 400 psi

Test results are summarized in Table A5. Test 9 was the only test made with $f_t = 25$ ksi. Ten cycles of ± 150 psi shear produced extremely small slips and crack widths (about 0.001 in. each) and essentially no damage to the concrete and bond strength of the bar. No load-slip curves were plotted for this test. The #4 bar stress increased about 2 ksi at peak shear load.

In Test 9a, the axial stress level was raised to 50 ksi and shear cycling at ± 150 psi was done for 15 cycles (cycles 11-26 in Fig. A10). It is seen in the figure that the shapes of the load-slip curves for cycles 15 and 25 are intermediate to those determined earlier for interface shear transfer alone and dowel action alone, and that the slips are smaller. After about five shear cycles, the slip stopped increasing and there was little further degradation of the shear transfer characteristics.

Test 9b consisted of 10 cycles at ± 250 psi shear with f_t held at 50 ksi. The slips increase rather sharply during the first seven cycles (Fig. A10b) and the shapes of the load-slip curves remained about the same as in Test 9a (Fig. A10a).

The final loading (Test 9c) was cycled ten times at ± 400 psi shear with $f_t = 50$ ksi. Again the slips increased quickly during the first three cycles and then leveled off at about 0.01 in. as shown in Fig. A10b.

Cracks widths and slips in each of the two shear planes in each test were quite nonuniform, particularly in the earlier load cycles. By the end of the 45 load cycles the two planes were responding nearly identically, as shown in Fig. A11a. The crack widths and slips and the incremental values are given in Table A5 (Cols. 4-9) for the first and last cycle of each test. Values are tabulated for each shear plane and the average of the two planes.

Restraint stiffness was determined at each shear plane from measurements such as those shown in Fig. A11b. The values are given in Col. 10 of Table A5. The right plane (marked R) showed a marked decrease in stiffness during cycling, decreasing from 373 ksi/in to 213 ksi/in, while the other plane (L) remained essentially constant at 111 ksi/in. The reason for the difference is not known. Bar stresses calculated from these stiffnesses and

the changes in crack width during shear loading are given in Col. 11 of Table A5. In both shear planes the bar stresses at the crack during peak shear increased over the applied force of 50 ksi during cycling, with the right plane showing significantly higher axial stress. The increase in bar stress is a measure of the normal forces developed between the two concrete surfaces as overriding occurs during shear loading.

Free slip values are given in Col. 12 of Table A5. The free slip increased from 0.0012 in. in the 5th cycle of Test 9a to 0.0054 in. in the 5th cycle of Test 9c. Shear stiffness after free slip had occurred remained nearly constant during cycling (Col. 13 in Table A5).

Tests 10, 10a, and 10b had the same stress levels as Tests 9a, 9b, and 9c. Since response had stabilized in Test 9a after 10 load cycles, Test 10 was done with only 10 cycles. Results are summarized in Fig. A12 and in Table A5. The load-slip curves for Tests 10 and 10a in Fig. A12b are nearly identical to those for tests 9a and 9b in Fig. A10; in both cases the final slip after cycling at ± 250 psi shear is about 0.0075 in. There was good correlation between the two sets of tests.

A major difference in behavior was observed at ± 400 psi shear, where slips and crack widths increased dramatically in Test 10b and the specimen was near failure from excessive cracking at the end of eight cycles. This rather severe degradation in Test 10b is also evident in Fig. A13, which compares the slips at similar load cycles, and in Col. 13 of Table A5 where the shear stiffness was only half the usual value by cycle 5 of Test 10b. Such differences in behavior at this very high shear stress and axial stress level, where cracking is imminent and slight differences in the quality of the specimen, or in secondary effects introduced by loading position inaccuracies can be important.

An estimate of the relative contribution of dowel action and interface shear transfer in carrying shear may be made by comparing the stiffness of #4 dowel action alone with the stiffness of the combined mode. In dowel action Tests 5 and 6 the shear stiffness was about 250 k/in after cycling, or $250/30 = 8.3$ ksi/in. This stiffness is not sensitive to the size of crack in this study and

thus may be used as a good estimate of the dowel stiffness in the combined mode, where the total stiffness was about 67 ksi/in. Thus it is concluded that for a #4 bar in 15 in² of concrete surface ($\rho = 1.33\%$), and with a shear stress of ± 150 psi, about 12% of the shear stiffness is provided by dowel action and 88% by interface shear transfer on the concrete surfaces.

Summary

Several general observations can be made from this study:

1. Small-scale interface shear transfer specimens give results comparable to large-scale specimens.

2. It is not known if dowel effects can be scaled with reasonable accuracy; it is felt that they most likely cannot if the scaling is to go from small bars such as #4 or #6 up to prototype #18 bars.

3. The load-slip relationship for dowel action alone is qualitatively similar to that for interface shear transfer except the return to a neutral slip position after unloading is more complete for dowel action.

4. Dowel action during the first cycle of shear loading differs sharply from that in subsequent cycles.

5. The presence of applied axial tension of 25 to 50 ksi on a #4 bar prior to application of shearing forces produces a substantial decrease in shear stiffness and large increases in slip at the shearing plane. High levels of axial tension can also contribute to earlier splitting failures along the bar. The larger #6 bar was less sensitive to axial load effects.

6. Yielding of reinforcing may be a problem when high axial loads are superimposed on dowel-action shearing stresses in the rebars; this needs very careful study in future tests.

7. The general behavior modes and sensitivities to axial stress observed for dowel action alone also hold true for combined dowel action and interface shear transfer.

REFERENCES

- A1. Baumann, T., "Versuch zum Studium der Verdubelungswirkung der Biegezugbewehrung eines Stahlbetonbalken," Bericht Nr. 77, Materialprüfungsamt für des Bauwesen der Technischen Hochschule München, 1968.

- A2. Teller, L. W. and Cashell, H. D., "Performance of Dowelled Joints Under Repetitive Loading", Public Roads, A Journal of Highway Research, Bureau of Public Roads, U.S. Department of Commerce, Washington, D.C., April 1958.

<u>Specimen</u>	<u>Bar size</u>	<u>f'_c, psi</u>	<u>f_y, ksi</u>	<u>Upper or Lower end</u>	<u>Test no.</u>	<u>Axial stress</u>	<u>Average shear stress</u>		
							<u>On surface area psi</u>	<u>On dowel ksi</u>	<u>Cy- cles</u>
D1	4	2890	40	U	1	0	150	11.25	2
				L	2	0	150	11.25	5
				U	3	0	150	11.25	19
D2	4	2980	40	U	3a	0	180	13.5	7
				L	4	0	150	11.25	15
				L	4a	0	180	13.5	10
D3	4	3080	75	U	5	25	150	11.25	15
				U	5a	50	150	11.25	1
				L	6	25	150	11.25	1
D4	6	3130	60	L	6a	50	150	11.25	4
				U	7	0	150	5.1	10
				L	8	0	150	5.1	5
				L	8a	25	150	5.1	10

Table A1 - Dowel Action Specimens

<u>Test</u>	<u>Cycle No.</u>	<u>Slip, in.</u>	<u>Free slip, in.</u>	<u>Shear stiffness, k/in.</u>
3	1	0.0165	0.0015	280
	2	-	0.0067	340
	10	-	0.0103	260
3a	1	0.082	0.011	150
	5	0.124	0.015	140
4	1	0.0082	0.0008	600
	2	-	0.0025	650
	10	-	0.0052	500
	15	0.0125	-	-
4a	1	0.0135	0.0056	500
	5	-	0.0070	510
	10	0.0170	0.0076	500

Table A2 - Dowel Action, #4 bar with $f_t = 0$ (Tests 3,3a,4,4a)

<u>Test</u>	<u>Cycle no.</u>	<u>f_t, ksi</u>	<u>Ave. crack width, in.</u>	<u>Slip, in.</u>	<u>Free slip, in.</u>	<u>Shear stiffness, k/in</u>
7	1	0		0.0112	0.0015	410
	2	0		-	0.0050	450
	10	0		0.0159	0.0077	480
8	1	0		0.0110	0.0017	400
	2	0		-	0.0045	430
	5	0		0.0156	0.0075	470
8a	1	25		0.018	0.0070	340
	5	25		-	0.0115	365
	10	25		0.023	0.0126	365

Table A3 - Dowel Action, #6 bar (Tests 7,8,8a)

<u>Test</u>	<u>Cycle no.</u>	<u>f_t, ksi</u>	<u>Ave. crack width, in.</u>	<u>Slip, in.</u>	<u>Free slip, in.</u>	<u>Shear stiffness, k/in</u>
5	1	25	0.0026	0.021	0.0025	220
	10	25	-	-	0.0108	310
	15	25	0.0051	0.033	-	-
5a	16	50	0.0101	0.0393	0.0130	200
6	1	25	0.0038	0.0185	0.0032	240
6a	2	50	0.0075	0.0265	0.0048	180
	5	50	0.0095	0.0333	-	-

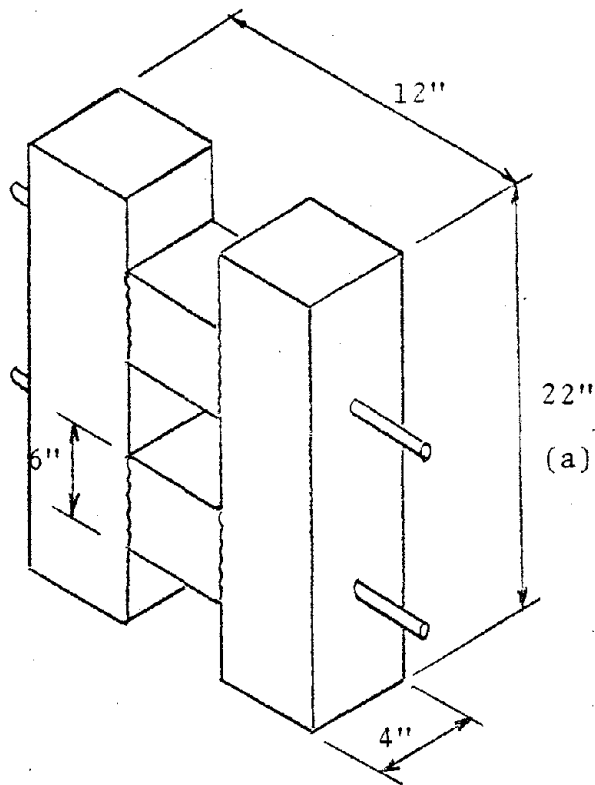
Table A4 - Dowel Action, #4 bar with
 $f_t = 25$ or 50 ksi (Tests
 5, 5a, 6, 6a)

Test	f_t , ksi (1)	shear, psi (2)	Cy- cles cycle (3)	Crack Width $x 10^4$, in lst cycle (4)	Crack Width $x 10^4$, in last cycle (5)	Δ cycle (6)	Slip $x 10^4$, in lst cycle (7)	Slip last cycle (8)	Δ cycle (9)	Re- straint stiff- ness (10)	Peak bar stress, ksi (11)	Free slip $x 10^4$ in, at cycle no. (12)	Shear stiff- ness, ksi/in at cycle no. (13)
9	25	150	10	8	12	4	7	12	5	-	27		
9a	50	150	15	L=100 Ave= 58 R= 16	100 71 42	0 14 28	45 26 8	45 30 16	0 4 8	{111 {373	54 60-68	12 @ 5 15 @ 15	65 @ 5 78 @ 15
9b	50	250	10	100 73 46	100 88 76	0 14 28	57 42 26	67 71 75	10 28 -	{111 {213 {111	56 70 62-68	27 @ 5 40 @ 10	66 @ 5 67 @ 10
9c	50	400	10	75	95	17	90	119	29	{191	73-82	54 @ 5	70 @ 5
10	50	150	10	180 96 12	180 120 60	- 24 -	42 21 4	42 31 20	0 10 16	{100 {130	60 50	13 @ 5 18 @ 10	104 @ 5 111 @ 10
10a	50	250	10	136	136	0	50	80	30	{78 {186	62 50-69	32 @ 5 39 @ 10	67 @ 5 67 @ 10
10b	50	400	8	148	268	120	115	335	220	{107 {167	65 66	105 @ 5	33 @ 5

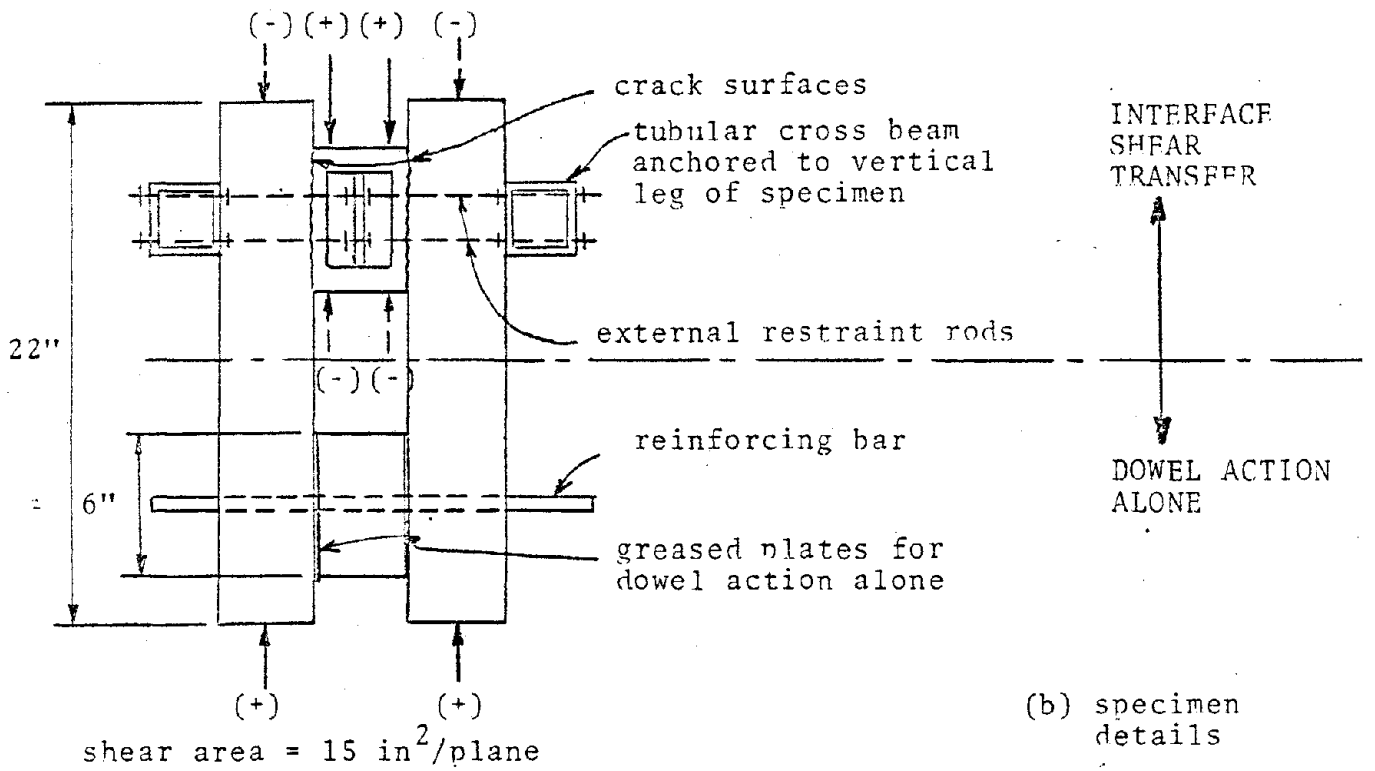
A19

Table A5 - Combined IST and Dowel Action

A20

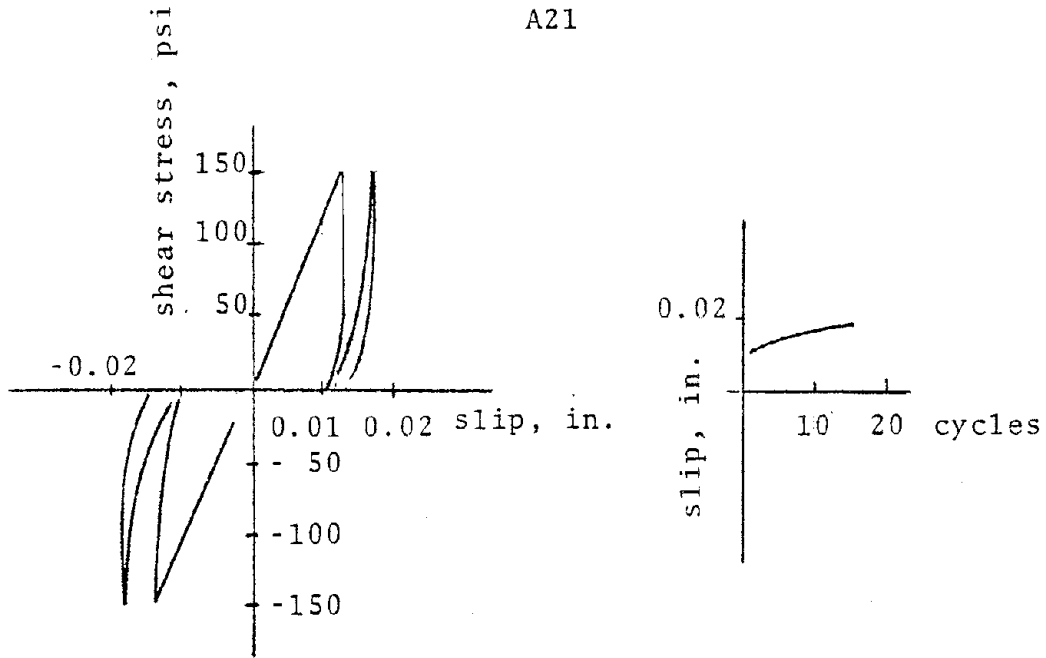


(a) specimen dimensions

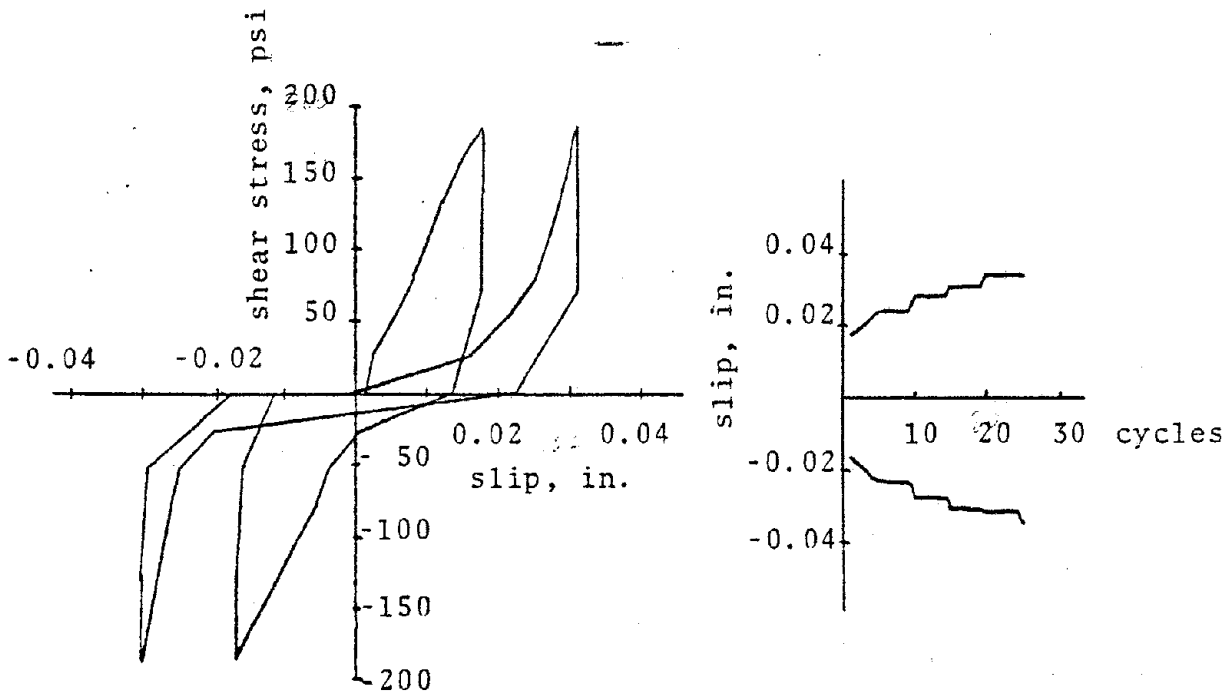


(b) specimen details

Fig. A1 - specimen geometry



(a) small scale specimen IST1, 15 in² shear area



(b) large scale specimen J3, 300 in² shear area

Fig. A2 - variation of slip with shear stress and with cycling, interface shear transfer

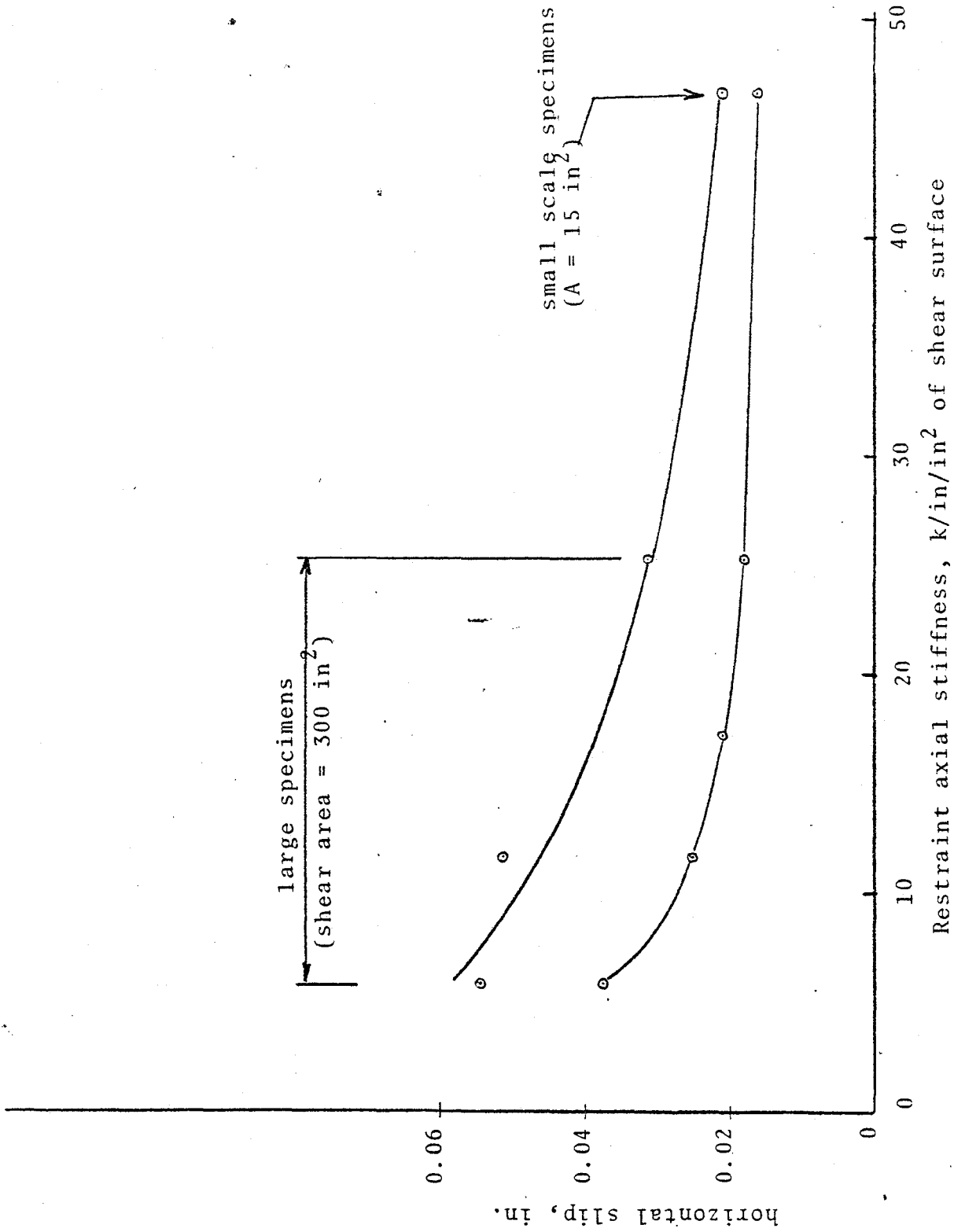


Fig. A3 - shear slip vs. restraint system stiffness

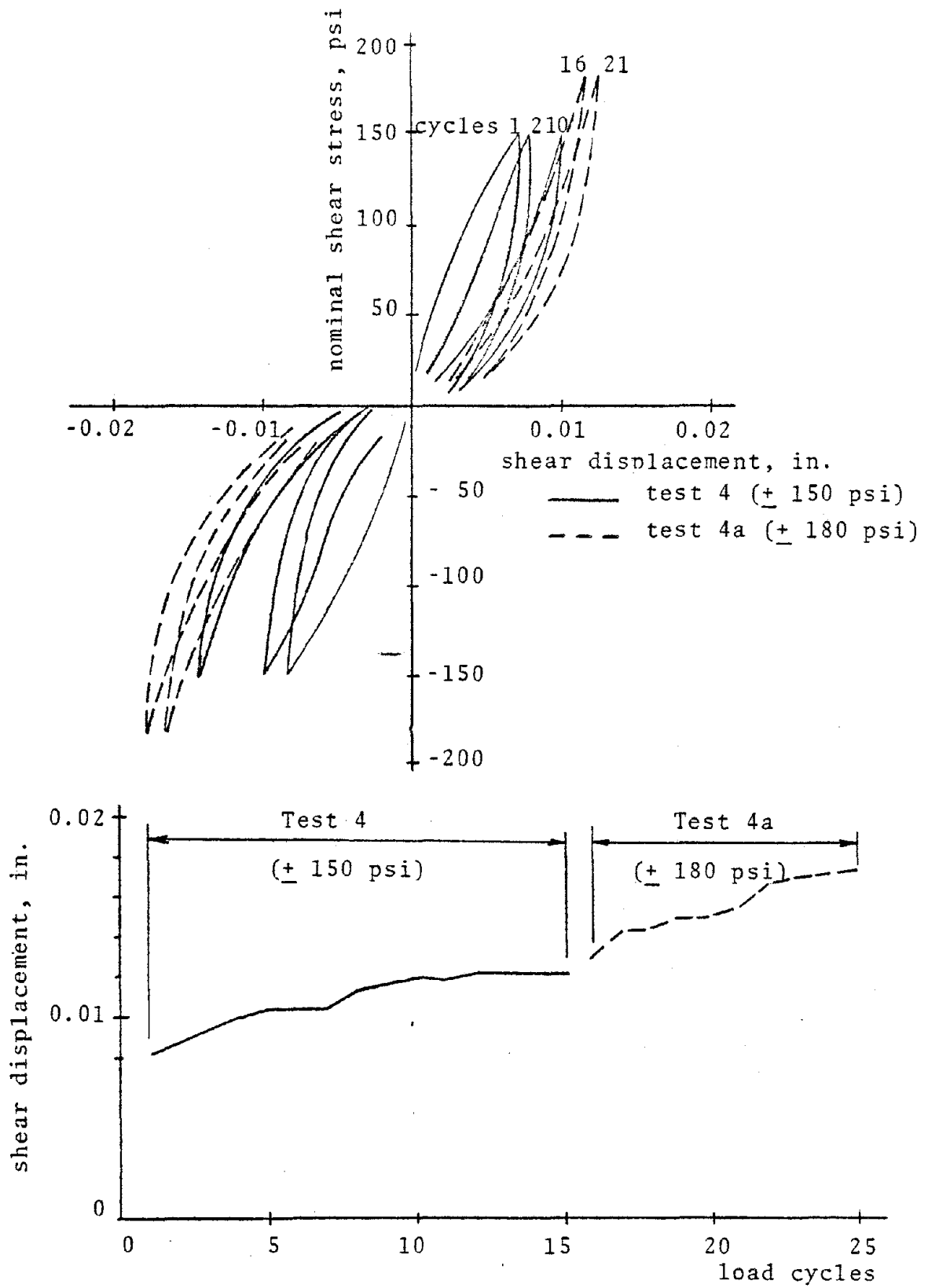


Fig. A4 - dowel action, #4 bar, axial stress $f_t = 0$

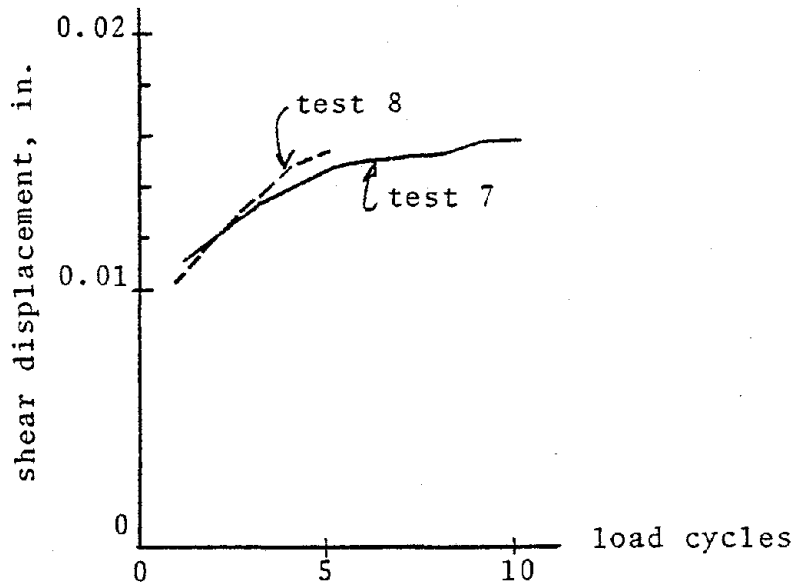
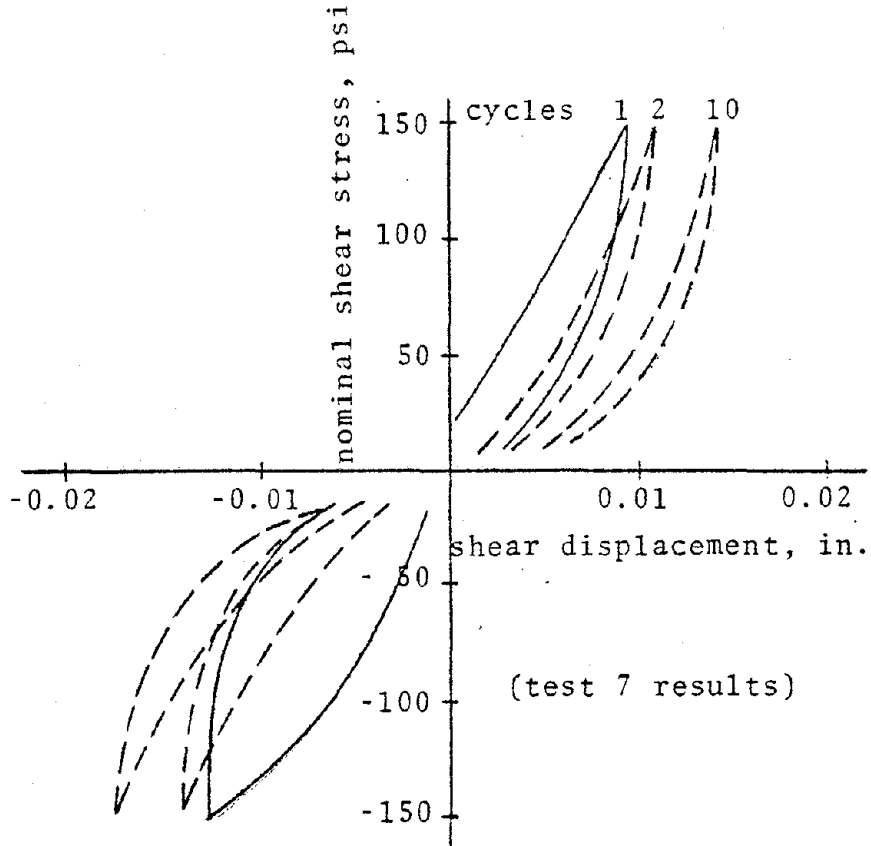


Fig. A5 - dowel action, #6 bar, axial stress $f_t = 0$

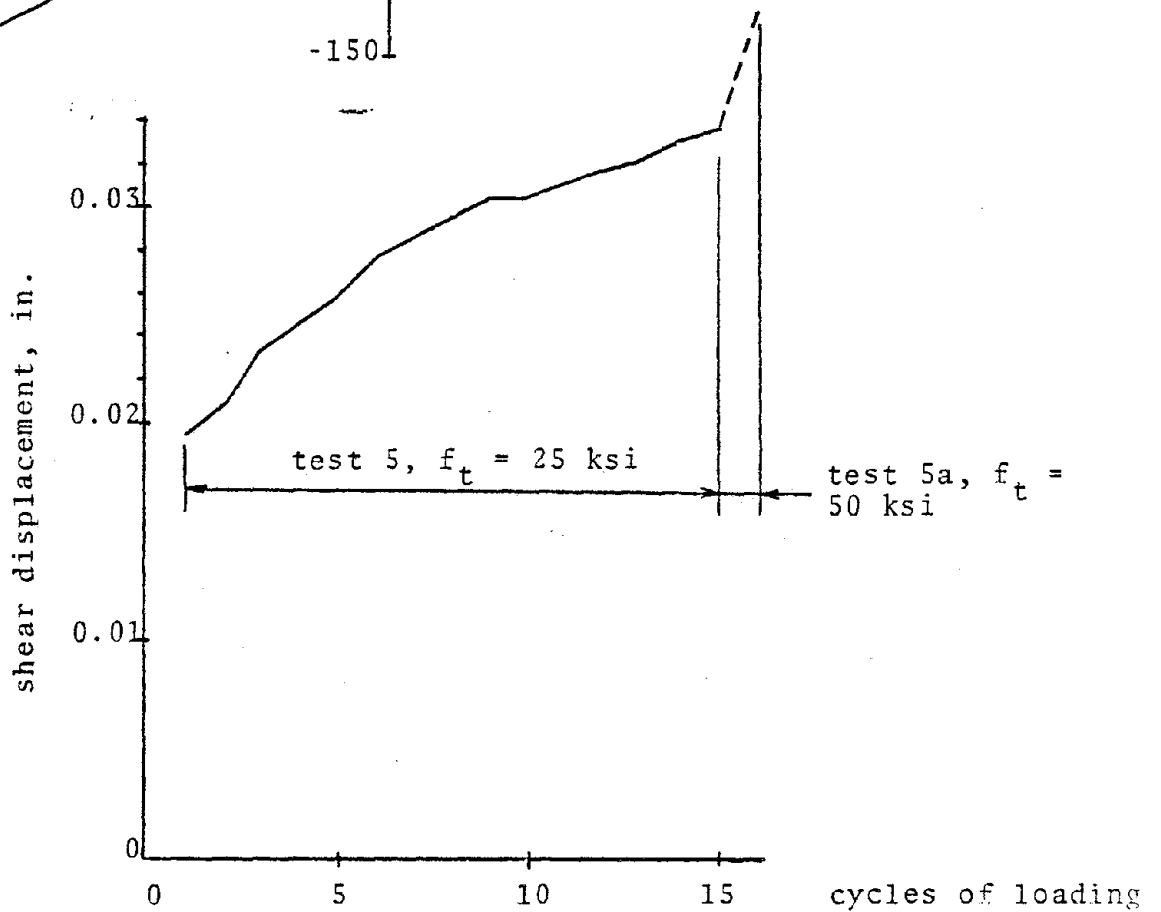
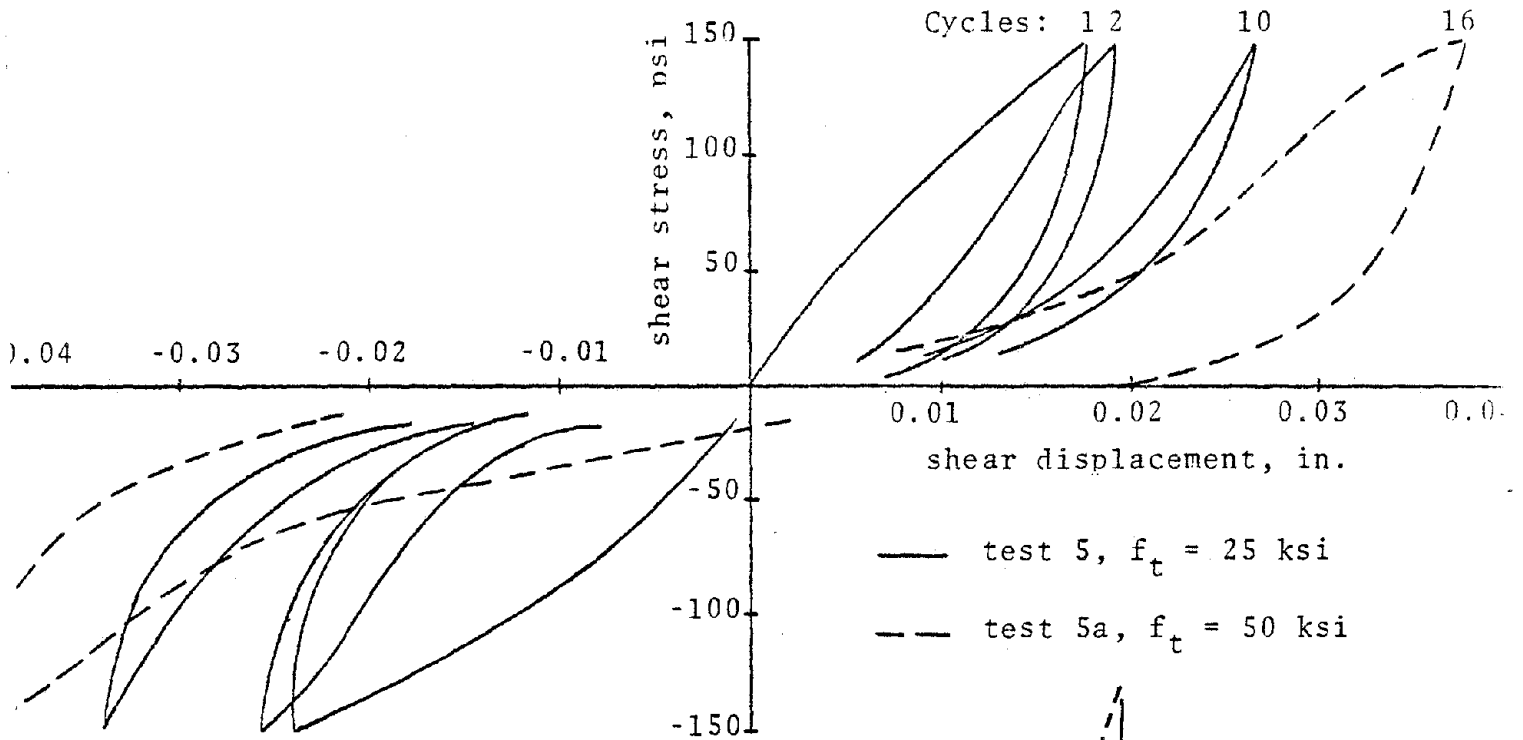


Fig. A6 - effect of axial stress on dowel action, #4 bar

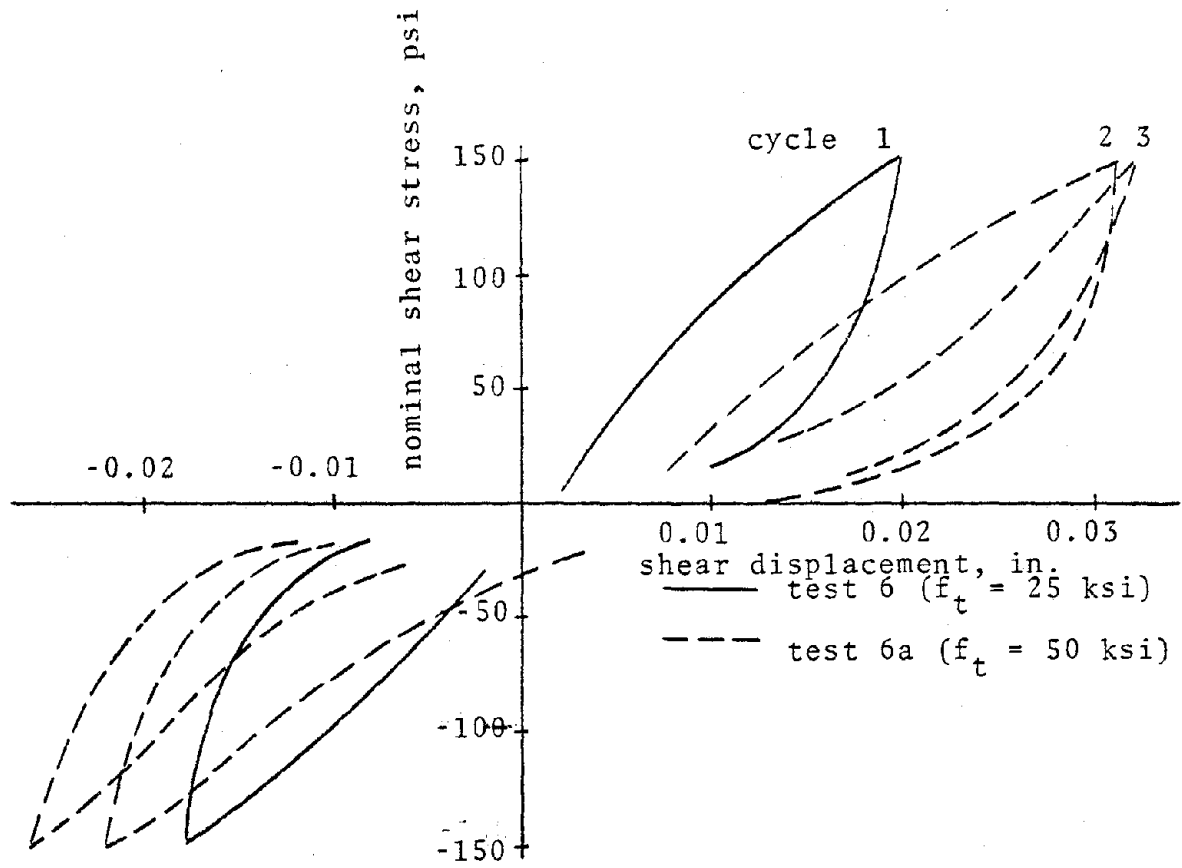


Fig. A7 - effect of axial stress on dowel action, #4 bar

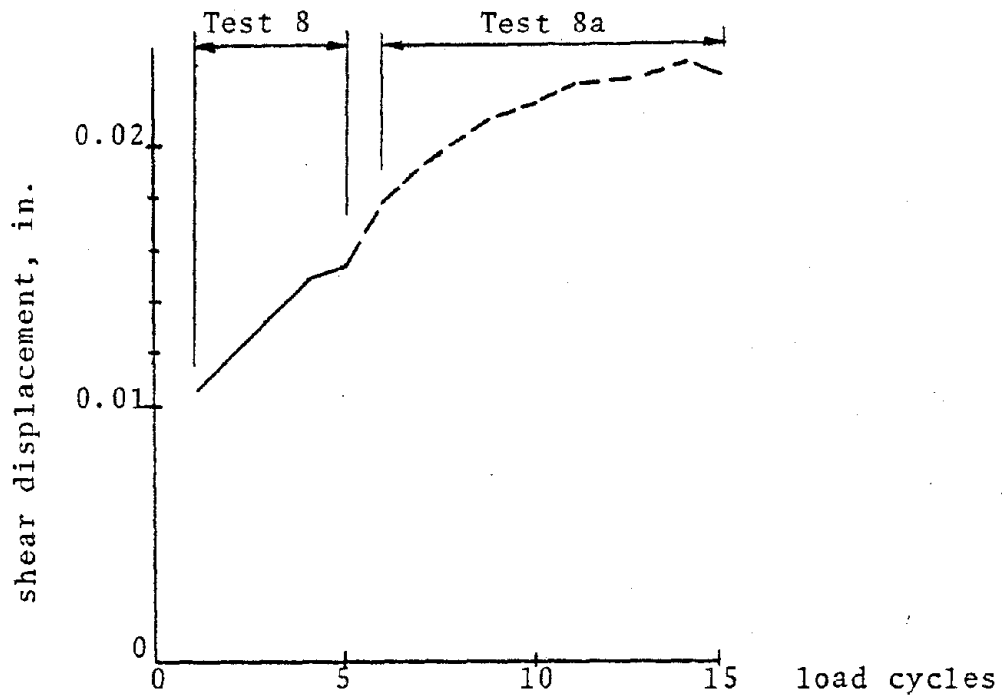
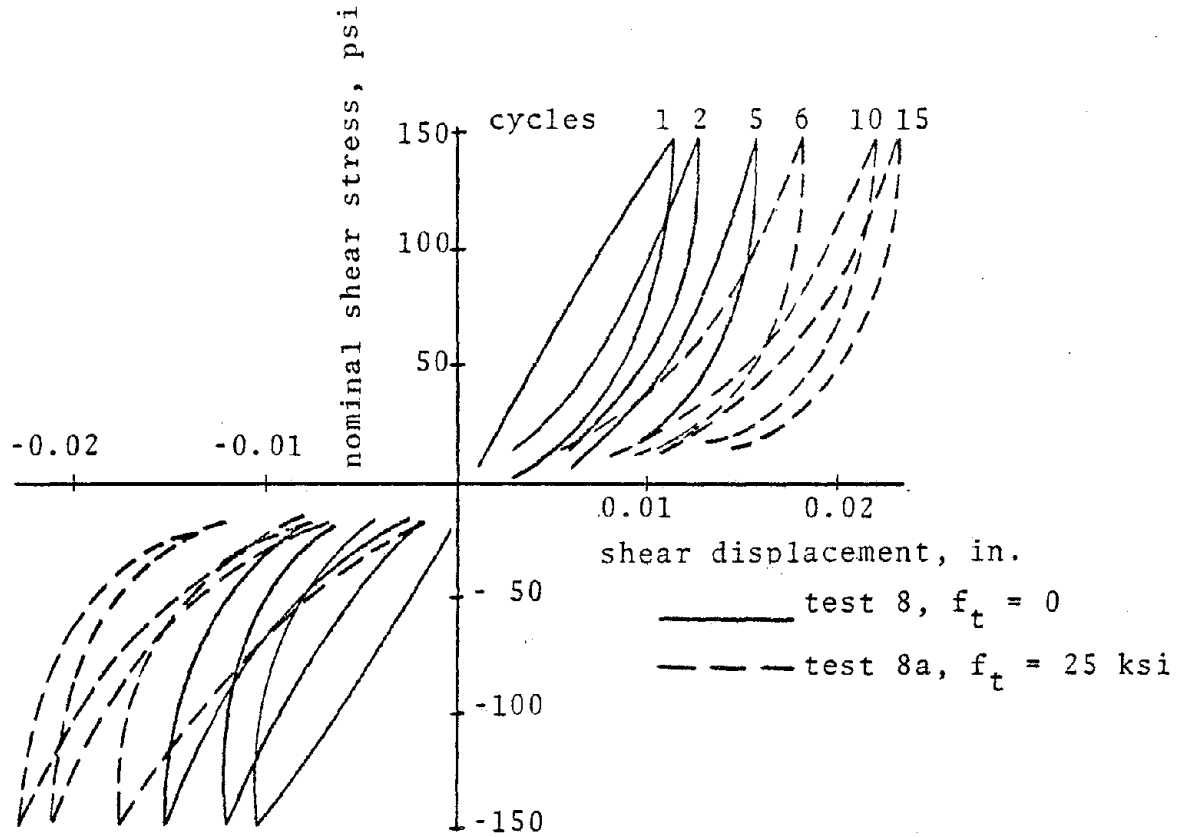


Fig. A8 - effect of axial stress on dowel action, #6 bar

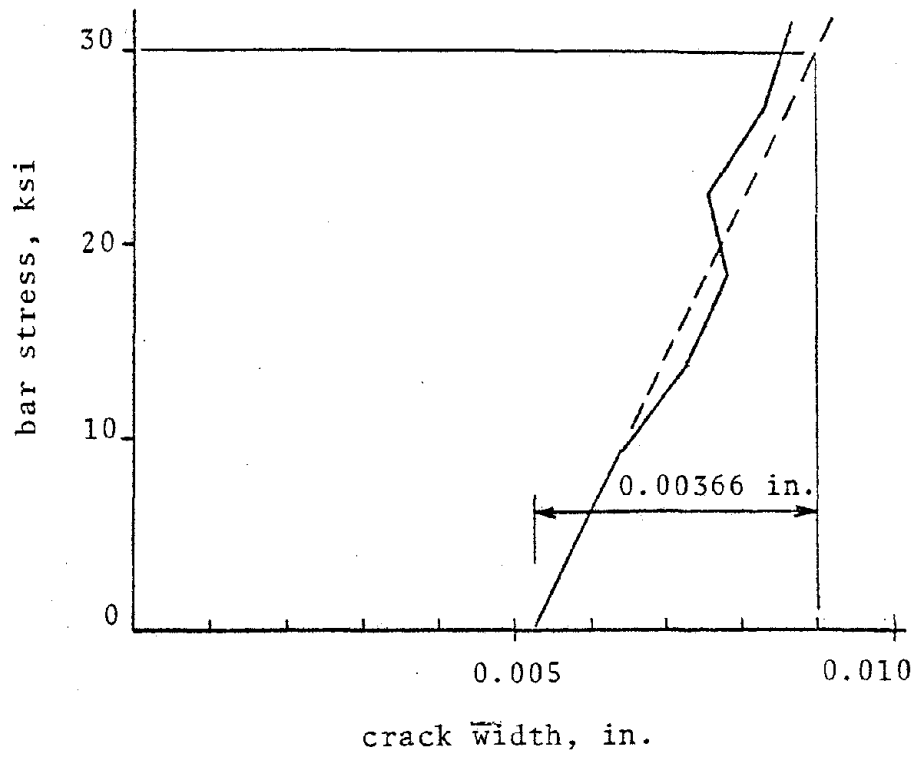
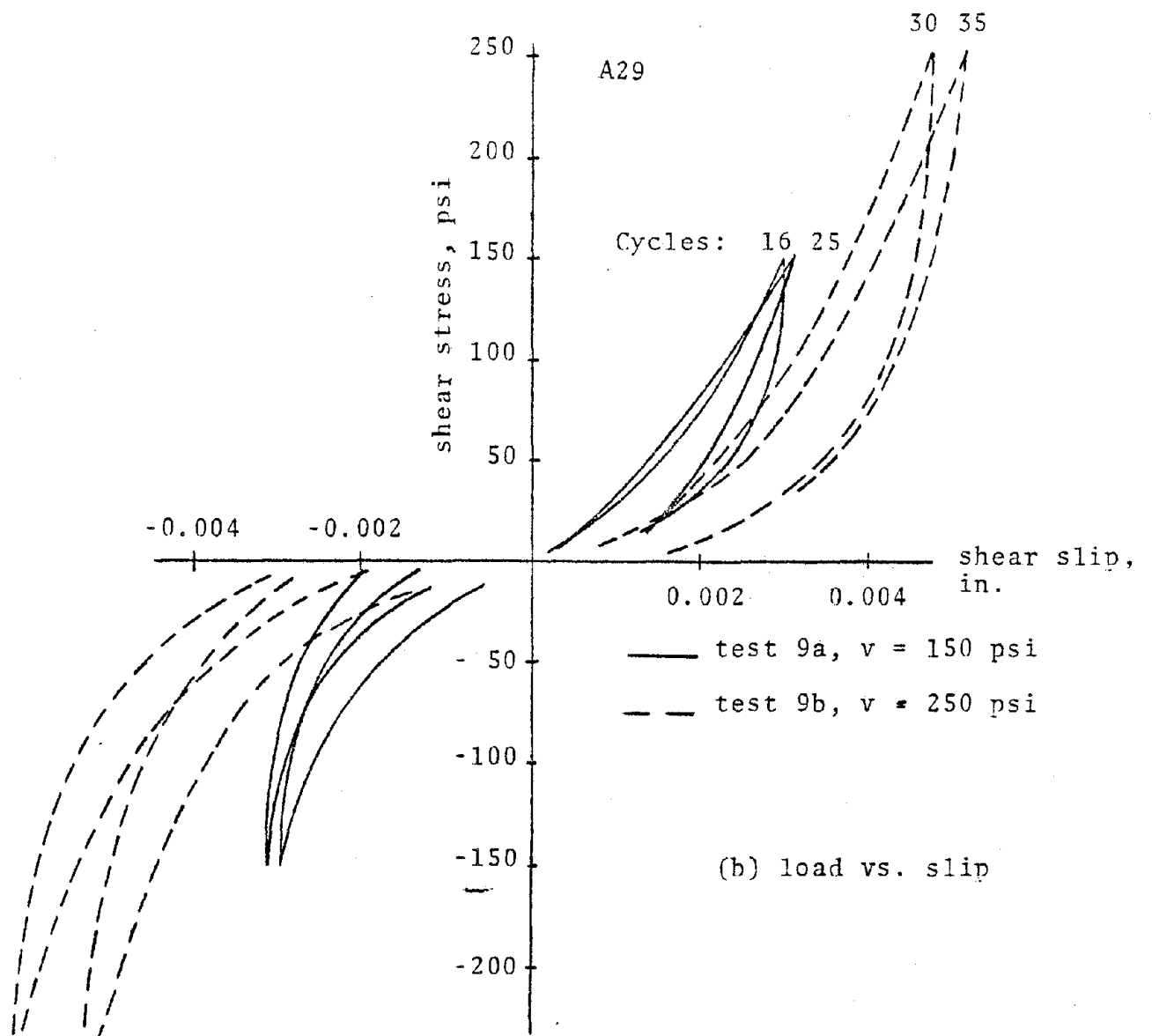


Fig. A9 - measurement of normal restraint stiffness of #6 bar after cycling



(b) load vs. slip

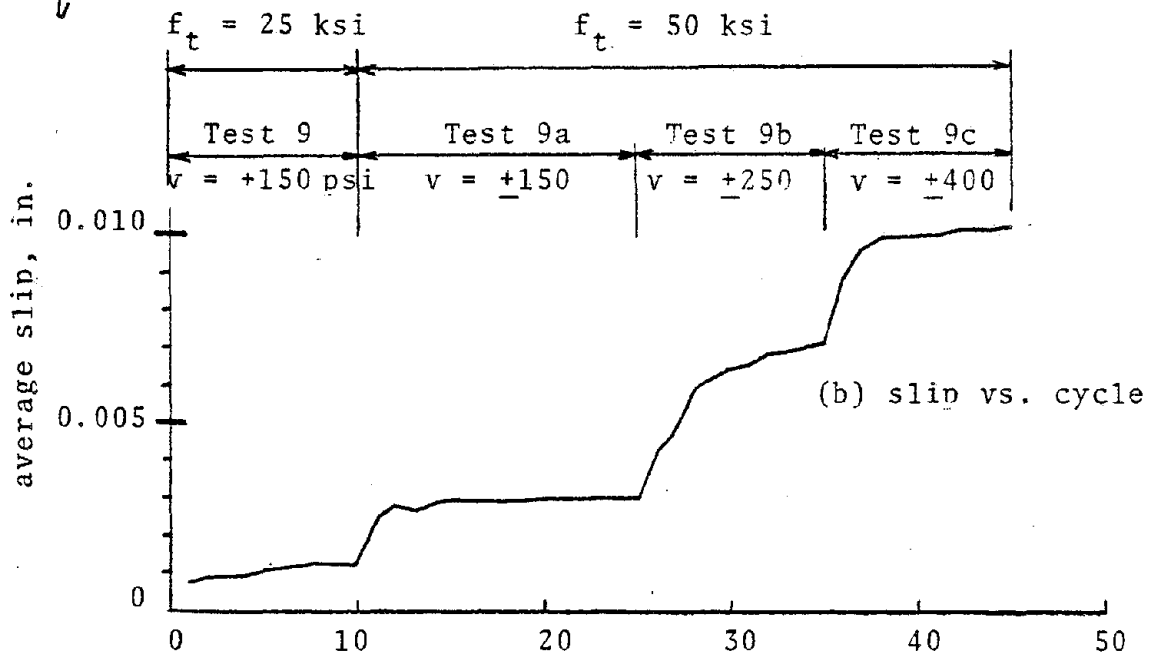
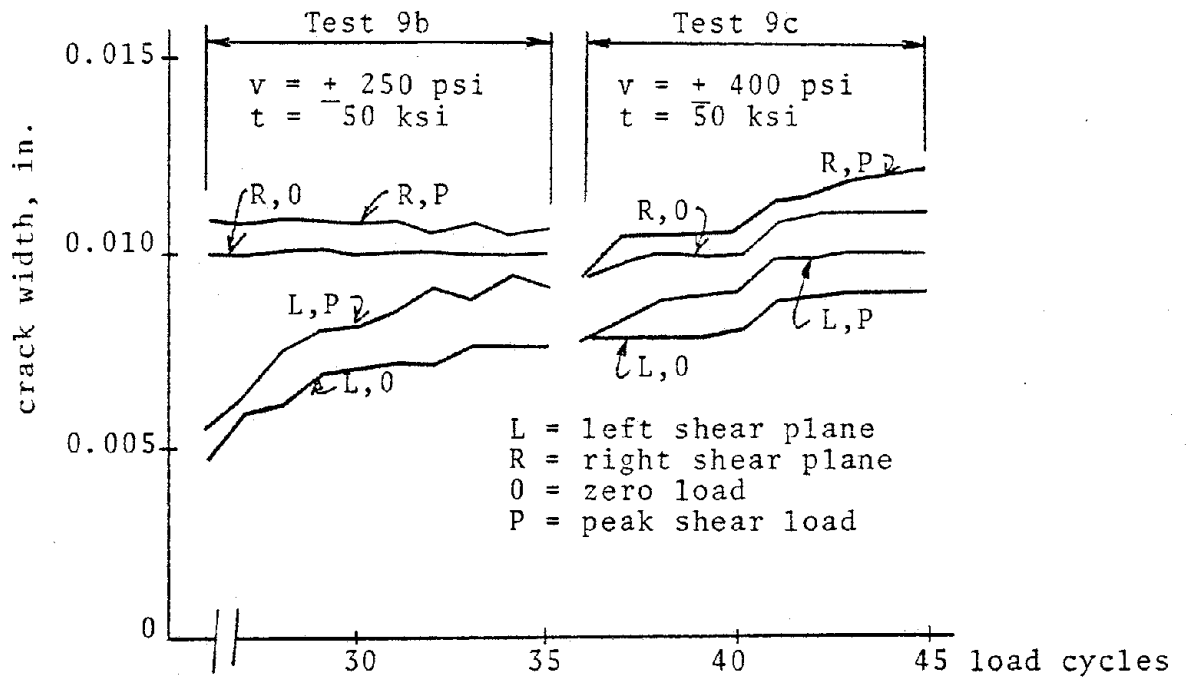
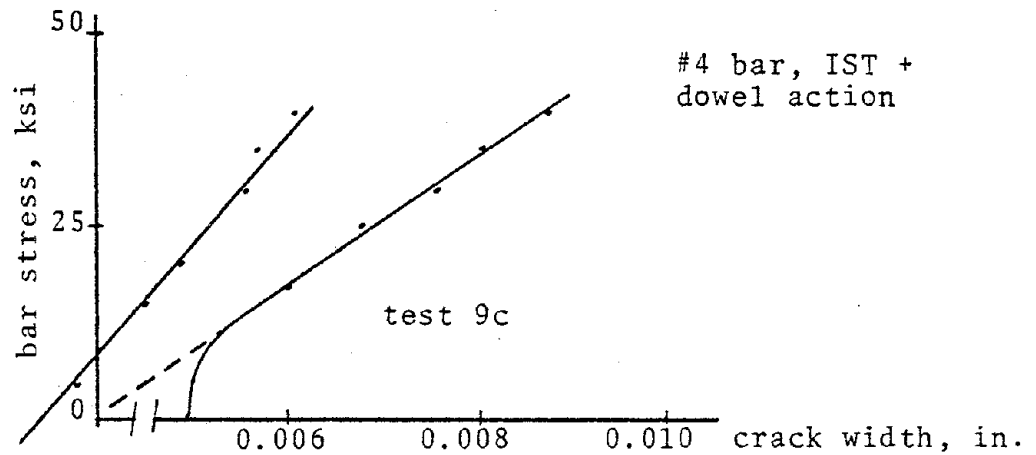


Fig. A10 - tests 9, 9a, 9b, 9c

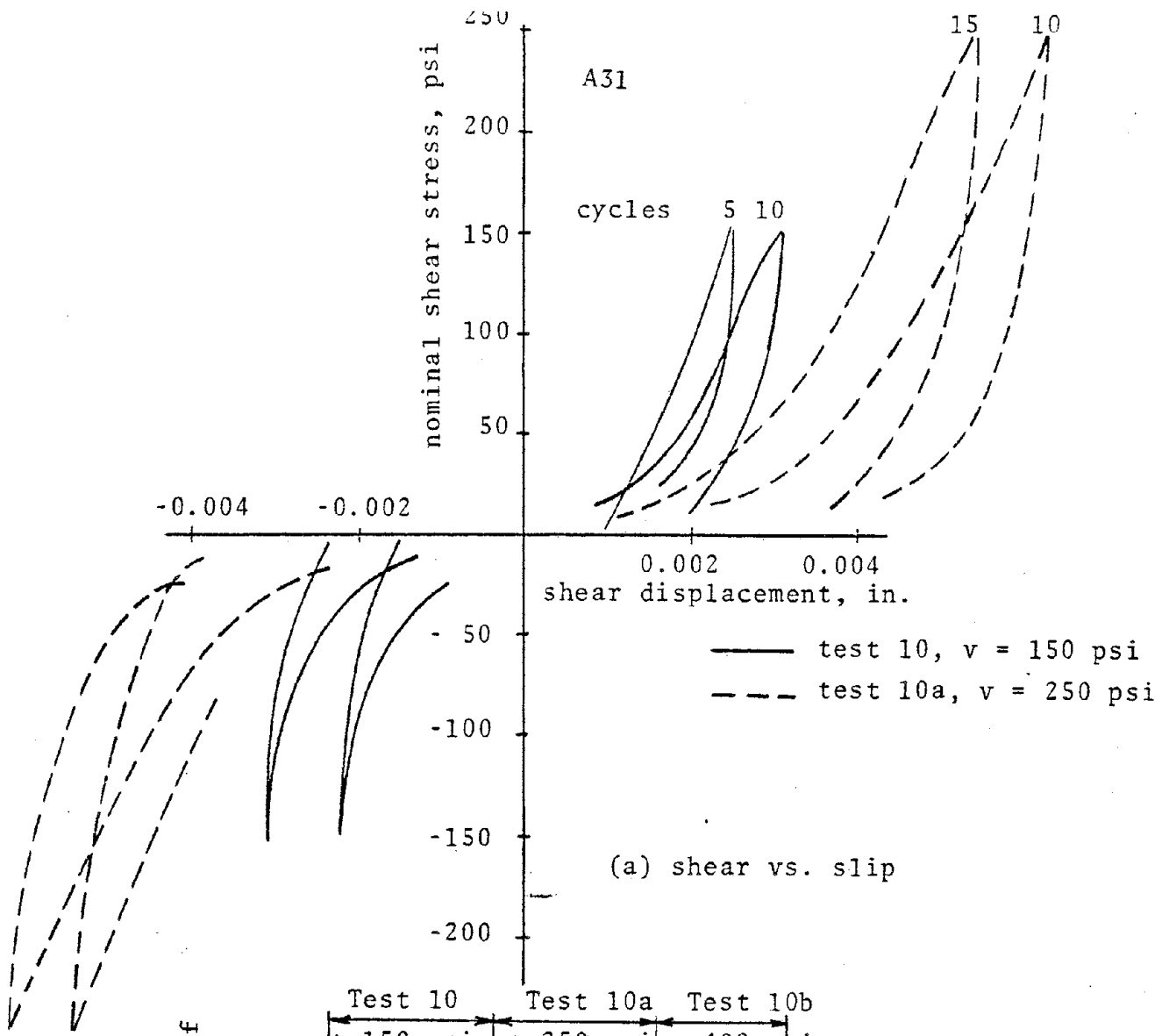


(a) crack widths for each shear plane at zero and peak shear loads

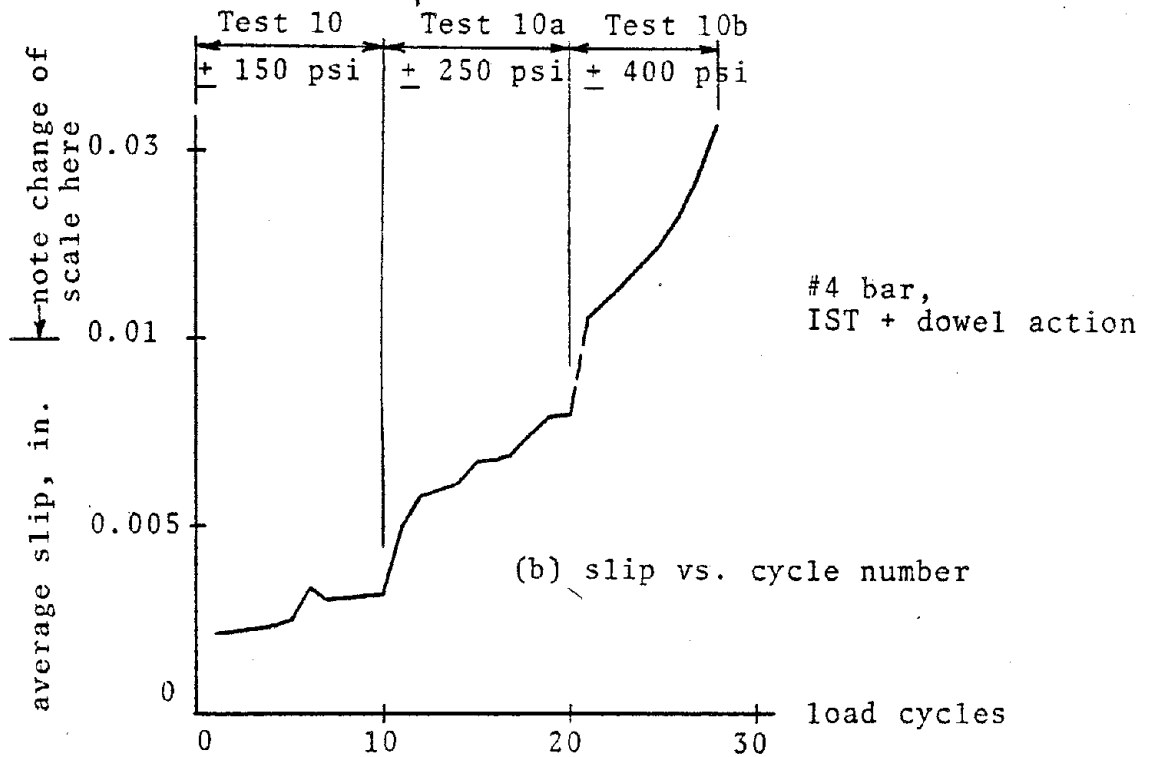


(b) bar stress vs. crack width

Fig. All - crack width variations, tests 9b and 9c



(a) shear vs. slip



(b) slip vs. cycle number

Fig. A12 - slip behavior, combined IST + dowel action, #4 bar

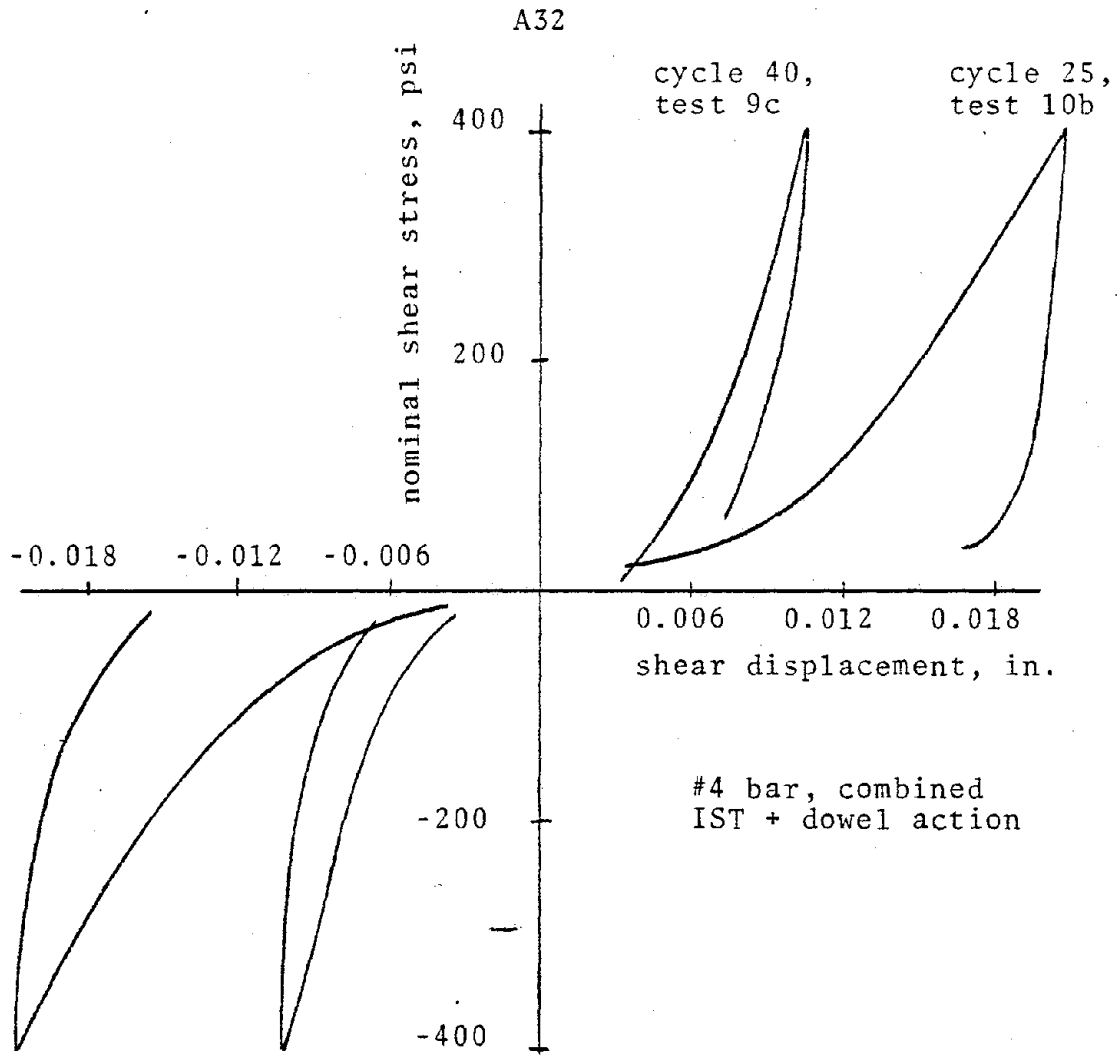


Fig. A13 - shear displacement during 5th cycle at $v = +400$ psi, $f_t = 50$ ksi, for tests 9c and 10b.

B. Dowel Action: A Mathematical Model for Unidirectional Shear;
and Dowel Experiments With Cyclic Shearing Forces

Dowel action of reinforcing bars in cracked, thick concrete sections is treated by considering the dowel as a beam on elastic foundation (Fig. Bla). Since the very high contact stresses in the concrete near the slip plane produce some crushing action, a portion of the bar with half-length b (Fig. Bla) is considered free to flex. The foundation modulus provided by the concrete is determined by cutting the concrete section into thin slices (Fig. Blb) and then analyzing a typical slice by plane stress elasticity methods. The loading on each slice is shown in Fig. B2 and is cosinusoidal in nature. The solution to this problem, given in detail in Ref. 2, provides foundation modulus values as well as giving stresses in the concrete around the dowel. It is considered an adequate solution up to the time of tensile cracking in the concrete; after cracking there may be a considerable adjustment in load carrying in both the dowel and concrete.

Values of circumferential tensile stresses in the concrete are

$$\sigma_{\theta} = 0.344 \left(\frac{2P}{\pi a} \right) \text{ at } \theta = 0$$

$$\sigma_{\theta} = 0.637 \left(\frac{2P}{\pi a} \right) \text{ at } \theta = \frac{\pi}{2}$$

Thus the tensile stress in the direction of the dowel force is highest, and the tensile force normal to the dowel force, which tends to produce a wedging action splitting, is only 54% of the maximum.

The foundation modulus k was determined from the average displacement (in the direction of the load) over the 60° sector of $\pm \frac{\pi}{6}$.

The behavior of the dowel in Fig. Bla is governed by

$$EI \frac{d^4 y}{dx^4} + ky = \text{loading}$$

The load V is applied at $x = -b$, and the total displacement at the slip-plane is determined by solving the equation for y and adding

the bending and shearing deformations of the free half-length b ;
it is

$$y_{(-b)} = \frac{V}{EI} \left[\frac{1+b\beta}{2\beta^3} + \frac{b(1+2b\beta)}{2\beta^2} + \frac{b^3}{3} + \frac{ba^2(1+\nu)}{2} \right]$$

where V = applied shear

EI = EI of the reinforcing bar

b = free half-length where concrete is crushed

$$\beta = 4 \sqrt{\frac{k}{4EI}}$$

k = foundation modulus

a = bar radius

The corresponding dowel stiffness is simply $V/2y_{(-b)}$.

The last term, $\frac{ba^2(1+\nu)}{2}$, in the above equation is the shearing deformation component. It can be shown that the effect of shear strain is limited to about 4% of the maximum displacement, regardless of bar size (Ref. 2).

Dowel stiffness values for one #11 bar (1 3/8 in. diameter) as a function of β and free half-length b are plotted as solid lines in Fig. B3. When $b = 0$, the stiffness reduces to

$$K = EI\beta^3 = \frac{a}{4} \sqrt[4]{\pi Ek^3}$$

and the stiffness varies linearly with bar diameter $2a$. This result is very different from the result obtained by assuming that the bar is fully fixed at both ends, in which case the stiffness varies with the fourth power of bar diameter.

The β value of 0.618 in Fig. B3 is for a 15 in. wide concrete specimen with one #11 bar and 4000 psi concrete strength. β decreases to 0.49 for a #14 bar and 0.39 for a #18 bar; the stiffness of one #18 bar is shown as a dashed line. Other concrete strengths would change β by the factor $\sqrt{\frac{F'_c}{4000}}$.

The rather sharp decrease in dowel stiffness with increasing free half-length is evident in Fig. B3.

The next step in the analysis is to combine the elasticity analysis for concrete stresses with the beam on elastic foundation solution. Assuming that concrete cracking initiates at a tensile stress of $7.5 \sqrt{f'_c}$, a #11 bar with $\beta = 0.618$, $b = 0$, and $f'_c = 4000$ psi gives $V_{\text{cracking}} = 650$ lbs. Similarly, equating peak radial stress to the compressive strength of the concrete, f'_c , the value of shear is $V_{\text{crushing}} = 3500$ lbs. for a #11 bar with the same properties as above. This result is quite approximate since the true stress level at which the concrete shows crushing is not known.

Bar bending stresses also may be computed from

$$f = M/S = -EI \frac{d^2y}{dx^2} S$$

$$\text{where } M_{\text{max}} = -\frac{V}{\beta} e^{-\beta x_1} \sqrt{\frac{1}{2} + \beta b + (\beta b)^2}$$

For a typical case of $f'_c = 4000$ psi, one #11 bar, $\beta = 0.618$, $b = 0.5$ in., and $V = 25$ k, the value of M_{max} is 25 in-kips and the corresponding elastic bar stress is 100 ksi, which means the bar will yield at the slip plane.

In the experimental phase of this study, five specimens with the geometry given in Fig. B4 were loaded with cyclic shear across planes where the shear force was carried by dowel action alone in a single reinforcing bar. The shearing forces were applied as shown in Fig. B4c and B4d, where the solid arrows indicate load in one direction (defined here as positive) and the dashed arrows represent a reversal of load direction (negative). Specific questions considered were: how the stiffness of dowel bars changes with increasing cycles of load, and what failure mode is to be expected.

Each specimen had a single #11 bar with greased 16 gage steel sheets separating the block into three sections. The loading for specimens 4 and 5 minimized the minor bending effects present in the first three tests. Specimens 1, 2, and 3 had no reinforcing other than the #11 dowel bar. Specimens 4 and 5 had transverse reinforcement, as detailed in Fig. B5, to assess its effect on delaying and restraining splitting effects produced by the dowel forces.

Slip of one block relative to the other was measured at each shear plane. Opening and closing tendencies of the "crack" were also measured. The major difficulty met in testing these specimens was the tendency for twisting to occur about the axis of the bar. The two ends of the specimens were seated in Hydrostone prior to loading, but some minor twisting action was still observed in some specimens. Twisting is highly undesirable because it may damage the concrete immediately surrounding the reinforcing bar. The cyclic loading sequence for the five specimens is given in Table B1. Specimen 1 was loaded in small increments from 5 k to 55 k. The other specimens were started at higher loads. Specimen 4 failed prematurely by local crushing at the 2 1/2 in. wide bearing plates used to support the specimen.

Discussion here will focus on Specimens 3 and 5; the complete results are given in Ref. 2. The increases in shear slip with load cycling are shown in Fig. B6 for the two specimens. In both specimens, cycling at loads of 30 or 35 kips (shear forces of 15 or 17.5 kips on each shear plane) produced only small increases in shear slip, while higher loads increased slip rather sharply. As in all specimens, the slips produced by negative loads were slightly larger than those from the positive loads.

Specimen 3, with no transverse reinforcement, failed by splitting along a warped vertical surface through the bar at $P = 70$ k (Fig. B7a) while Specimen 5, with transverse steel, failed at $P = 60$ k by splitting horizontally along the dowel (Fig. B7b). Specimen 5 showed first cracking on the 6th load cycle, with horizontal cracks beginning at the shear plane and extending out about 3 in. in the plane of the bar.

Load-shear slip relations for Specimens 3 and 5 are given in Figs. B8-B10. In all cases the shear load per bar is half the total applied load. The basic shapes of these curves are similar to those obtained on smaller dowels by Eleiott, and have a strong resemblance to the load-slip curves for interface shear transfer alone. However, the transverse stiffness of the dowel after "free slip" has occurred does not increase significantly with cycling as does the post-free slip stiffness of the interface shear transfer mechanism. The average

width of the hysteretic loop increases slightly with higher cyclic load levels, thus implying a higher percentage of equivalent viscous damping at high shear load levels.

The complete splitting failure of Specimen 3 permitted good inspection of damage to the concrete around the bar at the shear plane. A funnel-shaped volume of crushed concrete was observed, with visible damage extending about 1 in. in each direction from the slip plane. Similar damage was observed in Specimen 2, and other specimens must have suffered the same damage. It is believed that the higher shear slips in Specimen 5 (as compared to Specimen 3) were produced by the increased damage to the lower strength concrete of Specimen 5 (3000 psi in #5 vs. 4000 psi in #3).

The transverse reinforcement used in Specimen #5 had negligible influence on specimen strength.

Discussion of Results and Design Implications:

Several important points from Ref. 2 are presented here, including: (a) comparison of the dowel action analysis with results obtained from Fajardo's specimens and from interface shear transfer specimens, (b) prediction of dowel forces, bar stresses, and slips in typical containment vessels, and (c) overall conclusions.

Fajardo tested #11 bars in combined dowel action and interface shear transfer with a pre-defined unbonded length of bar at the slip plane. His specimen with a 1 in. unbonded length on each side of the shear plane had an average dowel shear stiffness after initial cycling of about 900 k/in, where the average stiffness is defined as the applied peak shear divided by the average of the peak positive and negative slips. This dowel stiffness value of 900 k/in was obtained by subtracting out the interface shear transfer stiffness of a specimen that had similar crack width and resisted shear by interface shear transfer alone.

The corresponding dowel force on each bar was then about 11 k. The analysis of this section can be applied with a free half length of 0.55 in. to get a predicted dowel stiffness of 580 k/in for each bar, as compared to the 900 k/in obtained by subtracting out the IST stiffness from Fajardo's Specimen #1. While the results are not conclusive they are quite encouraging.

An analysis for slips and bar forces in a typical containment vessel is given in Ref. 2. A 4.5 foot wall thickness with $\rho = 1.39\%$ for vertical #18 bars was assumed, and $f'_c = 4000$ psi was used. For an initial crack width of 0.015 in. and an applied maximum shear stress of 100 psi, the following results are obtained for various assumed free half lengths of each bar at the crack:

free half-length, in.	0	0.5	1	2	4	6
shear force per bar, k	11.2	8.5	6.4	3.7	1.5	0.7
% of shear carried by dowel	39	30	22	13	5	2
axial stress in bar, ksi*	30.2	30.4	30.6	30.8	30.9	31.0
bending stress in bar, ksi	8	9	9	8	6	4
shear stress in bar, ksi	2.8	2.1	1.6	0.9	0.4	0.2
slip at crack, thousandths of in.	5	6	6.5	7	8	8

A second analysis was done for the case of a maximum shear stress of 300 psi, which is the upper limit on dynamic shear stresses calculated earlier. The free half-length is estimated at 1.63 in., which gives a dowel force of 13.9 k/bar, a peak bar bending stress of 25 ksi, and a slip of 0.021 in. at the crack. The dowel load is less than the load needed to produce splitting in the #11 dowel tests reported here, but the latter specimens did not have tensile stress superimposed on the dowel forces, nor was the concrete in biaxial tension as it would be in a containment.

Conclusions that may be drawn from this work include:

- a. combined stress effects in reinforcing bars at crack locations may be appreciable and should be considered in design.
- b. potential splitting effects from dowel action must be accounted for in design. They appear to be much more dependent on

* Obtained from 28.8 ksi due to pressurization, plus the axial force generated by over-riding in the IST mechanism.

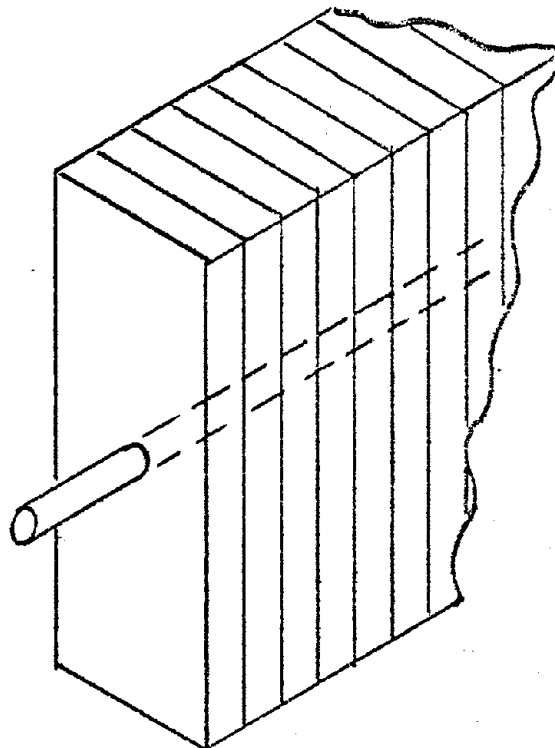
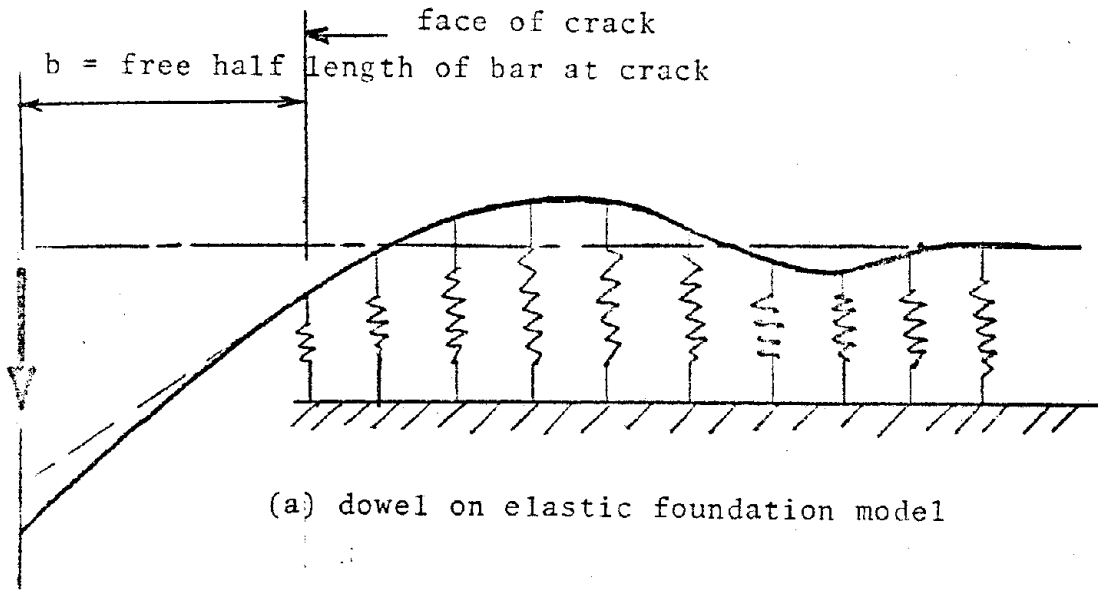
B7

shear stress level and on bar axial tension than on number of load cycles. Biaxially tensioned specimens are needed to resolve the many unanswered questions about dowel effects in containment structures.

Note: Loads below are twice the shear force on the #11 bar.

CYCLE NO.	SPECIMEN				
	1	2	3	4	5
1	5 k	30 k	20 k	45 k	30 k
2	10	35	35		30
3	15	35	35		30
4	20	35	35		30
5	20	45	35		30
6	20	65	35		30
7	25	65	35		30
8	30	65	35		30
9	35	80	35		30
10	35		45		30
11	35		50		40
12	40		70		40
13	45				40
14	55				40
15					40
16					60

Table B1 - Load sequence for dowel
action tests



(b) longitudinal slices of concrete

Fig. B1 - idealized model for dowel action analysis

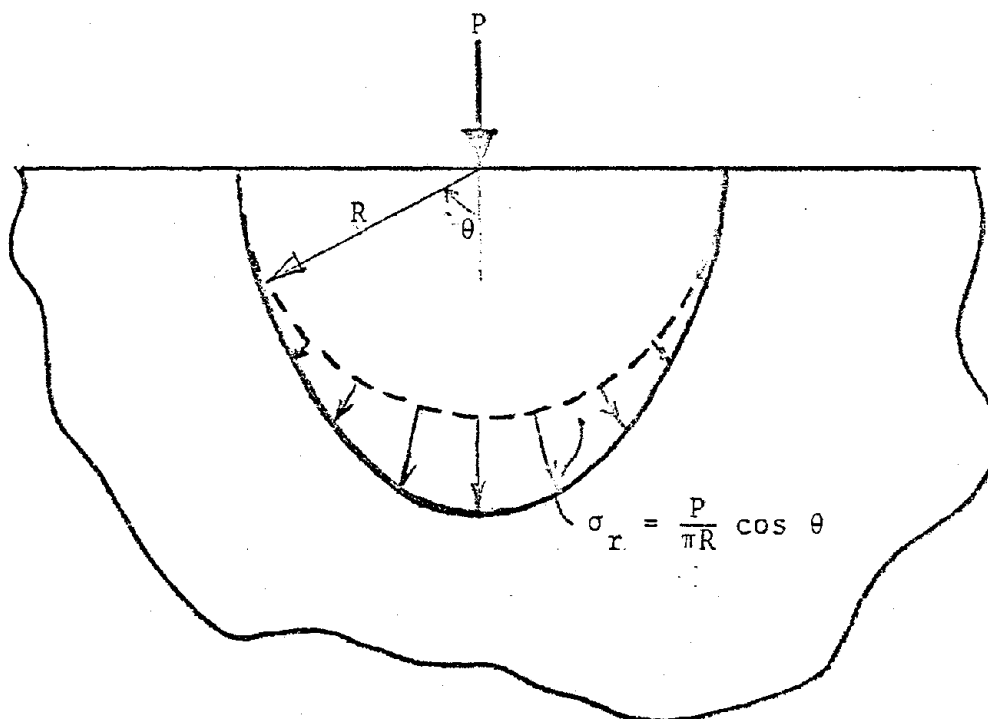


Fig. B2 - action of dowel of concrete

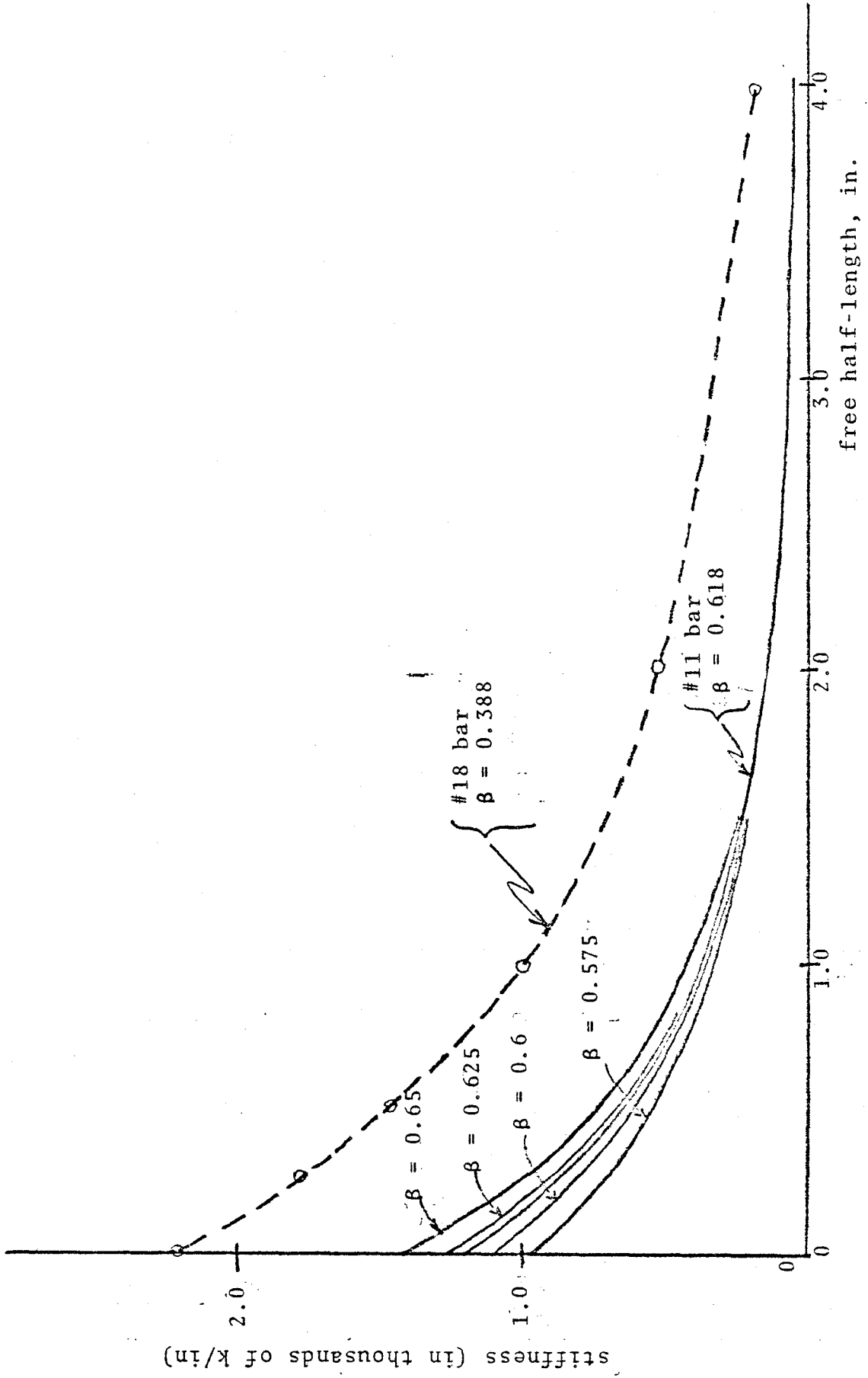
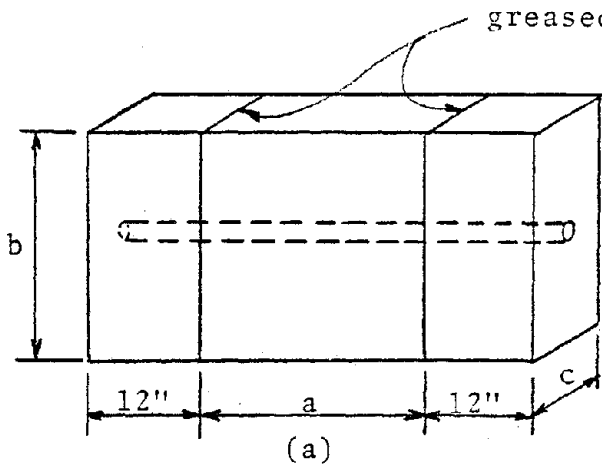
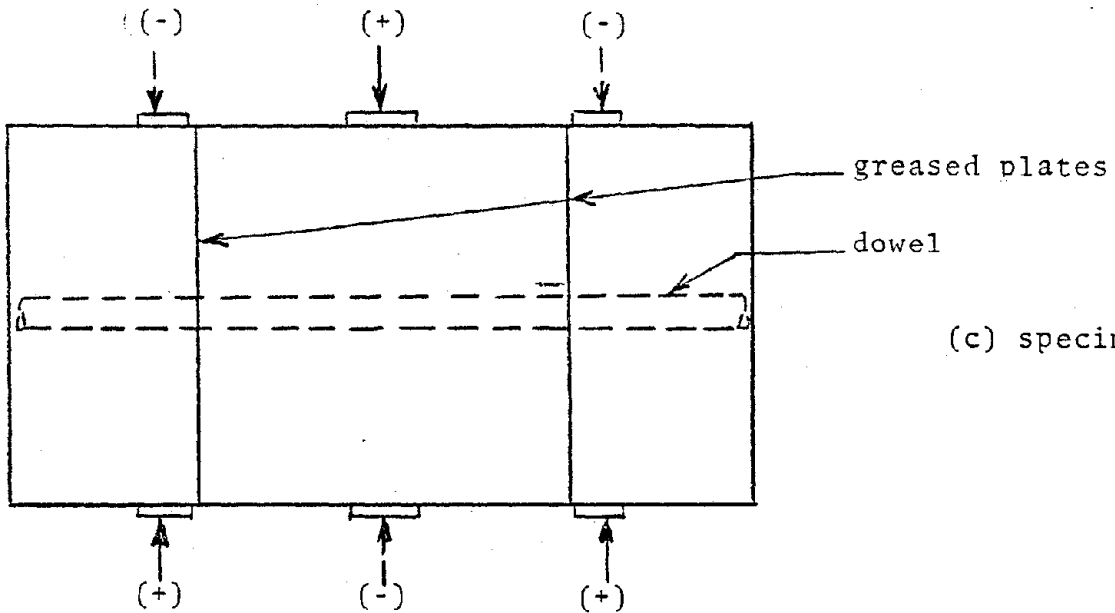


Fig. B3 - dowel stiffness as a function of free half-length

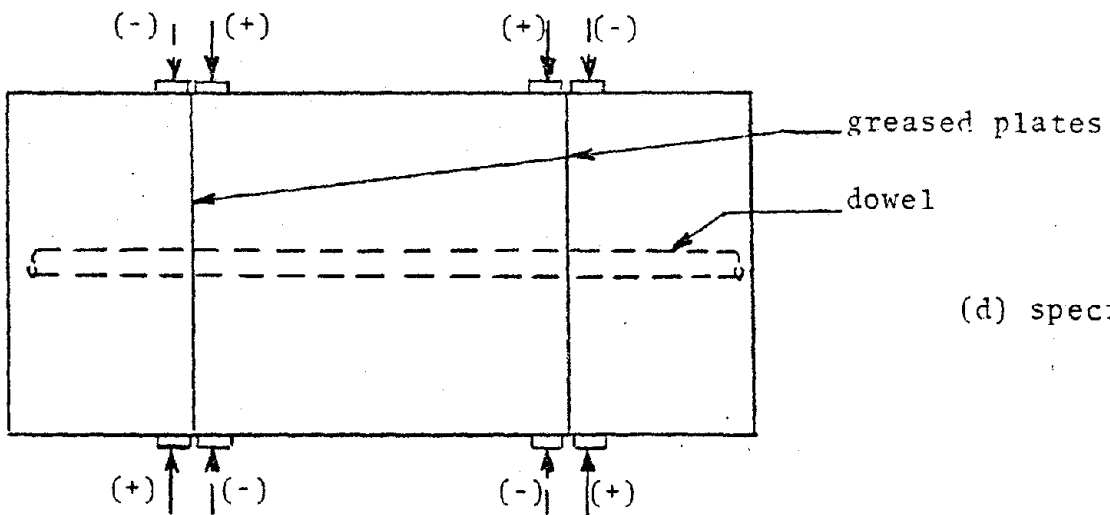


Spec.	a, in.	b, in.	c, in.	f'_c , psi
1	24	24	8	4020
2	12	24	12	4130
3	12	24	8	4080
4	24	20	$7\frac{1}{2}$	3200
5	24	20	$7\frac{1}{2}$	3080

(b)

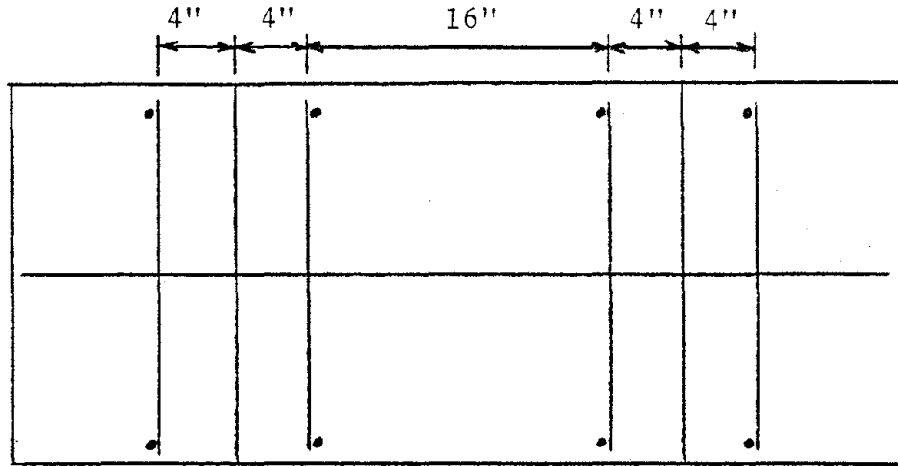


(c) specimens 1-3

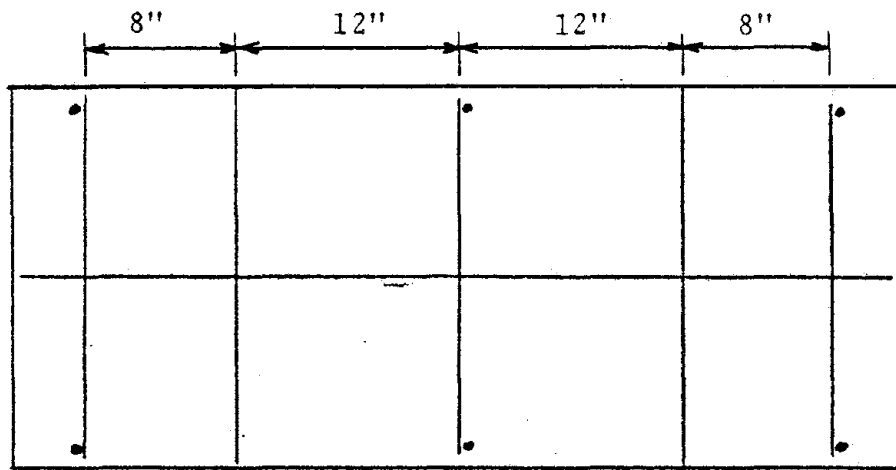


(d) specimens 4 &

Fig. B4 - dowel specimen geometry



specimen 4



specimen 5

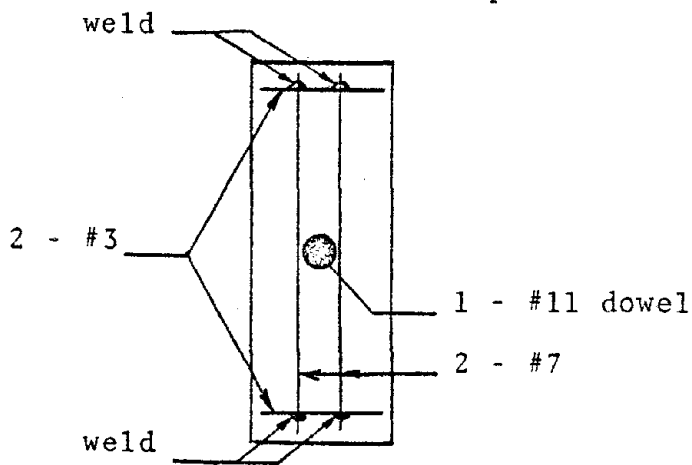


Fig. B5 - details of transverse steel in specimens 4 & 5

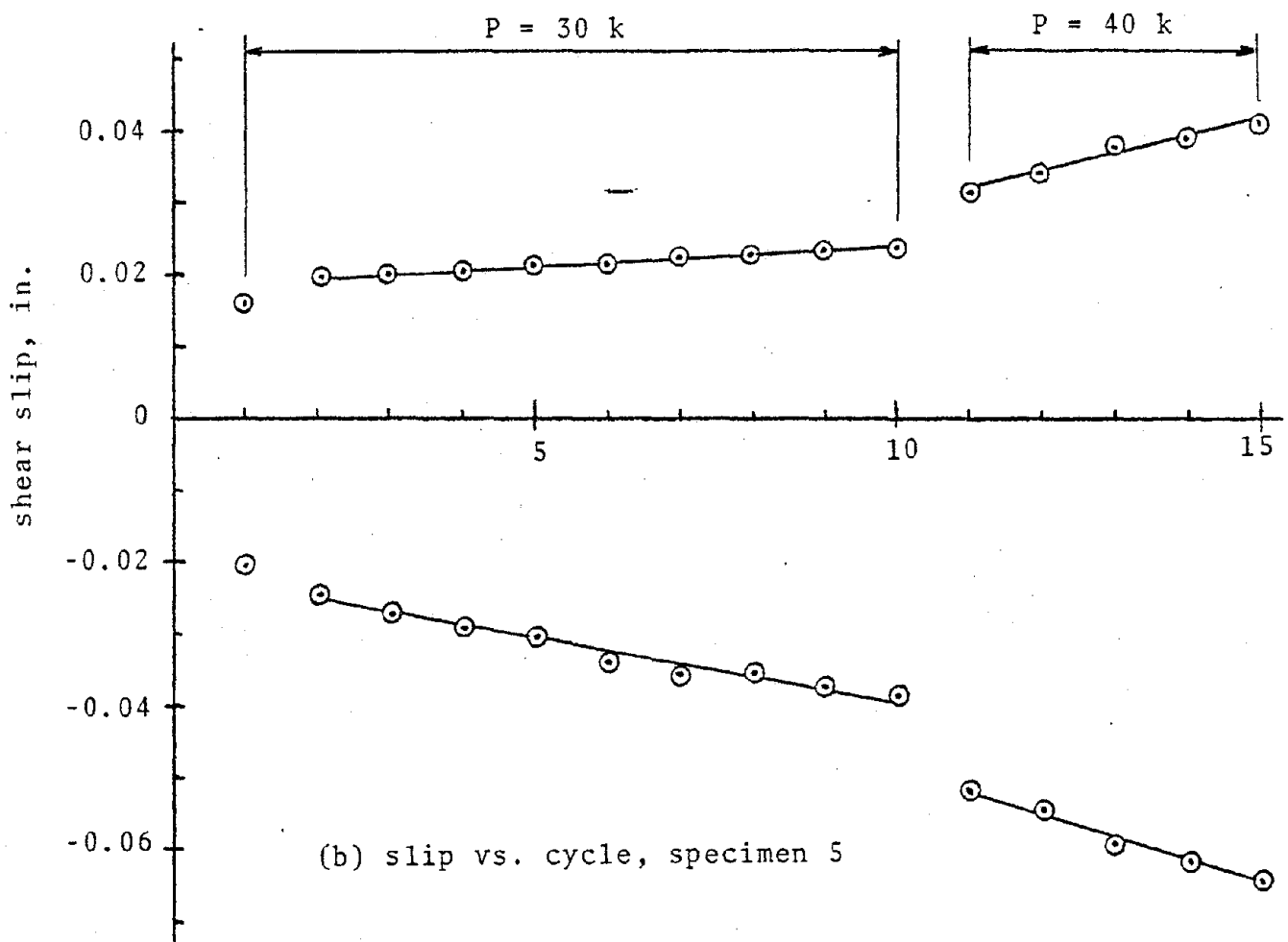
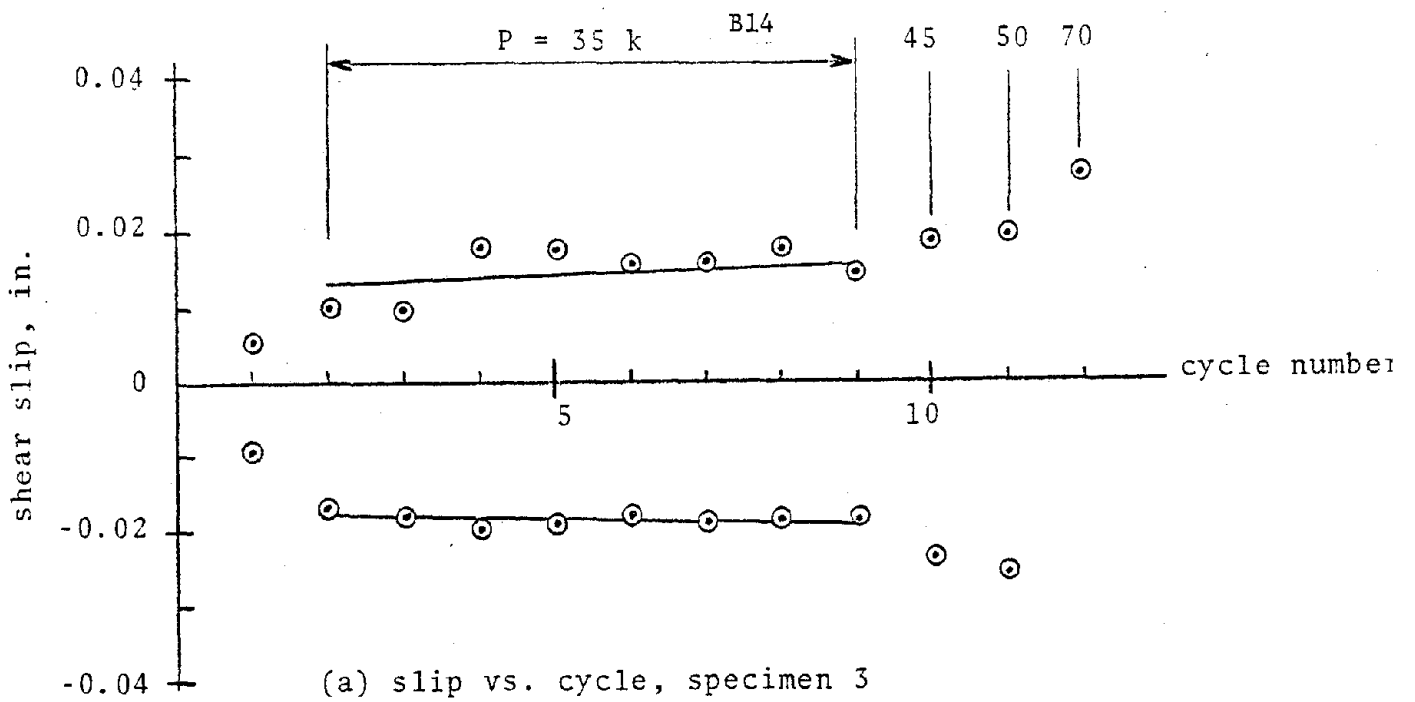
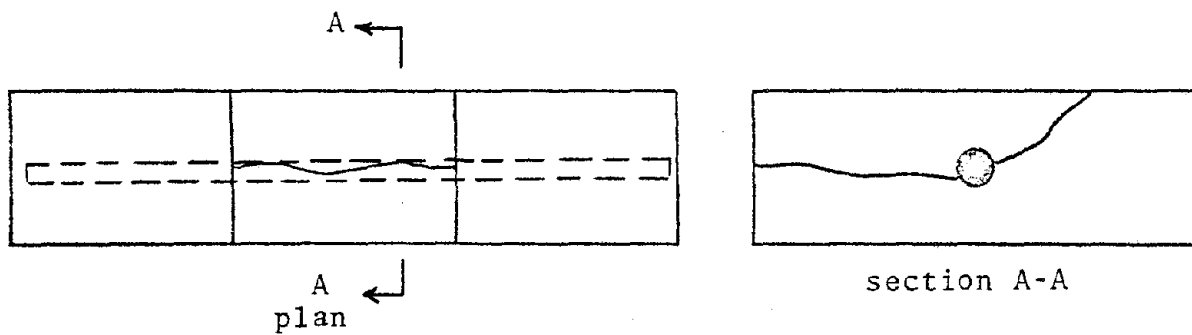
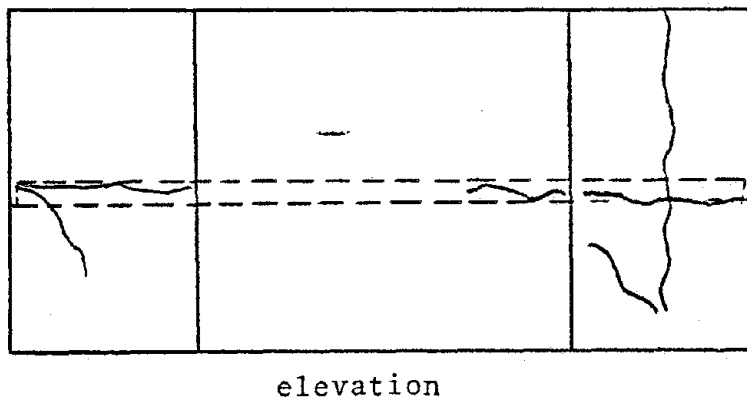


Fig. B6 - slip as a function of cycling, specimens 3 & 5



(a) specimen 3



(b) specimen 5

Fig. B7 - failure modes of specimens 3 & 5

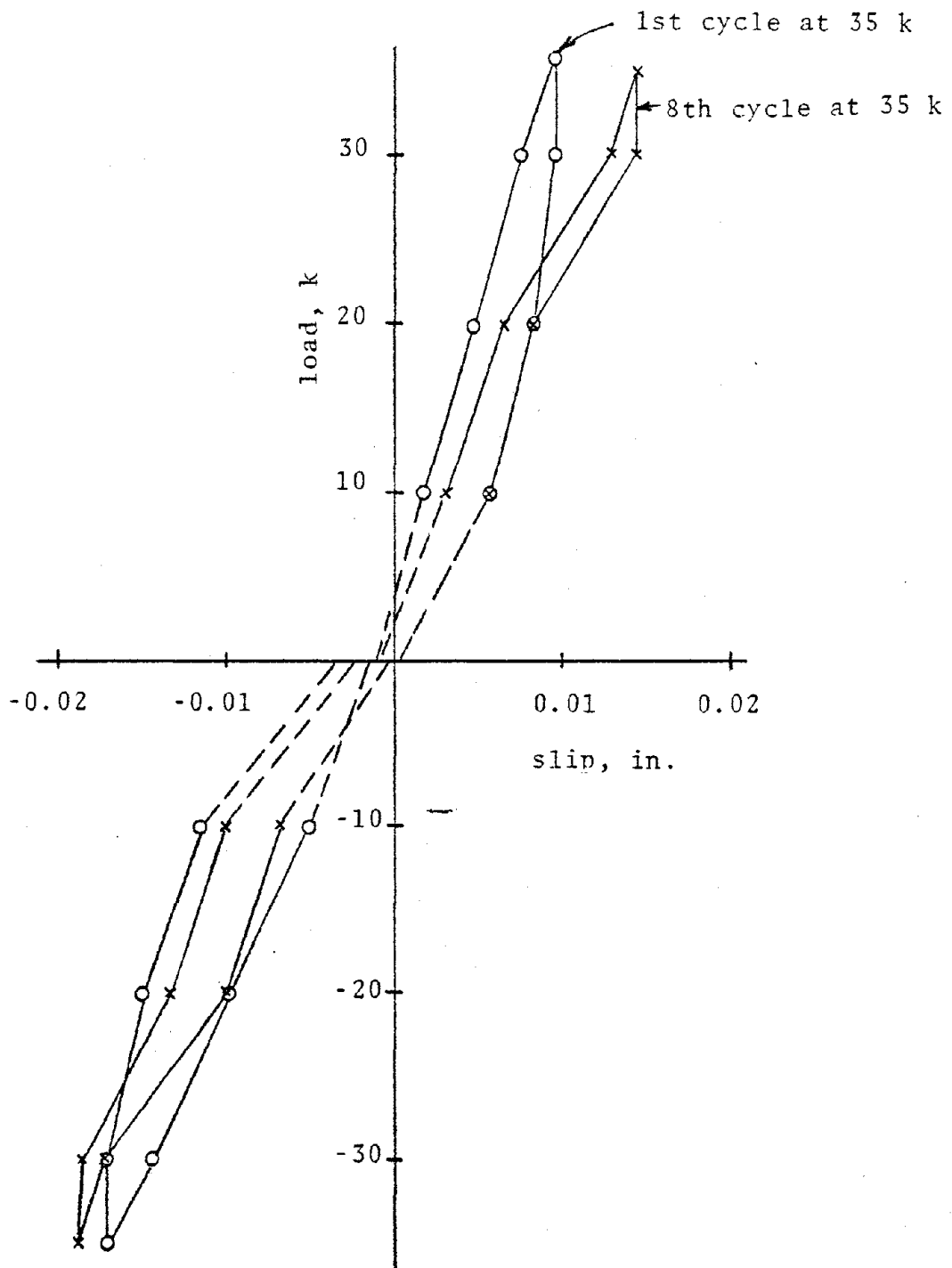


Fig. B8 - load vs. slip, specimen 3

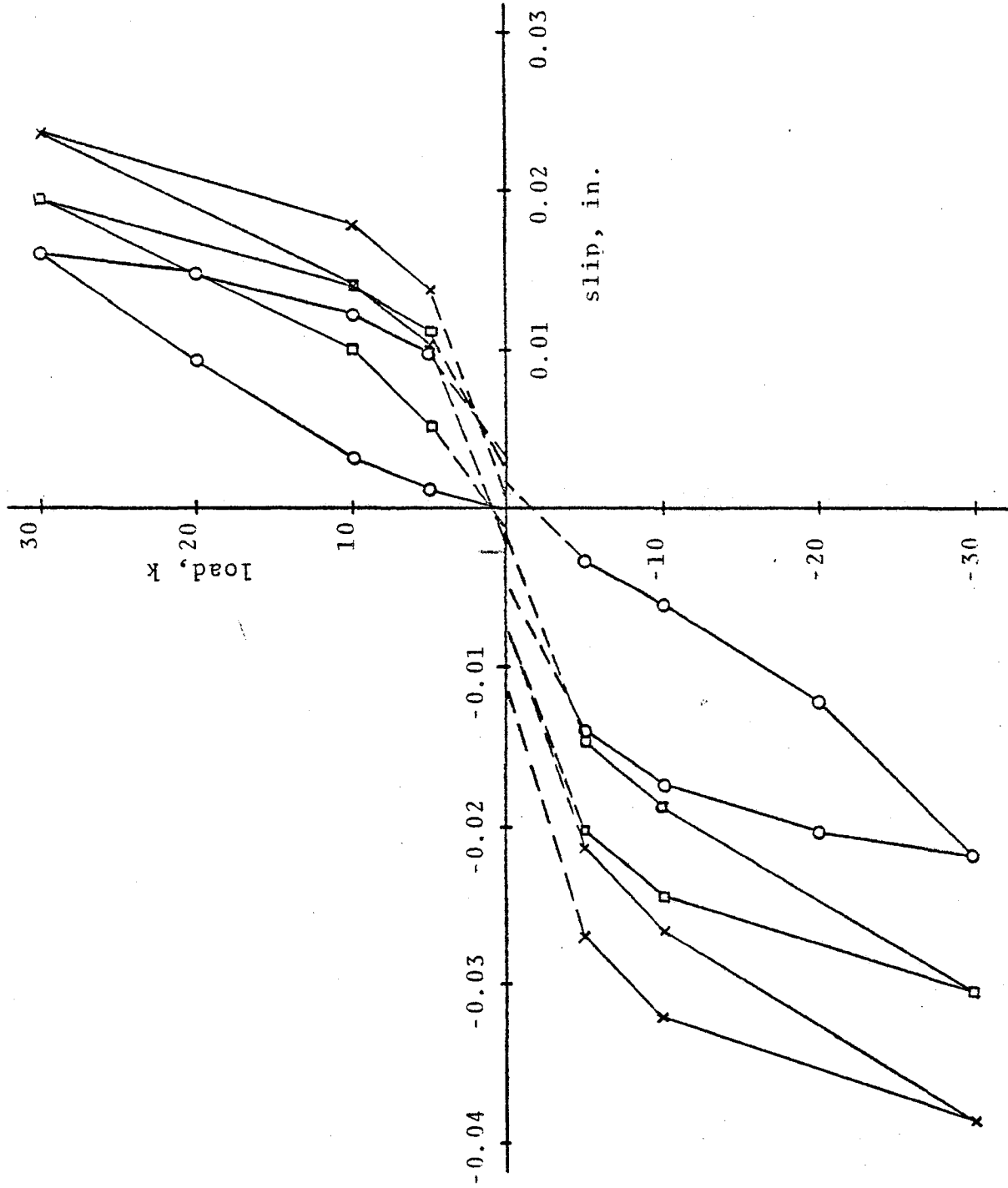


Fig. B9 - load vs. slip, specimen 5, cycled at ± 30 kips

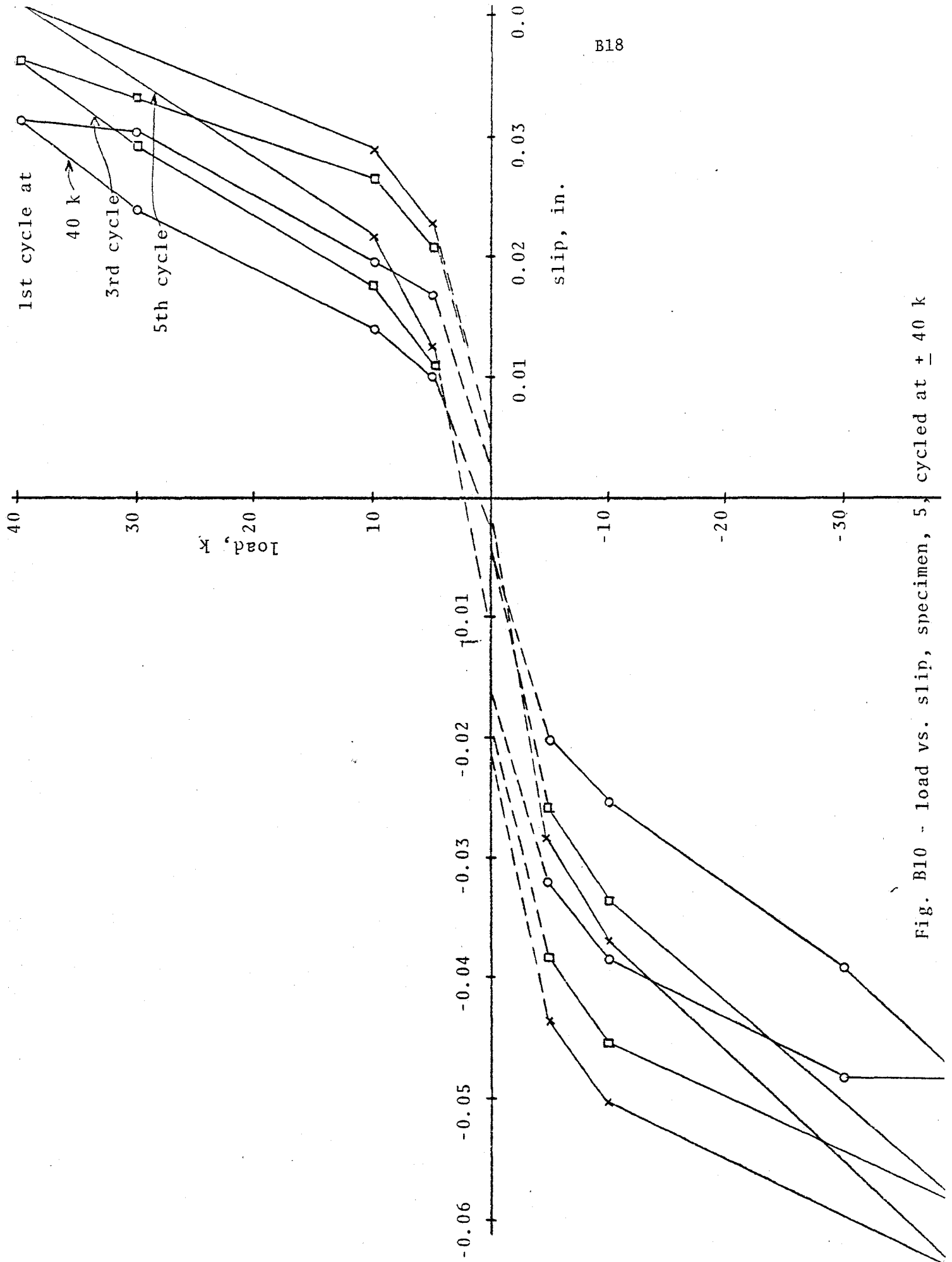


Fig. B10 - load vs. slip, specimen, 5, cycled at ± 40 k

C. LARGE-SCALE TESTS WITH COMBINED AXIAL TENSION AND DOWEL EFFECTS

The experimental program involving large-scale specimens was continued during the past year. In addition to the interface shear transfer and dowel force mechanisms, the effects of axial tension in the bars was studied. Such tension would occur in vertical bars of a nuclear containment vessel when internal pressure develops. Dowel bars are also in tension in other applications, such as in tall shear wall structures under severe seismic loads.

Two types of tests were used in this study. One was the same setup (Fig. C1) as employed from the beginning of the research, except the embedded #9 bars were tensioned to a certain stress level or until the initial crack width reached the desired magnitude. Two such block-type specimen tests are reported here.

The second type of test was essentially a large beam loaded transversely by two forces in such a manner that a plane of zero moment existed, (Fig. C5(a)). The specimens were precracked at this plane by tensioning the #14 longitudinal bar using an external force system. The transverse loads applied reversed cycling shear forces at the crack plane. Four specimens were tested.

Block Tests with Axial Tension

In the beam-type tests reported in the next section, the self-weight of both the specimen and the axial loading system made it difficult to achieve a uniform crack width at the shear plane before the initiation of the cyclic shear test. This problem was met by shifting away from the beam tests and using the modified block test setup shown in Fig. C1. In this test an independent frame is used to sustain the vertical tensile stresses applied to the reinforcing bars. A vertical beam distributes the applied horizontal load (shearing force) in the required proportions to the top and bottom concrete blocks. By moving the beams in the vertical plane, the shear stress acting in the shear plane is reversed. There is no moment at the crack location.

The specimen cross-sectional shearing area was 225 in^2 . Four #9 reinforcing bars ($\rho = 1.78\%$) extended through the 24 in. high specimen and were locked off against the independent stressing frame. The shear plane at mid-height of the specimen was formed

by tensioning the reinforcing bars. A crack-initiating groove formed into the specimen during casting controlled the crack location. The reinforcement was instrumented with internal strain gages, 3/8 in. gage length, placed 1 in. above and below the shear plane. The axial load induced in the reinforcement was measured by external strain gages.

After aligning the specimen in the loading frame, the crack at the shear plane was produced and an axial stiffness test was conducted to determine the reinforcement stress necessary to impose the desired crack width. Subsequently, the specimen was cycled for 25 cycles, of which cycles 1, 15, and 25 were loaded incrementally for detailed measurements of slip and reinforcing bar strains. An axial stiffness test was also conducted at the end of the cycling.

The results of two tests conducted on specimens with equal percentages of reinforcement ($\rho = 1.78\%$) but different initial crack widths are presented.

The first specimen had an initial crack width of approximately 0.02 in. that was formed by tensioning the bars. The bars were stressed to 33.1 ksi during the simultaneous shear loading of ± 160 psi. In Fig. C2(a), the average horizontal slip is plotted against the applied shear stress for cycles 1 and 15. The shape of both curves may be roughly characterized by a bilinear relationship. Peak values of slip as a function of cycle number are shown in Fig. C3(a). Observations include:

- a. The load at which "hardening" of the load-slip relationship is observed, decreases with increased cycling.
- b. After the 15th cycle, there is no appreciable increase in the horizontal slip of the specimen (Fig. C3(a)).
- c. The ability of the specimen to absorb energy decreased with increasing number of cycles.

The initial crack width of 0.02 in. did not increase measurably with increasing shear stress in any of the cycles, nor did it change with cycling (Fig. C3(a)). It was found, however, that maximum strains recorded by several internal strain gages were of the order of 2500 micro-in/in. (Fig. C4). The shape of the strain vs. shear load curve is very similar to that observed for horizontal

slip vs. shear load. The magnitude of the strains on the surface of the reinforcing indicates that the bars were partially plastic at 1 in. from the shear plane.

Specimen 2, also reinforced with four #9 bars, was tested with an initial crack width of 0.01 in. and an applied axial load during shear loading of 21.4 ksi. The horizontal slip is plotted against the applied shear stress in Fig. C2(b) for cycles 1 and 15, and maximum slip values for each cycle are given in Fig. C3(b). Comparing load-slip curves for specimens 1 and 2 (Figs. C2(a) and (b)), the following observations can be made:

a. For specimen 2, the shear stiffness during cycle 1 remains essentially constant up to maximum load, and it is higher than in specimen 1.

b. The horizontal slip attained at cycle 15 is approximately equal to that obtained in cycle 1 for specimen 1, showing the rather substantial reduction in slip as the initial crack width decreases.

The earlier observations (b) and (c) made for specimen 1 are also valid for specimen 2. As for specimen 1, there is little difference in crack width variation with increased cycling (Fig. C3(b)).

Further tests are underway to evaluate the effects of several important variables, namely, reinforcement diameter, level of axial stress in the reinforcement, concrete cover, and level of shear stress. Such tests are imperative to fully understand dowel action and interface shear transfer under cyclic loading.

Beam Tests

The beam-type specimen shown in Fig. C5(a) was loaded through two steel beams that reacted against the concrete specimen through rollers. With only the two rollers designated as (+) in position between the specimen and each loading beam, the shear and moment along the beam are as shown in Fig. C5(a). This load system produces shear but no moment at the critical shearing plane (neglecting dead weight effects). The direction of shear is reversed by removing the (+) rollers and loading through the four (-) rollers.

Each of the four beam-type specimens had a 225 in² shearing area with a single #14 reinforcing bar centrally located in the

specimen. The longitudinal bar was stressed until a crack occurred at the shear plane at mid-length. The weight of the beam and the tensioning frame produced variations in the crack width over the depth of the specimen. This configuration, which theoretically seems fine, was in reality very difficult to work with, particularly for the case of a single bar in the middle of the concrete.

In Specimen 1 the average crack width was about 0.020 in. and the axial force in the single #14 bar was 26 kips, or 12 ksi stress. At a shear stress of 100 psi the slip was 0.008 in. and the crack width increased by about 0.002 in. Unfortunately, the secondary reinforcement (which was about 4 in. away from the crack) was insufficient, and flexural cracks and subsequently large diagonal tension cracks developed because of the combined effect of tension and shear in the concrete. At a shear stress of 450 psi the test was discontinued. The inclination of the major diagonal crack was somewhat less than 45° from the axis of the beam and passed through the intersection of the bar axis and the shear crack.

Specimen 2 was identical to Specimen 1 and also had an average crack width of about 0.02 in. It was cycled twice at ± 100 psi shear stress with a bar tension of 16 ksi. Then four cycles at the same shear stress but with a bar tension of 29 ksi were applied, followed by two cycles at ± 125 psi and a bar tension of 29 ksi. In the latter stages, with the bar stressed to 29 ksi, the average peak crack width increased to about 0.026 in. The failure mode was similar to that in Specimen 1 and occurred at an applied shear stress of about 350 psi.

Fig. C6 shows the shear-slip relationships for cycling at 100 psi and 125 psi peak shear stress when the bar stress was 29 ksi tension. It can be seen that these curves are similar to those obtained in the block-type tests. However, comparison of the behavior of Specimen 2 with that of a block specimen with external reinforcing rods (no dowel action possible) shows that for the same level of loading, the former had slips about one-third those measured in the latter. This sharp reduction in slip is due to two causes: (a) dowel force in the #14 bar, and (b) increased effective axial stiffness of the bonded #14 bar as compared to the long external restraint bars of the block specimen. The relative magnitude of each contribution remains to be determined.

Specimens 3 and 4 had additional web reinforcement away from the shear plane and on either side of the level of the steel to prevent premature diagonal tension failure but not to restrict possible splitting along the steel. Strain gages were attached to the #14 bars at the shear crack.

The crack width was nonuniform in Specimen 3, 0.014 in. on top and 0.042 in. at the bottom at the beginning of the shear loading. Large slips occurred at low shear stresses, and cracking developed at a shear of 150 psi, as shown in Figure C7. The stress in the bar was about 28 ksi throughout the loading, measured outside the specimen. The internal gages were affected by local bending and the somewhat inconsistent readings have not yet been fully evaluated. The strains in the bars outside the specimens tend to decrease when shear is applied because of the overriding and crack width increase at the shear plane.

Specimen 4 is considered the most reliable since the initial crack width was uniform (0.025 in.) across the depth of the specimen. Accordingly, the results and discussion presented here are drawn mainly from this specimen. The axial stress applied to the bar was 28 ksi, and the loading history was:

- a. cycles 1-15 at \pm 100 psi shear stress
- b. cycles 16-25 at \pm 125 psi
- c. cycles 26-30 at \pm 150 psi

Major cracks appeared only in the 20th cycle, although several earlier cracks were caused by the axial tension alone. At 150 psi the cracks became very large (Fig. C8) and the test was stopped after the 5th cycle at this stress level.

Shear stress is plotted against slip in Fig. C9 and against crack width in Fig. C10. The behavior of each is similar to that observed in other tests. The rate of increase of peak slip values and crack width at peak loads are plotted in Fig. C11, where it is evident that behavior in the last 5 cycles (with 150 psi shear stress) was substantially different from the earlier cycles at lower stress levels. This may have been caused by additional internal cracking that was not visible, but that greatly decreased the effective axial stiffness of the bar and thereby increased the crack width, thus leading to larger slips. Or the reinforcing

bar could have undergone considerable yielding near the crack, which would increase the crack width and the level of slippage during shearing.

The results of these tests will be included in more detail in Fajardo's thesis, along with further analysis and discussion of these and other results.

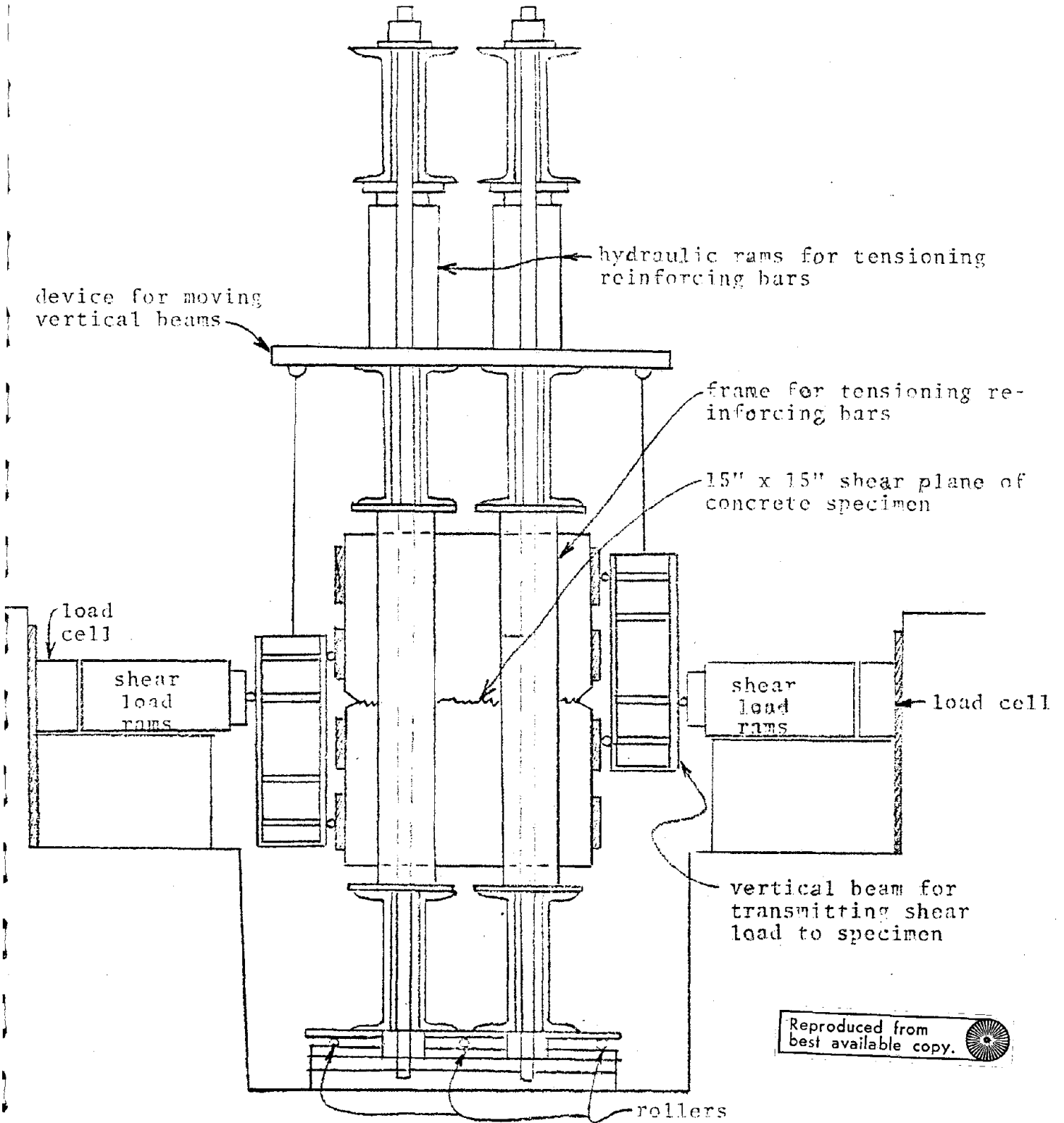
3. Comparison of Various Test Results

Load-slip curves for several types of specimens are summarized in Fig. C12.

Each curve was obtained during the 15th cycle of shear loading at the indicated stress levels. Curves A, B, and C were obtained from specimens with external restraint rods to give results for interface shear transfer alone (no dowel action with the condition of rather low axial stiffness. Curves D and E were measured on specimens that were cracked, separated to produce an initial crack width of 0.030 in., and then had four #11 reinforcing bars grouted in place with either 1 in. or 4 in. unbonded length at the shear plane. This eliminated most of the dowel action and also increased the axial stiffness of the restraining reinforcing that acts to prevent the crack from opening. Curve F is combined interface shear transfer and dowel action and was obtained from a beam-type specimen with parameters as indicated.

The basic shapes of both loading and unloading branches of all the curves in Fig. C12, B16, and A8 are quite similar for the three cases of interface shear transfer alone, dowel action alone, and combined interface shear transfer and dowel action. A rational model of shear transfer that incorporates all important parameters is under development. The effects of biaxial tension in the specimen may alter the behavior substantially because of the cracking that is expected to occur under these more severe stress conditions.

C7




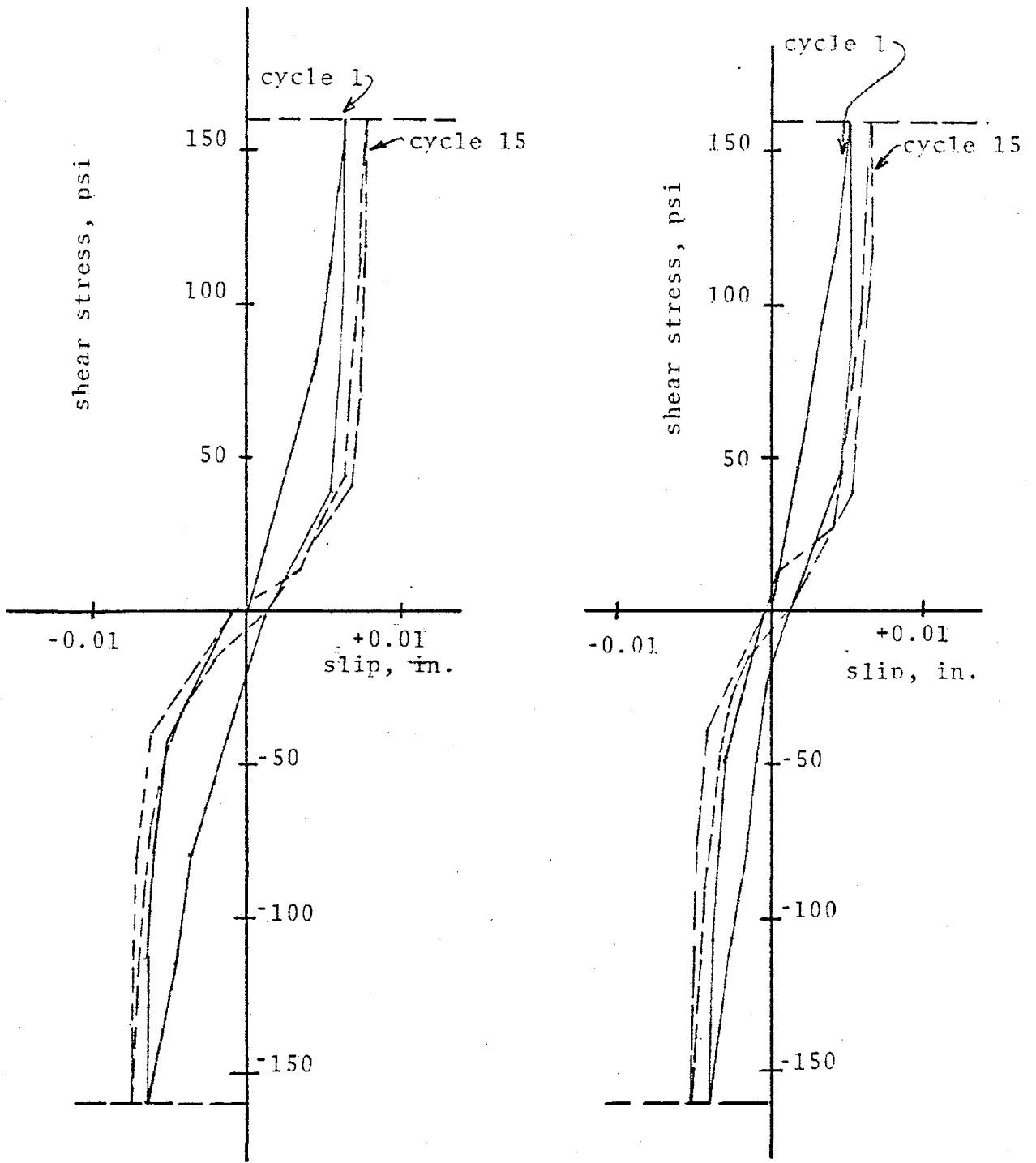
Reproduced from best available copy. 

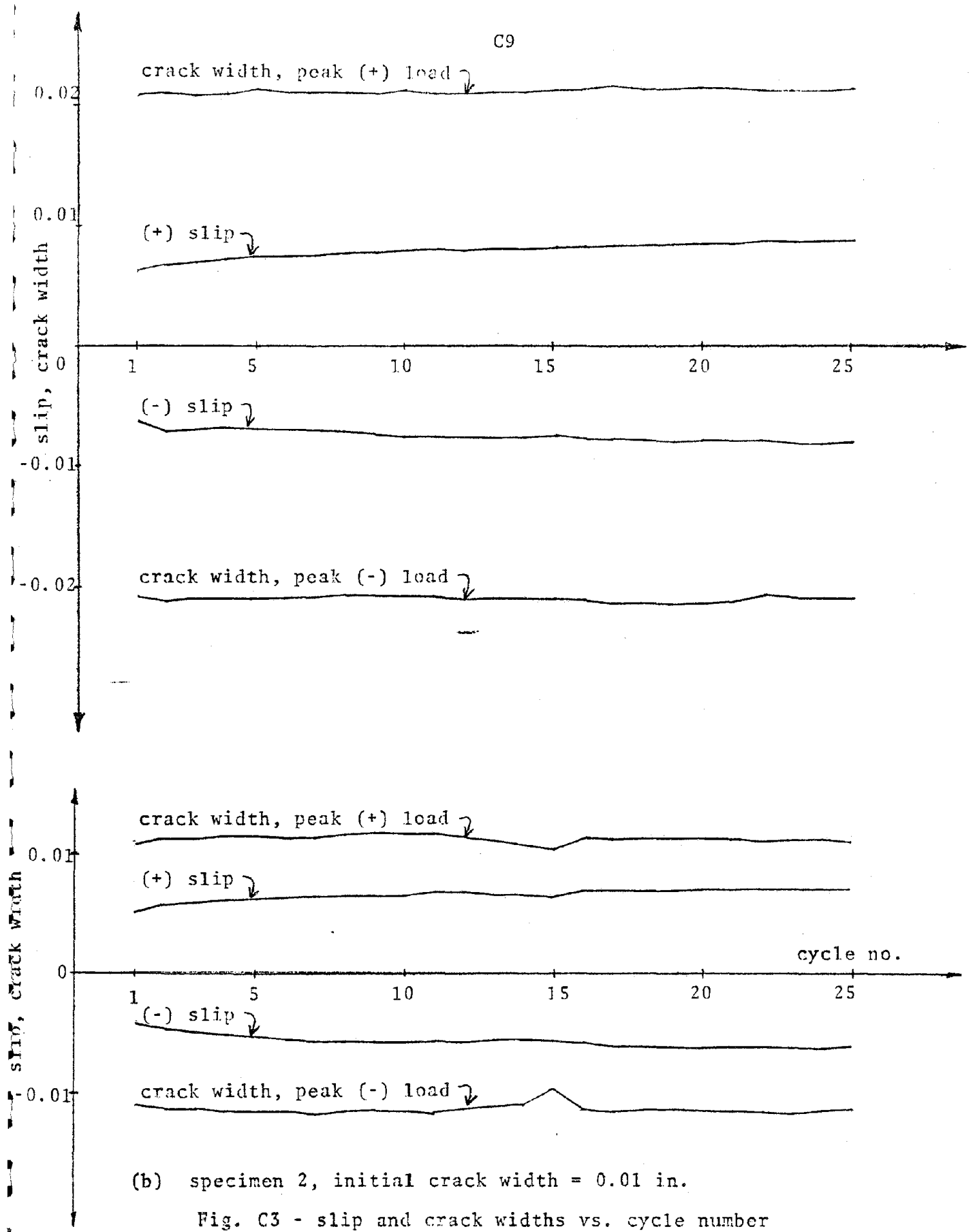
Fig. C1 - test specimen (reinforced with 4 - #9 bars)



(a) specimen 1; initial crack width = 0.02 in.

(b) specimen 2, initial crack width = 0.01 in.

Fig. C2 - load-slip curves



(b) specimen 2, initial crack width = 0.01 in.

Fig. C3 - slip and crack widths vs. cycle number

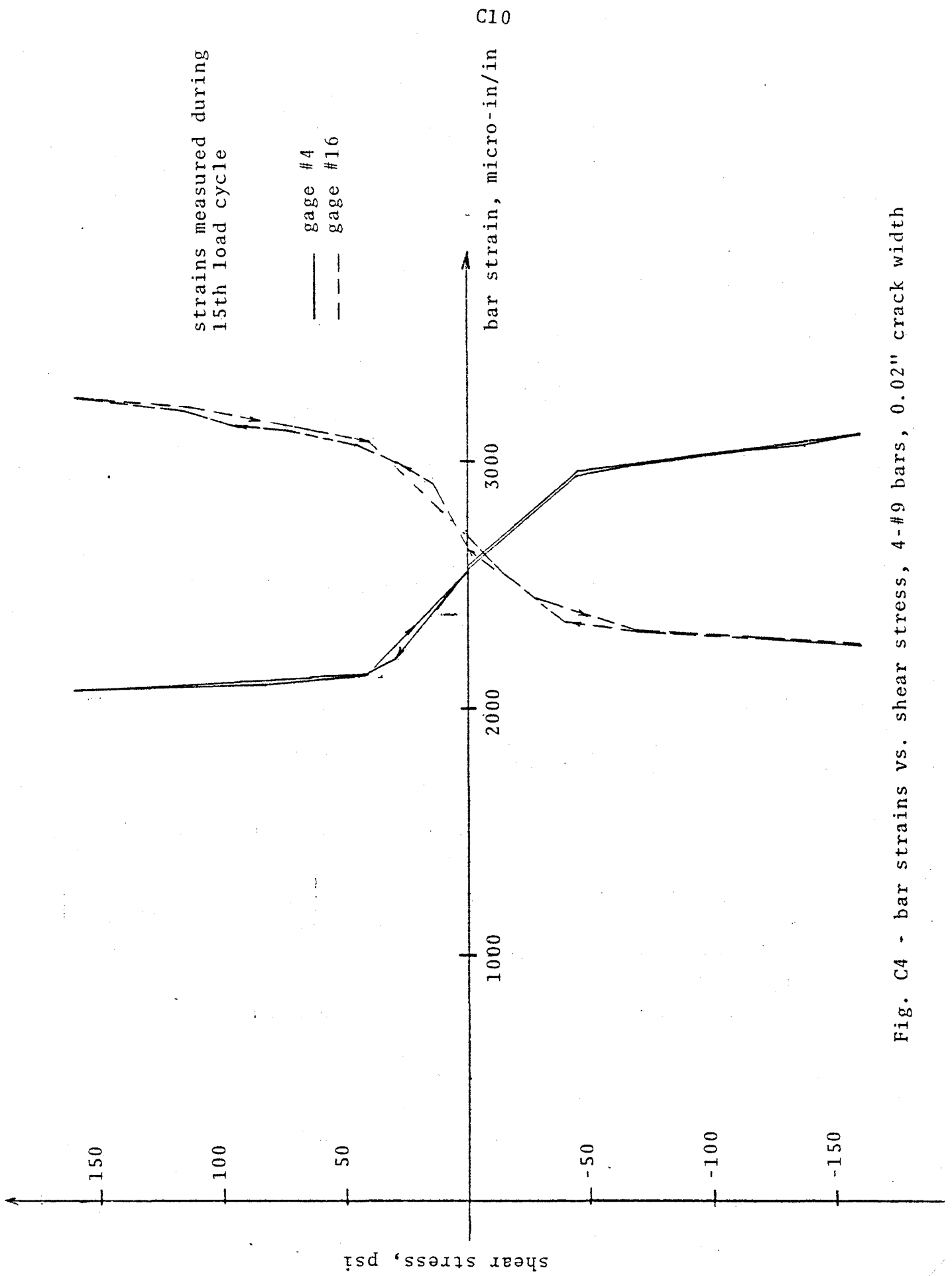
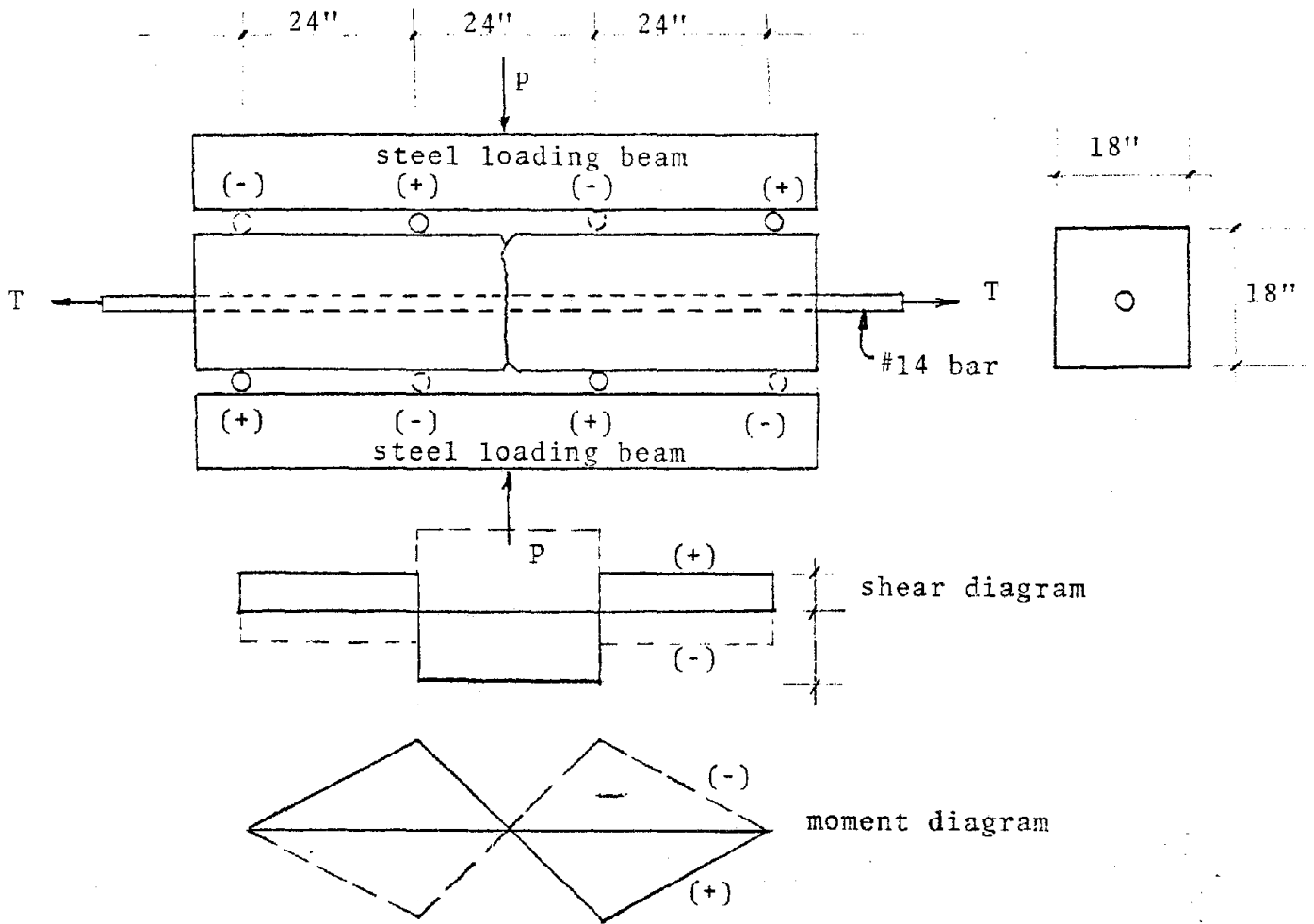
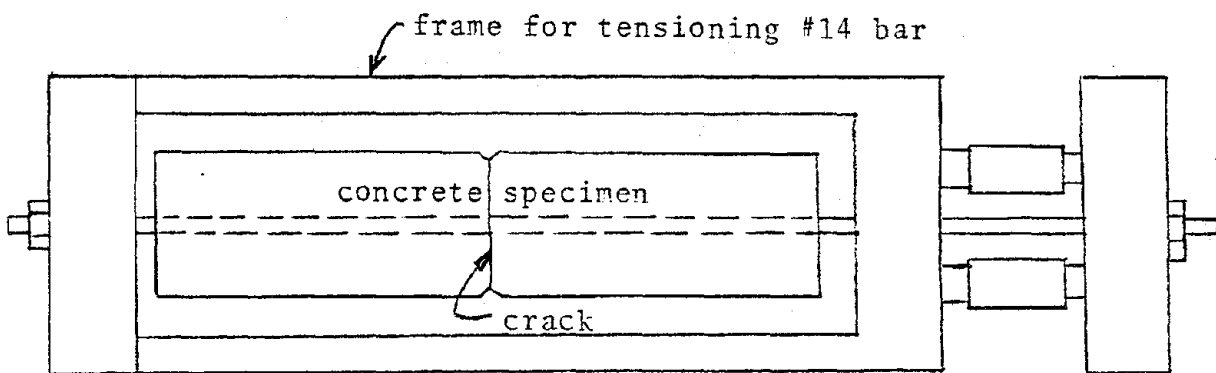


Fig. C4 - bar strains vs. shear stress, 4-#9 bars, 0.02" crack width

C11



(a) loading system to induce cyclic reversing system



(b) plan view of test specimens and frame

Fig. C5 - beam-type specimen

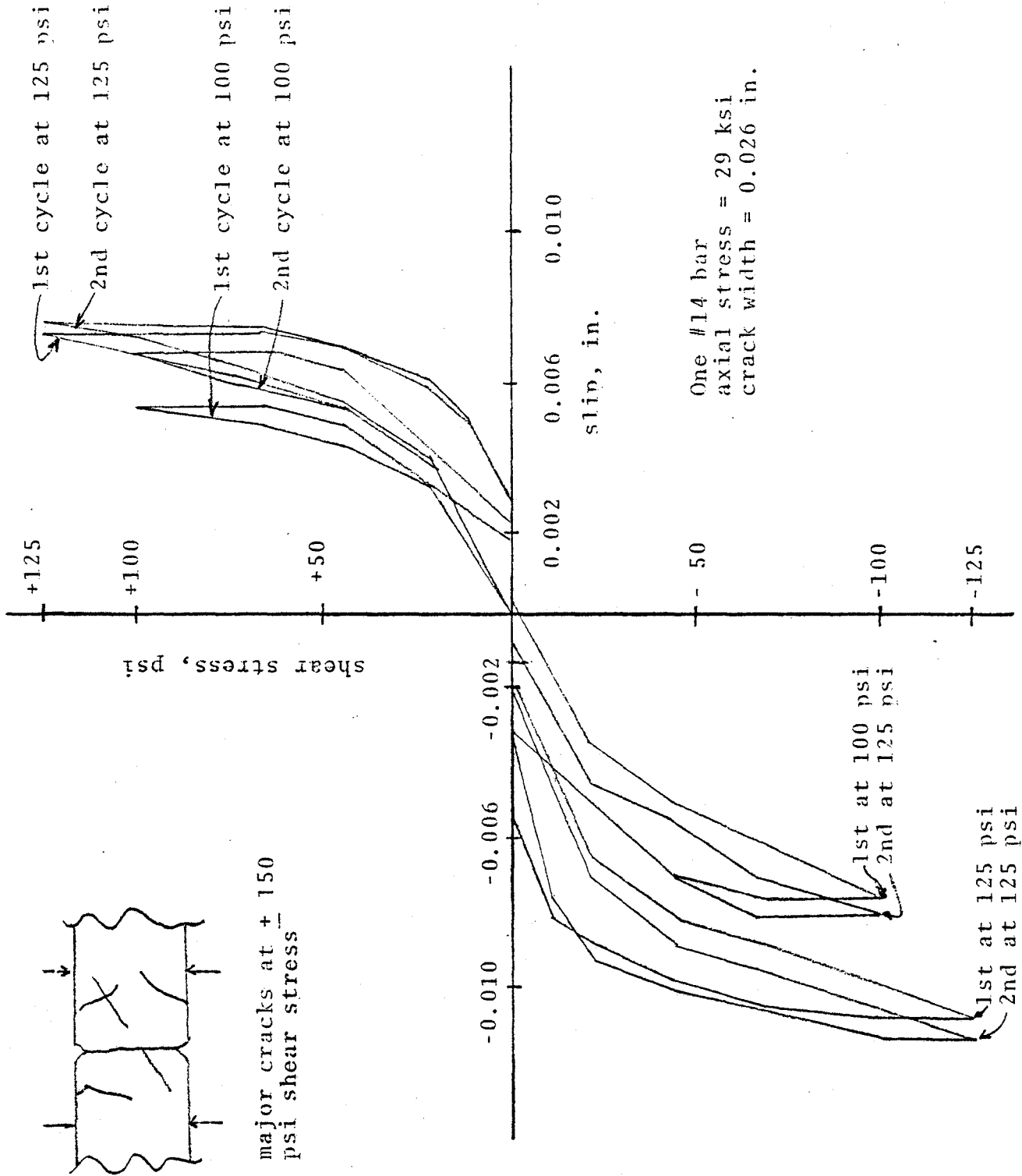
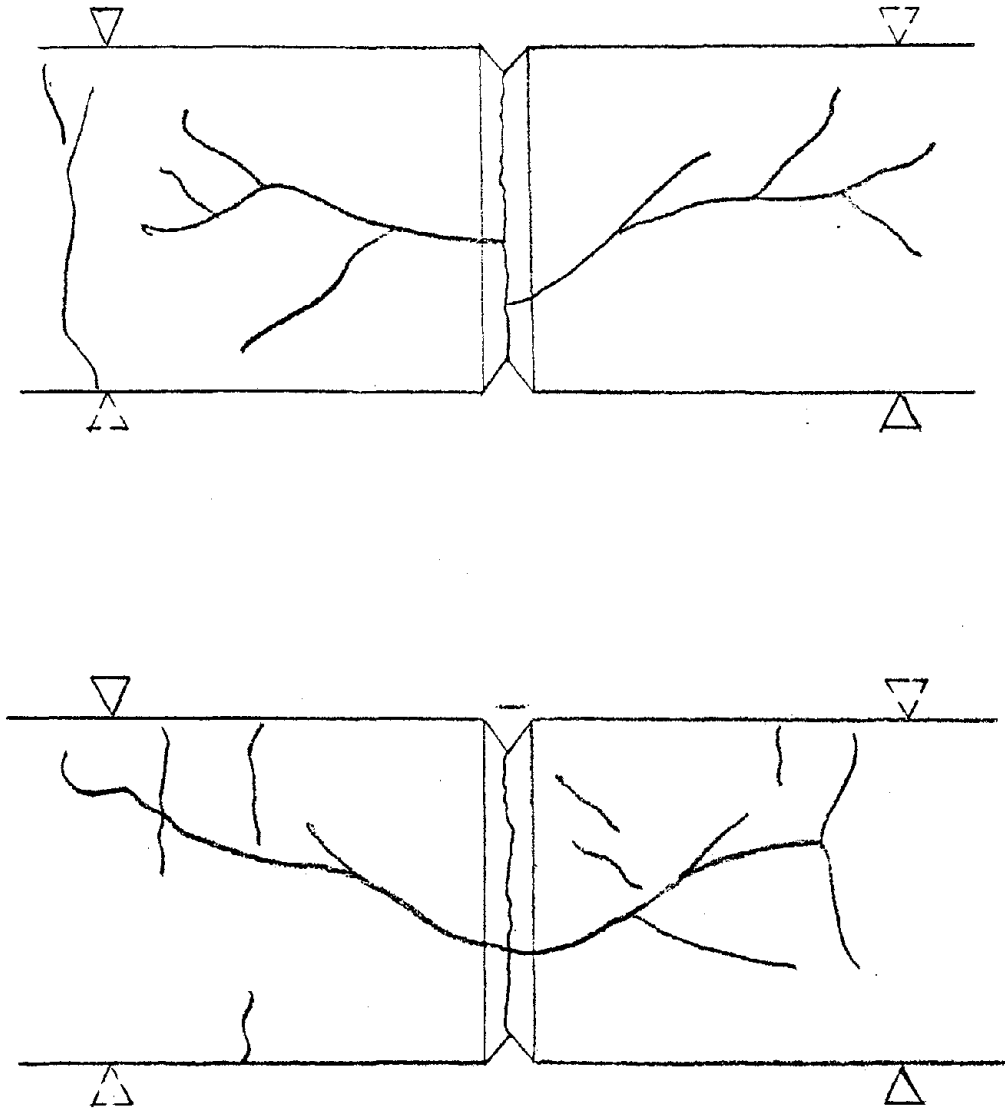
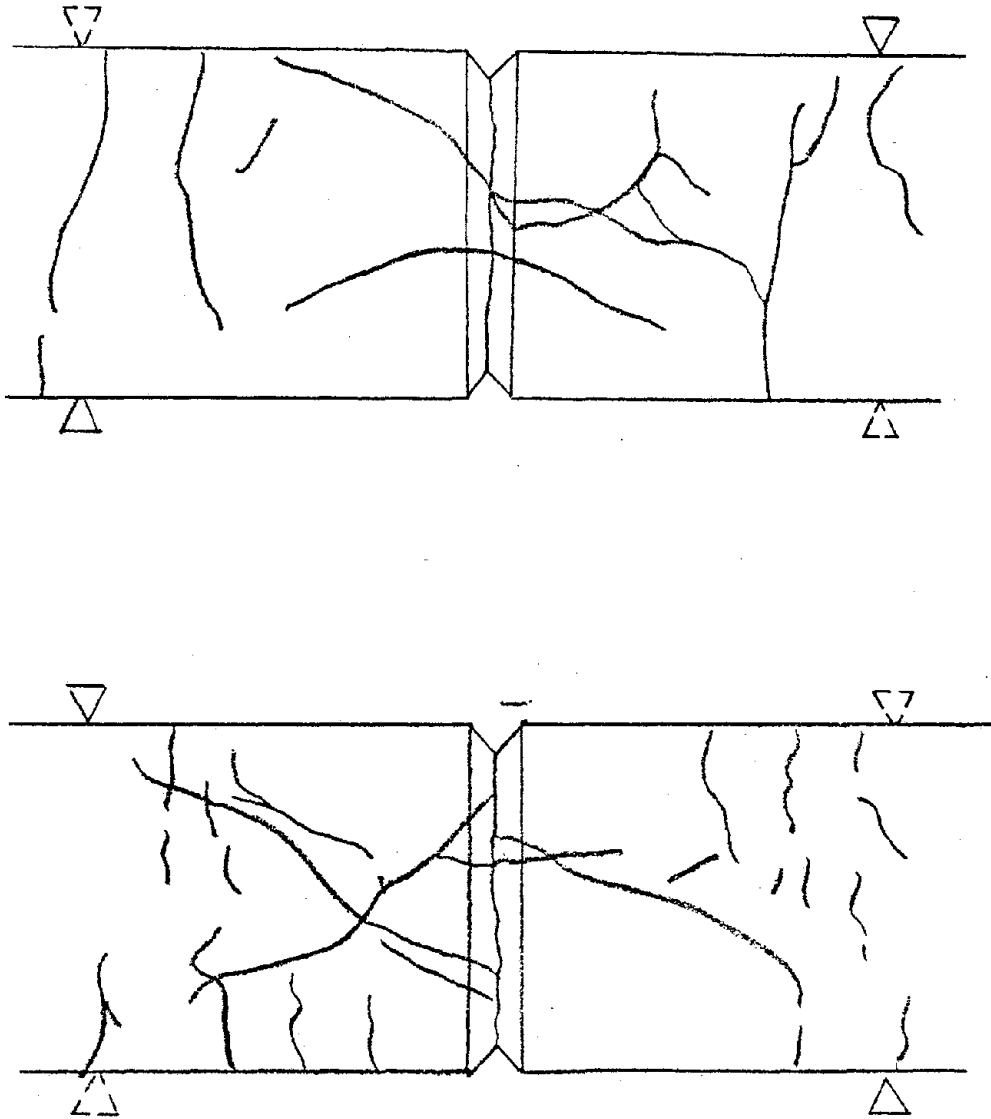


Fig. C6 - load-slip relationships, beam #2



Cracks developed after 2 cycles at 150 psi (point at which test was stopped).

Fig. C7 - cracking patterns, beam 3



Cracks developed after 5 cycles at 150 psi (total of 30 load cycles).

Fig. C8 - cracking patterns, beam 4

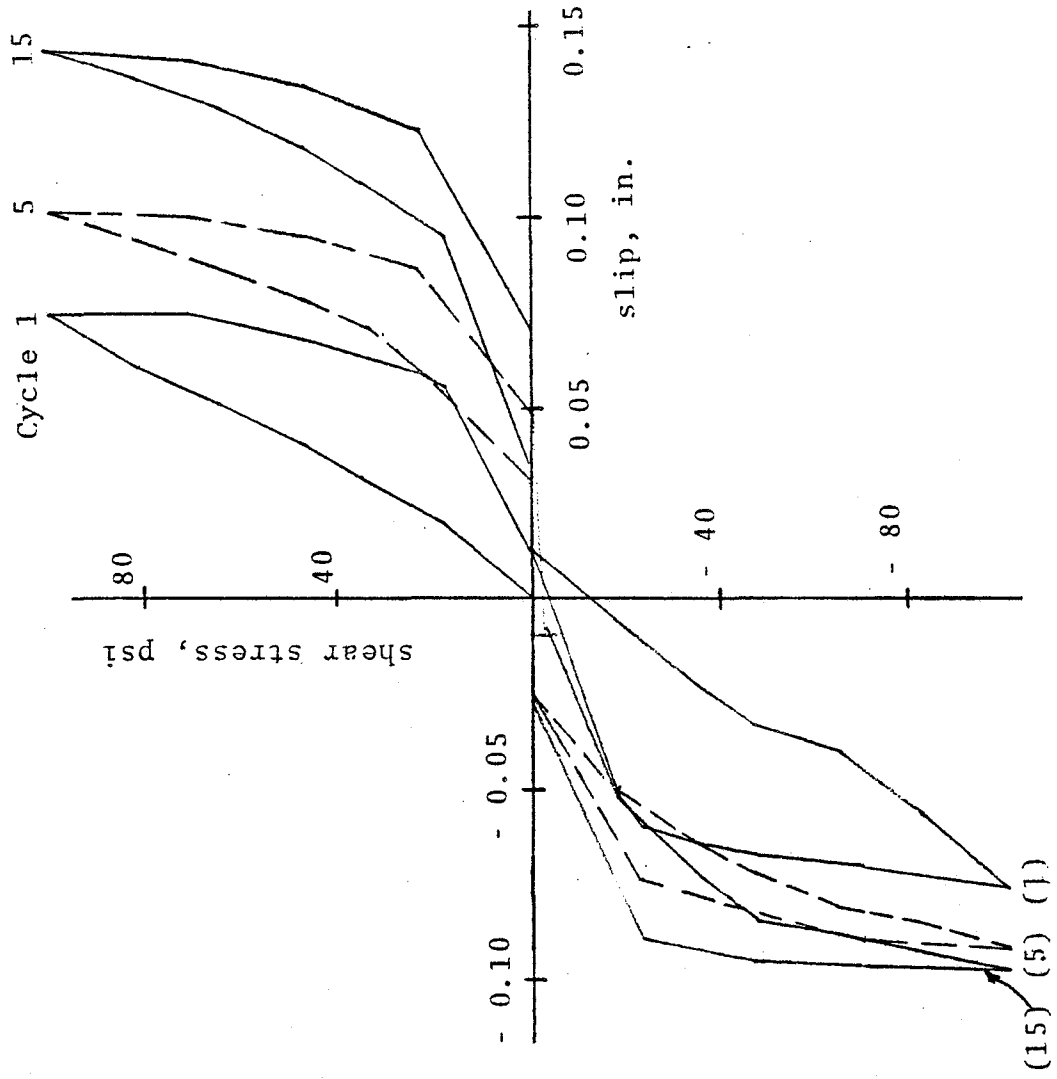


Fig. C9 - slip vs. shear load, beam 4 (cycles 1, 15, and 25)
(see also next sheet)

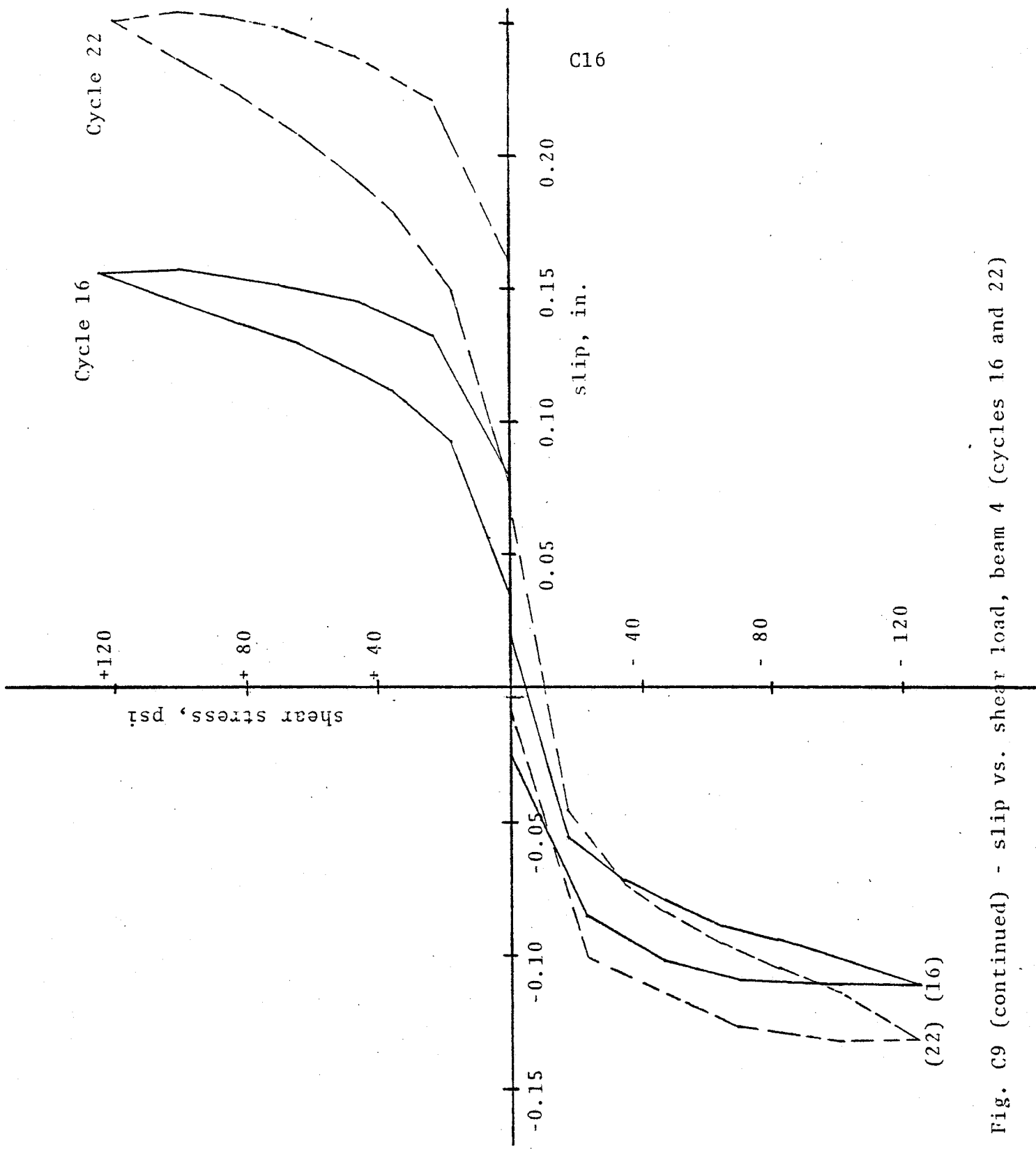


Fig. C9 (continued) - slip vs. shear load, beam 4 (cycles 16 and 22)

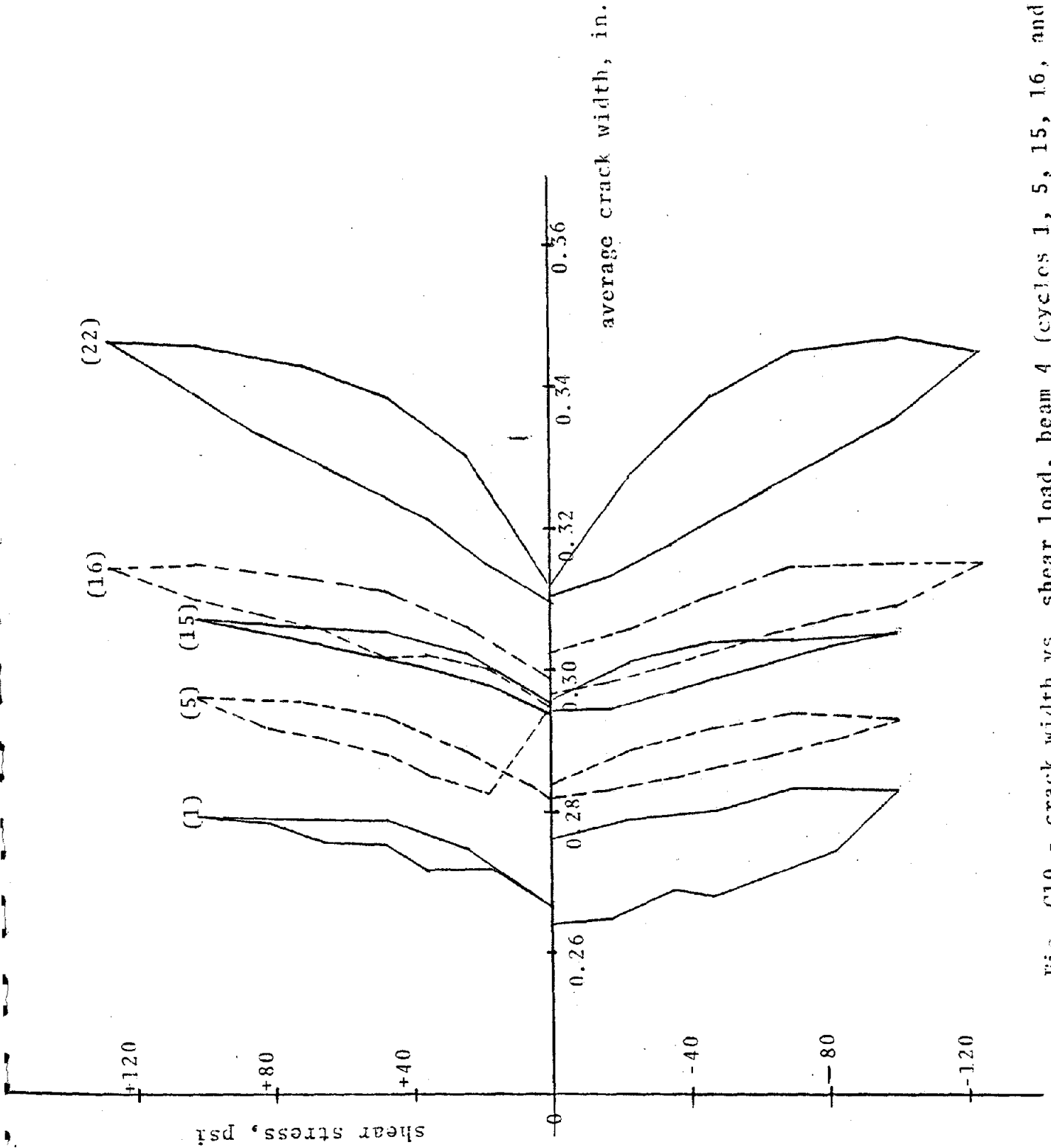


Fig. C10 - crack width vs. shear load, beam 4 (cycles 1, 5, 15, 16, and 22).

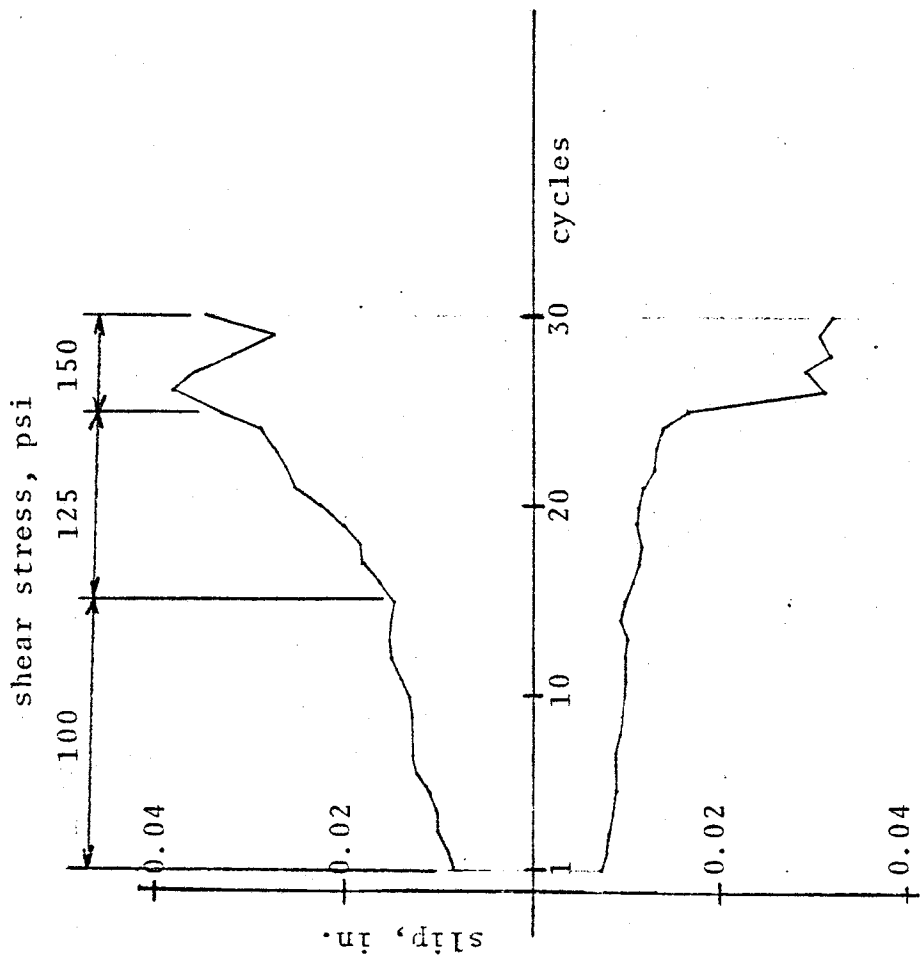
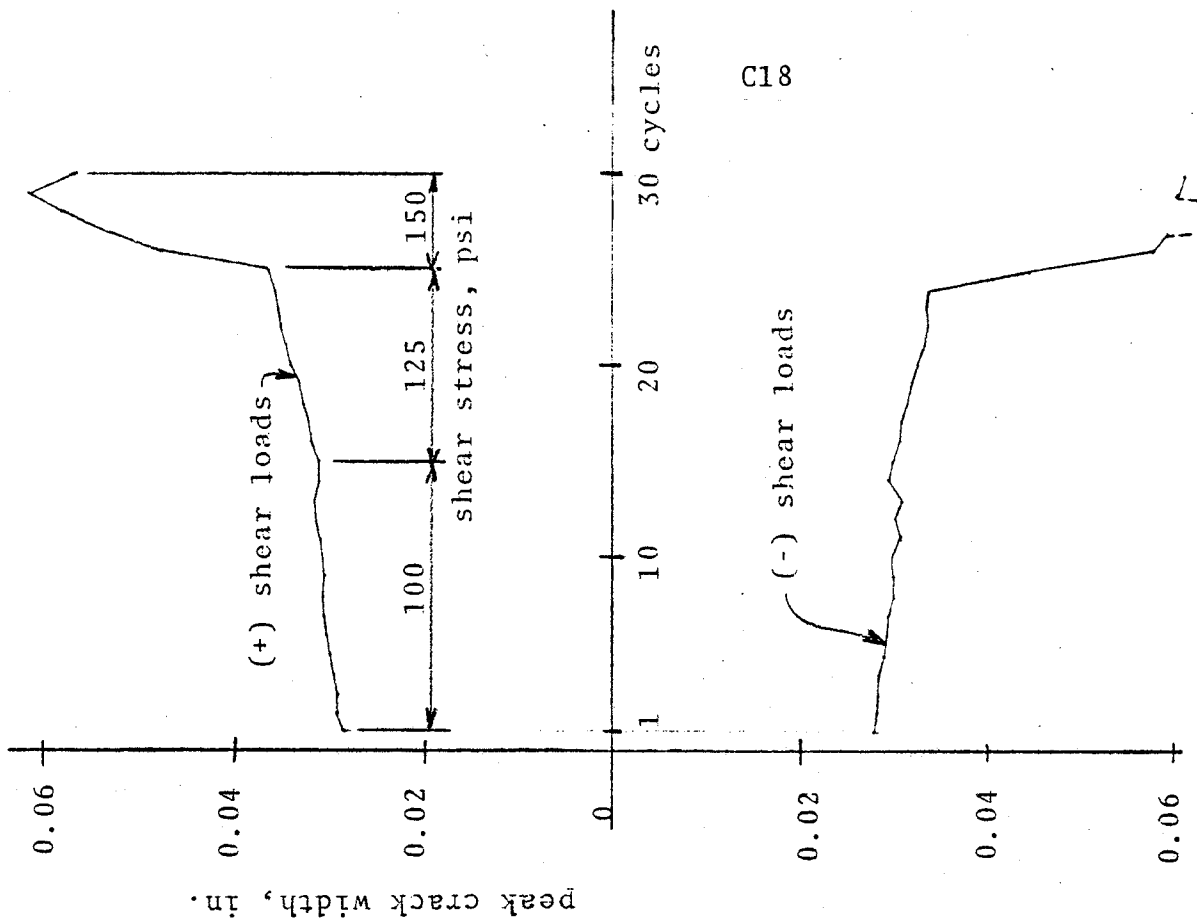
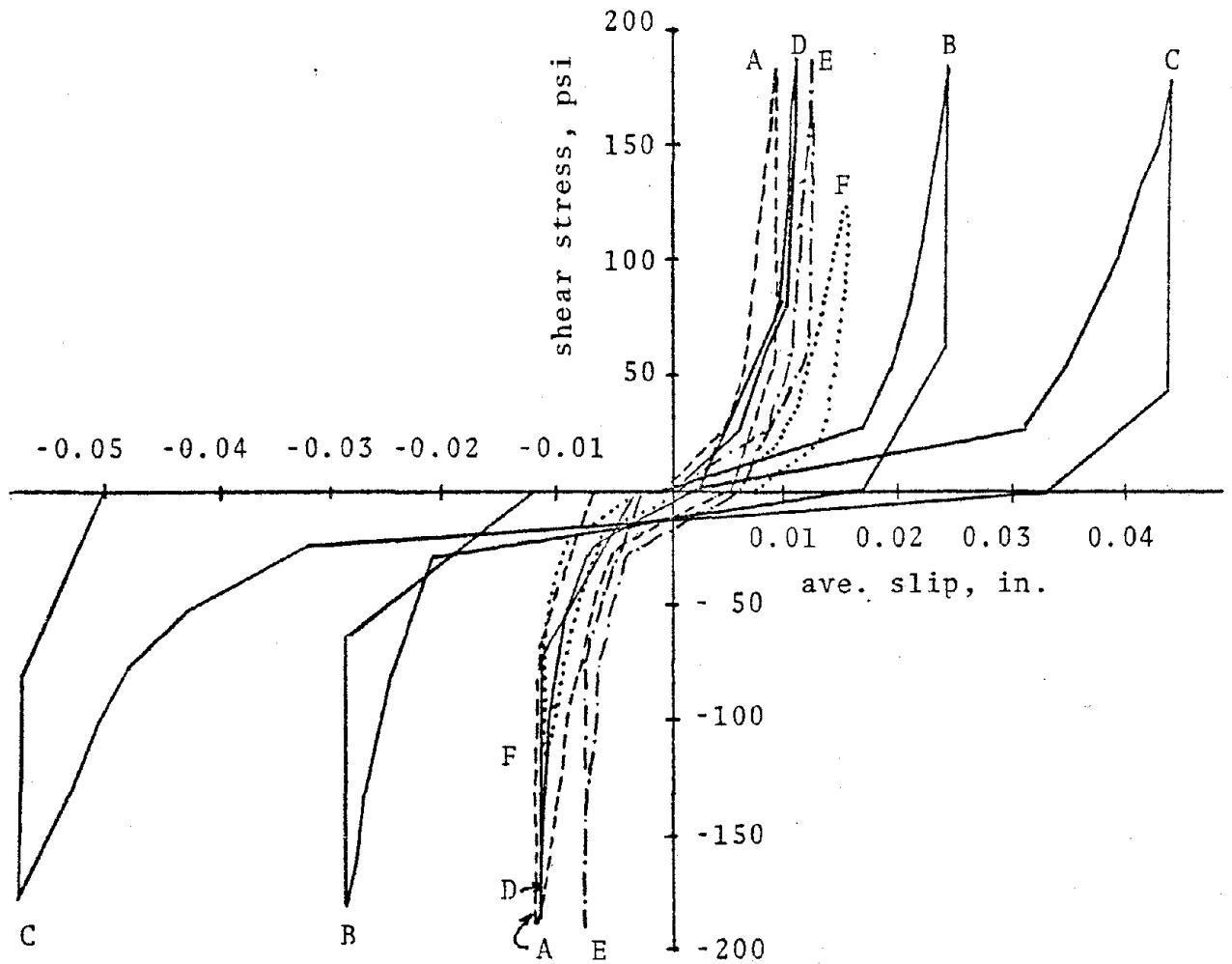


Fig. C11 - slip and crack width vs. cycle number, specimen 4



legend

- | | | |
|----|---|---------------------------|
| A. | 0.010 in. initial crack width | } external restraint bars |
| B. | 0.020 in. initial crack width | |
| C. | 0.030 in. initial crack width | |
| D. | Four #11 embedded bars, 0.030 ICW and 1 in. unbonded length | |
| E. | Four #11 embedded bars, 0.030 ICW and 4 in. unbonded length | |
| F. | One #14 embedded bar, 28 ksi tension, 0.030 in. ICW | |

Fig. C12 - typical hysteresis curves during 15th load cycle

D. The Effects of Cracks on the Seismic Analysis of Reinforced Concrete Nuclear Containment Vessels

This section has been published as a separate report but is included here in its entirety to provide complete documentation of this important segment of the research. Figure and table numbers are not prefixed with the letter D, and the cited references are listed on pages D65-D67.



TABLE OF CONTENTS

	<u>Page</u>
1. INTRODUCTION	1
1.1 Nuclear Containment Vessels	1
1.2 Scope of this Investigation	3
1.3 Design Philosophy	4
2. SHEAR TRANSFER IN NUCLEAR CONTAINMENT VESSELS	7
2.1 Cracks in Nuclear Containment Vessels	7
2.2 Interface Shear Transfer	8
2.3 Shear Stress Distributions	9
3. LINEAR SEISMIC ANALYSIS OF A CONTAINMENT VESSEL	17
3.1 Idealization of the Containment Shell Vessel	17
3.2 Modal Analysis	21
3.3 Rotational Degrees of Freedom	23
4. SOIL-STRUCTURE INTERACTION	26
4.1 Introduction	26
4.2 Brief Summary of Seismic Waves	27
4.3 Modeling of the Soil	29
4.4 Mass and Damping Matrices for SSI	32
5. SEISMIC ANALYSIS INCLUDING CRACKS	36
5.1 Introduction	36
5.2 Modeling of the Cracks	36
5.3 Nonlinear Seismic Analysis	43
5.4 Input to Linear and Nonlinear Analyses	46
5.5 Discussion of Results	48

5.6 System Identification	55
6. CONCLUSIONS	60
REFERENCES	63
LIST OF SYMBOLS	66
APPENDIX A	68
APPENDIX B	86
TABLES	118
FIGURES	127

Chapter 1

INTRODUCTION

1.1 Nuclear Containment Vessels

The heart of a nuclear power station is the nuclear reactor and its steam supply system. Of equal importance, for reasons of safety, is the containment vessel which houses the reactor along with its steam supply system components (see Figure 1.1). The purposes of the containment are to prevent leakage of radioactive substances to the outside environment and to support the structures and equipment connected to it. The vessel shown in Figure 1.1 is typical of the large reinforced concrete containment vessels now used in pressurized water reactors. It consists of a large cylindrical shell (4 1/2 feet thick) with a hemispherical head, resting on a circular foundation. The containment vessel volume must be able to dissipate the energy released during a loss of coolant accident in the reactor. This accident creates an internal pressure which stresses the containment vessel. The containment vessel shell must be able to transmit these and all other forces down to the foundation mat. In concrete containment vessels a 1/4 to 3/8 inch steel liner is attached to the inner surface of the shell to prevent leakage. This liner performs no load carrying function but must be able to undergo the strains which are imposed on it by the concrete shell wall.

Since the containment vessel is of great importance to nuclear safety, it must be able to maintain its structural integrity during an earthquake. This means that a material failure which could cause radioactive leakage should not occur in the steel liner. One of the design conditions for the containment combines the internal pressure from a loss of coolant accident acting simultaneously with the dead weight of the containment vessel and the Safe Shutdown Earthquake (SSE). The Safe Shutdown Earthquake, as defined by the Nuclear Regulatory Commission (NRC), is considered to be the "earthquake which produces the vibratory ground motion for which structures, systems and components important to safety are designed to remain functional." The horizontal design response spectra, given in the NRC Regulatory Figure Guide 1.60 as "the spectra representing the effects of the vibratory motion of the SSE," is shown in Figure 1.3.

Because concrete has little tensile strength, the internal pressurization will cause cracks in the containment in both the horizontal and vertical (principal) directions (see Figure 1.2). Both prestressed steel tendons and normal reinforcing steel are being used in concrete containment vessels. There is little or no cracking in prestressed vessels. However, the construction of these prestressed vessels is expensive because of the difficulty of prestressing in the circumferential direction. Only reinforced concrete containments will be discussed in this investigation. Presently most reinforced concrete vessel walls have steel not only in the two principal directions but also in directions inclined $\pm 45^\circ$ from these principal directions. This inclined steel is designed to transfer the SSE inertial shearing forces across the cracks in the vessel wall. In a cylindrical wall, inclined bars will form a

series of helixes. These continuously curved bars are very expensive to form and cause congestion problems during construction. If a design could be developed which eliminates these inclined bars, lower construction costs and improved concrete quality (because of reduced congestion of reinforcing bars) would result. If the orthogonal steel in the principal directions were assumed to carry shear across the cracks by dowel action and if the cracks themselves have shear transfer capability then a design could be formulated that does not rely on inclined steel. The earthquake shearing forces would then be carried to the foundation by a combination of dowel action of the vertical reinforcing bars and by the shear transfer capacity of the horizontal cracks.

1.2 Scope of this Investigation

The central purpose of this investigation is to study the feasibility of the above proposal for eliminating or reducing inclined steel in concrete containment vessels. Chapter 2 deals with the phenomenon of shear transfer across cracks in concrete. The results of tests which give the load-displacement behavior of the shear transfer mechanism of cracked concrete blocks (with internal reinforcing bars to include dowel action) are shown and discussed. The distribution of shear stresses at horizontal cracks is studied through use of a finite element model. The maximum shear stress is an important design parameter because a high shear stress could cause a diagonal tension failure or dowel splitting in the containment vessel wall.

In Chapter 3 a lumped mass model of the containment vessel shown in

Figure 1.1 is developed for linear seismic analysis. The effects of including rotational degrees of freedom in the analysis are discussed. A computer program which performs linear seismic analysis (modal analysis) is developed. Soil-Structure Interaction is added to the model in Chapter 4. In Chapter 5, the cracks caused by internal pressurization are included in the seismic analysis of the containment vessel. Since the load-displacement behavior of these cracks is nonlinear (as shown in Chapter 2) the seismic analysis becomes nonlinear. The modeling of the crack stiffness is discussed along with the analytical tools which are required to perform the nonlinear analysis. The computer program developed to perform nonlinear analysis is then used with the lumped mass model of the containment vessel shown in Figure 1.1 for a time history of ground accelerations corresponding to the NRC response spectrum of Figure 1.3. Soil-Structure Interaction is included in this model. Three different runs which correspond to three different stiffnesses of the underlying soil are made. The modal analysis program of Chapter 3 is input with the same ground accelerations and the results of the linear and nonlinear analyses are compared. System identification is used to obtain a linear model which produces results which "best fit" the results of the nonlinear analysis. Chapter 6 states the main conclusions of this investigation and proposes future work which relates to this topic.

1.3 Design Philosophy

The design of reinforced concrete containment vessels is governed

by Section III Division 2 of the ASME Boiler and Pressure Vessel Code [14]. The load combination of interest is the extreme environmental load. This load combination is

$$1.0 D + 1.0 L + 1.0 T_o + 1.0 E_{SS} + 1.0 P_v \quad (1.1)$$

where D , L , T_o , E_{SS} and P_v are the dead, live, temperature, SSE and external pressure loads, respectively. For the containment the only live load is the internal pressure due to the loss of coolant accident (LOCA). P_v and T_o are not included here because they are unknown.

The allowable membrane compression stress in the concrete is $.60 f'_c$ where f'_c is the compressive strength of the concrete (normally $f'_c \cong 4$ Ksi for containment vessels). Concrete tensile strength is neglected. The allowable tangential shear stress is dependent upon ρ , the reinforcement ratio:

$$v_c = 12,000 \rho \quad \rho \leq .01 \quad (1.2a)$$

$$v_c = 93 + 2,700 \rho \quad .01 \leq \rho \leq .025. \quad (1.2b)$$

v_c is the maximum tangential shear stress (in psi) which may be carried by the concrete. v_c may not exceed 160 psi. ρ is taken as the lesser of the reinforcement ratios in the meridional and circumferential directions.

The design yield strength of the steel reinforcement cannot exceed 60,000 psi. The average tension and compression stresses must not exceed $.9 f_y$, where f_y is the tensile yield strength of the reinforcing bars.

According to the ASME Section III [14], if v_u (the nominal design shear stress) is greater than v_c , then the following reinforcement shall be provided:

- (1) The meridional and circumferential reinforcement shall be designed to resist 1.5 times the shear force corresponding to v_c in addition to the membrane forces which result from the LOCA.
- (2) The excess shear force corresponding to $(v_u - v_c)$ shall be resisted by inclined reinforcement.

The steel liner is designed on the basis of allowable tensile and compressive strains. The ASME code states that for extreme environmental loads $\epsilon_{sc} = .002$ and $\epsilon_{st} = .001$ where ϵ_{sc} is the allowable liner compressive strain and ϵ_{st} is the allowable liner tensile strain. The anchors which attach the liner to the concrete containment are spaced at about 20 inches. The allowable relative displacement between the anchors that is commonly used in design is .1 inch.

Chapter 2

SHEAR TRANSFER IN NUCLEAR CONTAINMENT VESSELS

2.1 Cracks in Nuclear Containment Vessels

Current design criteria specify that the nuclear containment vessel must be able to withstand the simultaneous occurrence of a design basis accident which would give rise to internal pressurization and a strong motion (SSE) earthquake. The internal pressure creates tension forces in both the longitudinal and circumferential directions while the earthquake causes inertial forces which in turn cause shearing forces and bending moments in the vessel. These forces and moments must be transferred across the horizontal and vertical cracks in the reinforced concrete caused by pressurization. Clearly the crack patterns, crack widths and spacings are important. Crack widths (caused by internal pressurization) vary from .01 to .015 inches. Horizontal cracks with regular spacings throughout the vessel will be assumed. The possible effects of vertical cracks will be discussed later in this chapter and in Chapter 5. It has been found from tests at Cornell University [1,2] and elsewhere that a mechanism exists which makes it possible to transfer shear force across cracks in concrete. This mechanism is called interface shear transfer (IST) or aggregate interlock. The effect of the shearing stiffness of these cracks on the shear stress distribution in

the vessel is studied in this chapter. The maximum shear stresses may then be found once the shear forces acting at each section are known.

2.2 Interface Shear Transfer

Several types of tests have been conducted at Cornell to determine the behavior of IST in concrete [1]. Some of these tests were used solely to investigate IST, with no reinforcing bars crossing the crack plane. Other test specimens had internally embedded reinforcing bars and had a greased plate inserted at the crack plane so that the only shear stiffness was produced by dowel action. Still other specimens had internal bars crossing the crack plane and thus included the effects of both dowel action and IST. The early tests which included both IST and dowel action were done on the testing setup shown in Figure 2.1. This "beam-type" specimen was loaded by two beams, one above and one below the concrete specimen. When the positive (+) rollers were used the shear diagram is as shown. The shear loading direction could be reversed by use of the negative (-) rollers. All beam specimens had a single #14 bar located in the middle of the 15 in. x 15 in. specimen. This longitudinal bar was stressed until a crack occurred in the specimen at mid-length of the specimen. Unfortunately, there were variations in the width of this crack due to the self-weight of the beam and the axial tensioning system. With the tension held constant, fully reversing shear loads were applied. The 15th cycle load-slip curve for the beam specimen with the most uniform initial crack width is shown in Figure 2.2 (curve F). The load history was: cycles 1 - 15 at ± 100 psi shear,

cycles 16 - 25 at ± 125 psi and cycles 26 - 30 at ± 150 psi. Curve F is for an initial crack width (ICW) of .03 inches and an axial tension at 28 ksi. The tension in the bars was maintained through the test to model the stress which occurs in the longitudinal bars of a containment due to internal pressurization. By this time the shearing stiffness for small slippage has decreased from the early cycle stiffness because of the degradation of the contact surface due to the 15 load cycles. When the slip increases in the 15th cycle the stiffness increases also. This is caused by an increased overriding action at the crack plane. This overriding increases the axial force in the reinforcing bar which in turn increases frictional resistance. Thus each load increment must overcome greater frictional resistance and the load-slip curves are upward curving after the low initial stiffness. The seating against the concrete of the reinforcing bar also increases the stiffness with increasing slip. Curve F will be used as the input for IST + dowel stiffness for the remainder of this chapter.

2.3 Shear Stress Distributions

The shearing stiffness of the cracks (due to the IST mechanism) may affect the shear stress distribution in the containment vessel. A containment vessel after internal pressurization is shown in Figure 2.3. If no cracks were present and the concrete was assumed to remain elastic the sinusoidal shear stress distribution shown in Figure 2.5 is found. The presence of the cracks may change the shear stress distribution as shown by the dashed line in Figure 2.6. The increase in shear stress

(over the elastic distribution) near $\phi = 0^\circ$ is due to the behavior shown in the Figure 2.2. Curve F shows that the crack stiffness increases with increasing slip. Since the greatest slip occurs at $\phi = 0^\circ$ the stiffness is greatest here. A large stiffness concentration for low values of ϕ could cause higher shear stresses to occur for these values of ϕ than would be predicted by Figure 2.5.

The shear stress distribution in a section of the cracked cylinder will be found using the linear analysis program SAP IV [3]. It will be assumed that the stiffness of all of the cracks in the vessel can be characterized by curve F in Figure 2.2. While the initial crack width, axial stress and reinforcing percentage may be different in the actual vessel it is felt that the ratio of the high stiffness to the initial low stiffness of these curves will not change drastically with variations in these parameters. This ratio is the most important influence of the cracks on shear stress distribution. The bilinear idealization of curve F is shown in Figure 2.4.

The SAP IV model of the cracked cylindrical section is shown in Figure 2.7. Only the horizontal cracks are included in this model. The effects of the vertical cracks will be discussed later. Three horizontal cracks occur in the cylindrical section and these are modeled by the truss elements 1 - 27. It was felt that at least three crack layers were required to significantly affect the sinusoidal shear stress distribution. The horizontal crack spacing used in this model is 10 feet. This spacing was used to achieve nearly square flat shell finite elements (see next paragraph). This improves the results obtained from these elements. The stiffness of truss elements 1 - 27 will be the slope of either lines 1 or 2 in Figure 2.4. The length of each truss element (L_t)

is

$$L_t = \sqrt{(2 \times \sin 5^\circ \times 720)^2 + (.03)^2} = 125.5'' \quad (2.1)$$

The cross-sectional area (A_t) of elements 1 - 27 is taken as $1/9 \times$ the total cross-sectional area of the quarter cylinder

$$A_t = \frac{1}{9} \times \left(\frac{\pi (720) (48)}{2} \right) = 6032 \text{ in}^2 \quad (2.2)$$

Two different Young's moduli, E_1 and E_2 are chosen to model the slopes 1 and 2 in the following manner:

$$\text{Slope 1} = \frac{20 \times A_t}{.01} = \frac{E_1 A_t}{L_t}$$

$$E_1 = 251 \text{ ksi}$$

$$\text{Slope 2} = \frac{(125 - 20) A_t}{(.016 - .01)} = \frac{E_2 A_t}{L_t}$$

$$E_2 = 220 \text{ ksi.} \quad (2.3)$$

A series of flat shell finite elements developed by Clough and Felippa [4] which combine plate bending and plane stress behavior are used to model the quarter shell. This element uses four compatible triangles which each use the constant strain triangle and the LCCT9 element to represent the membrane and bending behavior, respectively. The LCCT9 element is based on a cubic displacement formulation for the transverse displacement which gives linearly varying moment fields (thus the name Linear Curvature Compatible Triangles with 3 degrees of freedom

at each node). These four triangles are combined to form a rectangle with a central node along with the four corner nodes. The six degrees of freedom associated with this central node are condensed out at the element formulation level. The resulting quadrilateral element has twenty-four degrees of freedom, i.e., six degrees of freedom per node in the global coordinate system. The thin shell elements model elastic uncracked concrete and have the appropriate Young's modulus (3640 ksi) and Poisson's ratio (.17).

Since only one-quarter of the shell is being modeled, certain boundary conditions must be used to adequately model the behavior of the full cross-section. The shear force V is assumed to act in the direction of the global Z -axis (see Figure 2.7). This means that the Z -axis must be a line of symmetry. To insure this, the X displacement and rotations about the Y and Z axes are deleted for nodes 1 - 8. For kinematic stability the Z displacement at node 8 is also deleted. The support reactions that were developed due to this deletion were negligible so that shear stress distribution in the cylinder was not affected. The vertical displacements in the direction of the global Y -axis were deleted for nodes 73 - 80. This nodal line represents the neutral axis of the cylindrical cantilever beam so no vertical displacements should exist along this line if bending only is considered.

The SAP IV model was loaded incrementally by imposing nodal loads at the top nodes 73, 65, 57, 49, 41, 33, 25, 17, 9, 1. Equal but opposite loads were imposed on nodes 80, 72, 64, 56, 48, 40, 32, 24, 16, 8. The idea was to examine the shear stress distribution at the central crack (elements 10 - 18) to see what changes from the original distribution had occurred due to the top two cracks. The original shear stress

distribution at the top nodes was assumed to be the elastic distribution for a beam of cylindrical cross-section. This distribution is shown in Figure 2.6 with $\tau_{\max} = 1.0$ psi. The shear area is $A/2$, where A is the cross-sectional area. The nodal loads are arrived at by computing work equivalent forces which correspond to this elastic shear stress. Since the displacements which correspond to the shear stress are linear, the work equivalent forces at node i are computed according to the following equation:

$$P_{zi} = \tau \int_{\phi_i - 5^\circ}^{\phi_i + 5^\circ} \tau(\phi) \cos\phi R_c d\phi$$

$$P_{xi} = \tau \int_{\phi_i - 5^\circ}^{\phi_i + 5^\circ} \tau(\phi) \sin\phi R_c d\phi \quad (i = 1, 9, 17, 25, 33, \\ 41, 49, 57, 65, 73)$$

$$\tau(\phi) = \tau_{\max} \cos\phi$$

$$\tau_{\max} = \frac{V}{\text{Shear Area}} = \frac{2V}{A} \quad (2.4)$$

The incremental loading procedure used will be described by reviewing some of the typical load steps that were used and the stiffness changes which occurred after each of the load steps. The result of the first load step is shown in Figure 2.8. Since all of the cracked elements (truss elements 1 - 27) had Young's modulus E_1 the cylinder acted as in the usual uncracked elastic manner with the SAP IV results being almost exactly the same as the elastic ($\tau = 1 \cos\phi$) distribution. Note that the maximum stress (which occurs in bars 1, 10 and 19 which correspond to $\phi = 5^\circ$) is 20 psi. This means that the actual SAP IV results, which

were based on a maximum shear stress (τ_{\max}) loading of 1 psi, have been scaled up by a factor of 20 so that the most highly stressed bars (1, 10, 19) will be at the break point in the shear-slip curve (Figure 2.5). Since the expected elastic shear stress distribution was obtained in the SAP IV model the boundary conditions discussed above would seem to be verified. In the second load step (Figure 2.9) bars 1, 10 and 19 had the high E_2 Young's modulus while the rest of the bars remained at E_1 . The loading corresponding to $1 \cos\phi$ distribution will stress bars 2, 11 and 20 to .6 psi (see Figure 2.9). Adding this to the 19.4 psi in these bars from the first load step produces a total of 20 psi which now puts these bars at the stiffness break point. For the next load step bars 1, 2, 10, 11, 19 and 20 will have the high modulus E_2 . The load increments continue in this manner, with each successive bar along the crack being loaded until it reaches the stiffness break point. From there on this bar will have the modulus E_2 . The remaining load steps (shown in Table 2.1) continue in this manner. Total stresses are obtained by simple addition of the results from each load step. The shear stress distributions from each load step are shown in Figures 2.8 - 2.16.

The stiffness change from the last stiff bar to the first flexible bar always causes a stress concentration at the last stiff bar. The magnitude of this stress concentration varies for the different load steps but the distortion from the elastic distribution is quite evident except for the run with bars 1 - 7 stiff, which is to be expected. The maximum stress ratio (maximum inelastic stress to maximum elastic stress) is approximately 1.7 and occurs with bars 1 and 2 stiff. While there are large stress concentrations in the individual load steps, these concentrations cancel each other out when total stresses after each load

step are computed. This can be seen from Figure 2.17 where the deviations from the elastic distribution of total stresses is very small. The reason for this is that the load steps with the highest stress concentrations (steps 2 - 6) are very small load steps with the maximum deviation from the elastic distribution being only 3 psi in step 6 (Figure 2.13). Therefore, the maximum shear stress distribution does not change appreciably from the elastic distribution shown in Figure 2.6 when the non-linear action of IST is included. The elastic shear area of $A/2$ may then be used at the cracks.

During an earthquake the overturning moment caused by inertial forces may cause the crack width to change. If the crack were to close completely over some portion of its circumference then this would be the source of a large stiffness concentration which may alter the shear stress distribution. In section 5.5 it is shown that for a total unbonded length at the crack of 2.5 inches the change in crack width is small compared to the initial crack width. Therefore the shear stress distribution is not significantly altered from the sinusoidal distribution. The unbonded length of 2.5 inches was observed in tests at Cornell. A much larger unbonded length, such as 15 inches, may cause a significant alteration in the shear stress distribution because the crack may then close completely. However, this (the closing of the crack) would only occur for an extremely brief period of time and the assumption of an unbonded length of 15 inches at the crack is far fetched.

Figure 2.3 shows that vertical cracks also exist in the containment. These cracks may effectively decrease the flexural and shear stiffness of the containment vessel. It is not yet known how much this stiffness decrease might be. The effects on seismic analysis of this stiffness

decrease will be discussed in Chapter 5.

Chapter 3

LINEAR SEISMIC ANALYSIS OF A CONTAINMENT VESSEL

3.1 Idealization of the Containment Shell Vessel

A seismic analysis of the containment shell must be performed to obtain the forces and deformations caused by the SSE which are required in design. The current practice is to use a linear model for seismic analysis which does not take into account the cracks in the vessel wall. The dynamic structural model which is used in seismic analysis attempts to model the real structure (in this case the containment vessel of a nuclear power plant) with a finite number of discrete node points. The number of nodes used in a dynamic analysis is normally much less than would be used in a static analysis of the same structure. The best rationalization for the inexactness of the dynamic model is that the earthquake loading itself is a totally random occurrence with characteristics which cannot be accurately predicted. Clearly there is no point in developing a highly refined dynamic model when the loadings are uncertain because of the random nature of earthquakes.

In this chapter a linear dynamic model of the containment shown in Figure 1.1 will be developed. The results from this model will be compared with the results of the nonlinear model (which includes the effects of cracking) developed in Chapter 5.

The equations of motion for a structure undergoing ground accelerations are

$$[M] \{\ddot{u}\} + [C] \{\dot{u}\} + [K] \{u\} = - [M] \{\ddot{x}_g\} \quad (3.1)$$

where \ddot{u} , \dot{u} , u and x_g are the relative acceleration, relative velocity, relative displacement and ground acceleration, respectively. These quantities are shown in Figure 3.1 where

$$\{u\} = [u_1 \ \theta_1 \ u_2 \ \theta_2 \ u_3 \ \theta_3 \ u_4 \ \theta_4 \ u_5 \ \theta_5]. \quad (3.2)$$

The relative displacements u_i are related to the total displacements x_i by

$$u_i = x_i - x_g \quad i = 1 \dots 5 \quad (3.3)$$

where x_g is the ground displacement. The rotational degrees of freedom $\theta_1 \dots \theta_5$ will be included in this analysis so $[M]$, $[C]$ and $[K]$ in (3.1) will be 10×10 matrices. Later in this chapter the effects of dropping the rotational degrees of freedom will be studied.

In Figure 3.2 the actual containment vessel and the dynamic model are shown. The lumped mass method is used to model the containment. The 120 ft. cylinder is broken up into four equal segments with mass of M_c and mass moment of inertia of I_{mc} . The density of the concrete is .150 k/ft³.

$$M_c = \frac{2\pi \times 69.75 \times 4.5 \times 120 \times .15}{4 \times 386.4} = 22.967 \text{ k-sec}^2/\text{in} \quad (3.3a)$$

$$I_{mc} = M_c \left[\frac{R_c^2}{2} + \frac{1}{3} \left(\frac{L_c}{4} \right)^2 \right] = 8.293 \times 10^6 \text{ k-sec}^2\text{-in} \quad (3.3b)$$

M_c and I_{mc} are the values of the lumped masses at nodes 2 - 5 in Figure 3.2. The hemispherical head is modeled by node 1. Node 1 is located at the center of gravity of the head ($R_s/2$ above the bottom of the head). The mass (M_s) and mass moment of inertia (I_{ms} taken about the CG) of the spherical head are

$$M_s = \frac{2\pi \times 68.75^2 \times 2.5 \times .15}{386} = 28.822 \text{ k-sec}^2\text{/in} \quad (3.4a)$$

$$I_{ms} = \frac{2}{3} M_s R_s^2 - M_s \left(\frac{R_s}{2} \right)^2 = 8.174 \times 10^6 \text{ k-sec}^2\text{-in} \quad (3.4b)$$

The mass matrix $[M]$ for a lumped mass representation is always a diagonal matrix. The diagonal members of $[M]$ for the model shown in Figure 3.2 are

$$\begin{array}{c}
 \boxed{M} = \boxed{M_s} \\
 \quad \quad \quad I_{ms} \\
 \quad \quad \quad M_c \\
 \quad \quad \quad I_{mc} \\
 \quad \quad \quad \dots \\
 \quad \quad \quad \dots \\
 \quad \quad \quad M_c \\
 \quad \quad \quad I_{mc}
 \end{array} \quad (3.5)$$

The stiffness matrix $[K]$ in equation (3.1) is based on the shear beam element stiffness matrix (see Figure 3.3 and Table 3.1). This reflects the assumption that the containment vessel acts as a vertical

cantilever beam with a thin walled cylindrical cross-section. The validity of this assumption is discussed in [8]. For concrete typical values of Young's modulus and the shear modulus are $E = 3640$ ksi and $G = 1540$ ksi. I and A_s are the moment of inertia and shear area of the beam. For the cylindrical beam segments $I = \pi R_c^3 t_c$ and $A_s = \pi R_c t_c$. The shear area is one-half the cross-sectional area, since the concrete is assumed to behave elastically. For the beam segment which models the hemispherical head average values of A_s and I are computed in the following manner:

$$A_{s1} = \pi R_s t_s \times \frac{412.5}{592.5} + \pi R_c t_c \times \frac{180}{592.5}$$

$$A_{s1} = 97270 \text{ in}^2 \quad (3.6a)$$

$$I_1 = \pi R_s^3 t_s \frac{\int_0^{\pi/6} \cos^2 \phi \, d\phi}{\int_0^{\pi/6} d\phi} \times \frac{412.5}{592.5} + \pi R_c^3 t_c \frac{180}{592.5}$$

$$I_1 = 6.7064 \times 10^{10} \text{ in}^4 \quad (3.6b)$$

The global stiffness matrix $[K]$ (see Table 3.2) is formed directly by simple addition of terms which correspond to the same degree of freedom.

The damping matrix $[C]$ is the most difficult part of the model to define. In this analysis $[C]$ will be based on the ratio of critical damping which occurs in each mode of vibration. This will be explained further in the next section on modal analysis.

3.2 Modal Analysis

In modal analysis the first step taken is the calculation of the natural frequencies and mode shapes of the idealized model. This corresponds to the solution of the undamped free vibration problem, which may be stated as

$$[M] \{\ddot{u}\} + [K] \{u\} = \{0\}. \quad (3.7)$$

We now assume a harmonic solution for the displacement $\{u\}$ in the form

$$\{u\} = \{\phi\} \sin \omega t$$

$$[\phi] = [\phi_1 \ \phi_2 \ \dots \ \phi_{10}]. \quad (3.8)$$

Substituting (3.8) into (3.7) we find that there are ten possible values of the frequency ω and ten associated eigenvectors $[\phi]$ which satisfy (3.7). The modal matrix $[A]$ is made up of these ten eigenvectors.

$$[A] = [\{\phi\}_1 \ \{\phi\}_2 \ \dots \ \{\phi\}_{10}]. \quad (3.9)$$

It may be shown [11] that the following relationships are true:

$$[A]^T [M] [A] = [I] = [\bar{M}] \quad (3.10a)$$

$$[A]^T [C] [A] = [\bar{C}] \quad (3.10b)$$

$$[A]^T [K] [A] = [E] \quad (3.10c)$$

where [I] is the identity matrix and [E] is a diagonal matrix containing $\omega_1^2 \dots \omega_{10}^2$ on the diagonal. In this formulation the eigenvectors have been orthonormalized with respect to the mass matrix. $[\bar{C}]$ is a diagonal matrix only if [C] is proportional to the stiffness and/or the mass matrix:

$$[C] = \alpha_1 [M] + \alpha_2 [K]. \quad (3.11)$$

Equation (3.1) may now be written as ten uncoupled equations:

$$\ddot{q}_k + (\alpha_1 + \alpha_2 \omega_k^2) \dot{q}_k + \omega_k^2 q_k = \bar{F}_k \quad (k = 1 \dots 10) \quad (3.12a)$$

$$\{q\} = [A] \{u\} \quad (3.12b)$$

$$\{\bar{F}\} = - [A]^T \{\bar{x}_g\}. \quad (3.12c)$$

Equation (3.12a) represents the contribution of the k^{th} mode to the motion of the 10 dof system and is completely uncoupled as far as (3.11) holds. The coefficients α_1 and α_2 can be used to get only two different values of modal damping. In this treatment a constant damping ratio will be used for all modes. For nuclear containment vessels, the commonly used value is about 5%.

$$\beta_k = \frac{\bar{C}_{kk}}{2M_{kk}\omega_k} = .05 \quad (\text{for all } k). \quad (3.13)$$

Equation (3.12a) now becomes

$$\ddot{q}_k + 2\beta_k \omega_k \dot{q}_k + \omega_k^2 q_k = \bar{F}_k \quad (3.14)$$

The computer program MODAL (source listing in Appendix A) has been developed to do modal analysis. The Jacobi method [11] is used to find frequencies and mode shapes. The Newmark β method [11] is used to integrate the uncoupled equations of motion (3.14).

3.3 Rotational Degrees of Freedom

The linear dynamic analysis program MODAL was tested and verified through use of the dynamic capabilities of SAP IV [3]. The test earthquake (ground accelerations \ddot{x}_g) is shown in Figure 3.4. The idealized structural model used is that shown in Figure 3.2. The results from both SAP IV and MODAL for the displacement of the top mass (defined as u_1) are given by curve 1 in Figure 3.5, the small differences between the two analyses not being discernible with the scale used.

It is standard procedure in dynamic analysis to eliminate rotational degrees of freedom. This can be done by using any one of a number of condensation methods or by dropping all terms in the stiffness and mass matrices which are associated with rotational degrees of freedom. Condensation procedures require that a matrix be inverted each time the stiffness matrix is set up. It would be expensive to use one of these condensation methods in a nonlinear analysis since it would require finding the inverse of a 5×5 matrix every time a stiffness change was encountered. A much simpler method would be to drop out rotational degrees of freedom from the model and subject this new model to the test

earthquake. Curve 2 in Figure 3.5 shows the effects of dropping the rotational degrees of freedom. Clearly the model is significantly stiffer than the model corresponding to curve 1. This can be seen quite clearly in Table 3.3. The first column shows the natural frequencies obtained when the rotational degrees of freedom are included.

Column 2 gives the frequencies obtained by dropping the rotational degrees of freedom. A comparison of the fundamental frequencies shows that the 5 DOF model has a fundamental frequency which is 25% higher than the 10 DOF model. Curve 2 shows that this increase in stiffness affects the motion of the top mass significantly for the base motion shown in Figure 3.4. However, it must be noted that this base motion is of extremely short duration (.25 seconds) and means nothing as far as design requirements go. The NRC response spectra shown in Figure 1.3 is the basis of seismic design of containment vessels (see Introduction). This figure shows that the frequencies of 6.0 cps and 7.5 cps occur in a flat region of the graph for the spectral acceleration. For a maximum base acceleration of 1.0 g both frequencies correspond to a spectral acceleration of about 3.5 g (for 5% critical damping). The maximum displacements for 6.0 cps and 7.5 cps are 1.0 inches and .5 inches, respectively. This would seem to indicate that dropping the rotational degrees of freedom will give forces and moments which are acceptable but will underestimate the maximum displacements by about 50%. This is borne out by the results of the test case since the maximum base shears were fairly close for the two models (.139 ksi for the 5 DOF model and .159 ksi for the 10 DOF model). Since the time history of displacements is of great importance it is concluded that rotational degrees of freedom should be included in the seismic analysis of a containment vessel. Rotational

degrees of freedom will be included in the rest of this study.

Chapter 4

SOIL-STRUCTURE INTERACTION

4.1 Introduction

If a seismograph were placed in an area in which no buildings were located the time history of the ground movements obtained would be the "free field" accelerations. Normally, the flexible multistory buildings built in this country do not have sufficient stiffness and mass to affect these free field accelerations. If a seismic analysis were to be performed on one of these buildings it would usually be sufficient to use the free field accelerations as the base accelerations defined as \ddot{x}_g in the previous chapter. However, a nuclear containment vessel is much stiffer than most multistory buildings. If the containment vessel is at least as stiff as the underlying soil then the inertial forces developed during an earthquake will cause local deformations in the soil in the area of the foundation. These local soil deformations may alter the free field motion considerably. The degree of alteration depends on the relative stiffness and mass ratios between the structure and the soil. Naturally if the structure is much stiffer than the soil the local foundation base motion may be quite different from the free field motion. This change in motion at the soil-structure interface is called soil-structure interaction. Soil-structure interaction should be differentiated

from soil amplification.

Soil amplification is the effect of local soil conditions on the seismic waves produced by an earthquake. The effect may be one of amplification, attenuation or filtering of the underlying "base rock" motions. In Figure 4.1 the base rock motion is shown as \ddot{x}_1 , the free field motions (which occur a large distance from the containment) are \ddot{x}_2 and ground accelerations at the base of the foundation (taking into account soil amplification and soil-structure interaction) are \ddot{x}_3 .

4.2 Brief Summary of Seismic Waves

The underlying causes of earthquakes are not yet well known. The most widely accepted theory at this time is the elastic rebound theory developed by H. F. Reid following the San Francisco earthquake of 1906. Reid's study of the large shear displacements along the San Andreas fault led him to conclude that the vibrational energy of earthquakes originates from the release of accumulated strain in the earth's crust. These strains are caused by the movement of large crustal plates. In the case of the San Andreas fault this movement is a counterclockwise rotation of the Pacific basin crustal plates relative to the North American continental land mass [11]. The strain release is a sudden shearing fracture.

The wave systems which result from this fracture are what actually cause the surface vibratory motion. It can be shown [5] by using the three dimensional wave equations that in an unbounded isotropic solid only two types of elastic wave may be propagated. These waves are called

the irrotational (P-waves) and equivoluminal (S-waves) waves. The velocities of the P-waves (C_1) and S-waves (C_2) are

$$C_1 = \sqrt{(\lambda_L + 2G)/\rho_s}$$

$$C_2 = \sqrt{G/\rho_s}. \quad (4.1)$$

λ_L is Lamé's constant, G is the shear modulus and ρ_s is the density of the medium through which the waves travel. Clearly the P-waves travel faster than the S-waves through all media. When there is a bounding surface, surface waves also occur. It can be shown that these surface waves (one type is Rayleigh waves) decay rapidly with depth of the medium but show much less amplitude decay than P-waves or S-waves at the surface boundary. The surface motion contains both vertical and horizontal (parallel to wave direction) components. They travel with a velocity (C_R) slightly less than that of the S-waves. For μ (Poisson's ratio) = .25, $C_R = .9194 C_1$.

Seismographic records show that earthquakes may be broken down into two stages. These are the preliminary tremor and main shock. The preliminary tremor consists of two phases, which correspond to the arrival of first the P-waves and then the S-waves through the interior body of the earth. The main shock may be broken down into three phases. In the first two phases the movement is horizontal and transverse to the direction of wave propagation. In the third phase the horizontal movement is in the propagation direction. The movements in the main shock are much larger than in the preliminary tremor. Originally it was felt that the main shock was caused by Rayleigh waves travelling over the surface

of the earth from the initial disturbance. However, the vertical component of motion is larger than the horizontal component at the surface for Rayleigh waves. Also the horizontal motion in Rayleigh waves is in the wave propagation direction. Thus Rayleigh waves don't explain the motion in the first two phases of the main tremor.

Love [6] proposed that the transverse movements in the main shock are caused by waves which travel through an outer crust of the earth which differs in material properties from the interior. These waves, called Love waves, do not penetrate deeply into the interior of the earth and because of this create large amplitude motions at large distances from the initial disturbance. For Love waves to be confined to this outer crust, the S-wave velocity C_2 for this outer layer must be less than C_2 for the next lower layer. Love waves will not occur unless this is true. The Love wave travels with a velocity somewhere between C_2 for the outer crust and C_2 for the next lower layer. The transverse motion in the first two phases of the main shock is then caused by Love waves. The longitudinal motion in the third phase must then be caused by Rayleigh waves, which travel at a speed less than C_2 .

4.3 Modeling of the Soil

The stiffness and damping effect of the soil will be modeled using equivalent springs and dashpots. The values for these springs and dashpots are found from the problem of a rigid circular footing which oscillates on an elastic half-space. For ground motion in the horizontal direction, we need spring constants which correspond to the u_f and ϕ_f degrees of

freedom shown in Figure 4.2. These springs are actually functions of the load frequency, but it has been found [7] that the following frequency independent expressions are adequate.

$$K_u = \frac{32(1 - \mu)Gr_o}{7 - 8\mu}$$

$$K_\phi = \frac{8Gr_o^3}{3(1 - \mu)} \quad (4.2)$$

G and μ are the shear modulus and Poisson's ratio for the soil and K_u and K_ϕ are the translational and rotational spring constants shown in Figure 4.3. Poisson's ratio varies from about .35 to .5 in soils, depending upon the degree of saturation. A value of .4 will be used in this investigation. From various in-situ tests, typical values of the shear wave velocity C_2 may vary from about 500 fps (weak soils) to 2000 fps (rock). G is directly related to C_2 by (4.1). Table 4.1 gives values of K_u and K_ϕ for shear velocities of 500 fps, 1200 fps and 2000 fps with $\mu = .4$ in all cases.

In an ideal elastic half-space only geometrical damping exists. Geometrical damping is caused by the loss of energy which occurs when the elastic waves travel from the footing out to infinity. Calling the translational and rotational geometric damping ratios D_{uG} and $D_{\phi G}$, we have from [7] that

$$D_{uG} = \frac{.288}{(B_u)^{1/2}} \quad B_u = \frac{(7 - 8\mu)m_f}{32(1 - \mu)\rho_s r_o^3}$$

$$D_{\phi G} = \frac{.15}{(1 + B_\phi)(B_\phi)^{1/2}} \quad B_\phi = \frac{3(1 - \mu)I_f}{8\rho_s r_o^5} \quad (4.3)$$

m_f and I_f are the mass and mass moment of inertia (calculated at the top of the foundation) of the circular foundation. ρ_s is the density of the underlying soil.

$$m_f = \frac{\pi r_o^2 t_f \gamma_c}{g} = 61.74 \text{ k-sec}^2/\text{in}$$

$$I_f = \frac{1}{4} M_f r_o^2 + \frac{1}{3} M_f t_f^2 = 12.742 \times 10^6 \text{ k-sec}^2\text{-in}$$

$$\gamma_c = \text{Unit weight of concrete} = .15 \text{ K/ft}^3$$

$$t_f = \text{Foundation thickness} = 9 \text{ ft}$$

$$r_o = \text{Foundation radius} = 75 \text{ ft}$$

B_u and B_ϕ are the modified mass ratios. They essentially describe the relationship between the mass of the foundation which undergoes either translational or rocking motion and the effective mass of the underlying soil. It is felt that equations (4.3) give soil damping percentages which are too high [8].

In real soils hysteretic damping is also important. Hysteresis occurs when loading and unloading follow different paths on the stress-strain diagram (see Figure 4.4). In each complete loading cycle an amount of energy equivalent to the area inside the hysteresis loop is dissipated. Hysteresis in soils is caused by slippage between particles and clearly is dependent upon the magnitude of maximum strain in the soil. For SSE earthquakes (peak ground acceleration greater than .1 g) this damping is usually taken as about 5%. The total damping ratios D_u and D_ϕ

are then the sum of geometric and hysteretic damping.

$$D_u = D_{uG} + .05$$

$$D_\phi = D_{\phi G} + .05 \quad (4.4)$$

If the above value of m_f and I_f are substituted into the equations for geometric damping (4.3) extremely high values of D_{uG} and $D_{\phi G}$ result (for $\mu = .4$, $D_{uG} = .56$ and $D_{\phi G} = .14$). Since the validity of equation (4.3) is in doubt, the values of $D_u = .25$ and $D_\phi = .05$ will be used in all subsequent analysis. These values are recommended in [9].

The necessary additions to the global stiffness matrix are shown in Table 4.2. The first ten rows and columns are exactly the same as in Table 3.2. The element stiffness matrix $[K_{ff}]$ contains the stiffness contributions of the translational and rotational soil springs.

4.4 Mass and Damping Matrices for SSI

Certain changes and additions must be made in the mass, stiffness and damping matrices described in Chapter 3 to implement the soil-structure interaction model shown in Figure 4.3. The degrees of freedom to be included in this analysis are

$$[u] = [u_1 \ \theta_1 \ u_2 \ \theta_2 \ u_3 \ \theta_3 \ u_4 \ \theta_4 \ u_5 \ \theta_5 \ u_f \ \theta_f]. \quad (4.5)$$

In (4.5) $u_1 \dots u_5$ and u_f are displacements relative to the ground.

tive critical damping ratio for each mode. In this method, the modal damping ratio D_m is the weighted average of dissipated strain energy:

$$D_m = \frac{\sum_{i=1}^{nm} E_{im} d_i}{E_m} \quad (4.7)$$

D_m = modal damping factor at m^{th} mode

d_i = fraction of damping factor of i^{th} mass

E_m = total energy in m^{th} mode

E_{im} = energy in i^{th} mass in m^{th} mode

nm = number of masses in analysis

$$E_{im} = \frac{1}{2} \phi_{\ell m} k_{\ell j}^{(i)} \phi_{jm} \quad \ell = 1 \dots nm \quad j = i \dots nm \quad \text{no sum on } m$$

$$E_m = \sum_{i=1}^{nm} E_{im}$$

ϕ_{ij} = modal displacement of i^{th} mass for j^{th} mode

$K_{\ell j}^{(i)}$ = element stiffness of i^{th} member connecting nodes ℓ and j (see Table 3.1). The modal damping ratios thus calculated may then be used in the program MODAL as described in Chapter 3 and the Appendix. If direct numerical integration of the equations of motion is to be performed (as will be done in the next chapter), then the fully populated damping matrix [C] may be found:

$$[C] = [A^T] [D] [A]^{-1} \quad (4.8)$$

[D] is a diagonal matrix which contains the modal damping factors obtained from (4.7).

Soil-structure interaction is included in all of the seismic analyses discussed in the next chapter. The effects of changing the stiffness of

the underlying soil will be studied in particular.

Chapter 5

SEISMIC ANALYSIS INCLUDING CRACKS

5.1 Introduction

In this chapter the effect of including cracks in seismic analysis will be studied. First, new IST test results are described. The idealization of these cracks for use in the nonlinear computer program SAC is shown. The numerical integration techniques used in SAC are described. A synthetic time history is used as input to SAC in a parameter study designed to study the effects of including cracks in seismic analysis and to show the significance of varying the values of the soil springs described in Chapter 4. Finally system identification is used to find a linear model which can best approximate the results obtained from SAC.

5.2 Modeling of the Cracks

The circumferential (horizontal) and longitudinal (vertical) cracks in the vessel may have a significant effect on the dynamic response of the vessel due to the SSE. The effect of cracks on seismic analysis has been studied previously at Cornell [15]. The important design parameters (as described in the Introduction) which may be affected are the liner distor-

tion and the maximum shear stress in the concrete containment vessel. For the seismic analysis, recent IST test results [2] are used. In the beam tests described in Chapter 2 the dead weight of the specimen and the axial loading system made it difficult to achieve a uniform crack width at the shear plane before the initiation of the cyclic shear test. In the more recent tests, the loading setup shown in Figure 5.1 was used. An independent frame was used to tension the internal reinforcing bars. The crack at mid-height of the block was formed by initially tensioning the reinforcing bars. The location of the crack was set by use of a crack-initiating groove which was formed into the specimen during casting. The shear loading was applied at the vertical beams, which could be moved up or down to reverse the loading direction. This setup resulted in less tilting at the crack plane and a more uniform crack width. After the desired initial crack width was obtained by stressing the reinforcing bars, the cyclic shear stress tests were begun.

In one of the test specimens two #14 reinforcing bars were cast into the specimen in a plane perpendicular to the direction of loading. The reinforcement ratio (steel area/cross-sectional area) for the block was .0178. The reinforcement ratio for the longitudinal steel in a typical containment vessel is .0185 (two #18's spaced at 8 inches) which is reasonably close to this test case. Presently, no tests have been done using #18 bars but the effects of increasing the bar diameter may be significant. The initial crack width was .02 inches with a bar tension of 31 ksi.

The cyclic loading schedule was: 9 cycles at 110 psi on the gross concrete area, 6 cycles at 125 psi, 11 cycles at 202 psi, 13 cycles at 260 psi and 4 cycles more at 260 psi with the bar tension increased to

41 ksi. Each loading cycle was composed of a complete reversal of the maximum stresses listed above. Cycles 1, 15 and 25 were loaded incrementally so that detailed measurements of horizontal slip, increase in crack width and bar strains could be taken. The specimen failed during the 42nd cycle at a stress of 230 psi. The mode of failure was a sudden brittle splitting fracture which was due to the dowel forces in the reinforcing bars. Figure 5.2 shows the shear stress versus horizontal slip measurements for the 1st, 15th and 25th cycle. The loading portion of the 1st cycle is almost linear, while the 15th and 25th cycles show the same hardening effects as was observed in the beam tests. After the 1st cycle the shape and slope of the hysteresis loops were essentially the same with only the maximum slip changing with each cycle. The maximum slip increased at a nearly constant rate in these tests. The crack width remained nearly constant at .02 inches until just before failure.

In the seismic analysis only the horizontal cracks will be included. As was mentioned previously in Chapter 2, the vertical cracks may significantly affect the shear and flexural stiffness of the containment vessel. Since only uniaxial tests have been performed at this time it is difficult to quantitatively assess the effects of horizontal cracks. It is felt that a decrease in the flexural stiffness of the containment is not a significant factor. Tests using the program MODAL have shown that if the flexural stiffness of the containment vessel is reduced by one-third the fundamental frequency changes by less than 1%. However, a large change in the shear stiffness of the vessel would produce significant changes in the seismic analysis. Current tests under way at Cornell include cracks in both the horizontal and vertical directions. These tests should give quantitative results on how much the vertical cracks affect the shear stiffness of the

containment vessel.

The stiffness of the horizontal cracks is found from the test results shown in Figure 5.2. To simplify the analysis these curves are idealized in the manner shown in Figure 5.3. In this figure the data from the 25th loading cycle and the idealization are shown. The idealization consists of six straight lines which were drawn to model as best as possible the slope of the hysteresis curves and the area inside the curves (energy loss/cycle). Note that in Figure 5.3 the shear-slip curve is nonsymmetric about the y-axis. It was felt that this was due to eccentricity in the axial loading system and the entire hysteresis loop is moved to the left in Figure 5.4 so that the loop is anti-symmetric about the y-axis.

In this same figure four assumptions which have not yet been experimentally verified are shown. Unloading from point A on line 1-2 is done along line A-B which is parallel to line 2-3. This assumption should be correct since the unloading stiffness remained almost constant for all cycles, including the early cycles which only went up to 110 psi maximum shear stress. The second assumption is that reloading from point C on line 2-3 goes along line C-D which is parallel to line 1-2. The reasoning behind this is that the higher loading stiffness (the slope of line 1-2) is activated when loading occurs at a shearing stress greater than the stress at point 1 (30 psi in this case). The last assumption is also based on this. Line E-F shows unloading from a stress greater than that at point 2 (202 psi). Reloading occurs along line F-G (parallel to line 1-2) since the stress at point F is greater than the stress at point 1. These three assumptions all hold true for the shear-displacement curves in the third quadrant. The arrows in Figure 5.4 show the possible load directions along each of the six lines. Along line 1-2 only loading occurs. Only

unloading occurs along (or parallel to) line 2-3. Slip may occur in both directions along lines 3-4 and 1-6. Loading in the negative direction occurs along line 4-5 and unloading along (or parallel to) line 5-6. Only unloading occurs along 3-H and 6-I. As mentioned above, loading starts in a direction parallel to line 2-3 from both these lines.

The hysteresis loops change with load cycling in the manner shown in Figure 5.2. The idealization of this phenomenon is shown in Figure 5.6. The first cycle of loading is assumed to be linear (for both loading and unloading). The hysteretic behavior first appears in the second cycle and continues through the rest of the load cycles. The slope of each of the six line segments that compose the hysteresis loop remains the same for all cycles. The stiffness break point is 30 psi (for loading) for all cycles. The manner in which one cycle of loading or unloading is defined is described in the next section.

The flexibility of the cracks must be included in the global stiffness matrix $[K]$. This is done by considering the cracked cantilever beam shown in Figure 5.7. For purposes of illustration, the element stiffness matrix will be developed for the case of one crack in the beam, but this formulation may easily be generalized to the case of N cracks in a beam. First the deflection u_1 and rotation due to the loads P_1 and M_1 are calculated. At the crack plane the bond between the reinforcing bars and concrete is destroyed for a certain length. In the tests described previously the unbonded length was about 2 inches. Since these tests were performed on #14 bars the unbonded length (L_u) was scaled up to $18/14 \times 2 = 2.5$ inches for use in this analysis. The linear scale factor was used because unbonded length is a function of the bar force/bond force ratio. The bar force and the bonding force (per unit length) are proportional to the

reinforcing bar area and circumference, respectively. Over the unbonded length a conservative assumption would be that the moment of inertia is provided only by the longitudinal reinforcement. This moment of inertia over the unbonded length at the crack plane will be called I_c . Including this in a moment area analysis of the cracked shear beam we find that

$$\begin{Bmatrix} u_1 \\ \theta_1 \end{Bmatrix} = \begin{bmatrix} \left(\frac{L^3}{3EI} + \frac{L}{GA_s} + \frac{1}{K_c} + A \right) & \left(\frac{L^2}{2EI} + B \right) \\ \left(\frac{L^2}{2EI} + B \right) & \left(\frac{L}{EI} + C \right) \end{bmatrix} \begin{Bmatrix} P_1 \\ M_1 \end{Bmatrix}$$

$$A = \frac{L^2 L_u}{4E} \frac{1}{I_c} - \frac{1}{I} \quad B = \frac{L L_u}{2E} \frac{1}{I_c} - \frac{1}{I} \quad C = \frac{L_u}{E} \frac{1}{I_c} - \frac{1}{I} \quad (5.2)$$

where K_c is the crack stiffness.

This equation is inverted to obtain

$$\begin{Bmatrix} P_1 \\ M_1 \end{Bmatrix} = \frac{1}{\det} \begin{bmatrix} \frac{L}{EI} + C & - \frac{L^2}{2EI} + B \\ - \frac{L^2}{2EI} + B & \frac{L^3}{3EI} + \frac{L}{GA_s} + \frac{1}{K_c} + A \end{bmatrix} \begin{Bmatrix} u_1 \\ \theta_1 \end{Bmatrix}$$

$$\det = \frac{L^4}{12E^2 I^2} + \frac{L}{EI} \left(\frac{L}{GA_s} + \frac{1}{K_c} \right) + \frac{AL}{EI} + C \left(\frac{L^3}{3EI} + \frac{L}{GA_s} + \frac{1}{K_c} + A \right) - B \left(\frac{L^2}{2EI} + B \right) \quad (5.3)$$

$$\begin{Bmatrix} P_1 \\ M_1 \end{Bmatrix} = \begin{bmatrix} K_{11} \end{bmatrix} \begin{Bmatrix} u_1 \\ \theta_1 \end{Bmatrix} \quad (5.4)$$

From equilibrium

$$\begin{Bmatrix} P_2 \\ M_2 \end{Bmatrix} = \begin{bmatrix} -1 & 0 \\ -L & -1 \end{bmatrix} \begin{Bmatrix} P_1 \\ M_1 \end{Bmatrix} \quad (5.5)$$

$$\begin{Bmatrix} P_2 \\ M_2 \end{Bmatrix} = [K_{21}] \begin{Bmatrix} u_1 \\ \theta_1 \end{Bmatrix} \quad (5.6)$$

$$[K_{21}] = \frac{1}{\det} \left[\begin{array}{c|c} -\left(\frac{L}{EI} + C\right) & \frac{L^2}{2EI} + B \\ \hline B - \frac{L^2}{2EI} - LC & \frac{L^3}{6EI} + BL - \frac{L}{GA_s} - \frac{1}{K_c} - A \end{array} \right] \quad (5.7)$$

If the cracked beam element is fixed at node 1 ($u_1 = 0, \theta_1 = 0$) and free at node 2, then u_2 and θ_2 for the loads P_2 and M_2 are

$$\begin{Bmatrix} u_2 \\ \theta_2 \end{Bmatrix} = \left[\begin{array}{c|c} \frac{L^3}{3EI} + \frac{L}{GA_s} + \frac{1}{K_c} + A & -\left(\frac{L^2}{2EI} + B\right) \\ \hline -\left(\frac{L^2}{2EI} + B\right) & \frac{L}{EI} + C \end{array} \right] \begin{Bmatrix} P_2 \\ M_2 \end{Bmatrix} \quad (5.8)$$

After inversion (5.8) becomes

$$\begin{Bmatrix} P_2 \\ M_2 \end{Bmatrix} = \frac{1}{\det} \left[\begin{array}{c|c} \frac{L}{EI} + C & \frac{L^2}{2EI} + B \\ \hline \frac{L^2}{2EI} + B & \frac{L^3}{3EI} + \frac{L}{GA_s} + \frac{1}{K_c} + A \end{array} \right] \begin{Bmatrix} u_2 \\ \theta_2 \end{Bmatrix} \quad (5.9)$$

$$\begin{Bmatrix} P_2 \\ M_2 \end{Bmatrix} = \begin{bmatrix} K_{22} \end{bmatrix} \begin{Bmatrix} u_2 \\ \theta_2 \end{Bmatrix} \quad (5.10)$$

$$\begin{Bmatrix} P_1 \\ M_1 \end{Bmatrix} = \begin{bmatrix} K_{12} \end{bmatrix} \begin{Bmatrix} u_2 \\ \theta_2 \end{Bmatrix} \quad (5.11)$$

From the reciprocal law we have that

$$\begin{bmatrix} K_{12} \end{bmatrix} = \begin{bmatrix} K_{21} \end{bmatrix}^T \quad (5.12)$$

The complete cracked beam element stiffness matrix for N equally spaced cracks is given in Table 5.1. Formulas for A, B, C and det are also given for N equally spaced cracks in the beam element.

The crack stiffness K_c is obtained from the hysteresis loops in Figure 5.6. The slopes of these lines are in units of ksi/in. The values must be multiplied by the shear area of A/2 (as was concluded in Chapter 2) to obtain the crack stiffness K_c . The factor of N/K_c (in Table 5.1) will be changing during the seismic analysis as the shear stress at the cracks traverses the hysteresis loops. Some method must be devised of keeping track of where each crack is on its respective loop. This is discussed in the following section.

5.3 Nonlinear Seismic Analysis

A program has been written to perform seismic analysis incorporating the effects of circumferential cracking. This program, which is named

SAC (Seismic Analysis including Cracks, see Appendix) uses numerical integration rather than the method of normal modes used by MODAL. Since the cracks are to be included the overall stiffness of the vessel is no longer constant but is a function of the shearing stresses in the vessel. Because of this direct numerical integration of the equations of motion (3.1) is performed. The mass [M] and damping [C] matrices have been described in Chapter 4. The element stiffness matrix shown in Table 5.1 is used in the manner shown in Table 4.2 to obtain the global stiffness [K]. Equations (3.1) are solved iteratively using the Newmark β method. The convergence criterion for ending the iterations is

$$(\Delta u_{ti+1} - \Delta u_{ti}) / \Delta u_{ti} \leq \text{TOL} \quad (5.13)$$

with Δu_{ti} being the change in relative displacement from time t to time $(t + \Delta t)$ for the i^{th} iteration and Δu_{ti+1} the same quantity for the $i + 1$ iteration. TOL is the convergence criterion which should be .001 or less for reasonable accuracy. The size of the time step, Δt , is critical as far as obtaining accuracy and rapid iteration convergence. It was found during test runs that did not include crack flexibilities that the maximum time step where convergence could be achieved was .0025 seconds. This time step will be used throughout this chapter also.

Stiffness changes will occur during some time steps. This is obvious when one sees the nonlinear stiffness idealization of the cracks shown in Figure 5.4. The SAC subroutine INHYST keeps track of where each crack is on the hysteresis loops of Figure 5.6 and makes changes in the crack stiffness when necessary. A time step is repeated only when the stiffness change from line 2-3 to line 3-4 or from line 5-6 to line 6-1 occurs (see

Figure 5.5). This is because the high velocities which occur during the unloading from lines 2-3 and 5-6 can cause the crack slip to go far below the specified slips at points 3 and 6, which causes the loop to grow much wider than originally specified. The iteration scheme designed to prevent this is shown in Figure 5.5. At time t , one of the cracks is at the position marked on line 2-3 of the hysteresis loop. At time $(t + \Delta t)$, point 3 has been missed by a significant amount. The program SAC goes back to time t , refines the time step Δt to $\Delta t'$ (according to simple linear interpolation) and computes the shear stress and crack displacement at $(t + \Delta t')$. If the shear stress is not within a specified limit ($\pm .05$ shear₃) of shear₃, then another iteration using a smaller time step $\Delta t''$ is performed. This process continues until the specified limits are met. The same procedure is used for the stiffness change between lines 5-6 (and all lines parallel to it) and for the change between lines parallel to 2-3 and 3-4.

The changing of hysteresis loops due to cycling is shown in Figure 5.6. All cracks start on the cycle 1 line. Once the shear stress of 30 psi is exceeded and unloading starts the unloading proceeds along a line parallel to line 2-3 (as shown by dashed line A-B). The 2nd cycle loop is reached when A-B intersects line 3-4. From there on the cycles are defined in the following manner: a cycle occurs when the shear stress across a crack unloads from a stress of at least ± 100 psi to a stress of less than ± 50 psi.

The lines which make up all the hysteresis loops have the same slopes. The only difference between these loops is that the points 1 and 4 move further away from the origin at a uniform rate as cycling proceeds. This is confirmed by the test data described previously which showed that the

maximum slip in each cycle increased at a fairly uniform rate (.0001 in/cycle). The method of changing from the 2nd cycle loop to the 3rd cycle loop is shown in Figure 5.8. The shear at a crack on the 2nd cycle loop has increased to above 100 psi. Unloading occurs along the dashed line and goes below 50 psi. Since this means that the 3rd cycle has now been reached the unloading continues along line 3'-4' of the 3rd cycle loop instead of 3-4 of the 2nd loop. These unloading paths have not yet been verified completely by testing but they seem to be a rational way of explaining a complex phenomenon and are the most convenient manner of including the effects of cycling in the program.

5.4 Input to Linear and Nonlinear Analyses

The earthquake to be used as ground motion is specified as a time history of ground accelerations which correspond to the horizontal design response spectrum from NRC provision 1.60 shown in Figure 1.3. A deterministic method described in [12] used a "spectrum-suppressing" technique to develop a ground motion time history which corresponds to this spectrum. This method is used to generate a base motion time history which has a maximum ground acceleration of .4 g (typical for an SSE) and a duration of 11.5 seconds.

Computer Run 1 makes use of the linear model described in Chapter 3. The member properties and lumped masses are given in Figure 3.2. The element and global stiffness matrices are given in Tables 3.1 and 4.1. The mass matrix is given in Table 5.6. The soil springs used are those given for the medium stiffness soils shown in Table 4.2. The damping

matrix is found using the method described in Chapter 4 with the critical damping percentages recommended there. Note that no cracks at all are assumed in the containment vessel and that the concrete is assumed to remain elastic throughout the earthquake. The linear seismic analysis program MODAL is used to perform the analysis.

Runs 2 - 4, made with the SAC nonlinear analysis program, included the effects of the cracks shown in Figure 1.2. This figure shows the cracking pattern of a containment vessel which has been internally pressurized for test purposes. Large horizontal cracks (about .015 inches wide) occurred at the construction joints, which were spaced at 5'-6" in this vessel. Between these joints smaller cracks occurred which did not run completely around the vessel. At the construction joints the moment of inertia is I_c , as was described in section 5.3. In between the joints small cracks do exist so it would be incorrect to use the moment of inertia of the full section there. Since the cracks do not extend to the neutral axis the fully cracked moment of inertia is also not correct. The moment of inertia I will then be taken as the average of the full section moment and the cracked section moment. The member properties for these three runs are given in Table 5.4. The element and global stiffness matrices are given in Tables 5.1 and 4.2, respectively. The mass and damping matrices are the same as for Run 1. The crack spacing is the 5'-6" shown in Figure 1.2. The only parameters to be varied in Runs 2 - 4 are the soil spring stiffnesses. Run 2 uses the K_u and K_ϕ given for medium stiffness soils in Table 4.2. Run 3 corresponds to soft soils and Run 4 uses the hard soil values. The medium soil stiffness of Run 2 is the most likely soil to be encountered in practice so the results of this run have the most importance for design considerations. Table 5.5 summarizes the

soil types and crack spacings used for each computer run.

5.5 Discussion of Results

The displacement time histories for the top (mass 1) and bottom masses (mass 5) are shown for Runs 1 - 4 in Figures 5.9 - 5.12. Figures 5.9 and 5.10 show the results for the uncracked containment founded on a soil of medium stiffness (Run 1) and for the cracked containment vessel founded on a medium soil (Run 2), respectively. These figures show the effects of including the cracks in the seismic analysis of a containment vessel. The maximum response for both runs occurs in the interval between $t = 10.15$ and $t = 10.5$. The most obvious difference is that both the maximum positive and negative displacement peaks are greater for Run 2. This is to be expected since the inclusion of the cracks creates a more flexible model. The difference in maximum peaks is not great; the ratio of peaks for Run 1 to Run 2 being about .85. This increase in flexibility is also apparent in the period of oscillation. In both runs a positive peak occurred at $t = 10.15$. For Run 1 the next positive peak occurs at $t = 10.46$ for a period of .31 seconds. For Run 2 the next positive peak occurs at $t = 10.53$ for a period of .38 seconds. These periods are about the same for both runs for the large oscillations which occur between $t = 8.9$ and $t = 9.3$. This lengthening of period can once again be explained by the inclusion of crack flexibility. The maximum values for displacement (of mass 1, the top mass) shear and crack slip are given in Table 5.2 for Runs 1 - 4. The difference in maximum shear stress is negligible for Runs 1 and 2. However, Table 5.2 points out that the linear analysis

gives no values for crack slip, an important design parameter which will be discussed later in this section.

Figures 5.9 and 5.10 show that significant differences exist in the displacement time histories for the uncracked and cracked seismic analyses. The displacement or acceleration time histories are of particular importance in seismic analysis of equipment which is supported by the containment vessel. Normally this equipment is not included in the analysis of the containment. If the equipment were included the results would probably be unreliable because of the large difference in mass between the containment and the equipment. Because of this the containment and the equipment are analyzed separately and the results from the containment analysis are used as input for seismic analysis of the equipment. In Figure 1.1 it is shown that a crane is supported by a concrete floor which frames into the containment wall. Certainly the motion of the top of this crane would be of importance in design. Because of the differences in maximum response and oscillation period, it may be necessary to use the results of the nonlinear analyses as input for seismic analysis of equipment. Figures 5.11 and 5.12 show the displacement time histories for Run 3 (cracked vessel with soft underlying soil) and Run 4 (cracked vessel with hard underlying soil), respectively. Figure 5.11 shows that soft underlying soil increases the maximum displacement by a factor of $2.565/1.543 = 1.67$ and increases the period of oscillation over the maximum response interval from .38 to .55 seconds. Figure 5.12 shows that a hard underlying soil decreases the maximum displacement by a factor of $1.2/1.543 = .78$. The oscillation period decreases from .38 to .32. The softening and hardening of the soils therefore produces the expected changes in response. This is also borne out by the maximum values given in Table 5.2. While the

hardening of the soil in Run 4 produced only a small increase in shear stress (which would be expected in a stiffer system) the softening of the soil produces an extremely large decrease in maximum shear stress of 54%. The maximum crack slip increases with maximum shear stress, as expected.

The maximum number of cycles (using the cycle definition of section 5.3) naturally increases with increasing soil stiffness. It should be noted that the number of cycles obtained is not equal to the duration of the earthquake divided by the oscillation period. A different cycle definition may have caused this to come about. Certainly the higher the number of cycles and maximum shear stress the greater is the chance of concrete failure by dowel splitting. In section 5.2 it was stated that the IST test specimen failed by dowel splitting during the 42nd cycle of loading. However, the loading schedule was more severe than could be expected during an SSE design earthquake. Most of these cycles were complete reversal cycles from shear stresses of greater than 200 psi to less than -200 psi. Certainly this is much more severe than the criterion of a decrease from at least 100 psi to less than 50 psi. The maximum shear stress of 280 psi was reached only once during the earthquake. Because of this it is felt that dowel splitting will probably not occur. The only reservation comes from the fact that the tests were performed on #14 bars instead of the #18 bars normally used in containment vessels. #18 bars unquestionably would pose a more critical dowel splitting problem, but how severe this problem is cannot be estimated without further testing.

Figures 5.13 - 5.15 show hysteresis loops for the bottom beam segment which models the bottom 180 inches of the containment (see Figure 4.3) for Runs 2 - 4. These loops were drawn for the period where the maximum shear stress for each run was obtained. These figures show that some error

exists in making the stiffness change from lines 6-1 and 3-4 to lines 1-2 and 4-5. In Figure 5.13 the loop shown is for the 15th cycle. This means that the crack slip at the stiffness break point should be $(15 - 2) \times .0001 + 2.67 \times 10^{-3} = 3.97 \times 10^{-3}$ inches. The shear stress at this stiffness break should always be 30 psi. At time $t = 10.42$ the shear stress is 38 psi and the crack slip is 5.5×10^{-3} inches. It would be possible to reduce these errors by repeating the previous time step with a smaller step size but it was not felt that these errors were critical enough to justify this procedure. The main effect of these errors may be to increase the maximum crack slip of 13.6×10^{-3} inches slightly from the value that would be obtained if the time step were repeated. However, the difference is likely to be very small and also would be on the conservative side.

Figure 5.13 also shows one of the main effects of cycling, which is the narrowing of the hysteresis loop at low slips. The line followed by the cracks from $t = 10.61$ to $t = 10.63$ slightly higher up and parallel to the line followed from $t = 10.17$ to $t = 10.22$. This is the same behavior as shown in Figure 5.6. Figure 5.14 shows an example of somewhat surprising behavior. Unloading occurred from $t = 10.36$ to $t = 10.43$ along the 7th cycle hysteresis loop. However, reloading occurred at $t = 10.43$ before the expected 6-1 line (dashed line) for the 7th cycle was reached. Reloading occurred along a line parallel to 6-1 because the shear stress was less than 30 psi. The effect of this was to cause a stiffness change at $t = 10.58$ at a crack slip of 5.25×10^{-3} inches rather than 3.17×10^{-3} inches. Since test results did not look into a change of loading like this it is hard to say if this is an inadequacy of the model. Clearly this may cause crack slips to be larger than they should be, but since the maximum slips in Table 5.2 are not unexpectedly large this is probably not

a critical problem.

Table 5.3 shows the maximum seismic bending stresses which occurred in Runs 1 - 4. The concrete stress occurs in the concrete between the construction joints. The moment of inertia for the concrete is I (see Table 5.4). The maximum concrete seismic bending stress is .696 ksi in Run 4. The steel stress shown in Table 5.3 occurs in the reinforcing bars at the horizontal cracks located at the construction joints. The moment of inertia here is I_c (see Table 5.4). The longitudinal tensile stresses due to an internal pressurization of 50 psi are $pR_c/2t_c = .388$ ksi. Including dead weight (.165 ksi) but not including the effects of vertical ground accelerations, the maximum total concrete compression stress in the longitudinal direction is $.696 - .388 + .165 = .473$ ksi, which is less than the concrete allowable of $.6 f_c$ (see section 1.3). The maximum longitudinal tensile stress is $.696 + .388 - .165 = .919$ ksi. The tensile stress in the circumferential direction is $pR_c/t_c = .776$ ksi. The maximum seismic shear stress is .280 ksi.

The seismic shear stress may cause additional cracking in the vessel. At $\phi = -45^\circ$ (Figure 2.7) the longitudinal stresses are tensile. The principal tensile stress at $\phi = -45^\circ$ is .95 ksi inclined at 40° from the horizontal. This means that new crack planes inclined at 40° from the vertical may be created by the earthquake. It should be noted that this angle of inclination will change around the circumference of the vessel as the shear stress and longitudinal bending stress change. These new cracks may have some effect on the seismic response of the vessel but at this time it is not known how significant this effect may be.

Using $\rho = .0185$ (the typical longitudinal reinforcement ratio for concrete containment vessels) equation (1.2b) gives $v_c = .140$ ksi.

According to the ASME code [14] the excess shear stress of .140 ksi (.280 - .140) must be carried by inclined steel. As explained previously in this section, it is felt that the recent IST tests performed at Cornell [2] show that the combination of IST plus dowel action can effectively transfer .280 ksi across the cracks without including inclined reinforcement.

If two layers of #18 reinforcing bars are spaced at 8 inches ($1.0 \text{ in}^2/\text{in}$) around the circumference of the vessel then the stress in each rebar due to internal pressurization would be

$$\frac{\pi R_c^2 p}{2\pi R_c} = \frac{p R_c}{2} = 20.9 \text{ ksi.}$$

Adding this to the maximum seismic bending stress of 29.2 ksi and subtracting 8.9 ksi (dead weight) the total rebar stress is 41.2 ksi. Since 60 ksi steel is normally used in containments this is less than $.9 f_y$. However, if the shear and bending stresses in the rebar due to dowel action are included, the yield point may be reached. Presently it is not possible to estimate what these additional stresses are. This yielding would only occur over the unbonded length of the rebar.

The changes in crack width (shown in Table 5.3) due to the seismic bending stresses are all small compared to the initial crack width of .015 inches. These changes were computed over the unbonded bar length of 2.5 inches. If the change of crack width had been at least half as large as the initial crack width, then it could have been argued that the crack stiffness changes during the seismic analysis, since it has been shown that crack stiffness is a function of crack width. However, this was not the case so the change in crack width does not affect the analysis.

In the Introduction it was stated that the steel liner and its anchors

must be able to withstand the deformations imposed upon it by the concrete. The maximum deformation imposed on the liner is the sum of the maximum crack slip shown in Table 5.2 and the elastic shear deformation in the concrete between the construction joints. The maximum crack slip is .0143 inches in Run 4. The maximum shear stress of 280 psi also occurs in this run. The elastic shear strain in the concrete is approximately

$$\frac{.280}{1540} = .000182.$$

If the anchors are spaced at 20 inches, the elastic shear deformation over this distance is

$$.000182 \times 20 = .00364 \text{ inches.}$$

The maximum relative displacement which occurs between the anchors is then

$$.0143 + .00364 = .01794 \text{ inches.}$$

This value is far below the allowable .1 inch used as a design requirement. Since the liner is attached to the concrete the liner strain is assumed to be compatible with the concrete strain. If the liner steel modulus is 29000 ksi then

$$\epsilon_c = .473/29000 = 1.63 \times 10^{-5} < .002$$

$$\epsilon_t = (.388 + .696 - .165)/29000 = 3.17 \times 10^{-5} < .001$$

where ϵ_c and ϵ_t are the maximum compressive and tensile strains in the liner. These values are far below the ASME allowables of .002 and .001 (see Introduction).

From the stresses shown in Tables 5.2 and 5.3 it would appear that flexible soils are the optimum soils for the foundation of nuclear containment vessels. This would be an incorrect conclusion. Besides the much larger displacements that occur, it would be doubtful that a soft soil such as clay or silty clays with sand could undergo the stresses imposed upon it by the foundation and a soil failure would be likely. However, the strength of the underlying soils undergoing dynamic stresses and strains is an extremely difficult problem which will not be studied here.

5.6 System Identification

The dynamic response of a single degree of freedom structural system can be described by the following single degree of freedom system:

$$\ddot{x} + a_1\dot{x} + a_2x = p(t). \quad (5.14)$$

Here x is the displacement of the single degree of freedom and $p(t)$ is the forcing function. The coefficients a_1 and a_2 represent the stiffness and damping properties of the system. The system identification problem is normally concerned with determining these properties so that the above mathematical model will yield results which are in best possible agreement with experimental data derived from the testing of a prototype structural system. Formulated in this manner, the identification problem reduces to

a best-fit problem. Here the parameters a_1 and a_2 will be determined so that (5.14) will yield results that give the best possible agreement with the results from the nonlinear analyses discussed in the previous section. This can be done by using the direct method [13] of system identification. In this method it is assumed that $x(t)$, $\dot{x}(t)$ and $\ddot{x}(t)$ are known from the nonlinear analysis at N discrete points over the time interval $t = 0$ to $t = T$. To obtain the "best fit" values for a_1 and a_2 , the quadratic functional

$$J(a) = \sum_{i=1}^N (\ddot{x}_i + a_1 x_i + a_2 \dot{x}_i - p_i)^2 \quad (5.15)$$

is minimized. Clearly (5.15) corresponds to a least squares curve fit. p_i is the inertial force due to the base accelerations of the earthquake. Minimizing (5.15) gives the following:

$$\frac{\partial J(a)}{\partial a_1} = 2x_i \ddot{x}_i + 2a_1 x_i^2 + 2a_2 x_i \dot{x}_i - 2x_i p_i = 0 \quad (5.16a)$$

$$\frac{\partial J(a)}{\partial a_2} = 2\dot{x}_i \ddot{x}_i + 2a_1 x_i \dot{x}_i + 2a_2 \dot{x}_i^2 - 2\dot{x}_i p_i = 0. \quad (5.16b)$$

Summing (5.16a) and (5.16b) over the N time points gives

$$a_1 \sum_{i=1}^N x_i^2 + a_2 \sum_{i=1}^N x_i \dot{x}_i = \sum_{i=1}^N (x_i p_i - x_i \ddot{x}_i). \quad (5.17a)$$

$$a_1 \sum_{i=1}^N x_i \dot{x}_i + a_2 \sum_{i=1}^N \dot{x}_i^2 = \sum_{i=1}^N (\dot{x}_i p_i - \dot{x}_i \ddot{x}_i). \quad (5.17b)$$

Using Cramer's rule,

$$a_1 = \frac{1}{\det} (D1 \times C22 - D2 \times C12) \quad (5.18a)$$

$$a_2 = \frac{1}{\det} (C11 \times D2 - D1 \times C12) \quad (5.18b)$$

$$C11 = \sum_{i=1}^N x_i^2 \quad D1 = \sum_{i=1}^N (x_i p_i - x_i \ddot{x}_i)$$

$$C12 = \sum_{i=1}^N x_i \dot{x}_i \quad D2 = \sum_{i=1}^N (\dot{x}_i p_i - \dot{x}_i \ddot{x}_i)$$

$$C22 = \sum_{i=1}^N \dot{x}_i^2 \quad \det = C11 \times C22 - C12^2$$

Therefore for a single degree of freedom system there exists a closed form solution (5.18) for the parameters a_1 and a_2 . In the nonlinear analysis performed in this chapter there are a total of 12 degrees of freedom:

Modal analysis will be used to uncouple the 12 simultaneous equations of dynamic equilibrium. Then separate values of a_1 and a_2 may be computed for each mode, with each modal equation (3.14) corresponding to (5.14). If the displacements, velocities and accelerations for each time step from the nonlinear analysis are stored in the vectors $[u]$, $[\dot{u}]$ and $[\ddot{u}]$, the transformation to the generalized coordinate $[q]$ is accomplished in the following manner (see [3.12b]):

$$\{q\} = [A]^{-1} \{u\} \quad (5.19a)$$

$$\{\dot{q}\} = [A]^{-1} \{\dot{u}\} \quad (5.19b)$$

$$\{\ddot{q}\} = [A]^{-1} \{\ddot{u}\} \quad (5.19c)$$

Comparing (3.4) and (5.4),

$$a_{1K} = \omega_K^2 \quad (5.20a)$$

$$a_{2K} = 2 \beta_K \omega_K \quad (5.20b)$$

for the K^{th} mode.

The above procedure for determining the parameters a_1 and a_2 was carried out during Run 2 (medium soil stiffness). This particular run was chosen because the values used for the two soil springs represent the soil stiffness most likely to be encountered at power plant sites. The values obtained for a_1 and a_2 for the first three modes are shown in Table 5.7. These values were then used as input for MODAL. The results for the displacement of the top mass using only the first mode are shown by the dashed line in Figure 5.10. The results obtained using the first two modes were almost the same. However, when three modes were included in the analysis, the displacements became extremely large. This is probably because the third mode participates very little in the motion of the model and because of this the system identification method computes a stiffness parameter a_1 which is very low. It would be expected that a_1 for the third mode would be significantly higher than a_1 for the two lower modes, but Table 5.5 shows otherwise. Because of this low stiffness in mode three the corresponding modal equation makes bogus contributions which yield ridiculously large displacements. It appears then that using the first mode only is the most effective way of using this particular application of system identification. As shown in Figure 5.10, the displacement time history yielded by the first mode gives a very good approximation to

the nonlinear analysis. The maximum shear stress (282 psi) is also reasonably close to the value obtained by the nonlinear analysis (272 psi). It is therefore concluded that the system identification using the first mode only gives satisfactory results for both displacement time histories and maximum stresses and displacements. If a_1 and a_2 for the first mode are divided by ω_1^2 and $2\beta_1\omega_1$ it is found that

$$\bar{a}_1 = a_1/\omega_1^2 = .667 \quad (5.21a)$$

$$\bar{a}_2 = a_2/2\beta_1\omega_1 = 1.493. \quad (5.21b)$$

\bar{a}_1 shows the effect of including the cracks in the analysis. For an uncracked vessel $\bar{a}_1 = 1.0$. Clearly $\bar{a}_1 = 1.0$ shows that the cracks increase the flexibility of the model. In the same way \bar{a}_2 takes into account the effects of the hysteretic behavior of the cracks by increasing the viscous damping coefficient. With no hysteretic behavior $\bar{a}_2 = 1.0$. It would probably be incorrect to generalize these results for all base acceleration time histories. By this it is meant that a different synthetic earthquake may very well produce different values for \bar{a}_1 and \bar{a}_2 . Further work must be done using different base acceleration histories and different soil stiffness before (5.21a) and (5.21b) could be recommended for use in design.

Chapter 6

CONCLUSIONS

The main conclusions of this study are:

1. The presence of cracks in the concrete does not significantly affect the shear stress distribution in a reinforced concrete containment vessel during an earthquake. The distribution is essentially the same sinusoidal distribution which exists in elastic thin-walled cylinders. Because of this, the shear area of $A/2$ normally associated with elastic uncracked analysis is used in the nonlinear analysis in stiffness formulations and for determining maximum shear stress.

2. In linear seismic analysis rotational degrees of freedom must be included to obtain accurate displacement time histories. This must also be true for nonlinear analysis. Therefore, rotational degrees of freedom were included in all analyses.

3. There is a significant difference in the displacement time histories obtained by linear (uncracked) and nonlinear (cracked) seismic analysis. The maximum shear stresses obtained by the two methods are quite close. The effect of soil-structure interaction can be quite substantial. As the soils which underly the containment become softer the maximum stresses in the vessel will decrease significantly but maximum displacement increase by a large degree.

4. The system identification method provides a good linear approxi-

mation to the nonlinear analysis. The resultant displacement time history gives sufficiently accurate results to be used as input for seismic analysis of equipment. However, some important design parameters such as maximum crack slip cannot be provided by a linear analysis.

5. The liner distortions and strains which result from the nonlinear analysis are within allowable values. The stresses in the concrete containment are either less than the allowables given by ASME or are less than the stresses which caused failure in the IST tests. The biaxial tension field which exists in the containment vessel may give dowel splitting failures at lower shear stresses than in the uniaxial IST tests that were described here. However, the combined mechanism of IST and dowel action appears capable of replacing the inclined bars presently used to transfer shearing forces down to the foundation mat.

It is felt that adequate analytical tools exist for seismic analysis of cracked containment vessels. More experimental work is needed to investigate the combined behavior of IST and dowel action, particularly for the larger #18 bars used in containment vessel construction. It would also be interesting to see the effects of cycling at low stresses in the range of 50 psi rather than the 200 psi actually used in the tests so far. During an earthquake shear as high as 200 psi occur very rarely while 50 psi is quite common. The loading schedule used in past IST tests has been too regular. The results of seismic analyses show that shear stress loadings in the containment are very irregular and may change directions at unexpected places in the hysteresis loop which represents the load-slip behavior of the cracks. Current IST tests underway include specimens with cracks which run in both the horizontal and vertical directions and are pretensioned in both directions to simulate biaxial tension. Input from

these tests could be used in the nonlinear analysis program developed in this study to give an improved model of the containment vessel.

REFERENCES

1. White, R. N., Gergely, P., Laible, J. P., and Fajardo, O. A., "Seismic Shear Transfer Across Cracks in Concrete Nuclear Reactor Containment Vessels," Proc. Fifth World Conf. On Earthquake Engineering, Rome, 1973.
2. Jimenez, R., Perdikaris, P., Gergely, P. and White, R. N., "Interface Shear Transfer and Dowel Action in Cracked Reinforced Concrete Subject to Cyclic Shear," Methods of Structural Analysis, V. 1, pps. 457-475, Proc. of the National Structural Engineering Conf., ASCE, University of Wisconsin, 1976.
3. Bathe, K., Wilson, E. L., and Peterson, F. E., "SAP IV - A Structural Analysis Program for Static and Dynamic Response of Linear Systems," Dept. of Civil Engineering, University of California, Berkeley, 1974.
4. Clough, R. W. and Felippa, C. A., "A Refined Quadrilateral Element for Analysis of Plate Bending," Proc. of the Second Conf. on Matrix Methods in Structural Mechanics, Wright-Patterson Air Force Base, Ohio, October, 1968.
5. Kolsky, H., Stress Waves In Solids, Dover Publications, New York, 1963.

6. Love, A. E. H., Some Problems of Geodynamics, University Press, Cambridge, 1911.
7. Richart, F. E., Hall, J. P. and Woods, R. P., Vibrations of Soils and Foundations, Prentice Hall Inc., Englewood Cliffs, New Jersey, 1970.
8. Hansen, R. J., Seismic Design for Nuclear Power Plants, M.I.T. Press, Cambridge, Mass., 1970.
9. Whitman, R. V., Christian, J. T. and Bigg, J., "Parametric Analysis of Soil - Structure Interaction for a Reactor Building," Proc. of the First Int. Conf. of Structural Mech. in Reactor Technology, V. 5, pps. 257-259, Berlin, 1971.
10. Chiu, K. D. and Kuo, H. J., "Modal Damping in Dynamic Analysis of Structures," Structural Design of Nuclear Plant Facilities, V. 2, pps. 499-514, ASCE, New York, 1973.
11. Clough, R. W. and Penzien, J., Dynamics of Structures, McGraw-Hill, New York, 1975.
12. Tsai, N., "Spectrum-Compatible Motions for Design Purposes," pps. 345-355, Journal of the Engineering Mechanics Division, ASCE, EM2, April, 1972.
13. DiStefano, N. and Rath, L., "Modeling and Identification in

Nonlinear Structural Dynamics - 1. One Degree of Freedom Models,"
EERC, Univ. of California, Berkeley, 1974.

14. ASME Boiler and Pressure Vessel Code, Section III, Division 2,
ACI 359-74, ASME Boiler and Pressure Vessel Committee, ASME, New York,
1975.
15. Laible, J. P. and Gergeley, P., "Nonlinear Dynamic Analysis of
Cracked Reinforced Concrete Nuclear Containment Structures," Nuclear
Design and Engineering, 30, September, 1974.

LIST OF SYMBOLS

A	Cross-sectional area
A_s	Shear area
[A]	Matrix containing the eigenvectors
[C]	Damping matrix
D_u	Translational critical soil damping ratio
D_ϕ	Rotational critical soil damping ratio
E	Young's modulus
f'_c	Compressive strength of concrete
f_y	Yield strength of reinforcing bars
G	Shear modulus
I	Moment of inertia
I_c	Cracked moment of inertia
K_c	Crack stiffness
K_u	Translational soil spring
K_ϕ	Rotational soil spring
[K]	Global stiffness matrix
L	Length of beam segment
[M]	Lumped mass matrix
p	Internal pressure caused by loss of coolant accident
q_i	Generalized coordinate for i^{th} mode
R_c	Radius of the containment vessel cylinder
SSE	Safe Shutdown Earthquake
t	Time during seismic analysis

t_c	Thickness of containment vessel cylindrical wall
$[u]^T$	Vector of relative displacements
$[\dot{u}]^T$	Vector of relative velocities
$[\ddot{u}]^T$	Vector of relative accelerations
v_c	Maximum tangential shear stress which may be carried by concrete according to existing codes
v_u	Design tangential shear stress
V	Total shear force at a cross-section
β_i	Critical damping ratio for the i^{th} mode
ρ	Steel reinforcement ratio
ϕ	Angle that meridional plane makes with x-axis in a cylinder (see Figure 2.7)
ω_i	Natural frequency for the i^{th} mode
Δ	Crack slip
τ	Shear stress
μ	Poisson's ratio
λ	Shear flexibility factor
λ_L	Lame's constant

APPENDIX A

1. Description of the Computer Program MODAL

This program computes the response of a linear structure subjected to base accelerations which model an earthquake. The structure is idealized as a vertical cantilever shear beam with the mass lumped at the node points (lumped mass model). Soil-structure interaction may be included. When soil-structure interaction is included effective damping ratios for each mode are calculated using the subregioned energy proportion method. The natural frequencies and mode shapes are calculated using the Jacobi method. The uncoupled modal equations are integrated using the linear acceleration method.

2. Input to MODAL

The input for a sample problem will be given. The model to be input is the model of the reinforced concrete containment vessel shown in Figure 4.3. Soil-structure interaction will be included. The soil springs K_u and K_ϕ have the values 100,000 K/in and 10×10^{10} k-in, respectively. The shear area and moment of inertia for all beam segments are 150,000 in² and 9×10^{10} in, respectively. The shear area is taken as $A/2$, where A is the cross-sectional area. The lumped masses are $m_1 = 30 \text{ K-sec}^2/\text{in}$, $m_2 = m_3 = m_4 = m_5 = 25 \text{ K-sec}^2/\text{in}$ and $m_f = 60 \text{ K-sec}^2/\text{in}$. The lumped mass moments of inertia are $I_1 = I_2 = I_3 = I_4 = I_5 = 8 \times 10^6 \text{ K-sec}^2\text{-in}$ and $I_f = 13 \times 10^6 \text{ K-sec}^2\text{-in}$. The material properties are G (shear modulus) = 1500 ksi and E (Young's modulus) = 3000 ksi. The modal damping ratio for

all modes of vibration of the concrete containment is .05. The modal damping ratios for the soil in the translational and rotational directions are .25 and .05, respectively. The test earthquake shown in Figure 3.4 will be used as the base accelerations. The IBM cards (with FORTRAM format) to be input after the *DATA card follow. The units are kips, inches and seconds. The maximum number of degrees of freedom is 12.

CARD 1 (5I5, F10.0)

cols 1-5: 12 (total number of degrees of freedom)
 cols 6-10: 3 (number of modes to be included in the analysis)
 cols 11-15: 12 (number of time steps in the analysis)
 cols 16-20: 10 (number of base acceleration time points)
 cols 21-25: 3 (number of Jacobi iterations, the suggested
 number is 3)
 cols 26-35: .01 (recommended length of time step in seconds)

CARD 2 (8F10.0)

cols 1-10: 30. (m_1)
 cols 11-20: 8.0E06 (I_1)
 cols 21-30: 25. (m_2)
 cols 31-40: 8.0E06 (I_2)
 cols 41-50: 25. (m_3)
 cols 51-60: 8.0E06 (I_3)
 cols 61-70: 25. (m_4)
 cols 71-80: 8.0E06 (I_4)

CARD 3 (4F10.0)

cols 1-10: 25. (m_S)
cols 11-20: 8.0E06 (I_S)
cols 21-30: 60. (m_F)
cols 31-40: 13.0E06 (I_F)

CARD 4 (2F10.0, I5, 2F10.0)

cols 1-10: 1500. (G)
cols 11-20: 3000. (E)
cols 21-25: 1 (1 = soil-structure interaction is to be
included, 0 = no soil-structure interaction)
cols 26-35: 10.0E10 (K_ϕ)
cols 36-45: 100000. (K_u)

CARD 5 (5F10.0)

cols 1-10: 592.5 (length of top beam segment, see Figure 4.3)
cols 11-20: 360. (length of 2nd beam segment)
cols 21-30: 360. (length of 3rd beam segment)
cols 31-40: 360. (length of 4th beam segment)
cols 41-50: 180. (length of 5th beam segment)

CARD 6 (5F10.0)

cols 1-10: 9.0E10 (moment of inertia of top beam segment)
cols 11-20: 9.0E10 (moment of inertia of 2nd beam segment)
cols 21-30: 9.0E10 (moment of inertia of 3rd beam segment)
cols 31-40: 9.0E10 (moment of inertia of 4th beam segment)
cols 41-50: 9.0E10 (moment of inertia of 5th beam segment)

CARD 7 (5F10.0)

cols 1-10: 150000. (shear area of top beam segment)

cols 11-20: 150000. (shear area of 2nd beam segment)

cols 21-30: 150000. (shear area of 3rd beam segment)

cols 31-40: 150000. (shear area of 4th beam segment)

cols 41-50: 150000. (shear area of 5th beam segment)

CARD 8 (3F10.0)

cols 1-10: .05 (critical damping ratio for concrete contain-
ment vessel)

cols 11-20: .25 (critical damping ratio for translational
motion in underlying soil; D_u in Figure 4.3)

cols 21-30: .05 (critical damping ratio for rotational motion
in underlying soil; D_ϕ in Figure 4.3)

CARD 9 (2F10.0)

cols 1-10: 0. (time in seconds of base acceleration)

cols 11-20: .084 (base acceleration, fraction of g acceleration
of gravity)

CARD 10 (2F10.0)

cols 1-10: .023 (time in seconds of base acceleration)

cols 11-20: .158 (base acceleration, fraction of g acceleration
of gravity)

CARD 11 (2F10.0)

cols 1-10: .058 (time of base acceleration)

cols 11-20: .271 (base acceleration)

CARD 12 (2F10.0)

cols 1-10: .083 (time of base acceleration)

cols 11-20: .349 (base acceleration, fraction of g acceleration
of gravity)

CARD 13 (2F10.0)

cols 1-10: .113 (time of base acceleration)

cols 11-20: .446 (base acceleration)

CARD 14 (2F10.0)

cols 1-10: .149 (time of base acceleration)

cols 11-20: .509 (base acceleration)

CARD 15 (2F10.0)

cols 1-10: .186 (time of base acceleration)

cols 11-20: .382 (base acceleration)

CARD 16 (2F10.0)

cols 1-10: .23 (time of base acceleration)

cols 11-20: .191 (base acceleration)

CARD 17 (2F10.0)

cols 1-10: .256 (time of base acceleration)

cols 11-20: .058 (base acceleration)

CARD 18 (2F10.0)

cols 1-10: .3 (time of base acceleration)

cols 11-20: 0. (base acceleration)

3. Output from MODAL

For each time step, the relative translational displacement and inertial force associated with each mass is printed out. The shear stress in each beam segment is also printed out. Previous to this the global stiffness matrix, natural undamped frequencies and eigenvectors are printed.

*** MODAL ***

C
C
C
C THIS PROGRAM COMPUTES THE EARTHQUAKE RESPONSE OF A LIN
C EAR
C STRUCTURE THROUGH THE USE OF THE NORMAL MODES TECHNIQU
C E.
C THE MAIN BODY OF THE PROGRAM (WHICH FOLLOWS DIRECTLY)
C READS IN DATA AND CALLS ALL THE SUBROUTINES. THE SUBRO
C UTINES
C ARE NAMED STIFF, JACOBY, RATIO, INQUAK AND LINACC. STIFF
C SETS UP THE
C STIFFNESS MATRIX AND JACOBY COMPUTES THE NATURAL FREQU
C ENCIES
C AND EIGENVECTORS OF THIS MATRIX. RATIO COMPUTES THE EF
C FECTIVE
C CRITICAL DAMPING RATIOS FOR EACH MODE TAKING SOIL-STRU
C CTURE
C INTERACTION INTO ACCOUNT.
C INQUAK READS IN THE EARTHQUAKE ACCELERATION DATA AND C
C OMPUTES
C THE CORRESPONDING GENERALIZED FORCE. LINACC NUMERICALL
C Y
C INTEGRATES THE EQUATIONS OF MOTION USING THE LINEAR
C ACCELERATION ASSUMPTION. A MORE IN DEPTH DESCRIPTION I
C S
C GIVEN IN THE SUBROUTINES THEMSELVES.
C
C
C COMMON /DYN/GSTIFF(3),GMASS(3),DAMP(3),EQFOR(12),GFORC
C E(3),
C IDISP(12),RKFOR(12)
C COMMON /EIG/GLOK(12,12),OMEGA(12),A(12,12),RMASS(12),A
C TR(12,12)
C COMMON /PROP/AS(5),RIZ(5),SL(5),SIZ(5)
C DIMENSION D(5)
C DIMENSION BETA(5)
C DIMENSION A1(3),A2(3)
C
C N IS THE NUMBER OF DEGREES OF FREEDOM. NM IS THE NUMBE
C R
C OF MODES TO BE SUPERIMPOSED. H IS THE TIME STEP AND NH
C IS THE
C TOTAL NUMBER OF TIME STEPS IN THE ANALYSIS. NTP IS THE
C NUMBER OF GROUND ACCELERATION POINTS READ IN SUBROUTIN
C E
C INQUAK. RMASS IS THE LUMPED MASS VECTOR, G IS THE SHEAR
C MODULUS
C , AS IS THE SHEAR AREA AND SL IS THE LENGTH OF EACH SHE
C AR
C BEAM SEGMENT. IF IROT=1 SOIL STRUCTURE INTERACTION IS
C INCLUDED. ROTK IS THE ROTATIONAL SOIL SPRING AND TRANS
C K
C IS THE TRANSLATIONAL SOIL SPRING. K IS THE NUMBER OF
C JACOBY ITERATIONS AND BETA IS THE CRITICAL DAMPING RAT

```

C      IO.
C      T=TIME OF ANALYSIS.
C
      READ(5,10) N,NM,NH,NTP,K,H
      READ(5,11) (RMASS(I),I=1,8)
      READ(5,11) (RMASS(I),I=9,12)
      READ(5,12) G,E,IROT,ROTK,TRANSK
      READ(5,14) (SL(I),I=1,5)
      READ(5,14) (RIZ(I),I=1,5)
      READ(5,14) (AS(I),I=1,5)
      READ(5,14) BETA,CTRANS,CROT
      NTHETA=1
      T=0.
      ICOUNT=0
      JCOUNT=0
      IFLAG=0
      NS=N
      IF (IROT.EQ.0) GO TO 20
      NS=N-2
20  CONTINUE
      DO 21 I=1,NM
21  D(I)=BETA
      CALL STIFF(NS,IROT,ROTK,TRANSK,G,NTHETA,E)
      CALL JACOBY(N,K)
      IF (IROT.EQ.0) GO TO 99
      CALL RATIO(N,BETA,CTRANS,CROT,TRANSK,ROTK)
99  CONTINUE
      DO 2 I=1,NM
      DAMP(I)=2.*D(I)*OMEGA(I)
      GSTIFF(I)=OMEGA(I)**2
      2  GMASS(I)=1.000
      WRITE(6,48) (GSTIFF(I),I=1,NM)
      WRITE(6,48) (DAMP(I),I=1,NM)
48  FORMAT(/10X,5E14.7)
      DO 4 I=1,NH
      CALL INQUAK(N,T,NTP,ICOUNT,NTHETA,NM,IROT)
      CALL LINACC(N,NM,H,T,JCOUNT)
      T=T+H
      4  CONTINUE
10  FORMAT(5I5,3F10.0)
11  FORMAT(8F10.0)
12  FORMAT(2F10.0,I5,2F10.0)
13  FORMAT(I5)
14  FORMAT(5F10.0)
      STOP
      END
      SUBROUTINE INQUAK(N,T,NTP,ICOUNT,NTHETA,NM,IROT)
      COMMON /DYN/GSTIFF(3),GMASS(3),DAMP(3),EQFOR(12),GFORC
C      E(3),
      IDISP(12),RKFOR(12)
      COMMON /EIG/GLOK(12,12),OMEGA(12),A(12,12),RMASS(12),A
C      TR(12,12)
      DIMENSION GRACC(20),TIME(20)

```

C


```

C     THIS SUBROUTINE INITIALLY READS IN THE GROUND ACCELE
C     TION
C     HISTORY AND KEEPS TRACK OF THE CURRENT VALUE. THE GENE
C     RALIZED
C     FORCE WHICH APPEARS ON THE RHS OF THE UNCOUPLED MODAL
C     EQUATIONS IS THE VECTOR GFORCE WHICH IS COMPUTED HERE.
C     GFORCE=-ATR*RMASS*GRACC,WHERE ATR IS THE TRANSPOSE OF
C     THE
C     MODAL MATRIX AND RMASS IS THE LUMPED MASS VECTOR.
C
C     IF (ICOUNT.EQ.1) GO TO 3
C     ICOUNT=1
C     DO 1 I=1,NTP
C     READ(5,11) TIME(I),GRACC(I)
1    CONTINUE
C     DO 2 I=1,NTP
C     GRACC(I)=386.4*GRACC(I)
2    CONTINUE
C
C     NOW FIND THE CURRENT VALUE (FOR TIME=T) OF THE GROUND
C     ACCELERATION X.
C
3    IF (T.GT.TIME(NTP)) GO TO 7
C     I=1
4    I=I+1
C     IF (T.GT.TIME(I)) GO TO 4
C     IF (T.LT.TIME(I-1)) GO TO 4
C     SLOPE=(GRACC(I)-GRACC(I-1))/(TIME(I)-TIME(I-1))
C     X=GRACC(I-1)+(T-TIME(I-1))*SLOPE
C     N1=N-1
C     DO 8 I=1,N1,2
C     EQFOR(I)=-RMASS(I)*X
C     EQFOR(I+1)=0.
8    CONTINUE
101  DO 6 I=1,NM
C     GFORCE(I)=0.
C     DO 6 J=1,N
C     GFORCE(I)=ATR(I,J)*EQFOR(J)+GFORCE(I)
6    CONTINUE
7    RETURN
11   FORMAT(2F10.0)
C     END
C     SUBROUTINE LINACC(N,NM,H,T,JCOUNT)
C     IMPLICIT REAL*4 (M)
C     COMMON /DYN/GSTIFF(3),GMASS(3),DAMP(3),EQFOR(12),GFORC
C     E(3),
C     1DISP(12),RKFOR(12)
C     COMMON /EIG/GLOK(12,12),OMEGA(12),A(12,12),RMASS(12),A
C     TR(12,12)
C     COMMON /PROP/AS(5),RIZ(5),SL(5),SIZ(5)
C     DIMENSION CFORCE(12),RINFOR(12),DELDSP(3),DELVEL(3),DE
C     LACC(3),
C     IMDISP(3),MVEL(3),MACC(3),B(12,12),C(12,12),ACC(12),VEL
C     (12)

```

```

C
C THIS SUBROUTINE USES THE ASSUMPTION THAT THE ACCELERAT
C ION
C VARIES LINEARLY IN EACH TIME STEP TO COMPUTE THE CHANG
C ES
C IN VELOCITY AND DISPLACEMENT FOR EACH UNCOUPLED MODAL
C EQUATION. RMASS AND GLOK ARE THE ACTUAL STRUCTURAL LUMP
C ED
C MASS VECTOR AND GLOBAL STIFFNESS MATRIX. THE GENERALIZE
C D
C MASS, STIFFNESS AND DAMPING ARE THE GMASS, GSTIFF AND DA
C MP VECTORS.
C THE RELATIVE DISPLACEMENTS AT TIME T ARE CONTAINED IN
C THE
C DISP VECTOR.
C MDISP, MVEL AND MACC ARE VECTORS CONTAINING THE DISPLAC
C EMENTS
C , VELOCITY AND ACCELERATION AT TIME T FOR EACH MODAL EQ
C UATION.
C RKFOR IS THE VECTOR OF SHEAR FORCES IN EACH STORY. DELD
C SP,
C DELVEL AND DELACC ARE VECTORS WHICH CONTAIN THE CHANGE
C IN
C DISPLACEMENT, VELOCITY AND ACCELERATION FOR EACH MODE.
C CFORCE AND RINFOR CONTAIN THE TOTAL DAMPING AND INERTI
C AL FORCES
C AT TIME T. EQFOR IS THE INERTIAL FORCE DUE TO THE EARTH
C QUAKE
C AND GFORCE IS THIS FORCE GENERALIZED IN THE UNCOUPLED
C EQUATIONS.
C
C AT TIME T=0 INITIALIZE DISPLACEMENTS, VELOCITIES AND AC
C CELERATIONS.
C
C IF (JCOUNT.GT.0) GO TO 300
C JCOUNT=1
C DO 1 I=1,N
C DISP(I)=0.
C RKFOR(I)=0.
C RINFOR(I)=0.
1 CONTINUE
C DO 71 I=1,NM
C MDISP(I)=0.
C MVEL(I)=0.
C MACC(I)=GFORCE(I)/GMASS(I)
C DELDSP(I)=0.
C DELVEL(I)=0.
C DELACC(I)=0.
71 CONTINUE
C GO TO 400
C
C FOR EACH TIME STEP SOLVE FOR DELACC. THEN, USING THE L
C INEAR
C ACCELERATION ASSUMPTION, COMPUTE DELVEL AND DELDSP.

```

```

C
300 DO 2 I=1,NM
    DELACC(I)=(GFORCE(I)-MACC(I)-DAMP(I)*(MVEL(I)+H*MACC(I)
C    ))-
    1GSTIFF(I)*(MDISP(I)+MVEL(I)*H+MACC(I)*(H**2/2.0E0)))/(
C    1.0E0+
    2DAMP(I)*H/2.0E0+GSTIFF(I)*(H**2/6.0E0))
    DELDSP(I)=MVEL(I)*H+(H**2/6.0E0)*(3.0E0*MACC(I)+DELACC
C    (I))
    DELVEL(I)=(H/2.0E0)*(2.0E0*MACC(I)+DELACC(I))
    MDISP(I)=MDISP(I)+DELDSP(I)
    MVEL(I)=MVEL(I)+DELVEL(I)
    MACC(I)=MACC(I)+DELACC(I)
2 CONTINUE

C
C
C    NOW COMPUTE THE TOTAL RELATIVE DISPLACEMENTS (DISP),
C    TOTAL INERTIAL FORCES (RINFOR) AND TOTAL SHEAR FORCES
C    (RKFOR) AND PRINT THESE QUANTITIES OUT.
C    DISP=A*MDISP
C    RINFOR=RMASS*A*OMEGA*MDISP.RKFOR (SHEAR FORCE) IS THE
C    SUM OF ALL INERTIAL FORCES (RINFOR) ABOVE AND INCLUDIN
C    G
C    MASS I.
C

    DO 3 I=1,N
    DISP(I)=0.
    DO 3 J=1,NM
    DISP(I)=A(I,J)*MDISP(J)+DISP(I)
3 CONTINUE
    DO 4 I=1,N
    DO 4 J=1,NM
    B(I,J)=RMASS(I)*A(I,J)
4 CONTINUE
    DO 5 I=1,N
    DO 5 J=1,NM
    C(I,J)=B(I,J)*OMEGA(J)**2
5 CONTINUE
    DO 9 I=1,N
    RINFOR(I)=0.
    DO 9 J=1,NM
    RINFOR(I)=C(I,J)*MDISP(J)+RINFOR(I)
9 CONTINUE
    DO 6 I=1,5
    RKFOR(I)=0.
    L=2*I-1
    DO 6 J=1,L,2
    RKFOR(I)=RINFOR(J)+RKFOR(I)
6 CONTINUE
    DO 68 I=1,5
    RKFOR(I)=RKFOR(I)/AS(I)
68 CONTINUE
400 WRITE(6,10) T
    DO 8 I=1,5
    L=2*I-1

```

```

WRITE(6,11) DISP(L),RINFOR(L),RKFOR(I)
8 CONTINUE
10 FORMAT(/10X,'TIME=',F7.2,' SECONDS',5X,'DISPLACEMENT',
18X,'INERTIAL FORCE',6X,'SHEAR STRESS'/)
11 FORMAT(35X,E10.3,10X,E10.3,10X,E10.3)
RETURN
END
SUBROUTINE STIFF(N,IROT,ROTK,TRANSK,G,NTHETA,E)

```

C
C
C
C
C
C
C

```

THIS SUBROUTINE COMPUTES THE GLOBAL STIFFNESS MATRIX,G
LOK.
SHEAR AREA AND ROTATIONAL DEGREES OF FREEDOM ARE INCLU
DED
IN THE VERTICAL CANTILEVER BEAM MODEL.

```

```

COMMON /EIG/GLOK(12,12),OMEGA(12),D(12,12),RMASS(12),A
C TR(12,12)
COMMON /PROP/AS(5),RIZ(5),SL(5),SIZ(5)
DIMENSION TK(10),ELK(4,4),VK(12)
DO 88 I=1,5
TK(I)=SL(I)/(G*AS(I))
TK(I)=1./TK(I)
88 CONTINUE
NN=N
N1=N-1
NN=N
IF (IRGT.EQ.0) GO TO 14
NN=N+2
14 DO 13 I=1,NN
DO 13 J=1,NN
GLOK(I,J)=0.
13 CONTINUE
DO 10 I=1,N1,2

```

C
C
C

```

SET UP THE BEAM ELEMENT STIFFNESS MATRIX,ELK(4,4)

```

```

SH=(3.*E*RIZ((I+1)/2)/SL((I+1)/2)**3)/TK((I+1)/2)
ELK(1,1)=12.*E*RIZ((I+1)/2)/SL((I+1)/2)**3
ELK(1,2)=-6.*E*RIZ((I+1)/2)/SL((I+1)/2)**2
ELK(1,3)=-ELK(1,1)
ELK(1,4)=ELK(1,2)
ELK(2,2)=4.*E*RIZ((I+1)/2)/SL((I+1)/2)
ELK(2,2)=ELK(2,2)*(1.+SH)
ELK(2,3)=-ELK(1,2)
ELK(2,4)=2.*E*RIZ((I+1)/2)/SL((I+1)/2)
ELK(2,4)=ELK(2,4)*(1.-2.*SH)
ELK(3,3)=ELK(1,1)
ELK(3,4)=-ELK(1,2)
ELK(4,4)=ELK(2,2)
DO 3 K=1,4
DO 3 J=1,K
ELK(J,K)=ELK(J,K)/(1.+4.*SH)
3 ELK(K,J)=ELK(J,K)
GLOK(I,I)=ELK(1,1)+GLOK(I,I)

```

```

GLOK(I+1,I+1)=ELK(2,2)+GLOK(I+1,I+1)
GLOK(I+1,I)=ELK(2,1)+GLOK(I+1,I)
GLOK(I+2,I)=ELK(3,1)
GLOK(I+3,I)=ELK(4,1)
GLOK(I+2,I+1)=ELK(3,2)
GLOK(I+3,I+1)=ELK(4,2)
GLOK(I+2,I+2)=ELK(3,3)
GLOK(I+3,I+2)=ELK(4,3)
GLOK(I+3,I+3)=ELK(4,4)
10 CONTINUE
DO 11 I=1,NN
DO 11 J=1,NN
11 GLOK(I,J)=GLOK(J,I)
IF (IROT.EQ.0) GO TO 45

C
C IF IROT=1 THEN SOIL STRUCTURE INTERACTION IS TO BE INC
C LUDED.
C

GLOK(NN-1,NN-1)=GLOK(NN-1,NN-1)+TRANSK
GLOK(NN,NN)=GLOK(NN,NN)+ROTK
45 RETURN
END
SUBROUTINE RATIO(N3,BETA2,CTRANS,CROT,TRANSK,ROTK)
COMMON /DYN/GSTIFF(3),GMASS(3),DAMP(3),EQFOR(12),GFORC
C E(3),
1DISP(12),RKFOR(12)
COMMON /EIG/GLOK(12,12),OMEGA(12),A(12,12),RMASS(12),A
C TR(12,12)
COMMON /PROP/AS(5),RIZ(5),SL(5),SIZ(5)
DIMENSION V(5),RMOM(5)
DIMENSION EN(12,12),ET(12),B(12)

C
C THIS SUBROUTINE IS CALLED ONLY IF SOIL STRUCTURE INTER
C ACTION
C IS TO BE INCLUDED IN THE ANALYSIS. SINCE THE CRITICAL
C DAMPING
C RATIOS IN THE STRUCTURAL AND SOIL DEGREES OF FREEDOM U
C SUALLY
C DIFFER BY A LARGE AMOUNT SOME COMMON MODAL DAMPING VAL
C UES
C ARE REQUIRED. THE SUBREGIONED ENERGY PROPORTION METHOD
C IS USED TO DO THIS. THE STEPS INVOLVED IN THE METHOD A
C RE
C EXPLAINED BELOW.
C
C FIRST SET UP THE VECTOR B WHICH CONTAINS THE CRITICAL
C DAMPING
C RATIO FOR EACH MASS. THE DAMPING RATIO FOR ALL THE STR
C UCTURAL
C MASSES IS BETA2. THE TRANSLATIONAL SOIL DAMPING RATIO
C IS CTRANS
C AND THE ROTATIONAL SOIL DAMPING RATIO IS CROT.
C
NM=12

```

```

      N=N3-2
      N2=N/2
      DO 100 I=1,N
      B(I)=BETA2
100  CONTINUE
      B(N+1)=CTRANS
      B(N+2)=CROT

C
C
C      NOW COMPUTE THE STRAIN ENERGY IN THE ITH MASS. THE STR
C      AIN
C      ENERGY FOR EACH LUMPED MASS FOR EACH MODE IS STORED IN
C      THE MATRIX EN. THE INTERNAL MODAL STRAIN ENERGY IS ONE
C      HALF THE PRODUCT OF THE AVERAGE INTERNAL FORCES AT THE
C      LUMPED MASS AND THE MODAL DISPLACEMENT.
C
      DO 1 J=1,NM
      DO 2 I=1,N2
      SK=SL(I)/(G*AS(I))
      XF=0.
      EI=E*RIZ(I)
      S=0.
      T=0.
      C=0.
      AA=0.
      BB=0.
      DET=SL(I)**4/(12.*EI**2)+SL(I)*SK/EI+S*SL(I)/EI+C*
1(SL(I)**3/EI+SK+S)-T*SL(I)**2/EI-T**2
      RMOM(I)=((A(2*I+1,J)-A(2*I-1,J))*(SL(I)**2/EI+T)+A(2*I
C      ,J)*
1(SL(I)**3/EI+SK+S)+A(2*I+2,J)*(SL(I)**3/EI+T*SL(I)
2-SK-S))/DET
      V(I)=((A(2*I-1,J)-A(2*I+1,J))*(SL(I)/EI+C)-A(2*I,J)*(S
C      L(I)**2
1/(2.*EI)+T)+A(2*I+2,J)*(T-SL(I)**2/(2.*EI)-SL(I)*C))/D
C      ET
      EN(2*I-1,J)=V(I)**2*SK/2.
      EN(2*I,J)=(1./(2.*E*RIZ(I)))*(RMOM(I)**2*SL(I)+RMOM(I)
C      *V(I)
1*SL(I)**2+V(I)**2*SL(I)**3/3.)
      EN(2*I,J)=EN(2*I,J)+RMOM(I)**2*UL*XF/2.+RMOM(I)*V(I)*B
C      B+
1V(I)**2*AA
2  CONTINUE
      EN(N+1,J)=TRANSK*A(N+1,J)**2*.5
      EN(N+2,J)=ROTK*A(N+2,J)**2*.5
1  CONTINUE

C
C
C      COMPUTE THE TOTAL ENERGY IN EACH MODE AND STORE IN VEC
C      TOR
C      ET.
C
      DO 7 I=1,NM
      ET(I)=0.
      DO 7 J=1,NM

```

```

      ET(I)=EN(J,I)+ET(I)
7  CONTINUE

```

C
C
C
C

```

      NOW COMPUTE THE MODAL DAMPING RATIOS (STORED IN VECTOR
      D).

```

```

      DO 8 I=1,NM
      D(I)=0.
      DO 8 J=1,NM
      D(I)=EN(J,I)*B(J)+D(I)
8  CONTINUE
      DO 13 I=1,NM
      D(I)=D(I)/ET(I)
13 CONTINUE
      DO 9 I=1,NM
      WRITE(6,12) I,D(I)
9  CONTINUE
12 FORMAT(/10X,'MODAL DAMPING FOR MODE',I1,'=',E10.3)
      RETURN
      END
      SUBROUTINE JACOBY(N,K)
      COMMON /DYN/GSTIFF(3),GMASS(3),DAMP(3),EQFOR(12),GFORC
      C  E(3),
      1DISP(12),RKFOR(12)
      COMMON /EIG/GLOK(12,12),OMEGA(12),A(12,12),RMASS(12),A
      C  TR(12,12)
      DIMENSION EM(12),STB(12,12),T(12,12),TT(12,12),B(12,12
      C  ),
      1ST(12,12),A1(12,12)
      DIMENSION C(12,12)

```

C
C
C
C
C
C
C
C
C
C
C
C
C
C
C
C

```

      THIS SUBROUTINE CALCULATES EIGENVECTORS AND EIGENVALUE
      S
      FROM A GIVEN STIFFNESS MATRIX AND MASS VECTOR. N IS TH
      E
      NUMBER OF STRUCTURAL DEGREES OF FREEDOM IN THE SYSTEM,
      EM IS THE MASS VECTOR AND ST IS THE STRUCTURAL STIFFNE
      SS MATRIX.
      ONLY THE STRUCTURAL PORTION OF THE GLOBAL STIFFNESS MA
      TRIX
      IS DIAGONALIZED SO THE FREQUENCIES AND MODE SHAPES ARE
      FOR
      A FIXED BASE STRUCTURE.

```

```

      DO 75 I=1,N
      DO 75 J=1,N
      ST(I,J)=GLOK(I,J)
75 CONTINUE
      DO 76 I=1,N
      EM(I)=RMASS(I)
76 CONTINUE
      CALL PRINT5(ST,N)
      CALL UNIT(A1,N)

```

C

```

C      STB=(1/SQRT(EM))*(ST)*(1/SQRT(EM)). THE STIFFNESS MATR
C      IX
C      ST IS TRANSFORMED INTO A FORM IN WHICH THE JACOBI METH
C      OD
C      CAN BE APPLIED.
C
      DO 10 I=1,N
10     EM(I)=SQRT(EM(I))
      DO 12 I=1,N
      DO 12 J=1,N
12     STB(I,J)=ST(I,J)/(EM(J)*EM(I))
      DO 20 KK=1,K
      DO 15 I=1,N
      DO 15 J=I,N
      IF (I-J) 14,15,14
C
C      T IS A UNIT MATRIX EXCEPT FOR T(I,I),T(J,J),T(I,J),
C      AND T(J,I). BY PRE AND POST MULTIPLYING STB BY T THE
C      ELEMENT STB(I,J) IS SET=0. THIS ACTUALLY A SERIES OF
C      ORTHOGONAL TRANSFORMATIONS TO DIAGONALIZE STB.AFTER ST
C      B
C      IS DIAGONALIZED IT WILL CONTAIN THE EIGENVALUES ON ITS
C      MAIN DIAGONAL.
C
14     IF (ABS(STB(I,J)).LT.1.0E-10) GO TO 15
      CALL UNIT(T,N)
      DIFF=STB(I,I)-STB(J,J)
      IF (ABS(DIFF)-.00005D0) 30,30,32
30     TH=.785398E0
      GO TO 33
32     THC=2.0E0*STB(I,J)/DIFF
      TH=.5E0*ATAN(THC)
33     T(I,I)=COS(TH)
      T(J,J)=T(I,I)
      T(I,J)=-SIN(TH)
      T(J,I)=-T(I,J)
C
C      CALCULATE THE TRANSPOSE OF T (TT).
C
      CALL TRA(T,TT,N)
C
      TT*STB*T=STB
C
      CALL PRMULT(STB,TH,I,J,N)
      CALL POMULT(STB,TH,I,J,N)
C
C      A1*T=A1. A1 STORES THE RESULTS OF
C      T1*T2*T3....TK.(THERE ARE K ITERATIONS).A1=SQRT(EM)*A
C      WHERE AIS THE MODAL MATRIX.T1 IS T FOR THE FIRST ITERA
C      TION
C      T2 IS T FOR THE SECOND ITERATION UP TO TK FOR THE KTH
C      ITERATION.
C
      CALL POMULT(A1,TH,I,J,N)

```



```

15 CONTINUE
C
C   THE MODAL MATRIX A=(1/SQRT(EM))*A1.THE FIRST ROW OF A
C   IS NORMALIZED TO 1
C
      DO 18 J=1,N
      DO 18 I=1,N
18  A(I,J)=A1(I,J)/EM(I)
20  CONTINUE
      DO 50 I=1,N
      OMEGA(I)=SQRT(STB(I,I))
50  CONTINUE
C
C   SORT FREQUENCIES AND EIGENVECTORS STARTING FROM MODE 1
C   (LOWEST)
C   AND GOING UP TO MODE N.
C
      NN=N-1
      DO 80 I=1,NN
      L=I+1
      DO 9 K=L,N
      IF (OMEGA(K).GT.OMEGA(I)) GO TO 9
      WX=OMEGA(I)
      OMEGA(I)=OMEGA(K)
      OMEGA(K)=WX
      DO 300 II=1,N
      AX=A(II,I)
      A(II,I)=A(II,K)
      A(II,K)=AX
300 CONTINUE
      9 CONTINUE
      80 CONTINUE
C
C   PRINT OUT THE NATURAL FREQUENCIES AND EIGENVECTORS.
C
      DO 11 I=1,N
11  WRITE(6,122) I,OMEGA(I)
122 FORMAT(/10X,'FREQUENCY',I5,'=',F10.2)
      CALL PRINT5(A,N)
      CALL TRA(A,ATR,N)
      RETURN
      END
      SUBROUTINE MULT(A,B,C,N)
      DIMENSION A(12,12),B(12,12),C(12,12)
      DO 10 I=1,N
      DO 10 J=1,N
      C(I,J)=0.0E0
      DO 10 L=1,N
10  C(I,J)=C(I,J)+A(I,L)*B(L,J)
      RETURN
      END
      SUBROUTINE UNIT(A,N)
      DIMENSION A(12,12)
      DO 10 I=1,N

```

```

      DO 8 J=1,N
      8 A(I,J)=0.0E0
    10 A(I,I)=1.0E0
      RETURN
      END
      SUBROUTINE TRA(A,B,N)
      DIMENSION A(12,12),B(12,12)
      DO 10 I=1,N
      DO 10 J=1,N
    10 B(I,J)=A(J,I)
      RETURN
      END
      SUBROUTINE POMULT(STB,TH,I,J,N)
      DIMENSION STB(12,12),C(12,2)
      DO 1 II=1,N
      C(II,1)=STB(II,I)*COS(TH)+STB(II,J)*SIN(TH)
      C(II,2)=STB(II,J)*COS(TH)-STB(II,I)*SIN(TH)
      1 CONTINUE
      DO 2 II=1,N
      STB(II,I)=C(II,1)
      STB(II,J)=C(II,2)
      2 CONTINUE
      RETURN
      END
      SUBROUTINE PRMULT(STB,TH,I,J,N)
      DIMENSION STB(12,12),C(2,12)
      DO 1 JJ=1,N
      C(1,JJ)=STB(I,JJ)*COS(TH)+STB(J,JJ)*SIN(TH)
      C(2,JJ)=STB(J,JJ)*COS(TH)-STB(I,JJ)*SIN(TH)
      1 CONTINUE
      DO 2 JJ=1,N
      STB(I,JJ)=C(1,JJ)
      STB(J,JJ)=C(2,JJ)
      2 CONTINUE
      RETURN
      END
      SUBROUTINE PRINT5(A,N)
      DIMENSION A(12,12)
      WRITE(6,20)
      DO 10 I=1,N
    10 WRITE(6,12) (A(I,J),J=1,N)
    12 FORMAT(10X,10E10.3)
    20 FORMAT(//)
      RETURN
      END

```

APPENDIX B

1. Description of the Computer Program SAC

This program performs the seismic analysis of cracked nuclear containment vessels. Only horizontal cracks are taken account of. Because shear transfer across cracks exhibits stiffness characteristics which change with the slip at the crack plane, the seismic analysis of cracked containment vessels is nonlinear. The structure is idealized as a vertical cantilever shear beam with the cracks contributing additional shear flexibility. The mass of the vessel is lumped at the node points. Soil-structure interaction is included through use of translational and rotational springs which model the stiffness of the underlying soil. The damping properties of the structure and soil are included by assigning critical damping ratios for each mode of vibration. Effective critical damping ratios for each mode (that include the large soil damping capacity) are calculated through use of the subregioned energy proportion method. The symmetric fully populated damping matrix is generated from the critical damping ratios in the manner shown in section 4.4. Because the model is nonlinear direct numerical integration of the equations of motion is performed using the linear acceleration method.

2. Input to SAC

The same sample problem will be used as in Appendix A. The input is similar except that the additional information of crack spacing and crack stiffness will be input. It will be assumed that the horizontal cracks

are spaced at 5'-6". The crack stiffness is input by specifying the six pairs of values for shear stress and crack slip which define the second cycle hysteresis loop (see Figure 5.6). Both cracked and uncracked values for the moment of inertia must be input. The "uncracked" moment of inertia occurs in the concrete between the horizontal cracks (see section 5.4). The cracked moment of inertia is the moment of inertia supplied solely by the longitudinal reinforcing bars which cross the open horizontal cracks. The maximum number of beam segments which may be used is 5. This could be increased by changing the pertinent DIMENSION statements (see source listing of SAC). The units are kips, inches and seconds. The times for which output is printed out may be controlled as described in the next section.

CARD 1 (2F10.0, 2I5)

cols 1-10: .0025 (recommended time step size)

cols 11-20: .25 (duration of analysis)

cols 21-25: 5 (number of beam segments)

cols 26-30: 10 (number of base acceleration time points)

CARD 2 (I5, 2F10.0)

cols 1-5: 1 (=1 if soil-structure interaction is to be included, = 0 if not)

cols 6-15: 10.0E10 (K_{ϕ})

cols 16-25: 100000. (K_u)

CARD 3 (3F10.0)

cols 1-10: .05 (critical damping ratio for the containment)

cols 11-20: .25 (critical damping ratio for translational
motion in underlying soil)

cols 21-30: .05 (critical damping ratio for rotational motion
in underlying soil)

CARD 4 (3F10.0)

cols 1-10: 1500. (G, shear modulus, ksi)

cols 11-20: 3000. (E, Young's modulus, ksi)

cols 21-30: 837. (R_c , radius of the containment vessel cylinder)

CARD 5 (2I5)

cols 1-5: 9 (number of cracks in top beam segment)

cols 6-10: 6 (number of cracks in 2nd beam segment)

cols 11-15: 6 (number of cracks in 3rd beam segment)

cols 16-20: 6 (number of cracks in 4th beam segment)

cols 21-25: 3 (number of cracks in bottom beam segment)

CARD 6 (4F10.0)

cols 1-10: 150000. (shear area of top beam segment)

cols 11-20: 592.5 (length of top beam segment)

cols 21-30: 9.0E10 (uncracked moment of inertia of top beam
segment)

cols 31-40: 2.0E10 (cracked moment of inertia of top beam
segment)

CARD 7 (4F10.0)

cols 1-10: 150000. (shear area of 2nd beam segment)

cols 11-20: 360. (length of 2nd beam segment)

cols 21-30: 9.0E10 (uncracked moment of inertia of 2nd beam
segment)

cols 31-40: 2.0E10 (cracked moment of inertia of 2nd beam
segment)

CARD 8 (4F10.0) (same as CARD 7 for 3rd beam segment)

CARD 9 (4F10.0) (same as CARD 7 for 4th beam segment)

CARD 10 (4F10.0)

cols 1-10: 150000. (shear area of bottom beam segment)

cols 11-20: 180. (length of bottom beam segment)

cols 21-30: 9.0E10 (uncracked moment of inertia of bottom
beam segment)

cols 31-40: 2.0E10 (cracked moment of inertia of bottom beam
segment)

CARD 11 (8F10.0)

cols 1-10: 30. (m_1)

cols 11-20: 8.0E06 (I_1)

cols 21-30: 25. (m_2)

cols 31-40: 8.0E06 (I_2)

cols 41-50: 25. (m_3)

cols 51-60: 8.0E06 (I_3)

cols 61-70: 25. (m_4)

cols 71-80: 8.0E06 (I_4)

CARD 12 (4F10.0)

cols 1-10: 25. (m_5)

cols 11-20: 8.0E06 (I_5)

cols 21-30: 60. (m_F)

cols 31-40: 13.0E06 (I_F)

CARD 13 (2F10.0)

cols 1-10: .03 (τ_1 in Figure 5.6)

cols 11-20: .0027 (Δ_1 in Figure 5.6)

CARD 14 (2F10.0)

cols 1-10: .110 (τ_2 in Figure 5.6)

cols 11-20: .005 (Δ_2 in Figure 5.6)

CARD 15 (2F10.0)

cols 1-10: -.00053 (τ_3 in Figure 5.6)

cols 11-20: .0037 (Δ_3 in Figure 5.6)

CARD 16 (2F10.0)

cols 1-10: -.03 (τ_4 in Figure 5.6)

cols 11-20: -.0027 (Δ_4 in Figure 5.6)

CARD 17 (2F10.0)

cols 1-10: -.110 (τ_5 in Figure 5.6)

cols 11-20: -.005 (Δ_5 in Figure 5.6)

CARD 18 (2F10.0)

cols 1-10: .00053 (τ_6 in Figure 5.6)

cols 11-20: -.0037 (Δ_6 in Figure 5.6)

CARD 19 (I5)

cols 1-5: 3 (number of printout intervals)

CARD 20 (3F8.0)

cols 1-8: .10 (1st printout interval)

cols 9-16: .20 (2nd printout interval)

cols 17-24: .26 (3rd printout interval)

CARD 21 (3F8.0)

cols 1-8: .025 (time between printouts in 1st interval)

cols 9-16: .01 (time between printouts in 2nd interval)

cols 17-24: .025 (time between printouts in 3rd interval)

CARD 22 (2F10.0)

cols 1-10: 0. (time in seconds of base acceleration)

cols 11-20: .084 (base acceleration, fraction of g, acceleration of gravity)

CARD 23 (2F10.0)

cols 1-10: .023 (time in seconds of base acceleration)

cols 11-20: .158 (base acceleration)

CARD 24 (2F10.0)

cols 1-10: .058 (time in seconds of base acceleration)

cols 11-20: .271 (base acceleration)

CARD 25 (2F10.0)

cols 1-10: .083 (time in seconds of base acceleration)

cols 11-20: .349 (base acceleration)

CARD 26 (2F10.0)

cols 1-10: .113 (time in seconds of base acceleration)

cols 11-20: .446 (base acceleration)

CARD 27 (2F10.0)

cols 1-10: .149 (time in seconds of base acceleration)

cols 11-20: .509 (base acceleration)

CARD 28 (2F10.0)

cols 1-10: .186 (time in seconds of base acceleration)

cols 11-20: .382 (base acceleration)

CARD 29 (2F10.0)

cols 1-10: .23 (time in seconds of base acceleration)

cols 11-20: .191 (base acceleration)

CARD 30 (2F10.0)

cols 1-10: .256 (time in seconds of base acceleration)

cols 11-20: .058 (base acceleration)

CARD 31 (2F10.0)

cols 1-10: .3 (time in seconds of base acceleration)

cols 11-20: 0. (base acceleration)

3. Output from SAC

The times at which output is desired is controlled in the manner shown by CARDS 19, 20, 21. CARD 19 inputs the number of printout time intervals. In this case the first printout interval is from $t = 0$ to $t = .10$ seconds. In this interval the time between printouts is .025 seconds so the first three printouts occur at $t = 0, .025, .05$. At $t = .10$ the time between printouts changes to .01 seconds. Printouts occur at $t = .10, .11, .12$ At $t = .20$ the time between printouts changes back to .025 seconds again. The maximum number of different printout time intervals which may be specified on CARD 19 is 10.

For each printout time the translational displacements, shear stresses and crack displacements in the containment are printed out. In the displacement column the top number corresponds to the displacement of the top mass, the second number corresponds to the displacement of the second mass and so on down. The shear stress and crack slip columns have the values for the top beam segment in the first row, the second beam segment values in the second row and so on. After the analysis is completed the maximum values for shear stress, bending stress, displacements (including rotational and soil degrees of freedom) and crack slip are output. Units are kips, inches and seconds.

C ***** SAC *****
 C THIS PROGRAM, NAMED SAC (SEISMIC ANALYSIS INCLUDING CRA
 C CKS),
 C PERFORMS THE SEISMIC ANALYSIS OF CRACKED NUCLEAR CONTA
 C INMENT
 C VESSELS. THE CONTAINMENT VESSEL IS MODELED BY A VERTIC
 C AL
 C CANTILEVER SHEAR BEAM WITH 5 LUMPED MASSES. AT EACH MA
 C SS
 C POINT 2 DEGREES OF FREEDOM EXIST, ROTATIONAL AND TRANSL
 C ATIONAL.
 C THE SOIL UNDERLYING THE CONTAINMENT VESSEL FOUNDATION
 C IS
 C MODELED BY 2 SPRINGS, TRANSLATIONAL AND ROTATIONAL. IN
 C ALL
 C THERE ARE 12 DEGREES OF FREEDOM.

C COMMON /DYN/RMASS(12), DAMP(12,12), CK(6), CFORCE(12), EQF
 C OR(12),
 C 1RKFOR(12), OLDFOR(12), RINFOR(12), ACC(12), DISP(12), VEL(1
 C 2),
 C 2OLDVEL(12), OLDACC(12), SHEAR(12), OLDSHR(12), REL(12), OLD
 C AMP(12),
 C 3SHEARK(5), GLOK(12,12), NCR(5), OLDCK(6), NLDIPD(5), OLDREL
 C (12), RK(8)
 C 4, TK(6), OLDISP(12)
 C COMMON /EIG/OMEGA(12), A(12,12), ATR(12,12), D(12)
 C COMMON /B/RLOAD(6), DELTA(6), IPD(5), NCYCLE(5), RLOADN(5,
 C 6),
 C 1DELTA(5,6)
 C COMMON /PROP/AS(5), RIZ(5), SL(5), E, G, SIZ(5)

C
 C H IS THE TIME STEP SIZE AND ENDTIM IS THE TOTAL DURATI
 C ON
 C OF THE SEISMIC ANALYSIS. NSEG IS THE NUMBER OF BEAM SE
 C GMENTS.
 C NTP IS THE NUMBER OF GROUND ACCELERATION TIME POINTS.
 C NH IS
 C THE TOTAL NUMBER OF TIME STEPS. BETA2 IS THE CONSTANT
 C CRITICAL DAMPING RATIO OF THE CONTAINMENT VESSEL. IF I
 C ROT
 C =1 THEN SOIL-STRUCTURE INTERACTION IS TO BE INCLUDED.
 C ROTK
 C AND TRANSK ARE THE ROTATIONAL AND TRANSLATIONAL SOIL S
 C PRING
 C CONSTANTS. CROT AND CTRANS ARE THE SOIL CRITICAL DAMPI
 C NG RATIOS
 C FOR ROTATIONAL AND TRANSLATIONAL MOTION. G AND E ARE T
 C HE SHEAR
 C AND YOUNG, S MODULII FOR CONCRETE. R IS THE RADIUS OF T
 C HE
 C CONTAINMENT VESSEL WALL. NCR(I) IS THE NUMBER OF HORIZ
 C ONTAL
 C CRACKS IN THE ITH BEAM SEGMENT. AS(I) AND SL(I) ARE TH

```

C      E SHEAR
C      AREA AND LENGTH OF THE ITH BEAM SEGMENT. RIZ(I) IS THE
C      MOMENT
C      OF INERTIA OF THE UNCRACKED CONCRETE. SIZ(I) IS THE MO
C      MENT
C      OF INERTIA AT THE HORIZONTAL CRACK OR THE MOMENT OF IN
C      ERTIA
C      PROVIDED BY THE LONGITUDINAL REBARS ONLLY. RMASS CONTA
C      INS THE
C      VALUES OF THE LUMPED MASSES. RLOAD(1...6) AND DELTA(1.
C      .6)
C      CONTAIN THE SHEAR STRESS AND CRACK SLIP FOR THE 6 POIN
C      TS
C      WHICH DEFINE THE SECOND CYCLE HYSTERESIS LOOP WHICH IN
C      TURN
C      DEFINES THE HORIZONTAL CRACK STIFFNESS. STIFF1 IS THE
C      CRACK
C      STIFFNESS FOR THE FIRST CYCLE. DINC IS THE INCREASE IN
C      DELTA(1)
C      WHICH OCCURS WITH EACH ADDITIONAL LOAD CYCLE.

```

```

C      READ(5,100) H,ENDTIM,NSEG,NTP,NH

```

```

      N=2*NSEG

```

```

      READ(5,106) IROT,ROTK,TRANSK

```

```

      READ(5,101) BETA2,CTRANS,CROT

```

```

      IFLAG=0

```

```

      JFLAG=0

```

```

      KFLAG=0

```

```

      ISTIFF=0

```

```

      KREF=1

```

```

      LFLAG=0

```

```

      K=3

```

```

      DINC=.0001

```

```

      T=0.

```

```

      BETA=.1666667

```

```

      OH=H

```

```

      NM=4

```

```

      NDOF=N

```

```

      NQUAKE=N

```

```

      READ(5,101) G,E,R

```

```

      READ(5,110) (NCR(I),I=1,NSEG)

```

```

      DO 1 I=1,NSEG

```

```

      READ(5,101) AS(I),SL(I),RIZ(I),SIZ(I)

```

```

      SHEARK(I)=G*AS(I)/SL(I)

```

```

1    CONTINUE

```

```

      IF (IROT.EQ.0) GO TO 60

```

```

      NDOF=N+2

```

```

      NQUAKE=N+1

```

```

60   CONTINUE

```

```

      READ(5,101) (RMASS(I),I=1,8)

```

```

      READ(5,101) (RMASS(I),I=9,NDOF)

```

```

C

```

```

C

```

```

      INPUT THE P-DELTA RELATIONSHIP FOR THE HYSTERESIS LOOP

```

```

C      S
C      BY READING IN RLOAD(1....6) AND DELTA(1....6).
C
      DO 200 I=1,6
      READ(5,201) RLOAD(I),DELTA(I)
201  FORMAT(2F10.0)
200  CONTINUE

C
C      NOW THAT THE P-DELTA RELATIONSHIP HAS BEEN READ IN
C      THE SLOPE OF EACH STRAIGHT LINE SEGMENT WHICH MAKES UP
C      THE
C      HYSTERESIS LOOP IS COMPUTED. THEN THE VECTOR OF SHEAR S
C      TIFFNESSES
C      FOR THE BEAM SEGMENTS (TK) IS COMPUTED.
C
      RK(1)=18.3
      RK(2)=(RLOAD(2)-RLOAD(1))/(DELTA(2)-DELTA(1))
      RK(3)=(RLOAD(3)-RLOAD(2))/(DELTA(3)-DELTA(2))
      RK(4)=(RLOAD(4)-RLOAD(3))/(DELTA(4)-DELTA(3))
      RK(5)=18.3
      RK(6)=RK(2)
      RK(7)=RK(3)
      RK(8)=RK(4)
      DO 700 I=1,8
      WRITE(6,701) RK(I)
701  FORMAT(10X,E14.7)
700  CONTINUE

C
C      THE MATRICES DELTAN AND RLOADN STORE THE SLIP AND SHEA
C      R STRESS
C      WHICH DEFINE THE HYSTERESIS LOOPS FOR EACH BEAM SEGMENT.
C      T.
C      INITIALLY THE HYSTERESIS LOOPS CORRESPONDING TO THE SE
C      COND CYCLE
C      ARE INPUT FOR ALL BEAM SEGMENTS.
C
      DO 703 I=1,NSEG
      DELTAN(I,1)=DELTA(1)
      DELTAN(I,2)=DELTA(2)
      DELTAN(I,3)=DELTA(3)
      DELTAN(I,4)=DELTA(4)
      DELTAN(I,5)=DELTA(5)
      DELTAN(I,6)=DELTA(6)
      RLOADN(I,1)=RLOAD(1)
      RLOADN(I,2)=RLOAD(2)
      RLOADN(I,3)=RLOAD(3)
      RLOADN(I,4)=RLOAD(4)
      RLOADN(I,5)=RLOAD(5)
      RLOADN(I,6)=RLOAD(6)
703  CONTINUE
      DO 10 I=1,NSEG
      CK(I)=RK(1)
10   CONTINUE
      UL=2.5

```

```

CALL STIFF(N,NSEG,IROT,ROTK,TRANSK,KREF,ISTIFF,UL)
CALL JACOBY(NDOF,K)
CALL RATIO(N,BETA2,CTRANS,CROT,TRANSK,ROTK,UL)
CALL INDAMP(NDOF)
DO 102 I=1,NH
  NFLAG=0
  IF (I.EQ.1) GO TO 300
  IF (H.LT.0.) GO TO 999
  CALL STIFF(N,NSEG,IROT,ROTK,TRANSK,KREF,ISTIFF,UL)
  CALL INQUAK(T,NTP,NQUAKE,H,IFLAG)
  CALL NUMINT(H,T,BETA,NDOF,IROT,ENDTIM,R)
  IF (T.GT.ENDTIM) GO TO 105
300 CALL INHYST(H,T,OH,NSEG,JFLAG,PRINT,KREF,NFLAG)
  IF (I.EQ.1) GO TO 102
  IF (NFLAG.EQ.1) GO TO 102
  CALL CYCLE(NSEG,LFLAG,DINC)
102 CONTINUE
100 FORMAT(2F10.0,5I5)
101 FORMAT(8F10.0)
106 FORMAT(I5,2F10.0)
110 FORMAT(5I5)
999 WRITE(6,998) T,H
998 FORMAT(/10X,2E14.7)
105 STOP
END
SUBROUTINE STIFF(N,NTR,IROT,ROTK,TRANSK,KREF,ISTIFF,UL
C )
C THIS SUBROUTINE COMPUTES THE GLOBAL STIFFNESS MATRIX W
C HICH
C IS STORED IN GLOK. THE VECTOR TK CONTAINS THE SHEAR
C FLEXIBILITIES OF THE CONTAINMENT VESSEL. 1./SHEARK(I)
C IS
C THE ELASTIC FLEXIBILITY OF THE UNCRACKED CONCRETE. FOR
C THE
C ITH BEAM SEGMENT  $NCR(I)/(AS(I)*CK(I))$  IS THE TOTAL SHE
C AR
C FLEXIBILITY OF ALL THE HORIZONTAL CRACKS IN THE BEAM S
C EGMENT.
C
COMMON /DYN/RMASS(12),DAMP(12,12),CK(6),CFORCE(12),EQF
C OR(12),
1RKFOR(12),OLDFOR(12),RINFOR(12),ACC(12),DISP(12),VEL(1
C 2),
2OLDVEL(12),OLDACC(12),SHEAR(12),OLDSHR(12),REL(12),OLD
C AMP(12),
3SHEARK(5),GLOK(12,12),NCR(5),OLDCK(6),NLDIPD(5),OLDREL
C (12),RK(8)
4,TK(6),OLDISP(12)
COMMON /PROP/AS(5),RIZ(5),SL(5),E,G,SIZ(5)
DIMENSION ELK(4,4),VK(5)
DIMENSION A(5),B(5),C(5)
C
C IF IROT=1 THEN SOIL STRUCTURE INTERACTION IS TO BE INC
C LUDED.

```

```

C
  IF (KREF.EQ.0) GO TO 45
  NN=N
  DO 1 I=1,NTR
  TK(I)=(NCR(I)/(CK(I)*AS(I)))+(1./SHEARK(I))
  1 CONTINUE
  20 CONTINUE

C
  SET UP THE GLOBAL STIFFNESS MATRIX ,GLOK(N,N).

C
  N1=N-1
  NN=N+2
  DO 13 I=1,NN
  DO 13 J=1,NN
  GLOK(I,J)=0.
  13 CONTINUE
  DO 10 I=1,N1,2
  IF (ISTIIF.GT.3) GO TO 222

C
  SET UP THE BEAM ELEMENT STIFFNESS MATRIX ELK(4,4) FOR
  C THE LTH
  C BEAM SEGMENT.
  C

  L=(I+1)/2
  EI=E*RIZ(L)
  SUM=0.
  SUM2=0.
  NC=NCR(L)
  RNC=NCR(L)
  DO 22 K=1,NC
  AK=K
  RX=(2.*AK-1.)/(2.*RNC)
  SUM=SUM+RX
  SUM2=SUM2+RX**2
  22 CONTINUE
  A(L)=((1./SIZ(L))-(1./RIZ(L)))*SL(L)**2*UL*SUM2/E
  B(L)=((1./SIZ(L))-(1./RIZ(L)))*SL(L)*UL*SUM/E
  C(L)=((1./SIZ(L))-(1./RIZ(L)))*UL*NCR(L)/E
  222 CONTINUE
  L=(I+1)/2
  EI=E*RIZ(L)
  DET=SL(L)**4/(12.*EI**2)+TK(L)*SL(L)/EI+A(L)*SL(L)/EI+
  C C(L)*
  1(SL(L)**3/(3.*EI)+TK(L)+A(L))-B(L)*SL(L)**2/EI-B(L)**2
  X=1./DET
  ELK(1,1)=X*((SL(L)/EI)+C(L))
  ELK(1,2)=-X*((SL(L)**2/(2.*EI))+B(L))
  ELK(1,3)=-ELK(1,1)
  ELK(1,4)=X*(B(L)-(SL(L)**2/(2.*EI))-C(L)*SL(L))
  ELK(2,2)=X*((SL(L)**3/(3.*EI))+TK(L)+A(L))
  ELK(2,3)=-ELK(1,2)
  ELK(2,4)=X*(SL(L)**3/(6.*EI)+B(L)*SL(L)-TK(L)-A(L))
  ELK(3,3)=ELK(1,1)
  ELK(3,4)=-ELK(1,2)

```

```

      ELK(4,4)=ELK(2,2)
      DO 3 K=1,4
      DO 3 J=1,K
3     ELK(K,J)=ELK(J,K)
      GLOK(I,I)=ELK(1,1)+GLOK(I,I)
      GLOK(I+1,I+1)=ELK(2,2)+GLOK(I+1,I+1)
      GLOK(I+1,I)=ELK(2,1)+GLOK(I+1,I)
      GLOK(I+2,I)=ELK(3,1)
      GLOK(I+3,I)=ELK(4,1)
      GLOK(I+2,I+1)=ELK(3,2)
      GLOK(I+3,I+1)=ELK(4,2)
      GLOK(I+2,I+2)=ELK(3,3)
      GLOK(I+3,I+2)=ELK(4,3)
      GLOK(I+3,I+3)=ELK(4,4)
10    CONTINUE
      DO 11 I=1,NN
      DO 11 J=1,NN
11    GLOK(I,J)=GLOK(J,I)
      IF (.IROT.EQ.0) GO TO 44
C
C     ADD TO THE GLOBAL STIFFNESS MATRIX THE TRANSLATIONAL
C     TRANSK) AND ROTATIONAL (ROTK) SOIL SPRINGS WHICH MODEL
C     THE STIFFNESS OF THE UNDERLYING SOIL.
C
      GLOK(NN-1,NN-1)=GLOK(NN-1,NN-1)+TRANSK
      GLOK(NN,NN)=GLOK(NN,NN)+ROTK
44    ISTIFF=ISTIFF+1
45    CONTINUE
      RETURN
      END
      SUBROUTINE NUMINT(H,T,BETA,N,IROT,ENDTIM,R)
C
C     THIS SUBROUTINE CALCULATES THE CHANGES IN DISPLACEMENT
C     ,
C     VELOCITY AND ACCELERATION FOR EACH TIME STEP IN THE SE
C     ISMIC
C     ANALYSIS. DDF(I) AND DSF(I) ARE THE CHANGES FOR EACH T
C     IME
C     STEP IN DAMPING AND SRING FORCE FOR THE ITH DEGREE OF
C     FREEDOM.
C     CFORCE(I),RKFOR(I) AND RINFOR(I) CONTAIN THE TOTAL DAM
C     PING
C     FORCES,SPRING FORCES AND INERTIAL FORCES AT TIME T. DI
C     SP(I)
C     ,VEL(I) AND ACC(I) ARE THE DISPLACEMENT,VELOCITY AND
C     ACCELERATION FOR THE ITH DEGREE OF FREEDOM AT TIME T.
C     SHEAR(I)
C     CONTAINS THE SHEAR FORCE IN THE ITH BEAM SEGMENT. REL(
C     I) IS
C     THE CRACK SLIP FOR THE CRACKS IN THE ITH BEAM SEGMENT.
C     OLDSHR(I),OLDAMP(I),OLDFOR(I),OLDACC(I),OLDVEL(I) AND
C     OLDISP(I) CONTAIN THE SHEAR, DAMPING FORCE,SPRING FORC
C     E,ACC-
C     ELERATION,VELOCITY AND DISPLACEMENT FOR THE ITH DEGREE

```



```

C      OF
C      FREEDOM AT THE PREVIOUS TIME POINT.
C
      DIMENSION ZMOM(5),ZMAX(5)
      DIMENSION DELACC(12),DELDSP(12),DELVEL(12)
      COMMON /PROP/AS(5),RIZ(5),SL(5),E,G,SIZ(5)
      DIMENSION X(12)
      COMMON /DYN/RMASS(12),DAMP(12,12),CK(6),CFORCE(12),EQF
C      OR(12),
      IRKFOR(12),OLDFOR(12),RINFOR(12),ACC(12),DISP(12),VEL(1
C      2),
      2OLDVEL(12),OLDACC(12),SHEAR(12),OLDSHR(12),REL(12),OLD
C      AMP(12),
      3SHEARK(5),GLOK(12,12),NCR(5),OLDOCK(6),NLDIPD(5),OLDREL
C      (12),RK(8)
      4,TK(6),OLDISP(12)
      DIMENSION DDF(12),DSF(12),EQERR(12)
      DIMENSION SHRMAX(12),DISMAX(12),RELMAX(12)
C
C      THE VELOCITIES AND DISPLACEMENTS OF THE LUMPED MASSES
C      ARE SET EQUAL TO THEIR INITIAL VALUE.
C
      IF (T.GT.0.) GO TO 302
      NP=N
      N1=NP-1
      NP2=N/2
      IF (IROT.EQ.0) GO TO 447
      NP=N-2
      N1=NP-1
      NP2=NP/2
447  CONTINUE
      DO 32 I=1,N
      DDF(I)=0.
      DSF(I)=0.
      CFORCE(I)=0.
      RKFOR(I)=0.
      DISP(I)=0.
      VEL(I)=0.
      ACC(I)=EQFOR(I)/RMASS(I)
      RINFOR(I)=RMASS(I)*ACC(I)
      DELDSP(I)=0.
      DELVEL(I)=0.
      DELACC(I)=0.
      SHEAR(I)=0.
      REL(I)=0.
      OLDSHR(I)=0.
      OLDAMP(I)=0.
      OLDISP(I)=0.
      OLDREL(I)=0.
      OLDFOR(I)=0.
      OLDACC(I)=0.
      OLDVEL(I)=0.
      SHRMAX(I)=SHEAR(I)
      DISMAX(I)=DISP(I)

```

```

RELMAX(I)=REL(I)
32 CONTINUE
DO 23 I=1,NP2
ZMAX(I)=0.
23 CONTINUE
GO TO 84

C
C THE CHANGES IN DISPLACEMENT AND VELOCITY FOR THIS TIME
C STEP ARE
C CALCULATED ACCORDING TO THE NEWMARK BETA METHOD. FIRST
C THE VALUE
C FOR THE CHANGE IN ACCELERATION (DELACC) FOR THE PREVIOUS
C TIME
C STEP IS ASSUMED FOR THE PRESENT TIME STEP. THE CHANGE
C IN THE
C VELOCITY (DELVEL) AND DISPLACEMENT (DELDSP) CAN THEN BE
C SOLVED
C FOR.
C

302 ITER=0
300 ITER=ITER+1
DO 49 L=1,N
X(L)=DELDSP(L)
DELVEL(L)=(2.*ACC(L)+DELACC(L))*H/2.
DELDSP(L)=(VEL(L)*H)+(.5-BETA)*ACC(L)*H**2 + BETA*(ACC
C (L)
1+DELACC(L))*H**2
49 CONTINUE
IF (ITER.LT.4) GO TO 48
JOUT=0
DO 45 I=1,N
IF (DELDSP(I).EQ.0.) GO TO 45
IF (ABS((DELDSP(I)-X(I))/DELDSP(I)).LE..001) GO TO 45
JOUT=1
45 CONTINUE
IF (JOUT.EQ.0) GO TO 350
48 DO 44 I=1,N
DO 99 K=1,N
DDF(I)=DAMP(I,K)*DELVEL(K)+DDF(I)
DSF(I)=GLOK(I,K)*DELDSP(K)+DSF(I)
99 CONTINUE

C
C EQERR IS THE ERROR IN EQUILIBRIUM DUE TO THE ASSUMPTION
C OF
C VALUES FOR DELACC.
C

EQERR(I)=(RINFOR(I)+RMAS(I)*DELACC(I))+(CFORCE(I)+DDF
C (I)
1+(RKFOR(I)+DSF(I))-EQFOR(I)
DSF(I)=0.
DDF(I)=0.
44 CONTINUE
DO 47 I=1,N
DELACC(I)=(RMAS(I)*DELACC(I)-EQERR(I))/(RMAS(I))

```

```

47 CONTINUE
GO TO 300
350 CONTINUE
DO 98 I=1,N
DO 97 K=1,N
DSF(I)=GLOK(I,K)*DEL DSP(K)+DSF(I)
DDF(I)=DAMP(I,K)*DELVEL(K)+DDF(I)
97 CONTINUE
OLDFOR(I)=RKFOR(I)
OLDISP(I)=DISP(I)
OLDVEL(I)=VEL(I)
OLDACC(I)=ACC(I)
OLDSHR(I)=SHEAR(I)
OLDAMP(I)=CFORCE(I)
OLDREL(I)=REL(I)
C
C THE VALUES OF DISPLACEMENT, VELOCITY AND ACCELERATION
C FOT TIME
C T ARE CALCULATED.
C
DISP(I)=DISP(I)+DEL DSP(I)
VEL(I)=VEL(I)+DELVEL(I)
ACC(I)=ACC(I)+DELACC(I)
RKFOR(I)=RKFOR(I)+DSF(I)
RINFOR(I)=RMASS(I)*ACC(I)
CFORCE(I)=CFORCE(I)+DDF(I)
SHEAR(I)=0.
DDF(I)=0.
DSF(I)=0.
98 CONTINUE
DO 401 I=1,NP2
IS=2*I-1
DO 72 K=1,IS,2
SHEAR(I)=RKFOR(K)+SHEAR(I)
IF (I.GT.1) GO TO 28
ZMOM(1)=RKFOR(1)*SL(1)
GO TO 72
28 ZMOM(I)=ZMOM(I-1)+SHEAR(I)*SL(I)
72 CONTINUE
401 CONTINUE
DO 201 I=1,NP2
SHEAR(I)=SHEAR(I)/AS(I)
ZMOM(I)=ZMOM(I)*R/RIZ(I)
201 CONTINUE
DO 540 I=1,NP2
REL(I)=OLDREL(I)+(SHEAR(I)-OLDSHR(I))/CK(I)
540 CONTINUE
DO 501 I=1,N
IF (ABS(DISMAX(I)).GE.ABS(DISP(I))) GO TO 501
DISMAX(I)=DISP(I)
501 CONTINUE
DO 701 I=1,NP2
IF (ABS(SHRMAX(I)).GE.ABS(SHEAR(I))) GO TO 601
SHRMAX(I)=SHEAR(I)

```

```

601 IF (ABS(ZMAX(I)).GE.ABS(ZMOM(I))) GO TO 801
    ZMAX(I)=ZMOM(I)
801 IF (ABS(RELMAX(I)).GE.ABS(REL(I))) GO TO 701
    RELMAX(I)=REL(I)
701 CONTINUE
    IF (T.LT.ENDTIM) GO TO 84
    WRITE(6,1)
    1 FORMAT(/11X,'MAXIMUM SHEAR',3X,'MAXIMUM DISPLACEMENT',
    C 3X,
    1'MAX CRACK DISPLACEMENT',3X,'MAX BENDING STRESS')
    DO 411 I=1,NP2
411 WRITE(6,2) SHRMAX(I),DISMAX(I),RELMAX(I),ZMAX(I)
    2 FORMAT(10X,E14.7,6X,E14.7,10X,E14.7,9X,E14.7)
    DO 412 I=6,N
412 WRITE(6,3) DISMAX(I)
    3 FORMAT(30X,E14.7)
    WRITE(6,333) (CK(I),I=1,5)
333 FORMAT(/10X,5E14.7)
    CALL PRINT5(GLOK,12)
84 RETURN
    END
    SUBROUTINE RATIO(N,BETA2,CTRANS,CROT,TRANSK,ROTK,UL)
    COMMON /DYN/RMASS(12),DAMP(12,12),CK(6),CFORCE(12),EQF
    C OR(12),
    IRKFOR(12),OLDFOR(12),RINFOR(12),ACC(12),DISP(12),VEL(1
    C 2),
    2OLDVEL(12),OLDACC(12),SHEAR(12),OLDSHR(12),REL(12),OLD
    C AMP(12),
    3SHEARK(5),GLOK(12,12),NCR(5),OLDCK(6),NLDIPD(5),OLDREL
    C (12),RK(8)
    4,TK(6),OLDISP(12)
    COMMON /EIG/OMEGA(12),A(12,12),ATR(12,12),D(12)
    COMMON /PROP/AS(5),RIZ(5),SL(5),E,G,SIZ(5)
    DIMENSION V(5),RMOM(5)
    DIMENSION EN(12,12),ET(12),B(12)

C
C THIS SUBROUTINE IS CALLED ONLY IF SOIL STRUCTURE INTER
C ACTION
C IS TO BE INCLUDED IN THE ANALYSIS. SINCE THE CRITICAL
C DAMPING
C RATIOS IN THE STRUCTURAL AND SOIL DEGREES OF FREEDOM U
C SUALLY
C DIFFER BY A LARGE AMOUNT SOME COMMON MODAL DAMPING VAL
C UES
C ARE REQUIRED. THE SUBREGIONED ENERGY PROPORTION METHOD
C IS USED TO DO THIS. THE STEPS INVOLVED IN THE METHOD A
C RE
C EXPLAINED BELOW.

C
C FIRST SET UP THE VECTOR B WHICH CONTAINS THE CRITICAL
C DAMPING
C RATIO FOR EACH MASS. THE DAMPING RATIO FOR ALL THE STR
C UCTURAL
C MASSES IS BETA2. THE TRANSLATIONAL SOIL DAMPING RATIO

```

```

C      IS CTRANS
C      AND THE ROTATIONAL SOIL DAMPING RATIO IS CROT.
C
      NM=12
      N2=N/2
      DO 100 I=1,N
      B(I)=BETA2
100  CONTINUE
      B(N+1)=CTRANS
      B(N+2)=CROT
C
C      NOW COMPUTE THE STRAIN ENERGY IN THE ITH MASS. THE STR
C      AIN
C      ENERGY FOR EACH LUMPED MASS FOR EACH MODE IS STORED IN
C      THE MATRIX EN. THE INTERNAL MODAL STRAIN ENERGY IS ONE
C      HALF THE PRODUCT OF THE AVERAGE INTERNAL FORCES AT THE
C      LUMPED MASS AND THE MODAL DISPLACEMENT.
C
      DO 1 J=1,NM
      DO 2 I=1,N2
      SK=NCR(I)/(CK(I)*AS(I))+(1./SHEARK(I))
      EI=E*RIZ(I)
      SUM=0.
      SUM2=0.
      NC=NCR(I)
      RNC=NCR(I)
      DO 22 K=1,NC
      AK=K
      RX=(2.*AK-1.)/(2.*RNC)
      SUM=SUM+RX
      SUM2=SUM2+RX**2
22  CONTINUE
      XF=(1./SIZ(I)-1./RIZ(I))/E
      S=XF*UL*SL(I)**2*SUM2
      T=XF*UL*SL(I)*SUM
      C=XF*UL*NCR(I)
      AA=XF*UL**3*SUM2/6.
      BB=XF*UL**2*SUM/2.
      DET=SL(I)**4/(12.*EI**2)+SL(I)*SK/EI+S*SL(I)/EI+C*
1(SL(I)**3/EI+SK+S)-T*SL(I)**2/EI-T**2
      RMOM(I)=((A(2*I+1,J)-A(2*I-1,J))*(SL(I)**2/EI+T)+A(2*I
C ,J)*
1(SL(I)**3/EI+SK+S)+A(2*I+2,J)*(SL(I)**3/EI+T*SL(I)
2-SK-S))/DET
      V(I)=((A(2*I-1,J)-A(2*I+1,J))*(SL(I)/EI+C)-A(2*I,J)*(S
C L(I)**2
1/(2.*EI)+T)+A(2*I+2,J)*(T-SL(I)**2/(2.*EI)-SL(I)*C))/D
C ET
      EN(2*I-1,J)=V(I)**2*SK/2.
      EN(2*I,J)=(1./(2.*E*RIZ(I)))*(RMOM(I)**2*SL(I)+RMOM(I)
C *V(I)
1*SL(I)**2+V(I)**2*SL(I)**3/3.)
      EN(2*I,J)=EN(2*I,J)+RMOM(I)**2*UL*XF/2.+RMOM(I)*V(I)*B
C B+

```

```

1V(I)**2*AA
2 CONTINUE
  EN(N+1,J)=TRANSK*A(N+1,J)**2*.5
  EN(N+2,J)=ROTK*A(N+2,J)**2*.5
1 CONTINUE

C
C   COMPUTE THE TOTAL ENERGY IN EACH MODE AND STORE IN VEC
C   TOR
C   ET.
C
  DO 7 I=1,NM
  ET(I)=0.
  DO 7 J=1,NM
  ET(I)=EN(J,I)+ET(I)
7 CONTINUE

C
C   NOW COMPUTE THE MODAL DAMPING RATIOS (STORED IN VECTOR
C   D).
C
  DO 8 I=1,NM
  D(I)=0.
  DO 8 J=1,NM
  D(I)=EN(J,I)*B(J)+D(I)
8 CONTINUE
  DO 13 I=1,NM
  D(I)=D(I)/ET(I)
13 CONTINUE
  DO 9 I=1,NM
  WRITE(6,12) I,D(I)
9 CONTINUE
12 FORMAT(/10X,'MODAL DAMPING FOR MODE',I1,'=',E10.3)
  RETURN
  END
  SUBROUTINE INDAMP(N)
  COMMON /DYN/RMASS(12),DAMP(12,12),CK(6),CFORCE(12),EQF
C   OR(12),
C   IRKFOR(12),OLDFOR(12),RINFOR(12),ACC(12),DISP(12),VEL(1
C   2),
C   2OLDVEL(12),OLDACC(12),SHEAR(12),OLDSHR(12),REL(12),OLD
C   AMP(12),
C   3SHEARK(5),GLOK(12,12),NCR(5),OLDCK(6),NLDIPD(5),OLDREL
C   (12),RK(8)
C   4,TK(6),OLDISP(12)
  COMMON /EIG/OMEGA(12),A(12,12),ATR(12,12),D(12)
  DIMENSION C(12,12)

C
C   FROM MODAL ANALYSIS,DAMP(N,N)=INV(ATR(N,N))*CBAR(N,N)*
C   INV(A(N,N)
C   WHERE CBAR(N,N) IS A DIAGONAL MATRIX WITH THE TERMS C(
C   I,I)2.*D(I)
C   *OMEGA(I).THE FOLLOWING STATEMENTS COMPUTE DAMP(N,N) U
C   SING THE
C   FACT THAT INV(A(N,N))=ATR(N,N)*RMASS(N,N).

```

```

      DO 1 I=1,N
      DO 1 J=1,N
      C(I,J)=2.*D(J)*OMEGA(J)*A(I,J)*RMASS(I)
1 CONTINUE
      CALL MULT(C,ATR,DAMP,N)
      DO 2 I=1,N
      DO 2 J=1,N
      DAMP(I,J)=DAMP(I,J)*RMASS(J)
2 CONTINUE
      DO 3 I=1,N
3 WRITE(6,4) (DAMP(I,J),J=1,N)
4 FORMAT(/10X,7E14.7)
      RETURN
      END
      SUBROUTINE INQUAK(T,NTP,N,H,IFLAG)
      COMMON /DYN/RMASS(12),DAMP(12,12),CK(6),CFORCE(12),EQF
C OR(12),
C 1RKFOR(12),OLDFOR(12),RINFOR(12),ACC(12),DISP(12),VEL(1
C 2),
C 2OLDVEL(12),OLDACC(12),SHEAR(12),OLDSHR(12),REL(12),OLD
C AMP(12),
C 3SHEARK(5),GLOK(12,12),NCR(5),OLDCK(6),NLDIPD(5),OLDREL
C (12),RK(8)
C 4,TK(6),OLDISP(12)

C
C THIS SUBROUTINE READS IN THE GROUND ACCELERATION HISTO
C RY AND
C KEEPS TRACK OF THE CURRENT VALUE OF THE GROUND ACCELER
C ATION.
C
      DIMENSION GRACC(10),TIME(10)
      IF (IFLAG.EQ.1) GO TO 44
      IFLAG=1
      DO 100 I=1,NTP
      READ(5,101) TIME(I),GRACC(I)
101 FORMAT(2F10.0)
100 CONTINUE
      DO 55 I=1,N,2
      EQFOR(I)=-RMASS(I)*GRACC(I)*38.64
      EQFOR(I+1)=0.
55 CONTINUE
      GO TO 200

C
C NOW FIND THE CURRENT VALUE OF THE GROUND ACCELERATION
C X.
C
44 CONTINUE
      IF (T.GT.TIME(NTP)) GO TO 200
      I=1
102 I=I+1
      IF (I.GT.NTP) GO TO 150
      IF (T.GT.TIME(I)) GO TO 102
      IF (T.LT.TIME(I-1)) GO TO 102
      J=I-1

```

C
C J IDENTIFIES WHICH OF THE STRAIGHT LINE SEGMENTS CONTA
C INS THE
C CURRENT GROUND ACCELERATION.
C

SLOPE=(GRACC(J+1)-GRACC(J))/(TIME(J+1)-TIME(J))
X=GRACC(J)+(T-TIME(J))*SLOPE
DO 98 I=1,N,2
EQFOR(I)=-RMASS(I)*X*386.4
EQFOR(I+1)=0.
98 CONTINUE
GO TO 200
150 WRITE(6,151)
151 FORMAT(20X,'THE GROUND ACCELERATION CORRESPONDING TO T
C IME T HAS
1NOT BEEN FOUND'//)
200 CONTINUE
RETURN
END

SUBROUTINE JACOBY(N,K)
COMMON /DYN/RMASS(12),DAMP(12,12),CK(6),CFORCE(12),EQF
C OR(12),
IRKFOR(12),OLDFOR(12),RINFOR(12),ACC(12),DISP(12),VEL(1
C 2),
2OLDVEL(12),OLDACC(12),SHEAR(12),OLDSHR(12),REL(12),OLD
C AMP(12),
3SHEARK(5),GLOK(12,12),NCR(5),OLDCK(6),NLDIPD(5),OLDREL
C (12),RK(8)
4,TK(6),OLDDISP(12)
COMMON /EIG/OMEGA(12),A(12,12),ATR(12,12),D(12)
DIMENSION EM(12),STB(12,12),T(12,12),TT(12,12),B(12,12
C),
1ST(12,12),A1(12,12)
DIMENSION C(12,12)

C
C THIS SUBROUTINE CALCULATES EIGENVECTORS AND EIGENVALUE
C S
C FROM A GIVEN STIFFNESS MATRIX AND MASS VECTOR. N IS TH
C E
C NUMBER OF STRUCTURAL DEGREES OF FREEDOM IN THE SYSTEM,
C EM IS THE MASS VECTOR AND ST IS THE STRUCTURAL STIFFNE
C SS MATRIX.
C ONLY THE STRUCTURAL PORTION OF THE GLOBAL STIFFNESS MA
C TRIX
C IS DIAGONALIZED SO THE FREQUENCIES AND MODE SHAPES ARE
C FOR
C A FIXED BASE STRUCTURE.
C

DO 75 I=1,N
DO 75 J=1,N
ST(I,J)=GLOK(I,J)
75 CONTINUE
DO 76 I=1,N
EM(I)=RMASS(I)


```

76 CONTINUE
  CALL PRINT5(ST,N)
  CALL UNIT(A1,N)

C
C   STB=(1/SQRT(EM))*(ST)*(1/SQRT(EM)). THE STIFFNESS MATR
C   IX
C   ST IS TRANSFORMED INTO A FORM IN WHICH THE JACOBI METH
C   OD
C   CAN BE APPLIED.
C
  DO 10 I=1,N
10  EM(I)=SQRT(EM(I))
  DO 12 I=1,N
  DO 12 J=1,N
12  STB(I,J)=ST(I,J)/(EM(J)*EM(I))
  DO 20 KK=1,K
  DO 15 I=1,N
  DO 15 J=I,N
  IF (I-J) 14,15,14

C
C   T IS A UNIT MATRIX EXCEPT FOR T(I,I),T(J,J),T(I,J),
C   AND T(J,I). BY PRE AND POST MULTIPLYING STB BY T THE
C   ELEMENT STB(I,J) IS SET=0. THIS ACTUALLY A SERIES OF
C   ORTHOGONAL TRANSFORMATIONS TO DIAGONALIZE STB.AFTER ST
C   B
C   IS DIAGONALIZED IT WILL CONTAIN THE EIGENVALUES ON ITS
C   MAIN DIAGONAL.
C
14  IF (ABS(STB(I,J)).LT.1.0E-10) GO TO 15
  CALL UNIT(T,N)
  DIFF=STB(I,I)-STB(J,J)
  IF (ABS(DIFF)-.00005D0) 30,30,32
30  TH=.785398E0
  GO TO 33
32  THC=2.0E0*STB(I,J)/DIFF
  TH=.5E0*ATAN(THC)
33  T(I,I)=COS(TH)
  T(J,J)=T(I,I)
  T(I,J)=-SIN(TH)
  T(J,I)=-T(I,J)

C
C   CALCULATE THE TRANSPOSE OF T (TT).
C
  CALL TRA(T,TT,N)

C
C   TT*STB*T=STB
C
  CALL PRMULT(STB,TH,I,J,N)
  CALL PCMULT(STB,TH,I,J,N)

C
C   A1*T=A1. A1 STORES THE RESULTS OF
C   T1*T2*T3....TK.(THERE ARE K ITERATIONS).A1=SQRT(EM)*A
C   WHERE AIS THE MODAL MATRIX.T1 IS T FOR THE FIRST ITERA
C   TION

```

```

C      T2 IS T FOR THE SECOND ITERATION UP TO TK FOR THE KTH
C      ITERATION.
C
      CALL POMULT(A1,TH,I,J,N)
15  CONTINUE
C
C      THE MODAL MATRIX A=(1/SQRT(EM))*A1.THE FIRST ROW OF A
C      IS NORMALIZED TO 1
C
      DO 18 J=1,N
      DO 18 I=1,N
18  A(I,J)=A1(I,J)/EM(I)
20  CONTINUE
      DO 50 I=1,N
      OMEGA(I)=SQRT(STB(I,I))
50  CONTINUE
C
C      SORT FREQUENCIES AND EIGENVECTORS STARTING FROM MODE 1
C      (LOWEST)
C      AND GOING UP TO MODE N.
C
      NN=N-1
      DO 80 I=1,NN
      L=I+1
      DO 9 K=L,N
      IF (OMEGA(K).GT.OMEGA(I)) GO TO 9
      WX=OMEGA(I)
      OMEGA(I)=OMEGA(K)
      OMEGA(K)=WX
      DO 300 II=1,N
      AX=A(II,I)
      A(II,I)=A(II,K)
      A(II,K)=AX
300 CONTINUE
      9 CONTINUE
      80 CONTINUE
C
C      PRINT OUT THE NATURAL FREQUENCIES AND EIGENVECTORS.
C
      DO 11 I=1,N
11  WRITE(6,122) I,OMEGA(I)
122 FORMAT(/10X,'FREQUENCY',I5,'=',F10.2)
      CALL PRINT5(A,N)
      CALL TRA(A,ATR,N)
      RETURN
      END
      SUBROUTINE MULT(A,B,C,N)
      DIMENSION A(12,12),B(12,12),C(12,12)
      DO 10 I=1,N
      DO 10 J=1,N
      C(I,J)=0.0E0
      DO 10 L=1,N
10  C(I,J)=C(I,J)+A(I,L)*B(L,J)
      RETURN

```

```

END
SUBROUTINE UNIT(A,N)
DIMENSION A(12,12)
DO 10 I=1,N
DO 8 J=1,N
8 A(I,J)=0.0E0
10 A(I,I)=1.0E0
RETURN
END
SUBROUTINE TRA(A,B,N)
DIMENSION A(12,12),B(12,12)
DO 10 I=1,N
DO 10 J=1,N
10 B(I,J)=A(J,I)
RETURN
END
SUBROUTINE POMULT(STB,TH,I,J,N)
DIMENSION STB(12,12),C(12,2)
DO 1 II=1,N
C(II,1)=STB(II,I)*COS(TH)+STB(II,J)*SIN(TH)
C(II,2)=STB(II,J)*COS(TH)-STB(II,I)*SIN(TH)
1 CONTINUE
DO 2 II=1,N
STB(II,I)=C(II,1)
STB(II,J)=C(II,2)
2 CONTINUE
RETURN
END
SUBROUTINE PRMULT(STB,TH,I,J,N)
DIMENSION STB(12,12),C(2,12)
DO 1 JJ=1,N
C(1,JJ)=STB(I,JJ)*COS(TH)+STB(J,JJ)*SIN(TH)
C(2,JJ)=STB(J,JJ)*COS(TH)-STB(I,JJ)*SIN(TH)
1 CONTINUE
DO 2 JJ=1,N
STB(I,JJ)=C(1,JJ)
STB(J,JJ)=C(2,JJ)
2 CONTINUE
RETURN
END
SUBROUTINE PRINTS(A,N)
DIMENSION A(12,12)
WRITE(6,20)
DO 10 I=1,N
10 WRITE(6,12) (A(I,J),J=1,N)
12 FORMAT(10X,10E10.3)
20 FORMAT(//)
RETURN
END
SUBROUTINE CYCLE(N,LFLAG,DINC)

```

C
C
C
C
C

THIS SUBROUTINE KEEPS TRACK OF WHICH CYCLE OF LOADING
EACH CRACK IN THE VESSEL IS ON. THE LOAD CYCLE NUMBER
FOR ALL

```

C     THE CRACKS IN THE ITH BEAM SEGMENT IS STORED IN NCYCLE
C     (I).
C     AT T=0, NCYCLE(I)=1. THE FIRST CYCLE CRACK STIFFNESS I
C     S
C     LINEAR WITH NO HYSTERESIS LOOP.
C
C     COMMON /DYN/RMASS(12),DAMP(12,12),CK(6),CFORCE(12),EQF
C     OR(12),
C     IRKFOR(12),OLDFOR(12),RINFOR(12),ACC(12),DISP(12),VEL(1
C     2),
C     2OLDVEL(12),OLDACC(12),SHEAR(12),OLDSHR(12),REL(12),OLD
C     AMP(12),
C     3SHEARK(5),GLOK(12,12),NCR(5),OLDCK(6),NLDIPD(5),OLDREL
C     (12),RK(8)
C     4,TK(6),OLDISP(12)
C     COMMON /B/RLOAD(6),DELTA(6),IPD(5),NCYCLE(5),RLOADN(5,
C     6),
C     IDELTAN(5,6)
C     DIMENSION PEAK(5)
C     IF (LFLAG.GT.0) GO TO 2
C     LFLAG=1
C     DO 1 I=1,N
C     PEAK(I)=0.
1     NCYCLE(I)=1
C     GO TO 45
C
C     THE PEAK SHEAR STRESS FOR THE CURRENT LOAD CYCLE IS ST
C     ORED
C     IN PEAK(I) FOR THE ITH BEAM SEGMENT.
C
C     2 DO 10 I=1,N
C     IF (ABS(SHEAR(I)).LE.ABS(PEAK(I))) GO TO 10
C     PEAK(I)=SHEAR(I)
10    CONTINUE
C
C     FOR THE FIRST CYCLE, IF ABS(PEAK(I)) IS GT RLOAD(1) AN
C     D
C     UNLOADING IS OCCURING THEN THE SECOND CYCLE HYSTERESIS
C     LOOP IS SWITCHED TO.
C
C     DO 3 I=1,N
C     IF (ABS(SHEAR(I)).GE.ABS(OLDSHR(I))) GO TO 3
C     IF (NCYCLE(I).GT.1) GO TO 4
C     IF (ABS(PEAK(I)).LT.RLOAD(1)) GO TO 3
C     IF (PEAK(I).LT.0.) GO TO 8
C     IPD(I)=3
C     CK(I)=RK(3)
C     PEAK(I)=0.
C     NCYCLE(I)=NCYCLE(I)+1
C     GO TO 3
C
C     AFTER THE FIRST CYCLE THE DEFINITION OF AN ADDITIONAL
C     LOAD CYCLE CHANGES. IF ABS(PEAK(I)) GT .1KSI AND ABS(
C     SHEAR(I)) LT .05 KSI THEN NCYCLE(I) IS INCREASED BY 1.

```

C THE HYSTERESIS LOOP FOR THE ITH BEAM SEGMENT, AS DEFIN
 C ED BY
 C DELTAN(I,1.....6) AND RLOADN(I,1.....6) ARE CHANGED
 C ACCORDINGLY.
 C

```

8 IPD(I)=7
  CK(I)=RK(7)
  PEAK(I)=0.
  NCYCLE(I)=NCYCLE(I)+1
  GO TO 3
4 IF (IPD(I).EQ.3) GO TO 5
  IF (IPD(I).EQ.7) GO TO 6
  GO TO 3
5 IF (ABS(PEAK(I)).LT..1) GO TO 3
  IF (SHEAR(I).GT..05) GO TO 3
  GO TO 7
6 IF (ABS(PEAK(I)).LT..1) GO TO 3
  IF (SHEAR(I).LT.(-.05)) GO TO 3
7 NCYCLE(I)=NCYCLE(I)+1
  PEAK(I)=0.
  DELTAN(I,1)=DELTAN(I,1)+DINC
  DELTAN(I,2)=DELTAN(I,2)+DINC
  DELTAN(I,4)=-DELTAN(I,1)
  DELTAN(I,5)=-DELTAN(I,2)
  DELTAN(I,3)=(RLOAD(2)-RLOAD(4)+RK(4)*DELTAN(I,4)-RK(3)
C *DELTAN(
  I,2))/(RK(4)-RK(3))
  RLOADN(I,3)=RK(4)*(DELTAN(I,3)-DELTAN(I,4))+RLOAD(4)
  DELTAN(I,6)=-DELTAN(I,3)
  RLOADN(I,6)=-RLOADN(I,3)
3 CONTINUE
45 RETURN
  END
  SUBROUTINE INHYST(H,T,OH,N,JFLAG,PRINT,KREF,NFLAG)

```

C
 C INHYST KEEPS TRACK OF WHERE THE SHEAR STRESS IN EACH B
 C EAM
 C SEGMENT IS IN THE CYCLE DEPENDENT HYSTERESIS LOOPS.
 C THE CRACK STIFFNESS FOR THE ITH BEAM SEGMENT IS CK(I).
 C

```

  DIMENSION TI(10),VPRINT(10)
  COMMON /DYN/RMASS(12),DAMP(12,12),CK(6),CFORCE(12),EQF
C OR(12),
  1RKFOR(12),OLDFOR(12),RINFOR(12),ACC(12),DISP(12),VEL(1
C 2),
  2OLDVEL(12),OLDACC(12),SHEAR(12),OLDSHR(12),REL(12),OLD
C AMP(12),
  3SHEARK(5),GLOK(12,12),NCR(5),OLDCK(6),NLDIPD(5),OLDREL
C (12),RK(8)
  4,TK(6),OLDISP(12)
  COMMON /B/RLOAD(6),DELTA(6),IPD(5),NCYCLE(5),RLOADN(5,
C 6),
  1DELTAN(5,6)
  IF (JFLAG.GT.0) GO TO 202

```

```

JFLAG=1
PRTIM=0.
OLDTIM=0.
READ(5,13) NTI
13 FORMAT(I5)
PRTOL=H/10.
READ(5,101) (TI(I),I=1,NTI)
READ(5,101) (VPRINT(I),I=1,NTI)
PRINT=VPRINT(1)
JJ=1
101 FORMAT(10F8.0)
C
C THE INITIAL STIFFNESS IS ASSUMED TO BE RK(1)
C
DO 46 I=1,N
CK(I)=RK(1)
IPD(I)=1
NCYCLE(I)=1
46 CONTINUE
GO TO 500
C
C IPD IDENTIFIES WHICH LINEAR SEGMENT OF THE HYSTERESIS
C LOOP YOU
C ARE ON.
C
202 CONTINUE
DO 131 L=1,N
OLDCK(L)=CK(L)
NLDIPD(L)=IPD(L)
131 CONTINUE
DO 299 I=1,N
IF (IPD(I).EQ.8) GO TO 212
IF (IPD(I).GE.3) GO TO 205
IF (IPD(I).GT.1) GO TO 204
C
C IPD HAS BEEN TESTED TO SEE IF IT IS EQUAL TO 1.THE
C SHEAR STRESS IS THEN CHECKED TO SEE IF IT IS NEGATIVE.
C IF SO,
C THE STIFFNESS CK IS SET EQUAL TO RK(5),THE INITIAL
C NEGATIVE STIFFNESS.
C
IF (SHEAR(I).GE.0.) GO TO 299
IPD(I)=5
CK(I)=RK(5)
GO TO 299
C
C CHECK TO SEE IF A CHANGE OF STIFFNESS HAS OCCURED DURIG
C THE
C LAST TIME STEP.IN THIS CASE THE STIFFNESS CK HAS CHANG
C ED
C FROM RK(1) TO RK(2).
C
C
C THE STATEMENTS BELOW PERTAIN TO CRACKS ON THE RK(2) SE

```

```

C      CTION OF
C      THE LOOP. A CHECK IS MADE TO SEE WHETHER UNLOADING HAS
C      STARTED
C      DURING THE LAST TIME STEP. IF SO, THE STIFFNESS BECOME
C      S RK(3).
C
204 IF (SHEAR(I).GE.OLDSHR(I)) GO TO 299
    IPD(I)=3
    CK(I)=RK(3)
    GO TO 299
205 IF (IPD(I).GT.3) GO TO 207
C
C      THE FOLLOWING STATEMENTS DEAL WITH CRACKS ON THE RK=RK
C      (3)
C      SECTION OF THE HYSTERESIS LOOP. A CHECK IS MADE TO SEE
C      IF THE
C      RK(4) BRANCH HAS BEEN REACHED.
C
    IF (SHEAR(I).LT.OLDSHR(I)) GO TO 29
    IF (SHEAR(I).LT.RLOAD(1)) GO TO 68
    IPD(I)=2
    CK(I)=RK(2)
    GO TO 299
68 IPD(I)=4
    CK(I)=RK(4)
    GO TO 299
29 FLAG3=RLOADN(I,3)+(REL(I)-DELTAN(I,3))*RK(4)
    IF (SHEAR(I).GT.(FLAG3+.05*RLOAD(1))) GO TO 299
C
C      NOW CHECK TO SEE HOW MUCH FLAG3 HAS BEEN EXCEEDED BY.
C      THE
C      ACCEPTABLE ERROR IS 5 PER CENT. IF THE ERROR IS GREATER
C      THAN
C      THIS GO BACK TO THE LAST TIME STEP AND USE A SMALLER H
C      .
C
    ERROR=SHEAR(I)-FLAG3
    IF (ABS(ERROR).LE.ABS(.05*RLOAD(1))) GO TO 300
    IF (OLDSHR(I).GT.FLAG3) GO TO 90
    OLDCK(I)=RK(4)
    NLDIPD(I)=4
    KREF=1
    GO TO 60
90 H=((FLAG3-OLDSHR(I))/(SHEAR(I)-OLDSHR(I)))*H
    GO TO 59
300 CONTINUE
301 IPD(I)=4
    CK(I)=RK(4)
    GO TO 299
C
C      THE FOLLOWING STATEMENTS CHECK TO SEE IF THE CRACK STI
C      FFNESS
C      EQUALS RK(4). IF SO ,A CHECK IS MADE TO SEE IF RELOADI
C      NG IS

```

C OCCURRING. IF IT IS AND SHEAR(I) IS GREATER THAN RLOAD(
 C 1) THEN THE
 C STIFFNESS IS CHANGED TO RK(2). IF NO RELOADING HAS OCC
 C URED
 C A CHECK IS MADE TO SEE IF A CHANGE TO RK(6) SHOULD BE
 C MADE.
 C

207 IF (IPD(I).GT.4) GO TO 209
 IF (SHEAR(I).LE.OLDSHR(I)) GO TO 208
 IF (SHEAR(I).LT.RLOAD(1)) GO TO 299
 IPD(I)=2
 CK(I)=RK(2)
 GO TO 299
 208 IF (RLOAD(4).LT.SHEAR(I)) GO TO 299
 IPD(I)=6
 CK(I)=RK(6)
 GO TO 299

C
 C THE FOLLOWING STATEMENTS APPLY TO CK=RK(5). A CHANGE O
 C F
 C STIFFNESS IS CHECKED FOR.
 C

209 IF (IPD(I).GT.5) GO TO 210
 IF (SHEAR(I).LT.0.) GO TO 299
 IPD(I)=1
 CK(I)=RK(1)
 GO TO 299

C
 C THE FOLLOWING STATEMENTS APPLY TO CK=RK(6). RELOADING
 C IS CHECKED
 C FOR.
 C

210 IF (IPD(I).GT.6) GO TO 211
 IF (SHEAR(I).LE.OLDSHR(I)) GO TO 299
 IPD(I)=7
 CK(I)=RK(7)
 GO TO 299

C
 C THE FOLLOWING STATEMENTS APPLY TO CK=RK(7). A CHANGE O
 C F STIFFNESS
 C IS CHECKED FOR.
 C

211 IF (SHEAR(I).GT.OLDSHR(I)) GO TO 39
 IF (SHEAR(I).GT.RLOAD(4)) GO TO 78
 IPD(I)=6
 CK(I)=RK(6)
 GO TO 299
 78 IPD(I)=8
 CK(I)=RK(8)
 GO TO 299
 39 FLAG6=RLOADN(I,6)+(REL(I)-DELTAN(I,6))*RK(8)
 IF (SHEAR(I).LT.(FLAG6-.05*RLOAD(1))) GO TO 299

C
 C CHECK TO SEE HOW MUCH FLAG6 HAS BEEN EXCEEDED BY. THE

C ACCEPTABLE ERROR IS 5 PER CENT. IF THIS IS EXCEEDED TH
 C EN GO BACK T
 C LAST TIME STEP AND USE A SMALLER H.
 C

ERROR=SHEAR(I)-FLAG6
 IF (ABS(ERROR).LE.ABS(.05*RLOAD(1))) GO TO 400
 IF (OLDSHR(I).LT.FLAG6) GO TO 91
 OLDCK(I)=RK(8)
 NLDIPD(I)=8
 KREF=1
 GO TO 60
 91 H=((FLAG6-OLDSHR(I))/(SHEAR(I)-OLDSHR(I)))*H
 GO TO 59
 400 CONTINUE
 401 IPD(I)=8
 CK(I)=RK(8)
 GO TO 299

C THE FOLLOWING STATEMENTS APPLY TO IPD=1,CK=RK(8).CHANG
 C E OF
 C STIFFNESS AND UNLOADING ARE CHECKED FOR.
 C

212 IF (SHEAR(I).GE.OLDSHR(I)) GO TO 213
 IF (SHEAR(I).GT.RLOAD(4)) GO TO 299
 IPD(I)=6
 CK(I)=RK(6)
 GO TO 299
 213 IF (SHEAR(I).LT.RLOAD(1)) GO TO 299
 IPD(I)=2
 CK(I)=RK(2)
 299 CONTINUE
 H=OH
 KREF=0
 DO 99 I=1,N
 IF (NLDIPD(I).EQ.IPD(I)) GO TO 99
 KREF=1
 99 CONTINUE
 IF (T.LT.10.) GO TO 94
 IF (T.GT.10.8) GO TO 94
 WRITE(6,93) T,SHEAR(5),REL(5),NLDIPD(5)
 93 FORMAT(/10X,3E14.7,I5)
 94 CONTINUE
 IF ((T+PRTOL-PRTIM).LT.0.) GO TO 450
 IF (ABS(T-PRTIM).LE.PRTOL) GO TO 17
 H=PRTIM-OLDTIM
 59 CONTINUE
 KREF=0
 60 NFLAG=1
 T=OLDTIM
 DO 89 K=1,N
 IPD(K)=NLDIPD(K)
 SHEAR(K)=OLDSHR(K)
 REL(K)=OLDREL(K)
 CK(K)=OLDCK(K)

```
89 CONTINUE
DO 189 K=1,12
DISP(K)=OLDISP(K)
VEL(K)=OLDVEL(K)
ACC(K)=OLDACC(K)
RKFOR(K)=OLDFOR(K)
RINFOR(K)=RMASS(K)*ACC(K)
CFORCE(K)=OLDAMP(K)
189 CONTINUE
GO TO 461
```

C
C
C

```
PRINT OUT DYNAMIC RESULTS AT TIME=T.
```

```
17 CONTINUE
WRITE(6,12) (NCYCLE(I),I=1,N)
12 FORMAT(/10X,5I5)
WRITE(6,22) T
22 FORMAT(/10X,'FOR TIME = ',F8.2,8X,'DISPLACEMENT',8X,
1'SHEAR STRESS',9X,'CRACK DISP',10X,'STIFFNESS'/)
DO 73 I=1,N
WRITE(6,76) DISP(2*I-1),SHEAR(I),REL(I),OLDCK(I)
76 FORMAT(36X,E14.7,6X,E14.7,6X,E14.7,6X,E14.7)
73 CONTINUE
IF (T.LT.TI(JJ)) GO TO 5
JJ=JJ+1
PRINT=VPRINT(JJ)
5 PRTIM=PRTIM+PRINT
450 OLDTIM=T
461 T=T+H
500 RETURN
END
```

TABLE 2.1

INCREMENTAL LOADS FOR THE SAP IV MODEL

Step	Load*	Bars with E_2 Modulus
1	20 $\cos\phi$	None
2	1 $\cos\phi$	1, 10, 19
3	2 $\cos\phi$	1, 2, 10, 11, 19, 20
4	4 $\cos\phi$	1-3, 10-12, 19-21
5	6 $\cos\phi$	1-4, 10-13, 19-22
6	9 $\cos\phi$	1-5, 10-14, 19-23
7	23 $\cos\phi$	1-6, 10-15, 19-24
8	77 $\cos\phi$	1-7, 10-16, 19-25
9	138 $\cos\phi$	1-8, 10-17, 19-26
Total	280 $\cos\phi$	

* These loads are shear stress distributions which are converted to equivalent nodal loads using equations (2.4).

TABLE 3.1

BEAM ELEMENT STIFFNESS MATRIX

$$[K_E] = \frac{EI}{1 + 4\lambda} \begin{bmatrix} \frac{12}{L^3} & -\frac{6}{L^2} & -\frac{12}{L^3} & -\frac{6}{L^2} \\ -\frac{6}{L^2} & \frac{4}{L}(1 + \lambda) & \frac{6}{L^2} & \frac{2}{L}(1 - 2\lambda) \\ -\frac{12}{L^3} & \frac{6}{L^2} & \frac{12}{L^3} & \frac{6}{L^2} \\ -\frac{6}{L^2} & \frac{2}{L}(1 - 2\lambda) & \frac{6}{L^2} & \frac{4}{L}(1 + \lambda) \end{bmatrix}$$

$$\lambda = \frac{3EI}{L^3} \frac{L}{A_s G}$$

TABLE 3.2

GLOBAL STIFFNESS MATRIX

$$\begin{array}{ccccc}
 u_1^{\theta_1} & u_2^{\theta_2} & u_3^{\theta_3} & u_4^{\theta_4} & u_5^{\theta_5} \\
 \left[\begin{array}{ccccc}
 K_{11} & -K_{12} & 0 & 0 & 0 \\
 -K_{21} & K_{11}' + K_{22} & K_{23} & 0 & 0 \\
 0 & -K_{32} & K_{22}' + K_{33} & -K_{34} & 0 \\
 0 & 0 & -K_{43} & K_{33}' + K_{44} & -K_{45} \\
 0 & 0 & 0 & -K_{54} & K_{44}' + K_{55}
 \end{array} \right]
 \end{array}$$

$$K_{ii} = \frac{EI_i}{1+4\lambda_i} \begin{bmatrix} \frac{12}{L_i^3} & -\frac{6}{L_i^2} \\ -\frac{6}{L_i^2} & \frac{4}{L_i}(1+\lambda_i) \end{bmatrix}$$

$$K_{ii}' = \frac{EI_i}{1+4\lambda_i} \begin{bmatrix} \frac{12}{L_i^3} & \frac{6}{L_i^2} \\ \frac{6}{L_i^2} & \frac{4}{L_i}(1+\lambda_i) \end{bmatrix}$$

$$K_{ij} = \frac{EI_i}{1+4\lambda_i} \begin{bmatrix} -\frac{12}{L_i^3} & -\frac{6}{L_i^2} \\ \frac{6}{L_i^2} & \frac{2}{L_i}(1-2\lambda_i) \end{bmatrix}$$

$$M_{ij} = K_{ij}^T$$

TABLE 3.3

NATURAL FREQUENCIES (CYCLES/SEC)

Mode	10 DOF	5 DOF
1	6.0	7.5
2	15.3	18.4
3	24.0	31.2
4	30.2	43.9
5	43.2	51.0
6	43.5	----
7	50.6	----
8	68.2	----
9	94.5	----
10	109.2	----

TABLE 4.1

Soil Type	C_2 (fps)	K_u (k/in)	K_ϕ (k-in/rad)
Soft Soil	500	30,647	2.184×10^{10}
Medium Soil	1,200	176,528	1.258×10^{11}
Hard Soil	2,000	490,356	3.494×10^{11}

TABLE 4.2

$u_1^{\theta_1}$	$u_2^{\theta_2}$	$u_3^{\theta_3}$	$u_4^{\theta_4}$	$u_5^{\theta_5}$	$u_f^{\phi_f}$
K_{11}	K_{12}	0	0	0	0
K_{21}	$K_{11}' + K_{22}$	K_{23}	0	0	0
0	K_{32}	$K_{22}' + K_{33}$	K_{34}	0	0
0	0	K_{43}	$K_{33}' + K_{44}$	K_{45}	0
0	0	0	K_{54}	$K_{44}' + K_{55}$	K_{5f}
0	0	0	0	K_{f5}	$K_{55}' + K_{ff}$

$$K_{ff} = \begin{bmatrix} K_u & 0 \\ 0 & K_\phi \end{bmatrix}$$

$$K_{5f} = \frac{EI_5}{1 + 4\lambda_5} \begin{bmatrix} -\frac{12}{h_5^2} & -\frac{6}{h_5} \\ \frac{6}{h_5^2} & \frac{2}{h_5}(1 - 2\lambda_5) \end{bmatrix}$$

$$K_{f5} = K_{5f}^T$$

TABLE 5.1

$\left(\frac{L}{EI} + C\right)$	$-\left(\frac{L^2}{2EI} + B\right)$	$-\left(\frac{L}{EI} + C\right)$	$\left(B - \frac{L^2}{2EI} - CL\right)$
$-\left(\frac{L^2}{2EI} + B\right)$	$\left(\frac{L^3}{3EI} + \frac{L}{GA_S} + \frac{N}{K_C} + A\right)$	$\left(\frac{L^2}{2EI} + B\right)$	$\left(\frac{L^3}{6EI} + BL - \frac{L}{GA_S} - \frac{N}{K_C} - A\right)$
$-\left(\frac{L}{LI} + C\right)$	$\left(\frac{L^2}{2EI} + B\right)$	$\left(\frac{L}{EI} + C\right)$	$\left(\frac{L^2}{2EI} + B\right)$
$\left(B - \frac{L^2}{2EI} - CL\right)$	$\left(\frac{L^3}{6EI} + BL - \frac{L}{GA_S} - \frac{N}{K_C} - A\right)$	$\left(\frac{L^2}{2EI} + B\right)$	$\left(\frac{L^3}{3EI} + \frac{L}{GA_S} + \frac{N}{K_C} + A\right)$

$$|K|_{\text{Element}} = \frac{1}{\det}$$

$$A = \left(\frac{1}{I_C} - \frac{1}{I}\right) \sum_{i=1}^N \left(\frac{2i-1}{2N}\right)^2 \frac{L^2 L_u}{E} \quad B = \left(\frac{1}{I_C} - \frac{1}{I}\right) \frac{L L_u}{E} \sum_{i=1}^N \left(\frac{2i-1}{2N}\right) \quad C = \left(\frac{1}{I_C} - \frac{1}{I}\right) \frac{N L_u}{E}$$

$$\det = \frac{L^4}{12E^2 I^2} + \frac{L}{EI} \left(\frac{L}{GA_S} + \frac{N}{K_C}\right) + \frac{AL}{EI} + C \left(\frac{L^3}{3EI} + \frac{L}{GA_S} + \frac{L}{N} + \frac{N}{K_C} + A\right) - \frac{BL^2}{EI} - B^2$$

TABLE 5.2

Run	Displacement (inches)	Shear Stress (psi)	Crack Slip (inches)	Cycles
1	1.330	288	-----	----
2	1.543	272	.0136	18
3	2.565	126	.0125	7
4	1.200	280	.0143	25

TABLE 5.3

Run	Concrete Stress (ksi)	Steel Stress (ksi)	Change in Crack Width (inches)
1	----	-----	-----
2	.599	25.10	.0022
3	.237	9.93	.0009
4	.696	29.17	.0025

TABLE 5.4

Beam	I (in ⁴)		I _c (in ⁴)		A _s (in ²)
1	4.483	10 ¹⁰	1.074	10 ¹⁰	97,270
2	6.202	10 ¹⁰	1.179	10 ¹⁰	142,000
3	6.202	10 ¹⁰	1.179	10 ¹⁰	142,000
4	6.202	10 ¹⁰	1.179	10 ¹⁰	142,000
5	6.202	10 ¹⁰	1.179	10 ¹⁰	142,000

TABLE 5.5

Run	Soil Type	Crack Spacing
1	Medium	-----
2	Medium	5' - 6"
3	Soft	5' - 6"
4	Hard	5' - 6"

TABLE 5.6

DOF	u_1, θ_1	$u_2-u_5, \theta_2-\theta_5$	u_f, ϕ_f
Mass (k-sec ² /in)	28.82	22.97	61.74
Mass Moment (k-sec ² -in $\times 10^6$)	8.17	8.29	12.74

DOF = Degree of Freedom

TABLE 5.7

Mode	1	2	3
a_1	240.38	1070.33	443.02
a_2	5.78	4.27	- 2.25

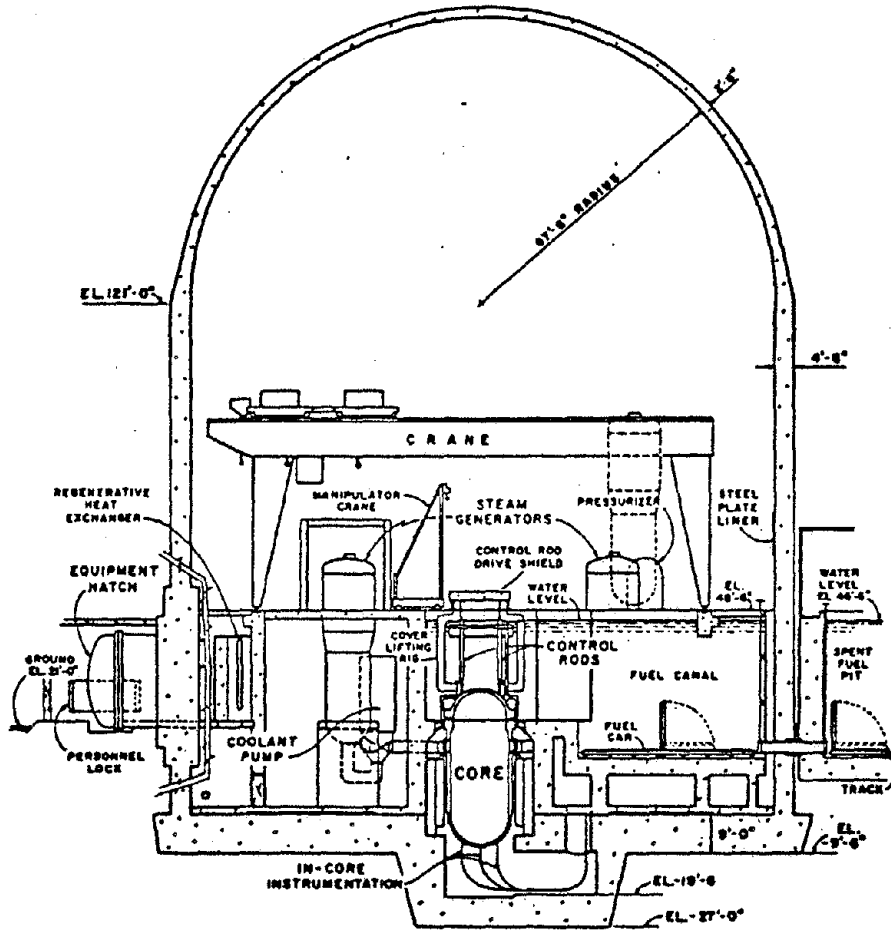
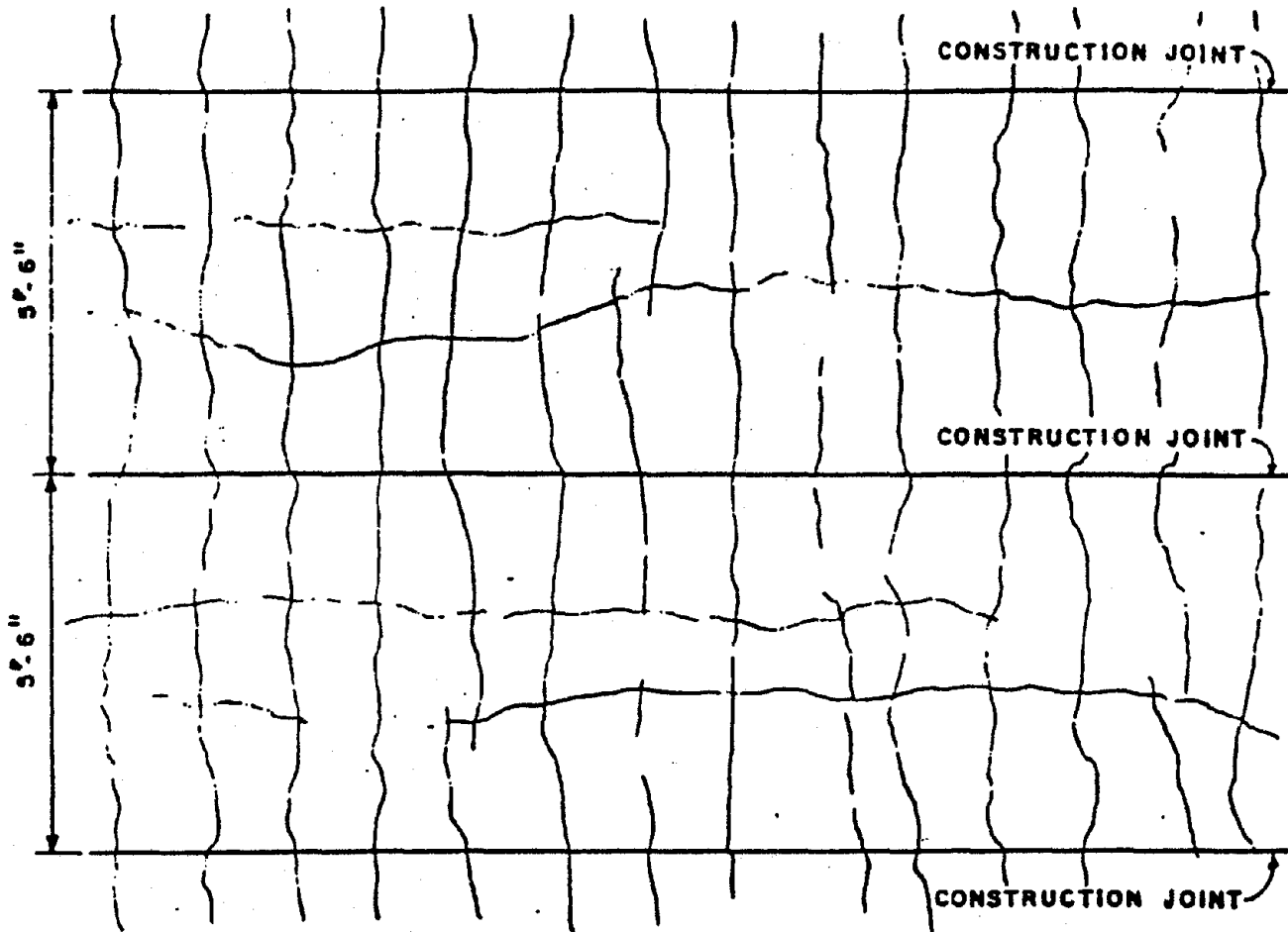


Figure 1.1 - Typical Nuclear Containment Vessel

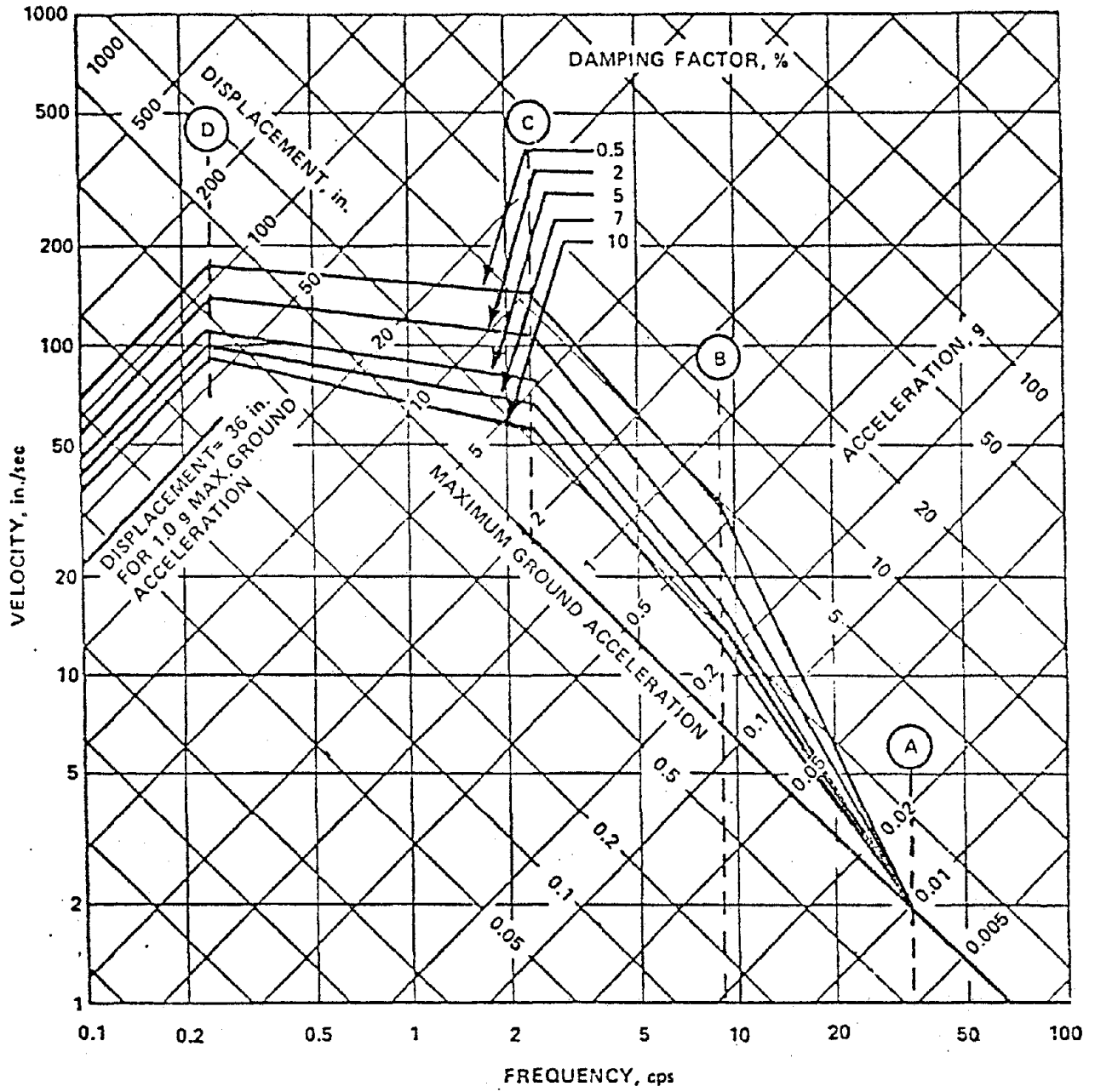


Vertical cracks at approximately 15" O.C. Maximum width .010"

Horizontal cracks at each construction joint plus one or two much smaller cracks between joints.

No spalling of concrete.

Figure 1.2



Horizontal design response spectra - scaled to 1g horizontal ground acceleration.

Figure 1.3

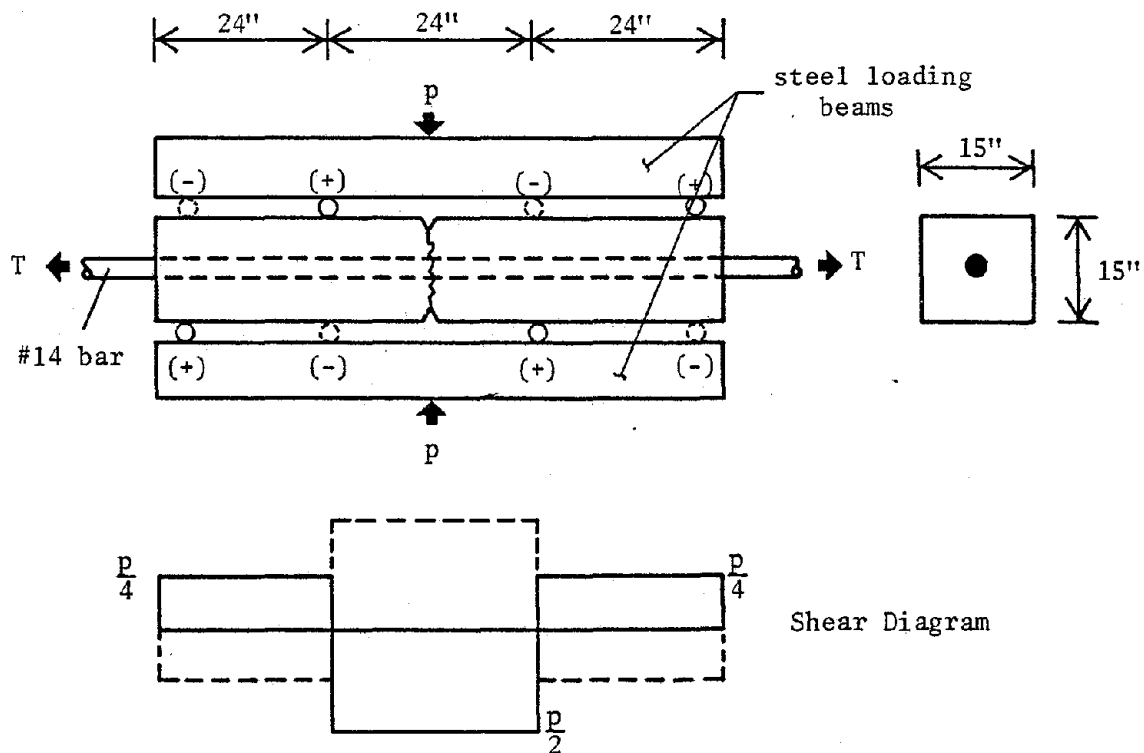


Figure 2.1 - Beam-type Specimen

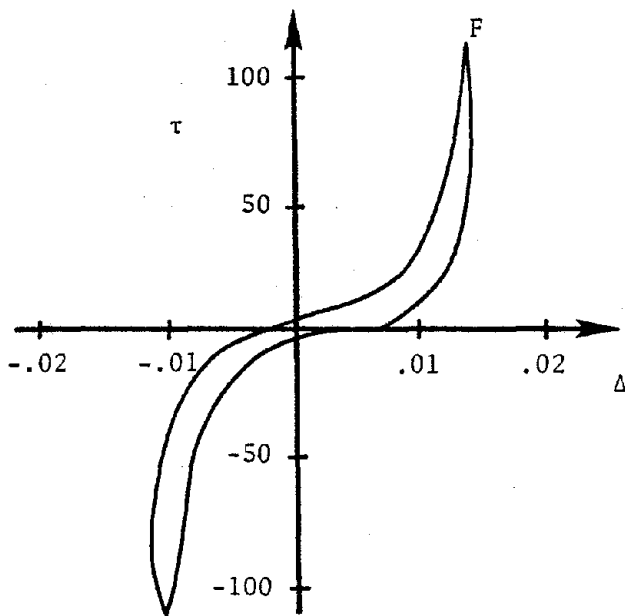


Figure 2.2

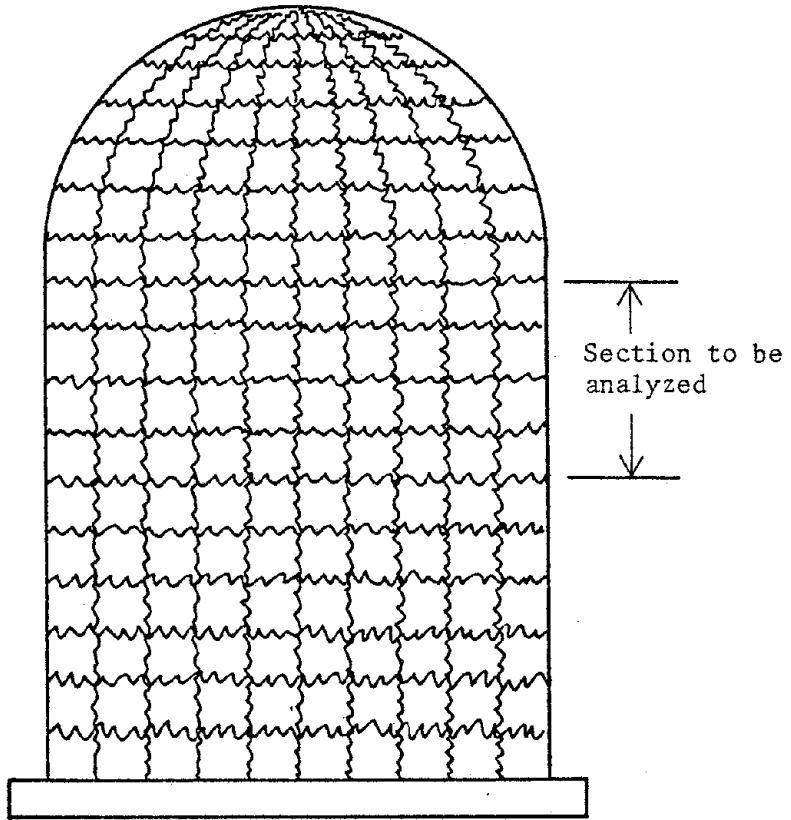


Figure 2.3 - Containment with Horizontal and Vertical Cracking

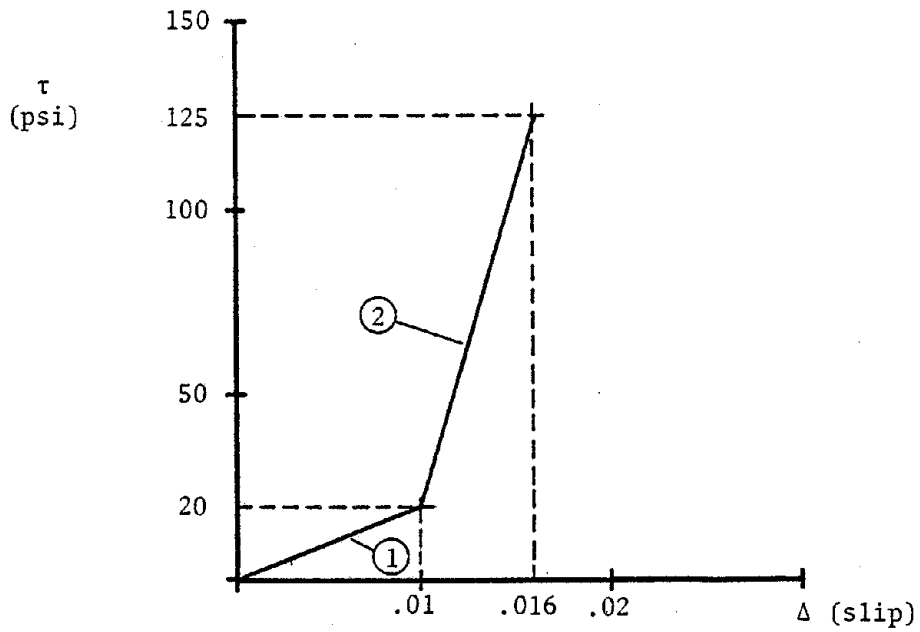


Figure 2.4 - Idealized Load-Slip Curve
(From Curve F of Figure 2.1)

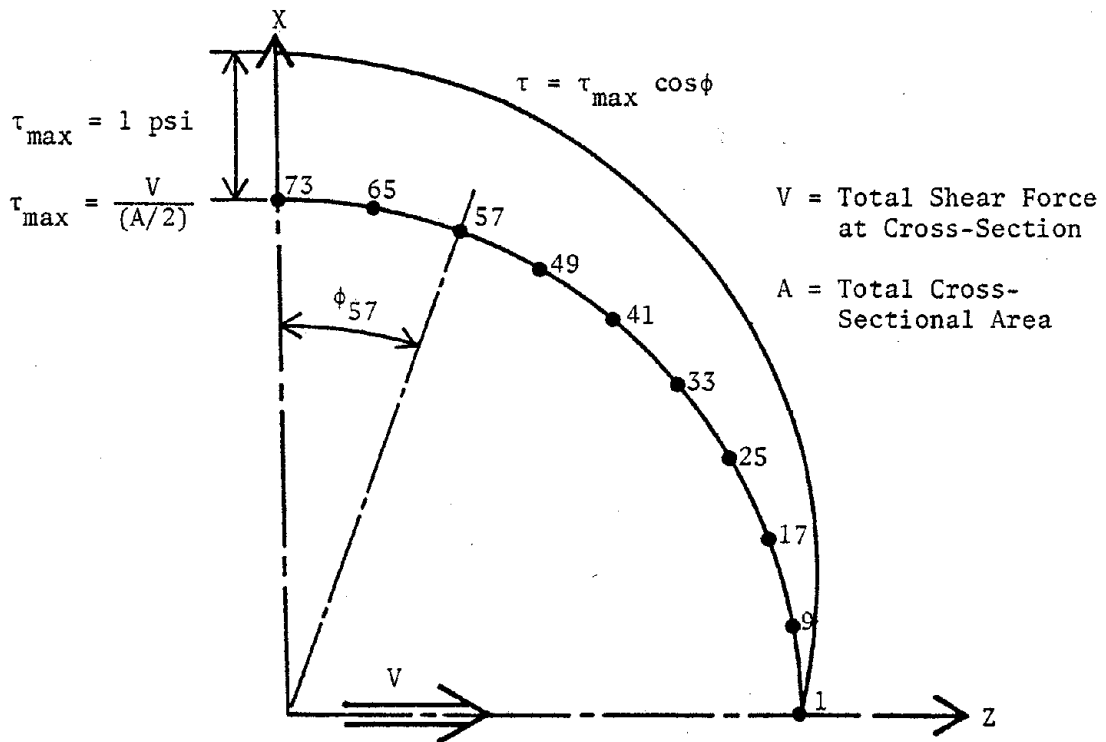


Figure 2.5 - Elastic Shear Stress Distribution

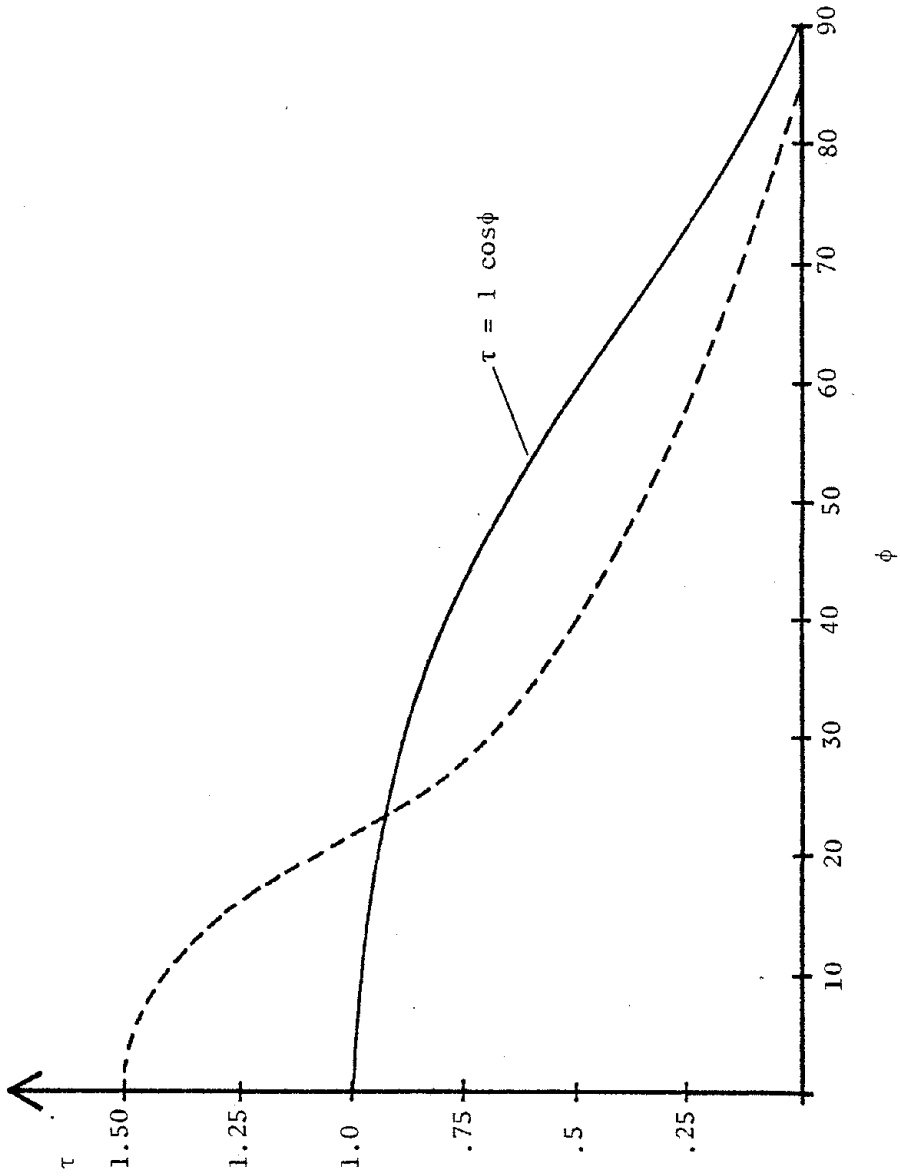
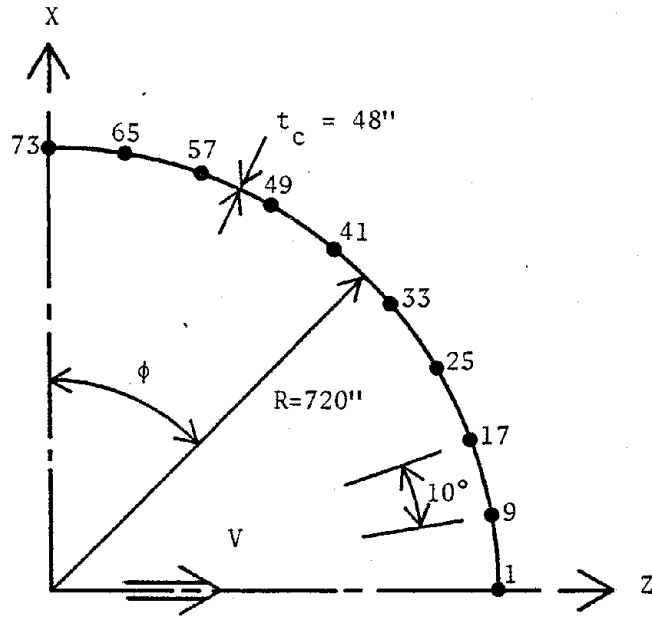
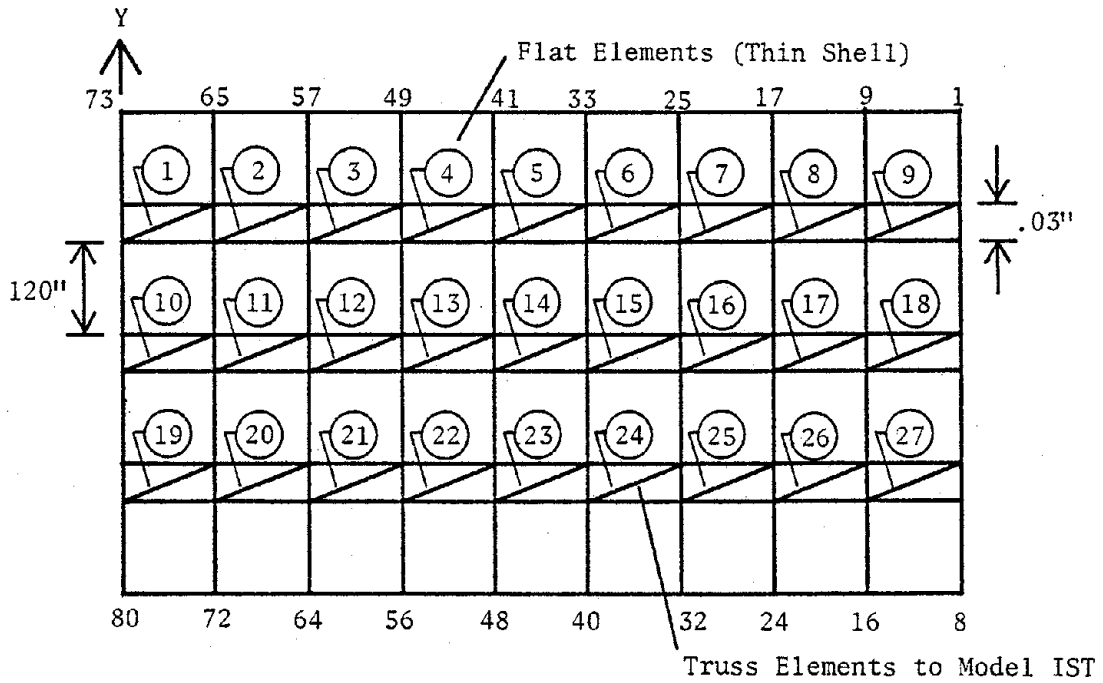


Figure 2.6



PLAN VIEW



ROLLOUT VIEW

Figure 2.7 - SAP IV Model

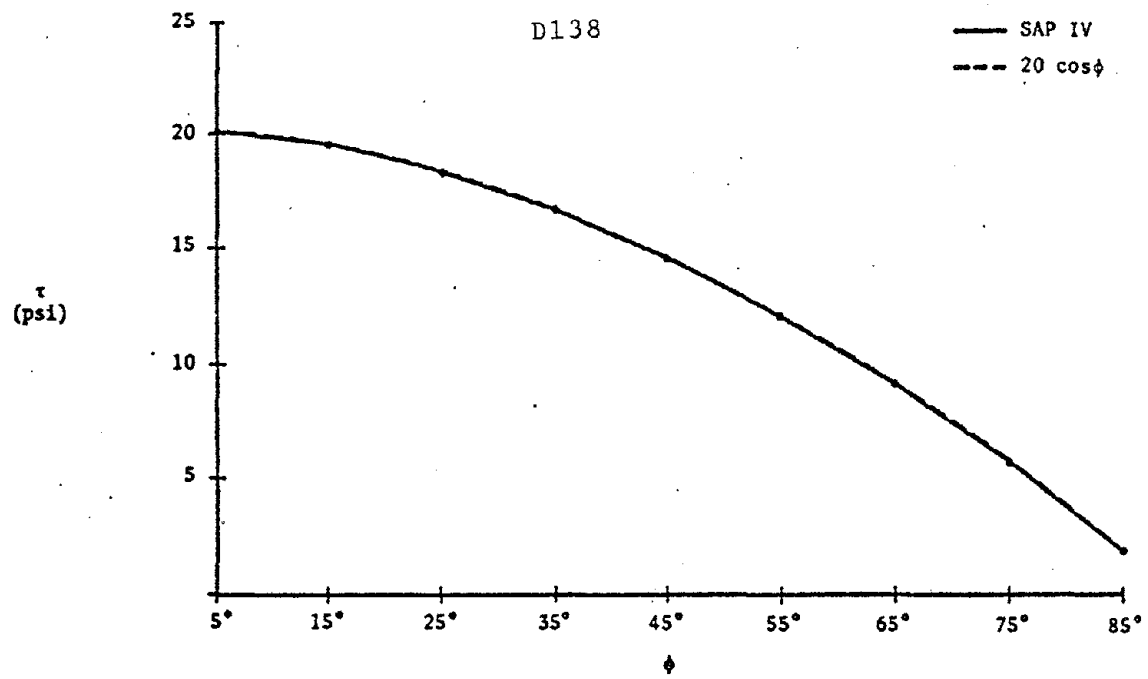


Figure 2.8

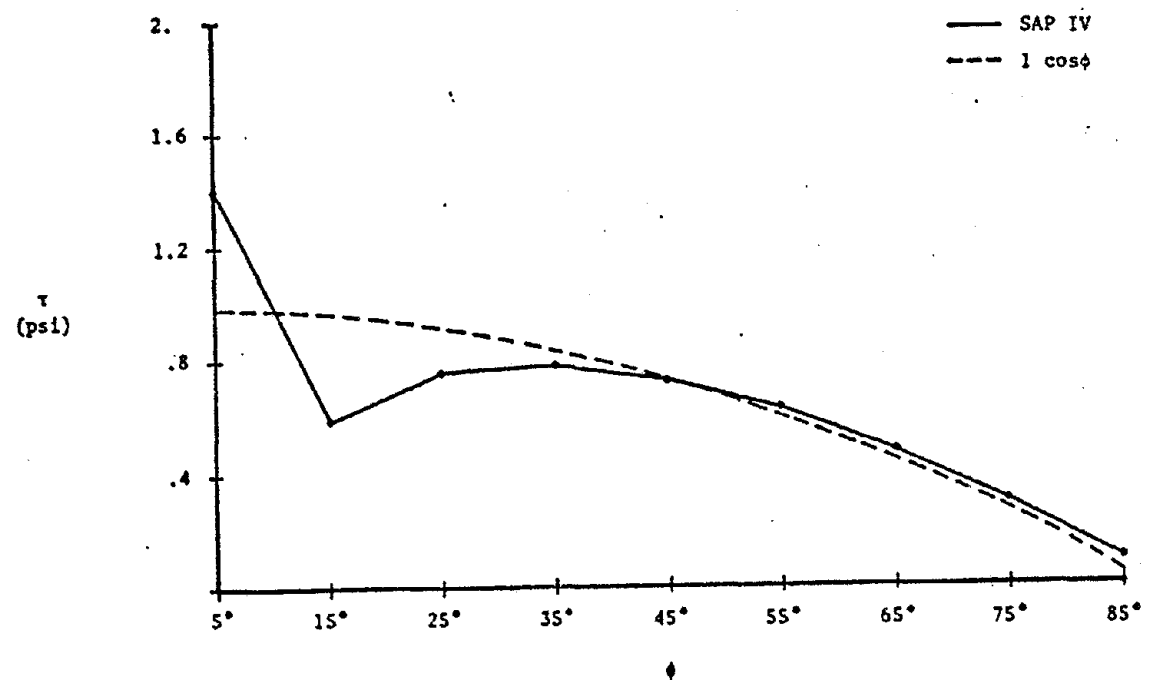


Figure 2.9 - $\phi = 0$ to 10° Stiff (E_2)

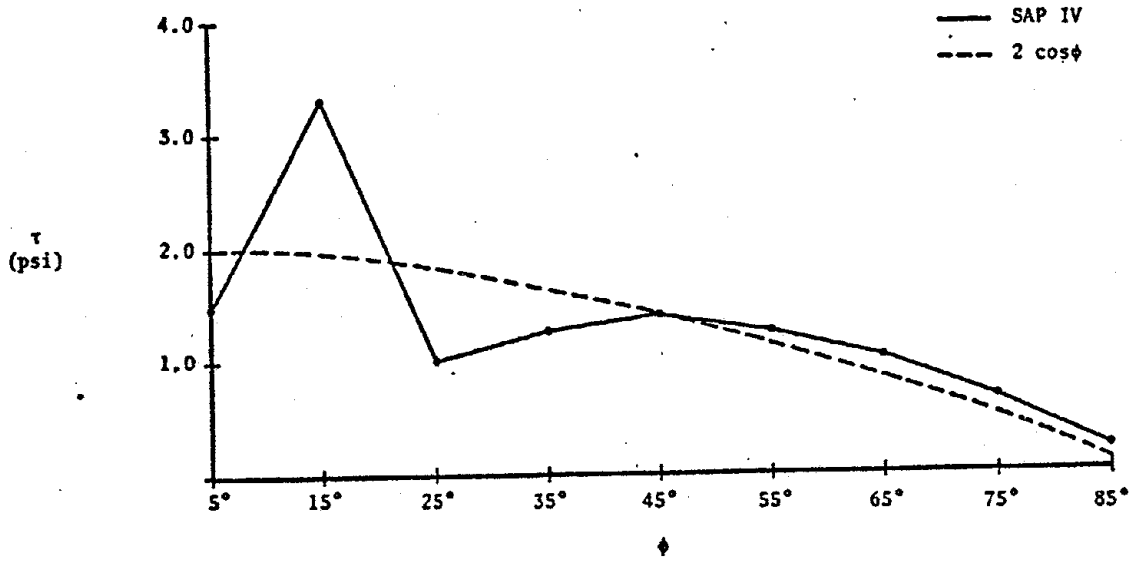


Figure 2.10 - $\phi = 0$ to 20° Stiff

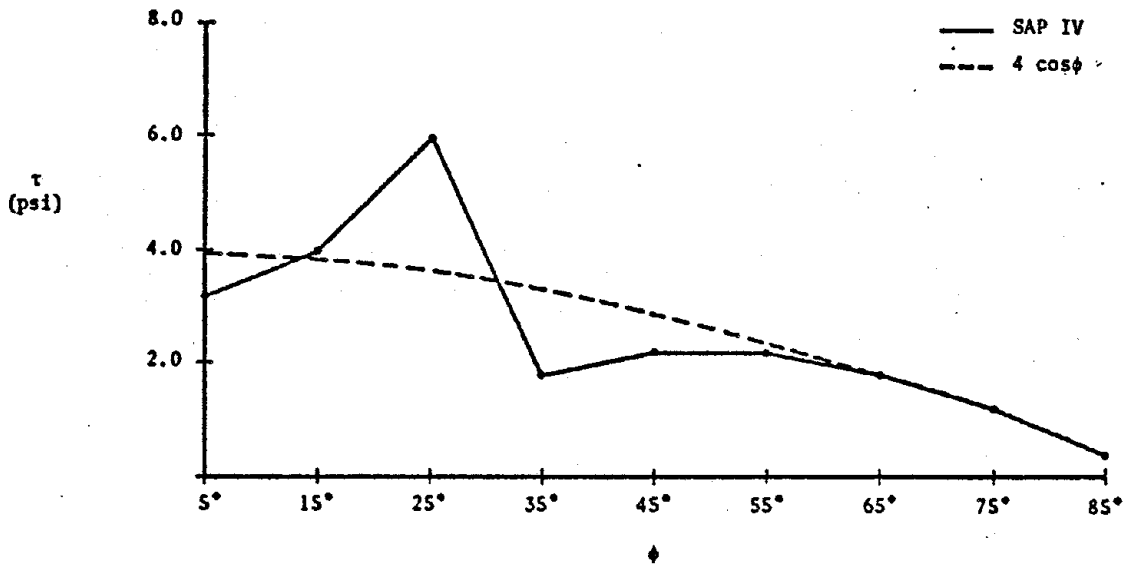


Figure 2.11 - $\phi = 0$ to 30° Stiff

D140

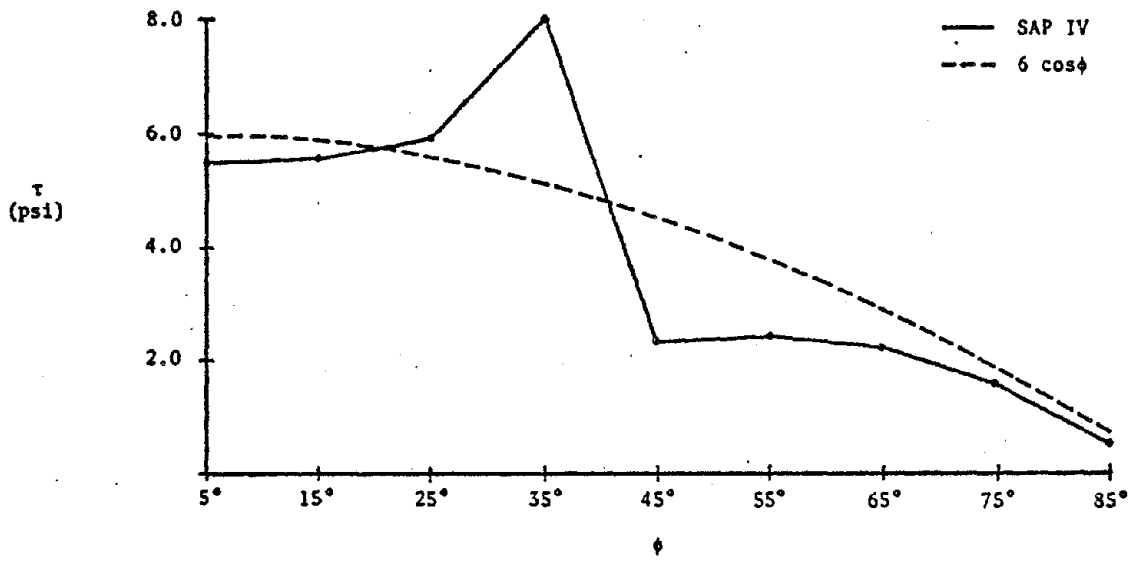


Figure 2.12 - $\phi = 0$ to 40° Stiff

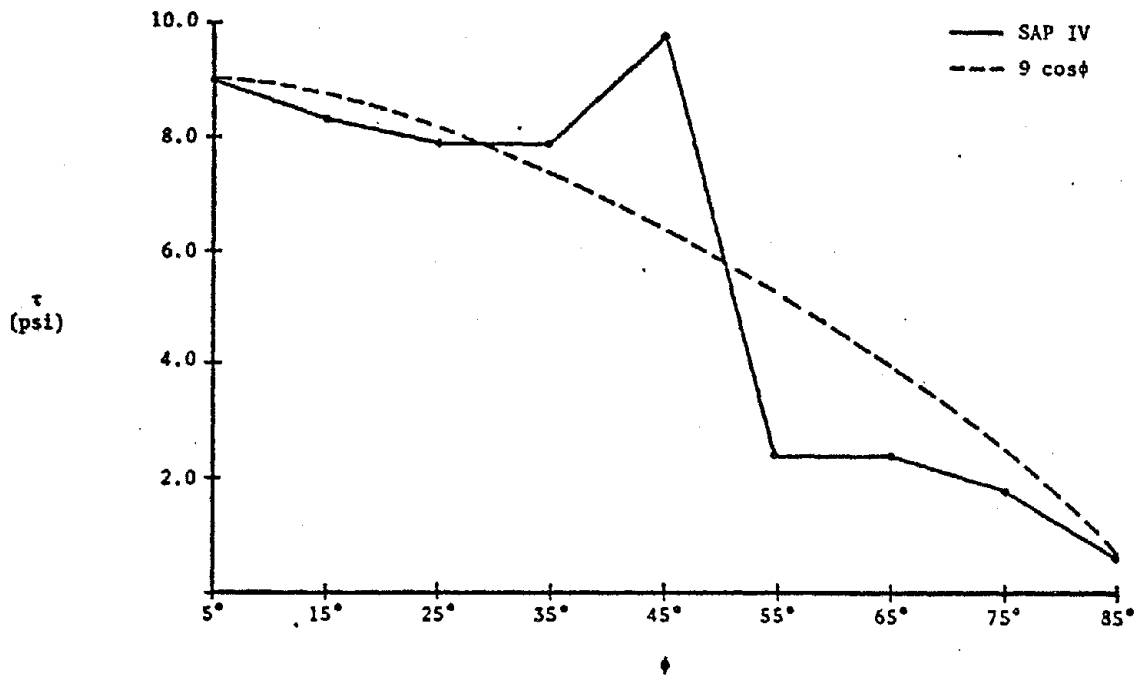


Figure 2.13 - $\phi = 0$ to 50° Stiff

D141

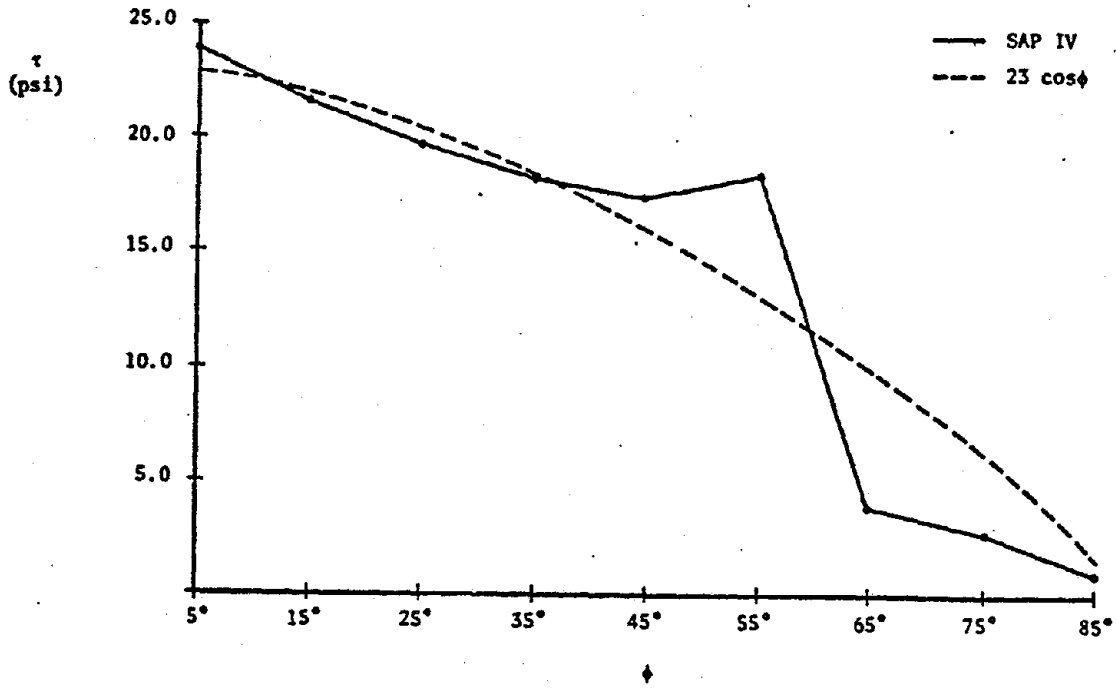


Figure 2.14 - $\phi = 0$ to 60° Stiff

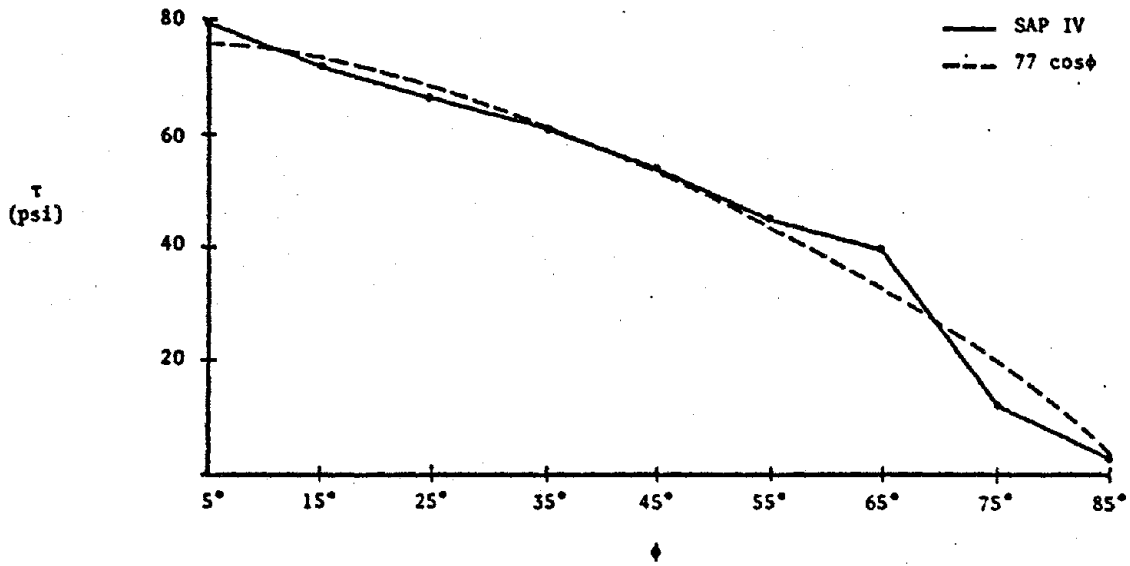


Figure 2.15 - $\phi = 0$ to 70° Stiff

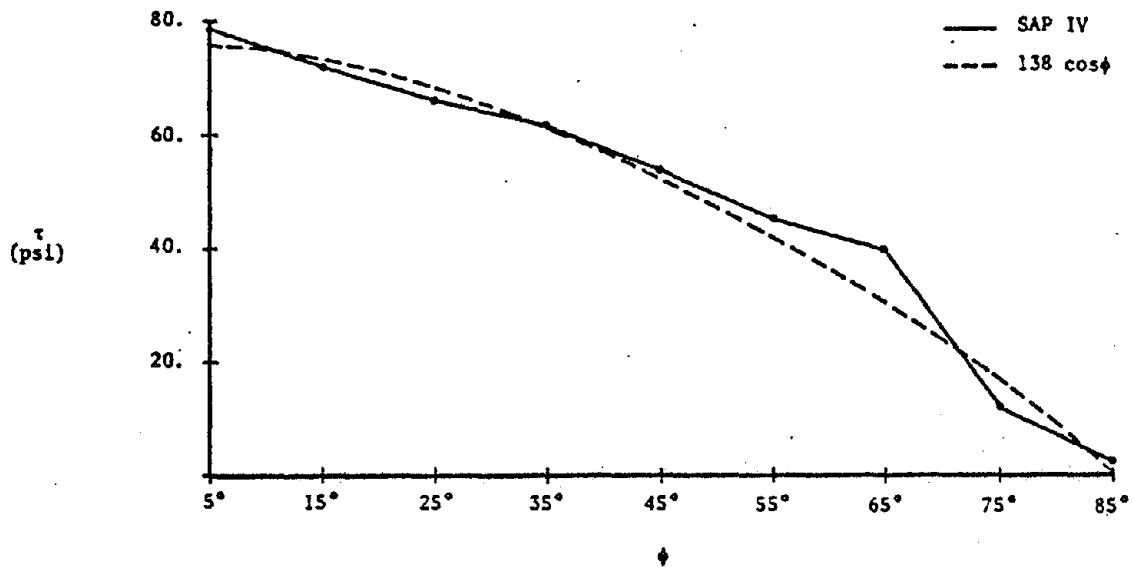


Figure 2.16 - $\phi = 0$ to 80° Stiff

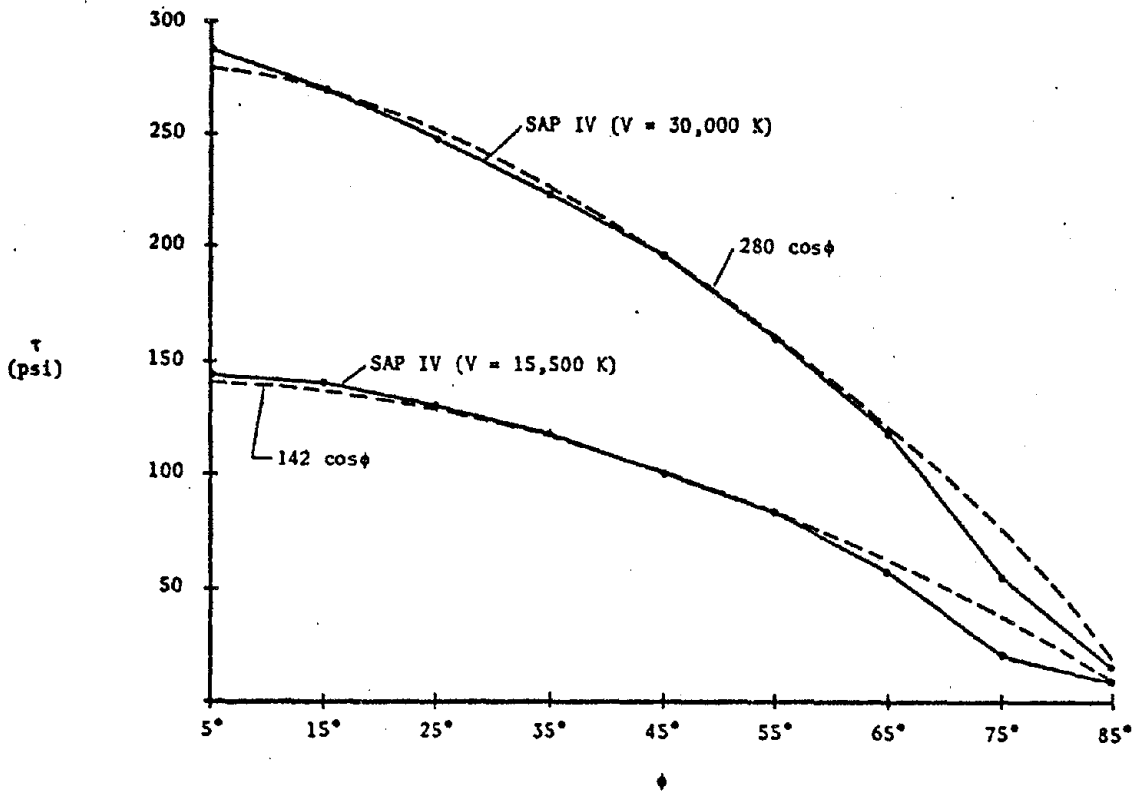


Figure 2.17 - Total Stresses for $V = 30,000$ K and $V = 15,555$ K

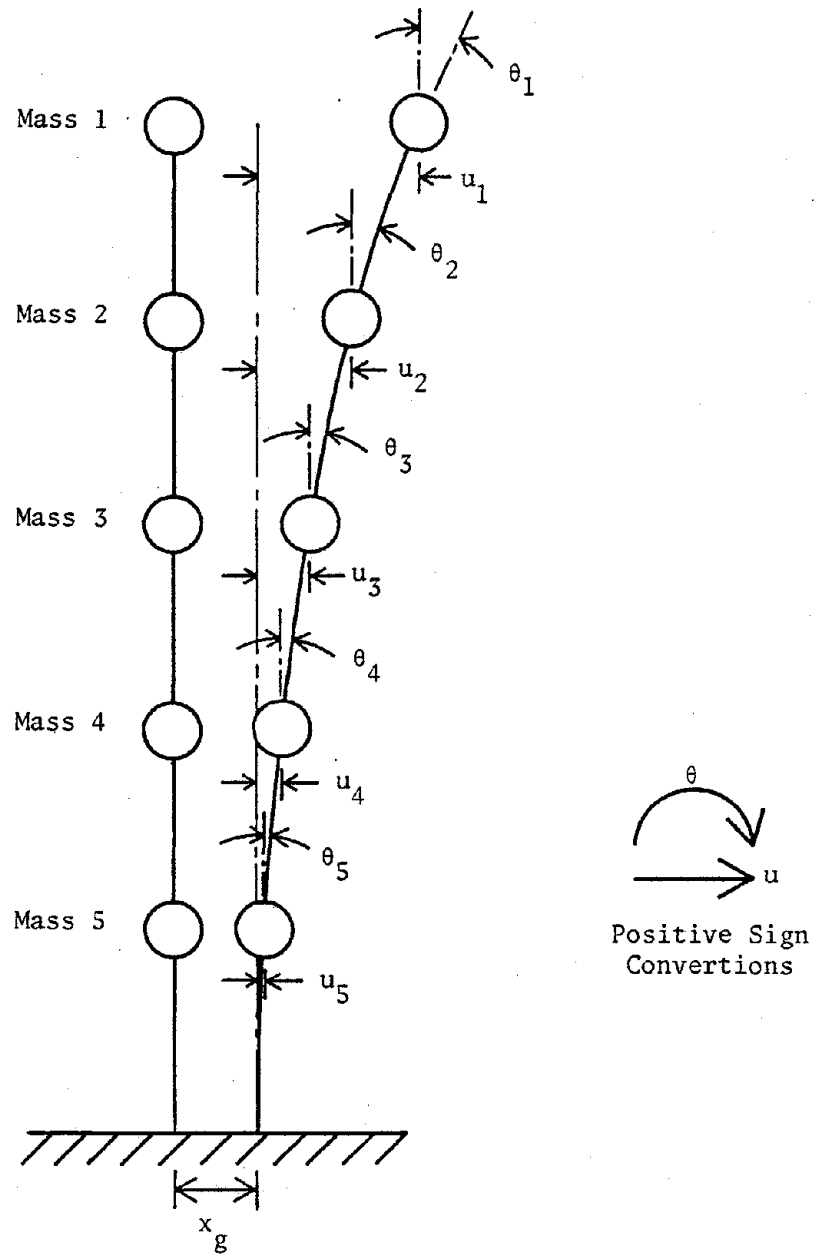
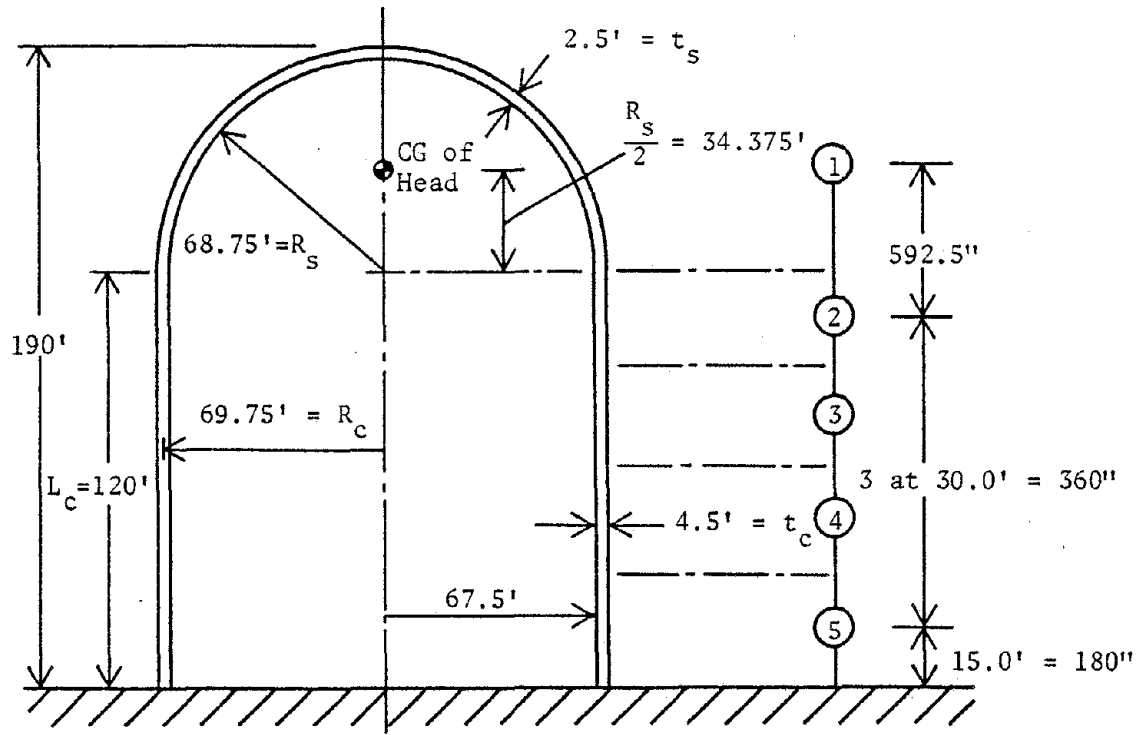


Figure 3.1 - The Structural Degrees of Freedom



a. Actual Containment Vessel

b. Lumped Mass Model

Node	Mass (k-sec ² /in)	Moment of Inertia (in ⁴)	Mass Moment (k-sec ² -in)	Shear Area (in ²)
1	28.822	6.7064×10^{10}	8.174×10^6	97,270
2	22.967	9.9476×10^{10}	8.293×10^6	142,000
3	22.967	9.9476×10^{10}	8.293×10^6	142,000
4	22.967	9.9476×10^{10}	8.293×10^6	142,000
5	22.967	9.9476×10^{10}	8.293×10^6	142,000

Figure 3.2

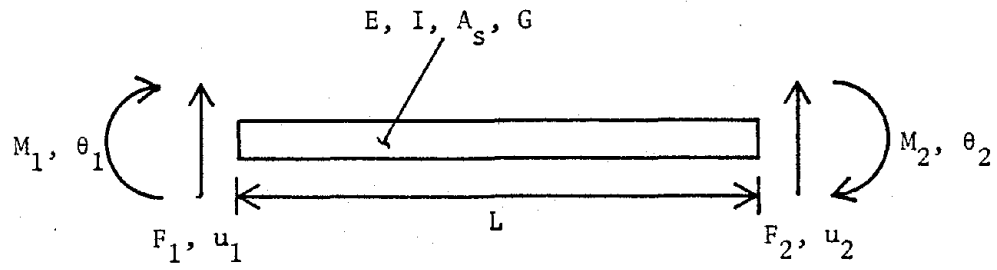


Figure 3.3 - Beam Element

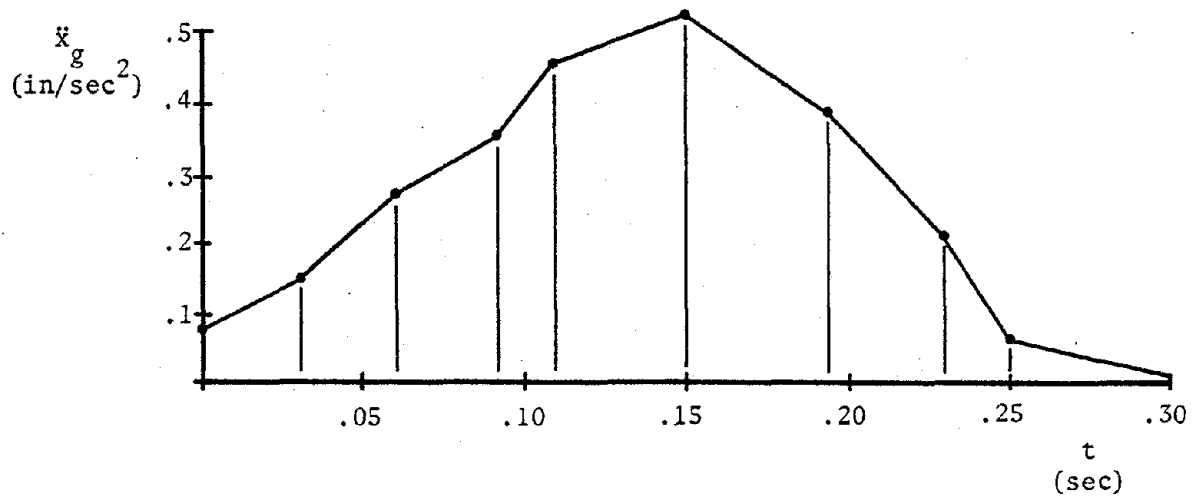


Figure 3.4 - Test Earthquake

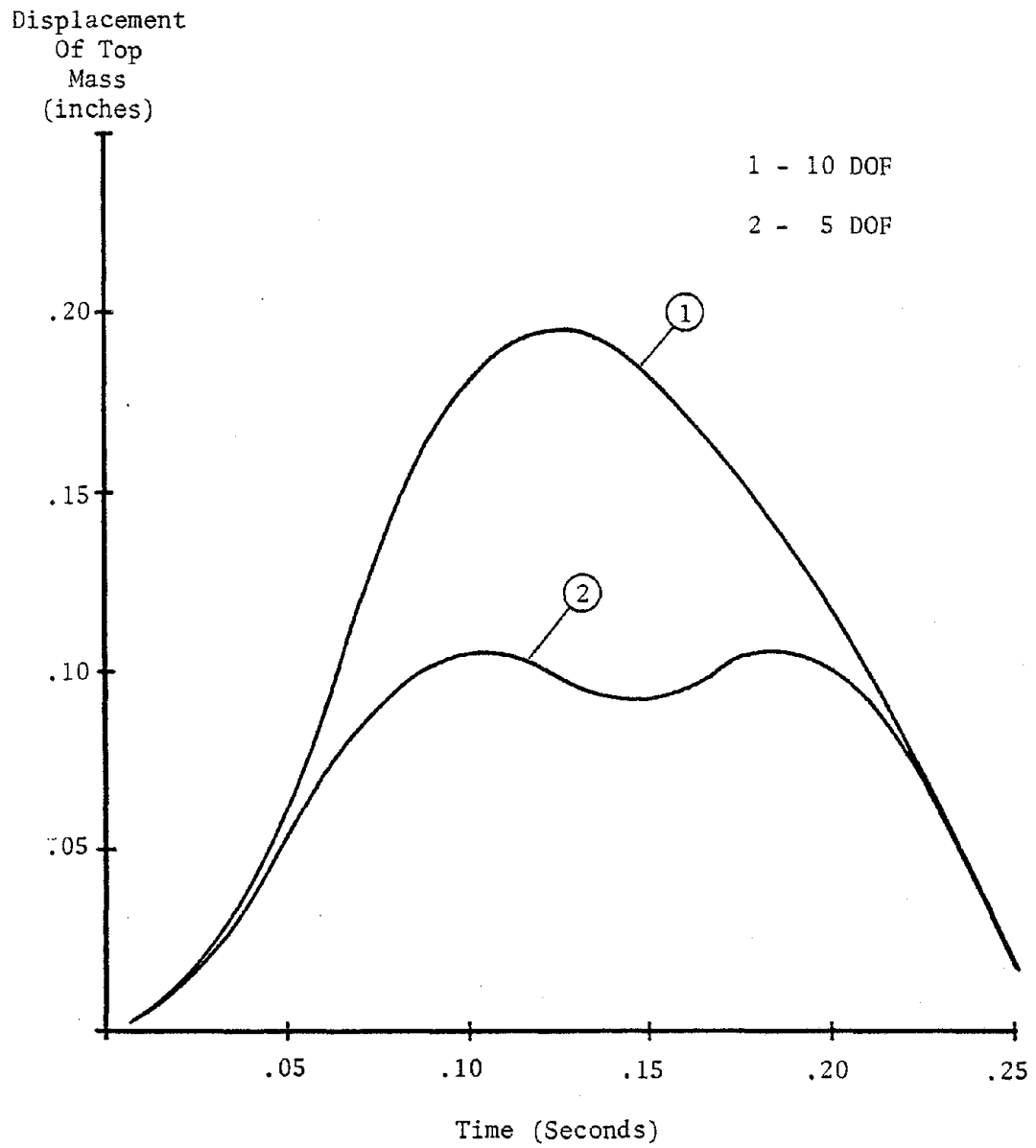


Figure 3.5

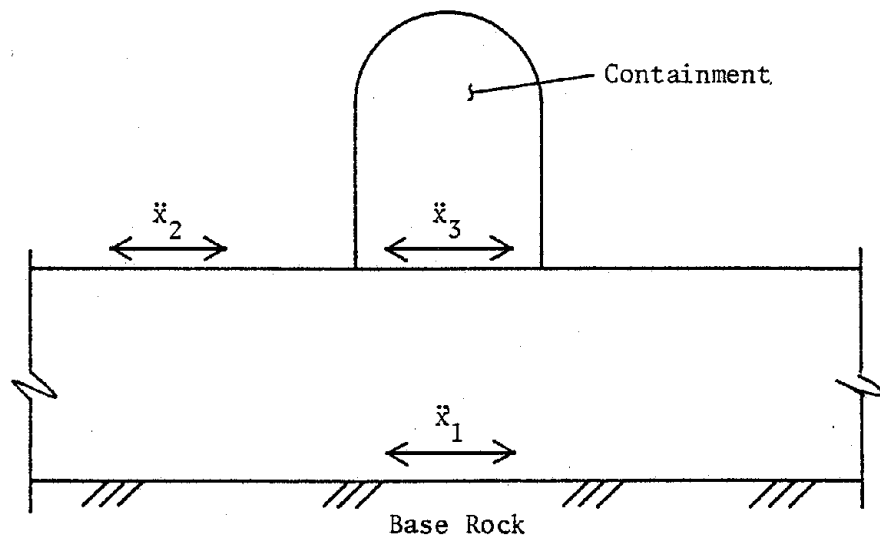


Figure 4.1

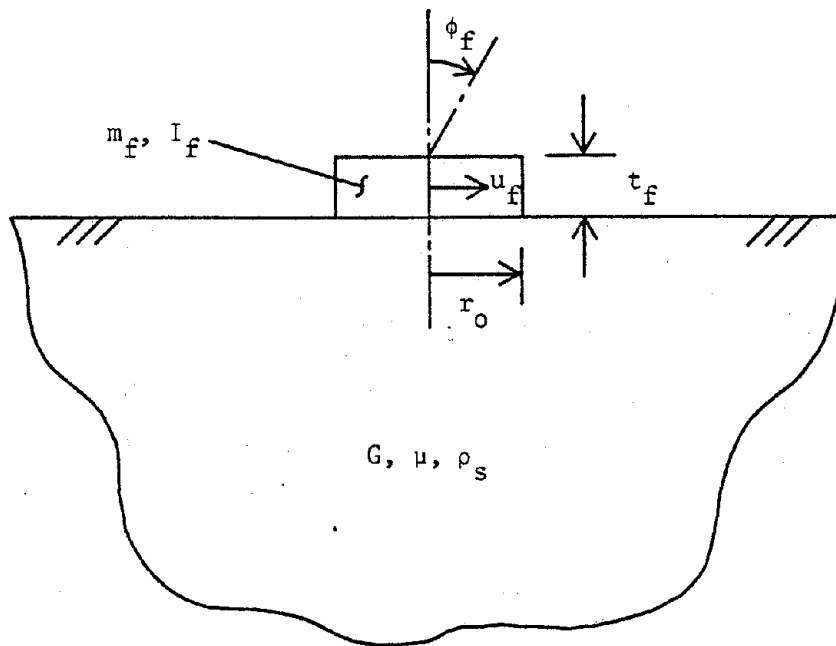


Figure 4.2

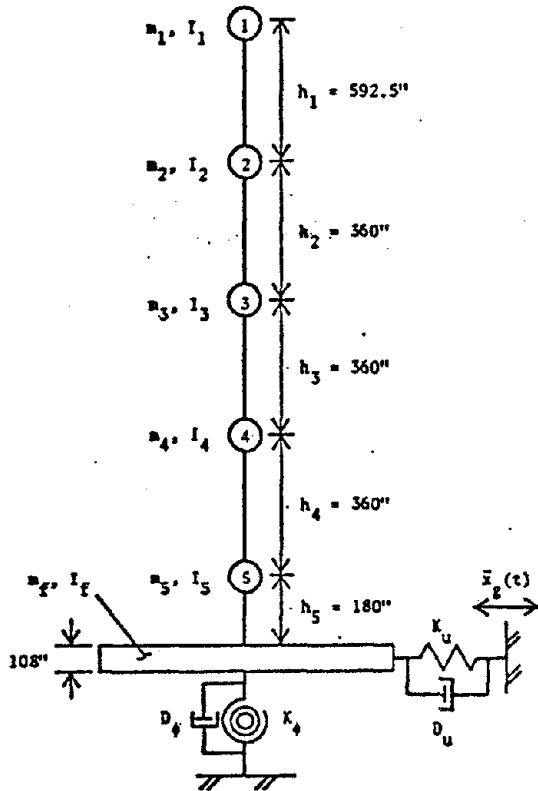


Figure 4.3 - Containment Model
Including SSI

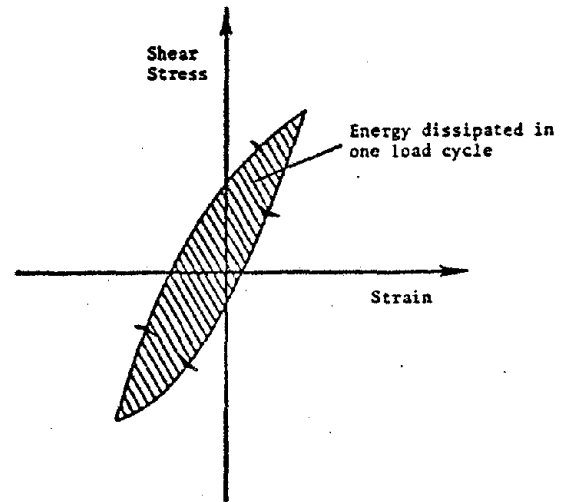


Figure 4.4 - Hysteresis In Soils

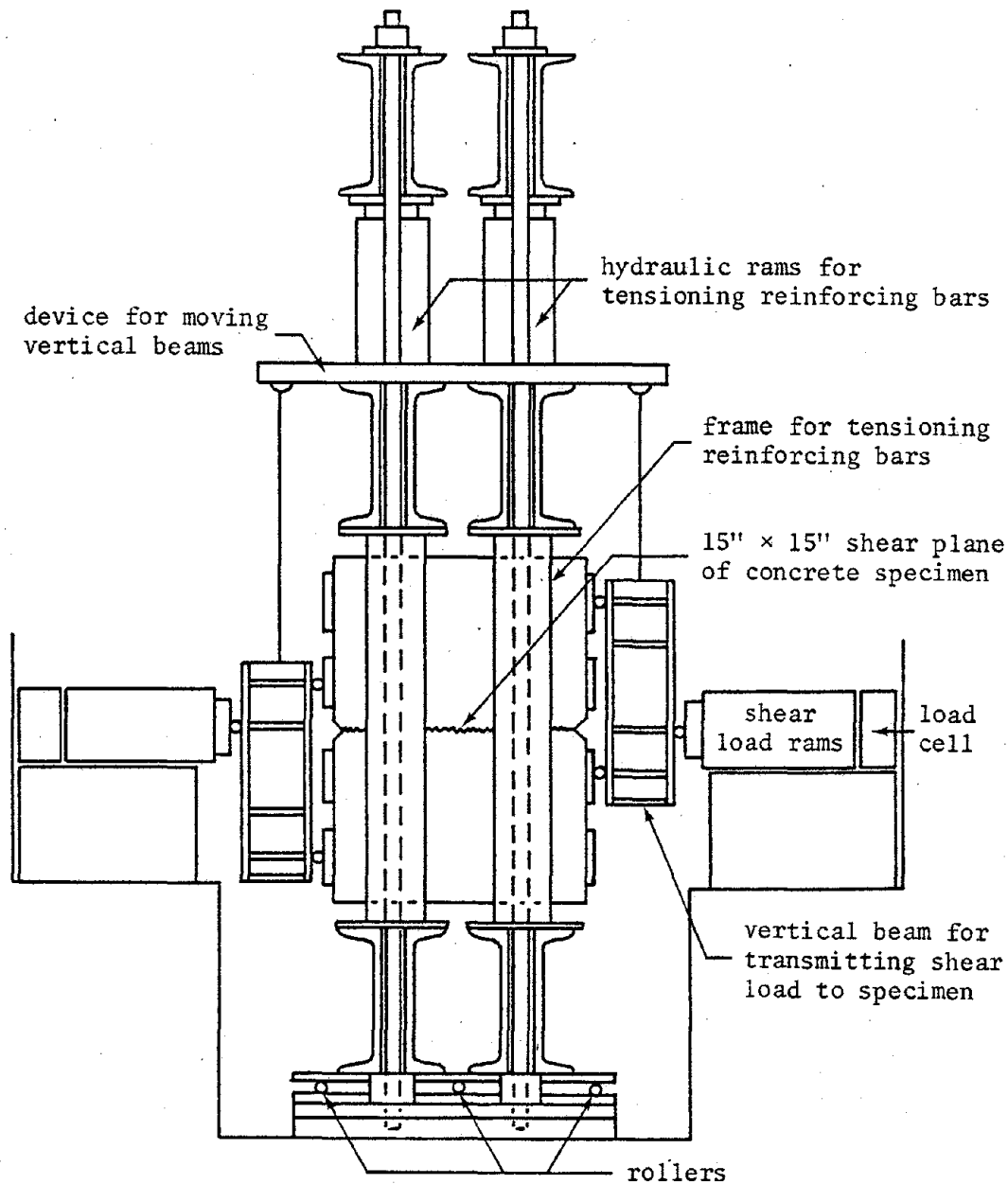


Figure 5.1 - Test Specimen (reinforced with 4 #9 bars)

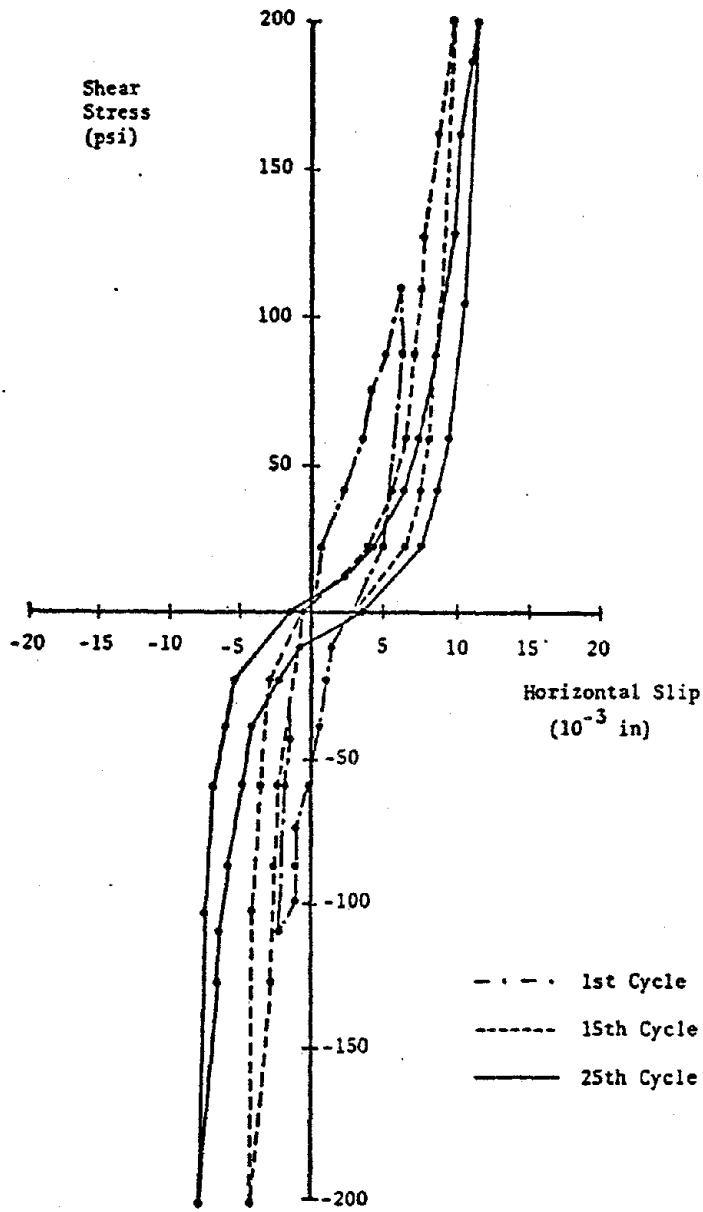


Figure 5.2 - Shear Stress vs. Horizontal Slip

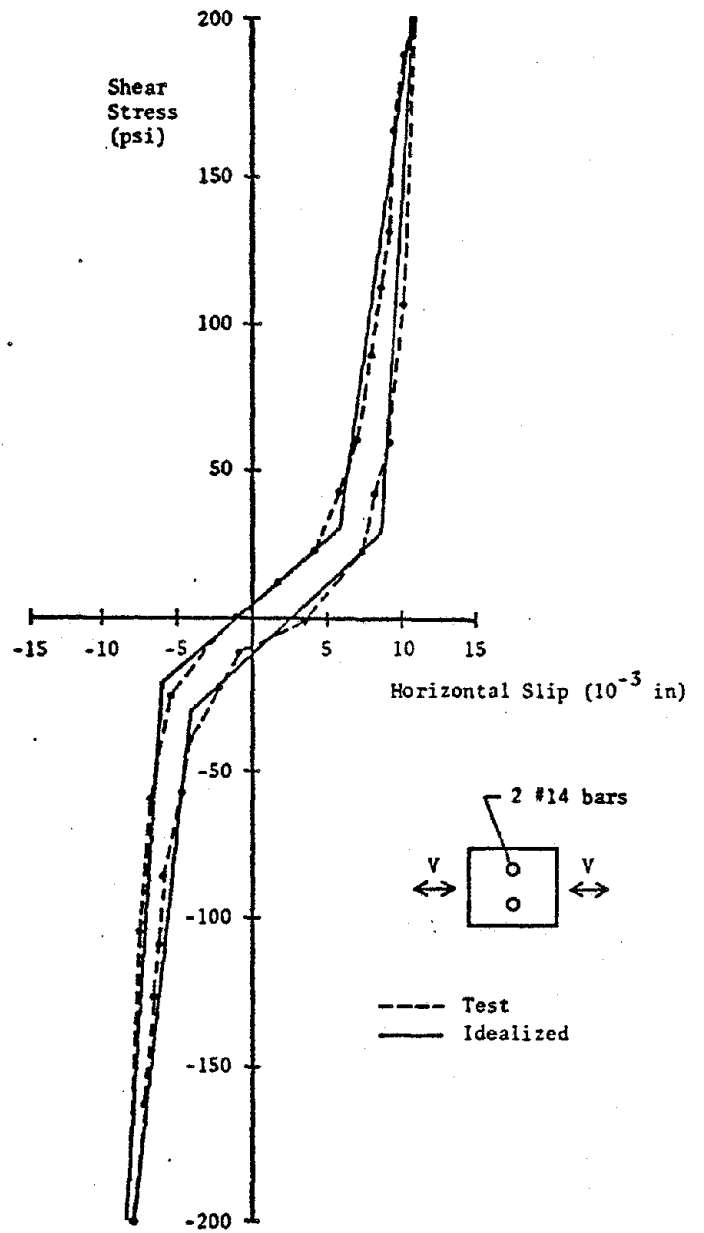


Figure 5.3 - Shear Stress vs. Horizontal Slip, 25th Cycle

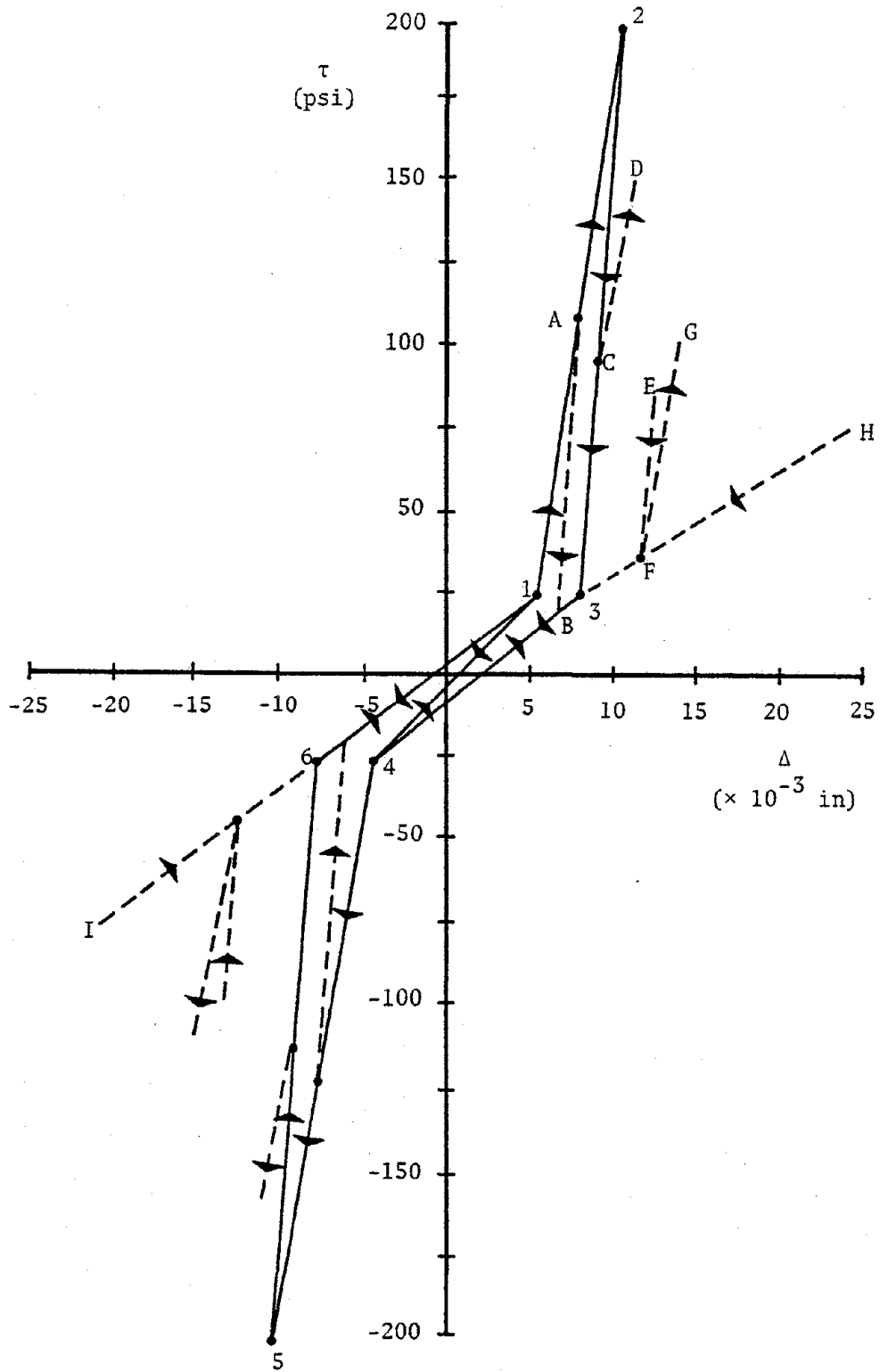


Figure 5.4 - Idealization of the 25th Cycle

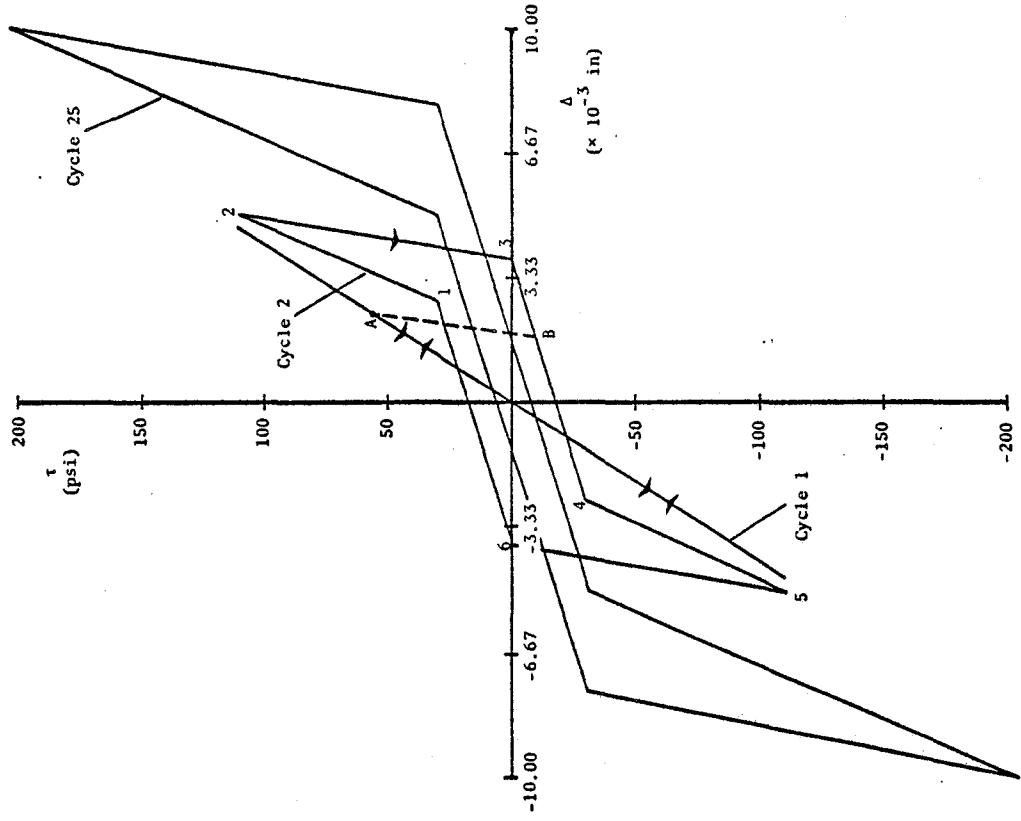


Figure 5.6

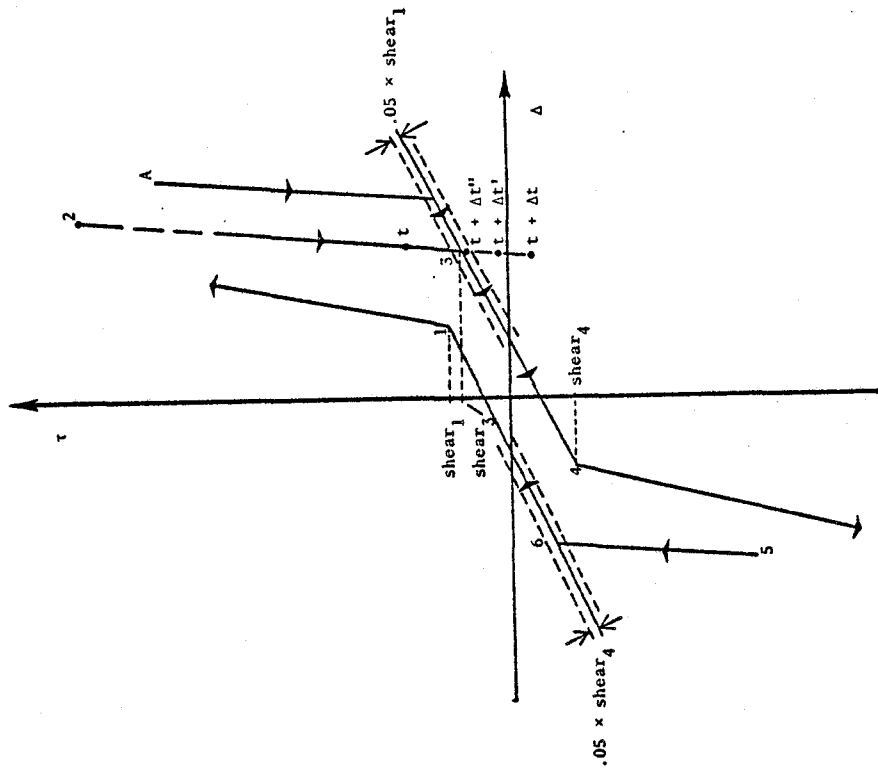


Figure 5.5

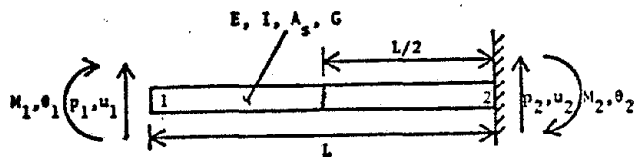


Figure 5.7 - Cracked Beam Element

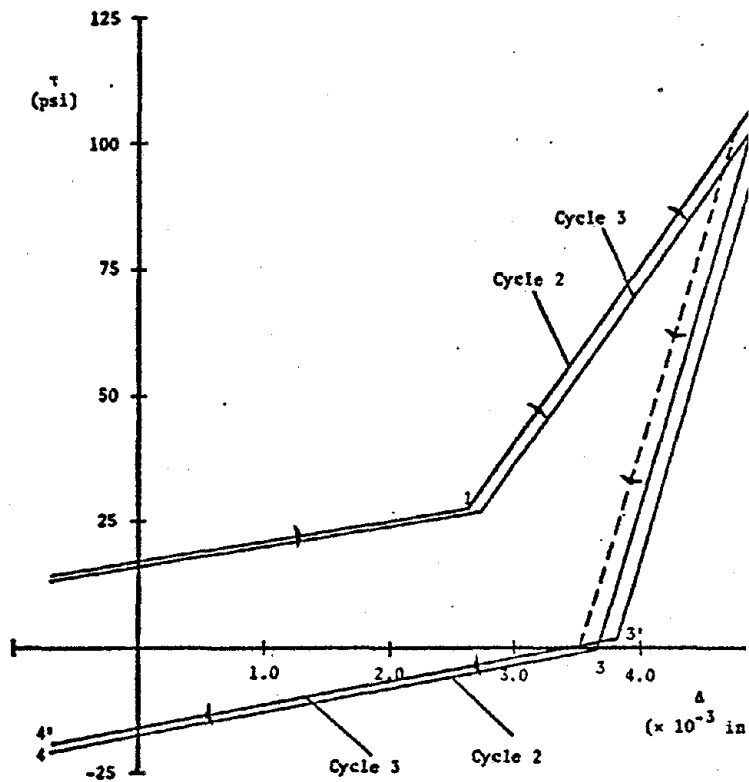


Figure 5.8

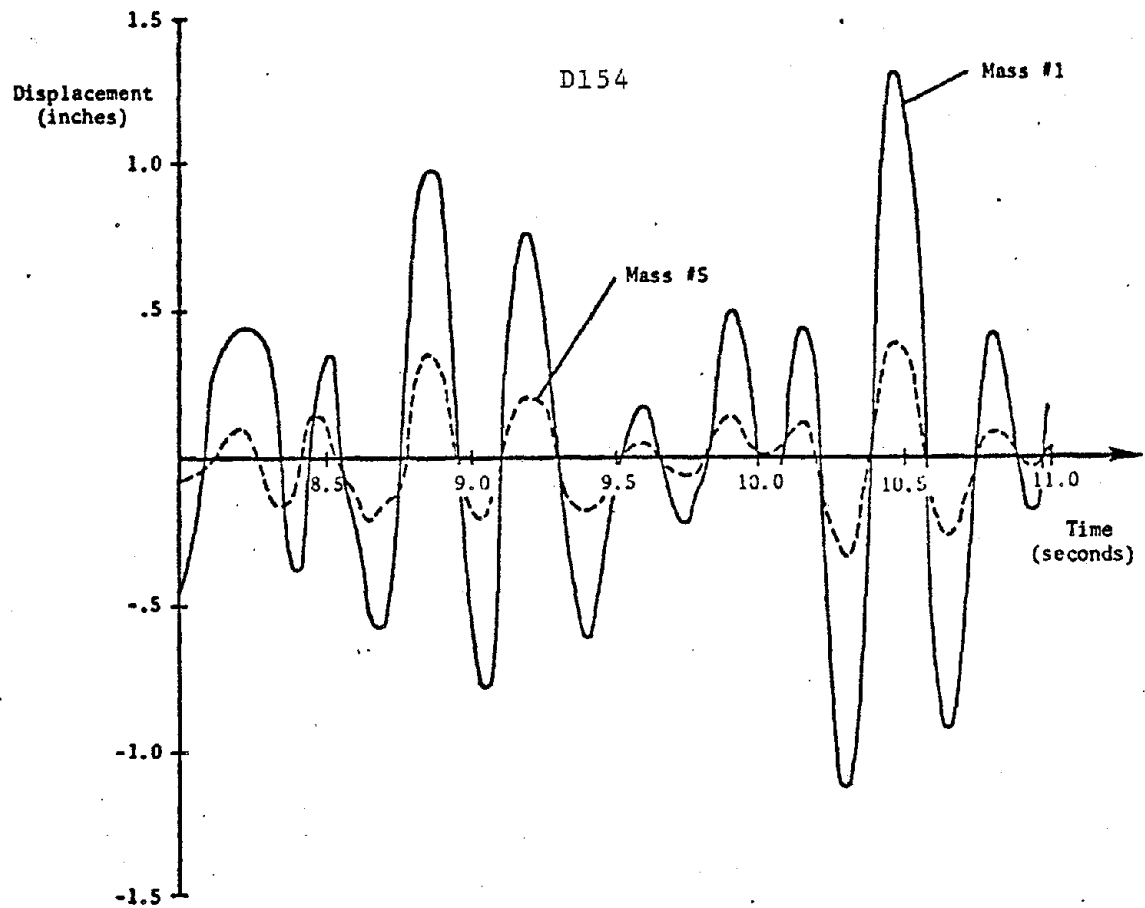


Figure 5.9 - Displacement vs. Time for Uncracked Containment

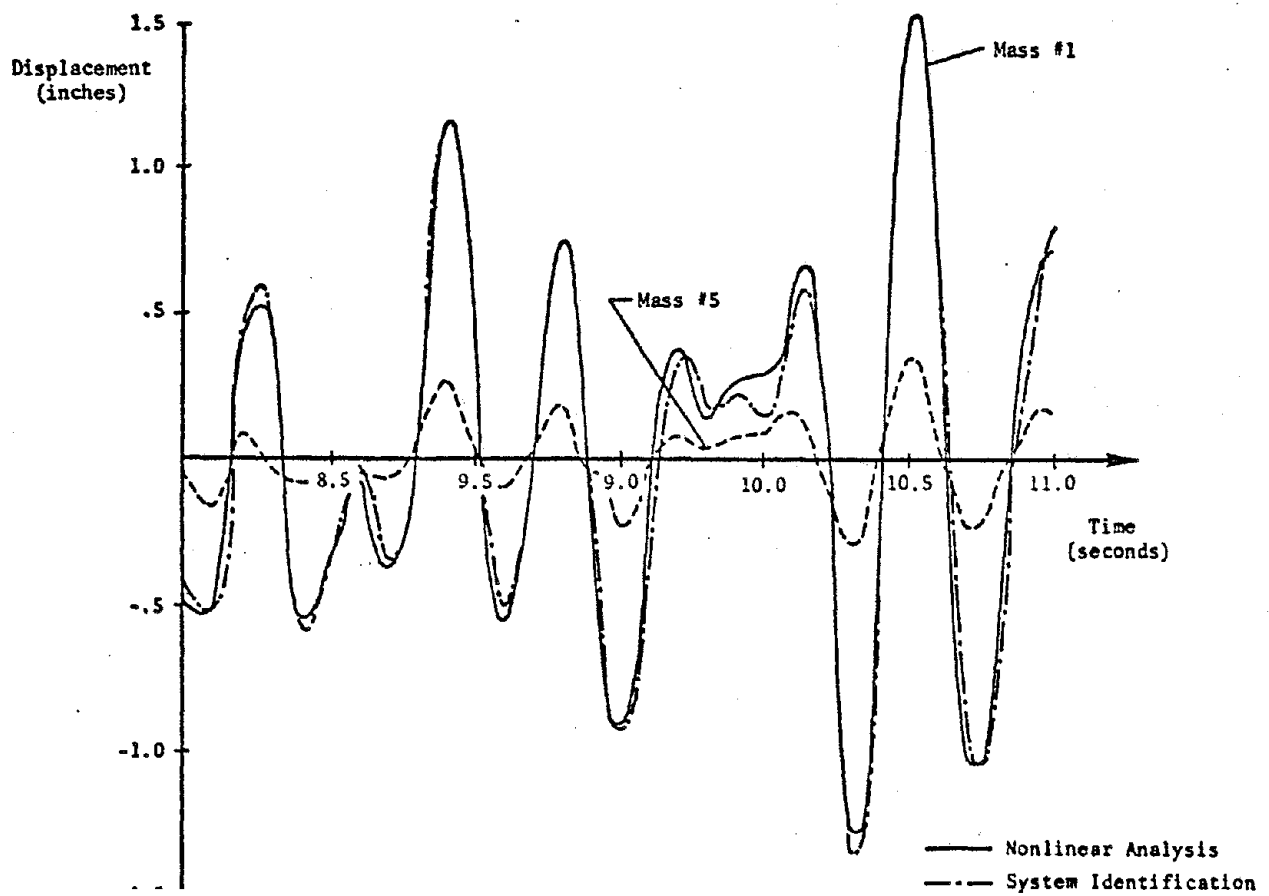


Figure 5.10 - Displacement vs. Time for Medium Soil Stiffness

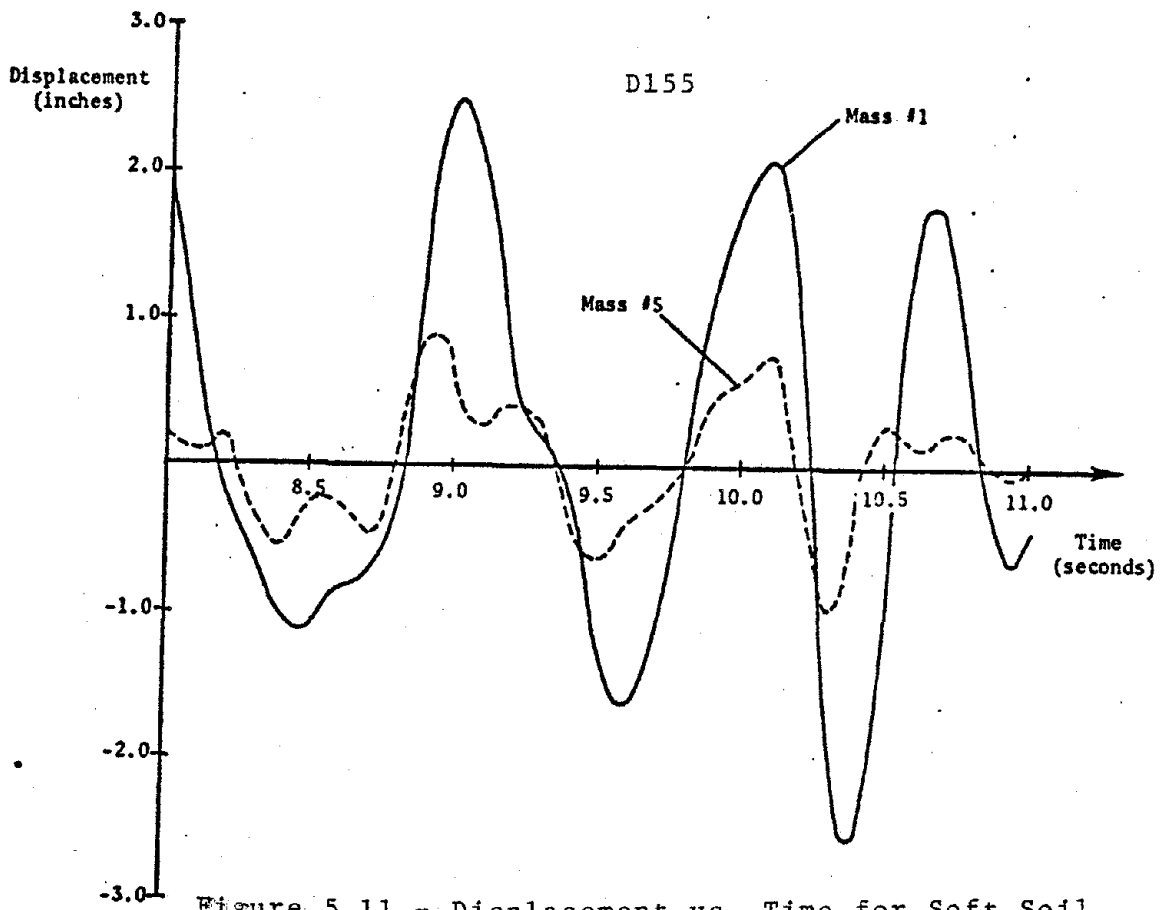


Figure 5.11 - Displacement vs. Time for Soft Soil

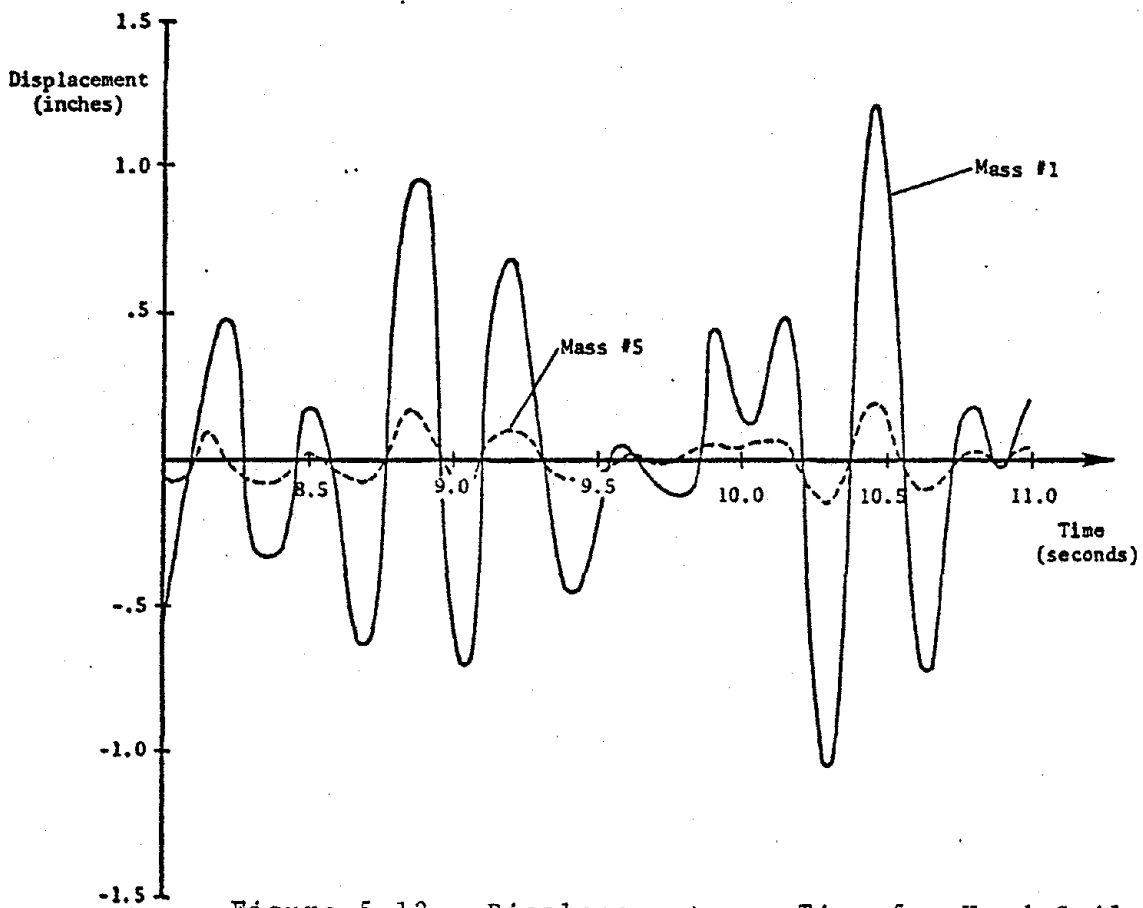


Figure 5.12 - Displacement vs. Time for Hard Soil

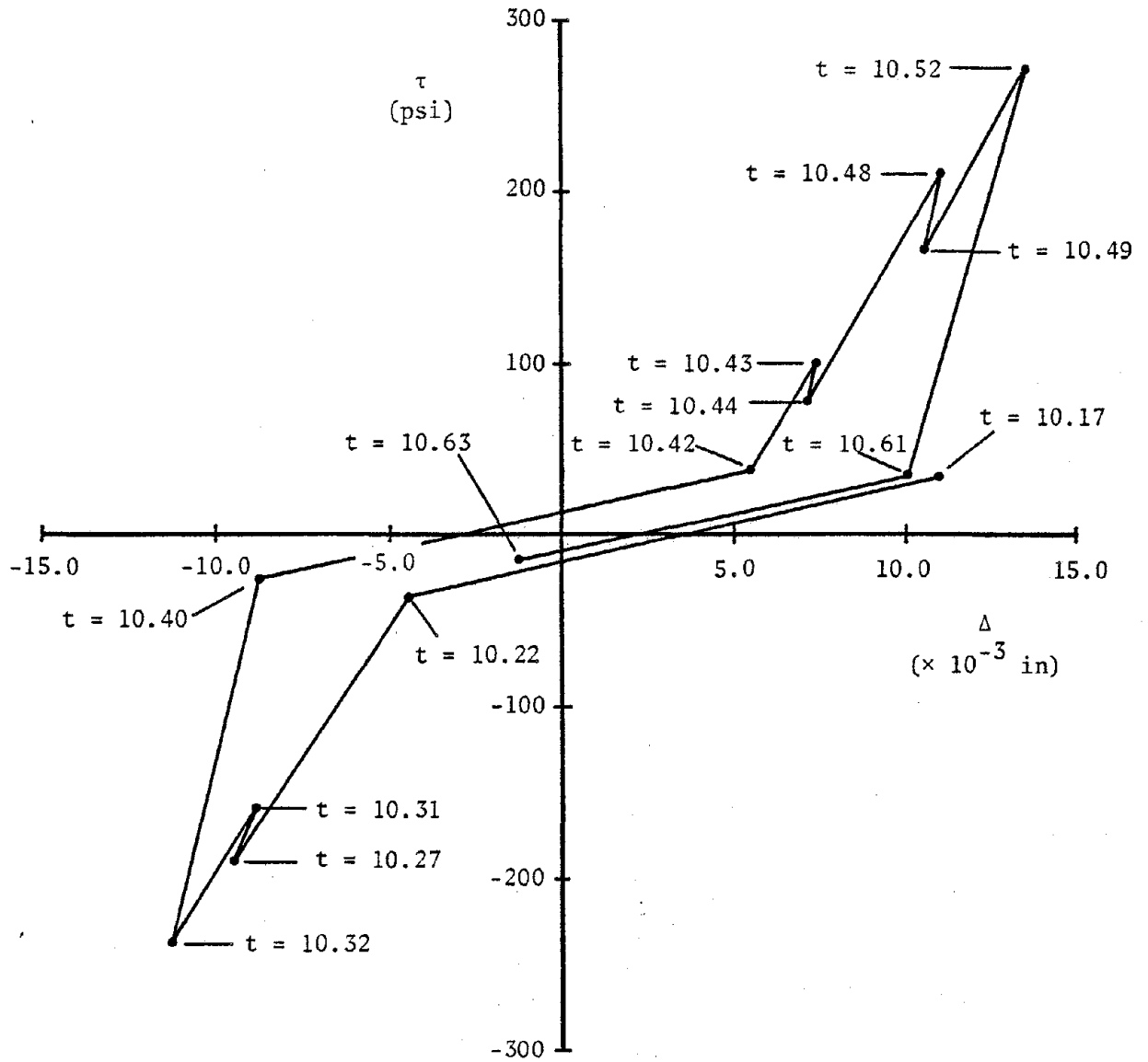


Figure 5.13 - Shear Stress Vs. Crack Slip for Medium Soil Stiffness

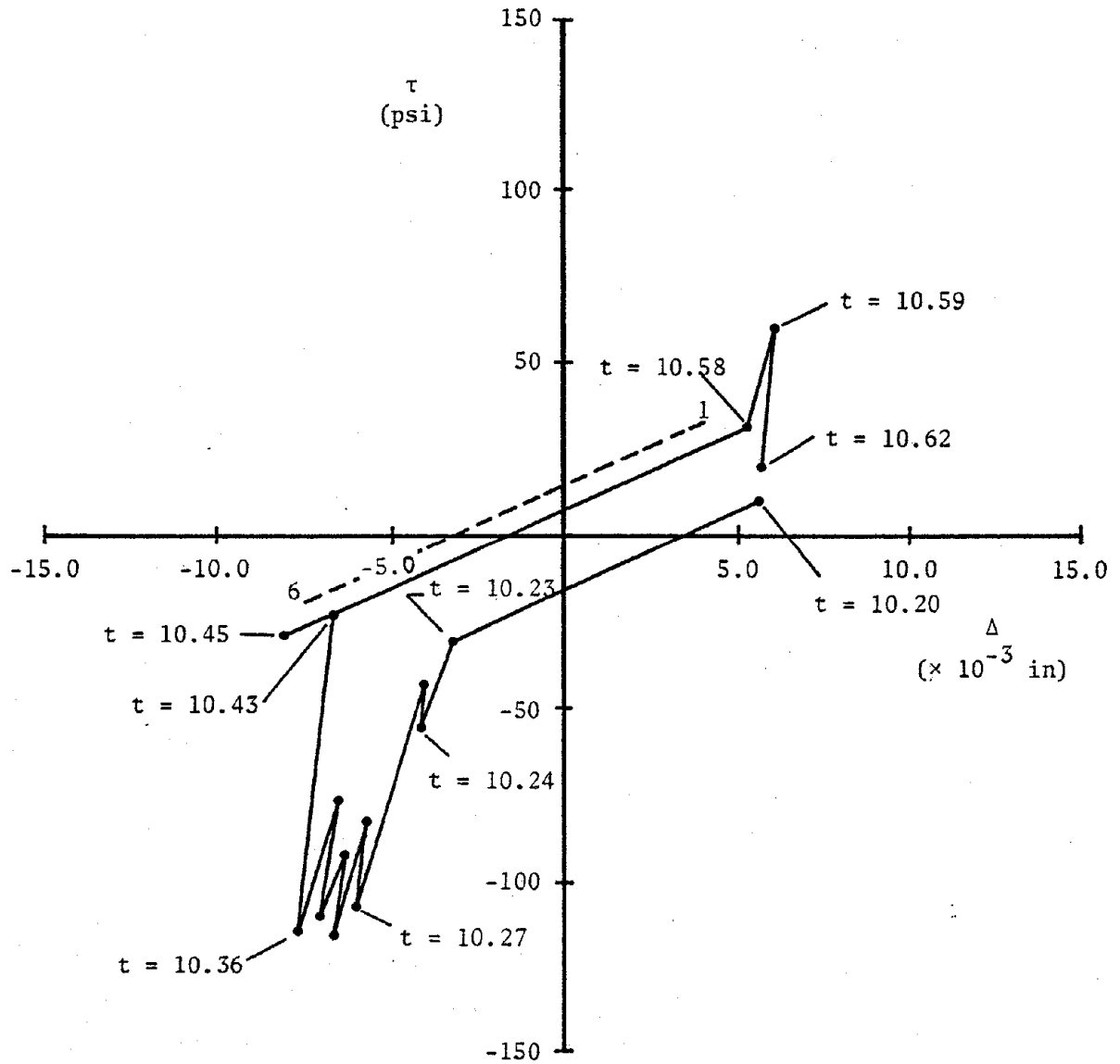


Figure 5.14 - Shear Stress Vs. Crack Slip for Soft Soil

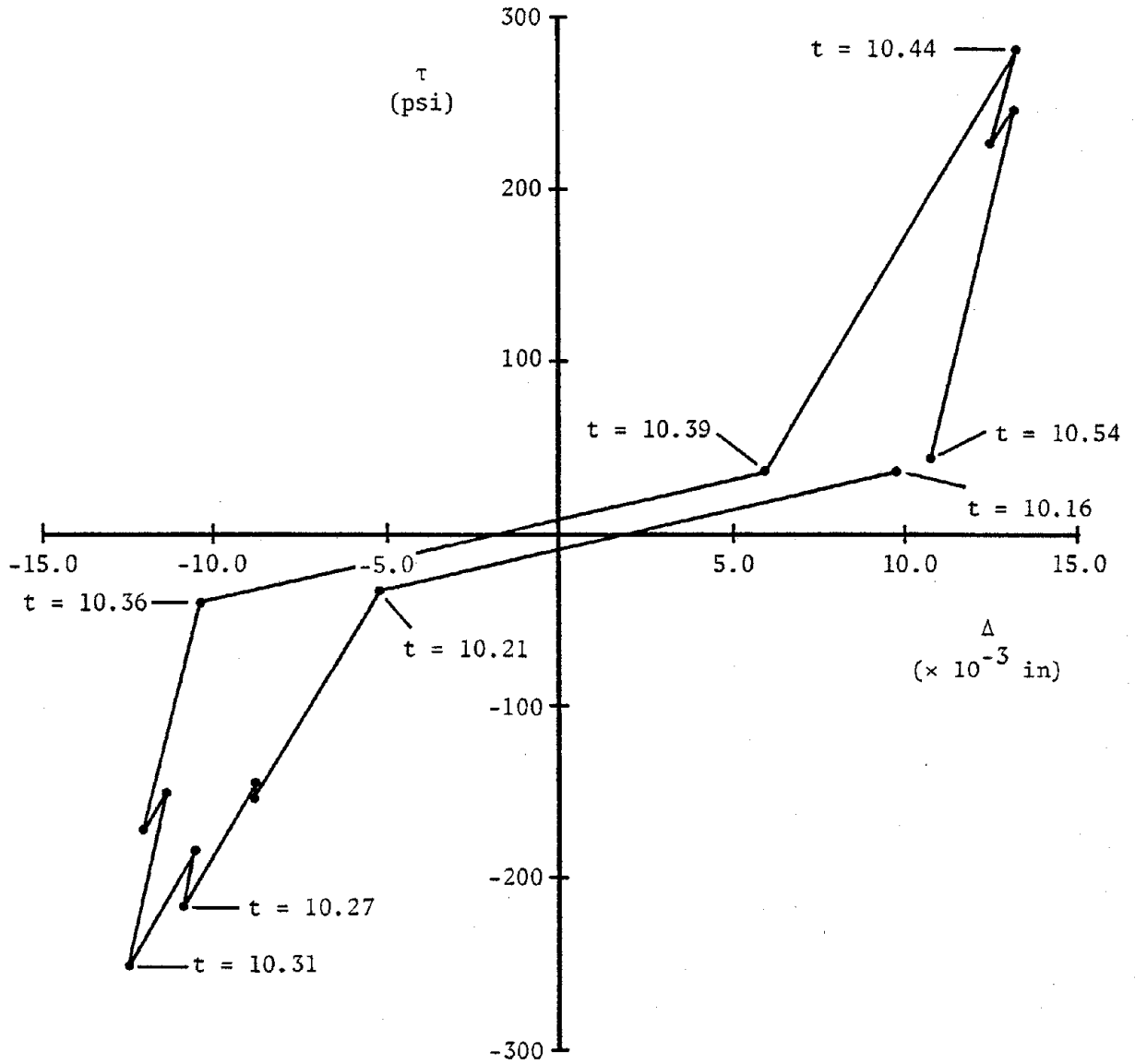


Figure 5.15 - Shear Stress Vs. Crack Slip for Hard Soil

E. Ongoing Research

Experimental results for a series of shear transfer specimens are presented on pages E1-E10 in the form of a reprinted paper (Ref. 5). These results and others will be factored into a comprehensive model for shear transfer in a pending publication (Ref. 6).

Interface Shear Transfer and Dowel Action in
Cracked Reinforced Concrete Subject to Cyclic Shear

by Rafael Jimenez¹, Philip Perdikaris²,
Peter Gergely³, M. ASCE, and Richard White⁴, M. ASCE

Introduction

Seismic shear transfer in thick reinforced concrete sections that are precracked by tensile stresses in the reinforcement is treated in this paper. This situation arises in various structures, including reinforced concrete secondary nuclear containment structures where a combined internal pressurization and seismic loading is considered in design. The pressurization results in a large number of small cracks, normally horizontal and vertical in the typical domed cylinder containment, and seismic action produces membrane shears that must be transmitted across these cracks.

Experimental results are reported for several specimens with five different bar sizes (#4, #6, #7, #9 and #14). Each specimen was loaded in fully reversing non-dynamic cyclic shear to simulate the effects of seismic action. Shear is transferred across cracks by two separate mechanisms: dowel action (DA), and interface shear transfer (IST) along the cracked concrete surfaces. Selected specimens were built with greased plates at the crack location to eliminate the IST component of shear transfer; hence these specimens (with #4, #6, and #9 bars) transmit shear by dowel action alone. Most specimens had independent external tensile loads applied to the bars during the shear loading.

Measured response includes shear slip vs. shear load, growth of crack width with cycling, degradation characteristics of IST and dowel action, bending effects in the reinforcing, and splitting tendencies produced by combined dowel action and axial tension in the reinforcing.

Experiments involving #7 and larger bars were conducted

¹Graduate Research Assistant, Department of Structural Engineering, Cornell University, Ithaca, New York 14853.

²Graduate Research Assistant, Department of Structural Engineering, Cornell University, Ithaca, New York 14853

³Professor of Struct. Engrg., Department of Structural Engineering, Cornell University, Ithaca, New York 14853

⁴Professor of Struct. Engrg., Department of Structural Engineering, Cornell University, Ithaca, New York 14853

on specimens with shearing areas on the order of several hundred square inches, while the #4 and #6 bar tests were done at a small scale to study the feasibility of using a new specimen design for large scale experiments. Additional experiments with #14 bars are currently underway at Cornell University and the #14 bar results reported here should be considered as preliminary.

This experimental program is part of a continuing investigation into seismic shear transfer in thick-walled concrete structures, sponsored currently by the National Science Foundation and the Nuclear Regulatory Commission, and earlier by Stone and Webster Engineering Corporation and several of its clients. Previous papers have focused on the interface shear transfer mode alone, with no dowel action present, and on dynamic response of cracked containment structures that exhibit the typical nonlinear shear-slip behavior at cracks (Refs. 1-4). Results reported here are drawn from several reports and theses (Refs. 5-8). Studies are now beginning at Cornell on specimens subjected to combined biaxial tension and cyclic shear, with the first results scheduled for presentation at the Fall 1976 ASCE Conference Research Session.

Geometry, material properties, and loading histories for the test specimens are summarized in Table 1. Only typical specimens are included in this paper; full details are contained in the references.

Shear Transfer Mechanisms - General Comments

A brief general discussion of dowel action and interface shear transfer across slightly open cracks in reinforced concrete is in order prior to considering specific test results.

Transfer of shear by dowel action is dependent upon preventing major dowel cracking along the bar, or by controlling such cracks with transverse reinforcement. Before cracking, slippage along the shear transfer plane is produced by bending of the bar and by local deformation of the concrete under the very high local contact stresses. Bar bending stresses will be elastic at low dowel loads, but may become plastic as the dowel force increases. Hence, the critical physical parameters are the diameter and yield strength of the reinforcement, the tensile strength of the concrete under complex localized stress states and the stiffness of the concrete. Splitting tendencies are sharply influenced by bar size, concrete cover, ratio of dowel area to concrete shearing area, and presence of axial stress in the reinforcement. The degradation of dowel stiffness with cyclic shear is a complex function of these same variables and parameters.

Interface shear transfer (also called aggregate interlock) on the rough surfaces of the crack is a strong function of the initial crack width and of the degree of restraint that acts to prevent further opening of the crack.

In the first full cycle of shear loading the load-slip relation tends to be linear during loading. On subsequent cycles there is a steadily increasing "free slip" action at low shear stress levels, but once firm contact is made between the two surfaces, the stiffness is higher than in the first cycle. The overall effect is a nonlinear, hardening-type response with peak slips that grow at a decreasing rate with cycling. Over-riding (and frictional resistance) becomes more prevalent as cycling wears down the surfaces. As the shear displacement increases, the over-riding action causes the crack to widen, thereby increasing the forces in the restraining reinforcement across the crack, which in turn increases the frictional resistance. Interface shear transfer is documented in detail in Refs. 1 and 2.

Testing Procedure

All specimens involved the transfer of cyclic shear stresses across a precracked surface, subjected to an initial crack width. A schematic representation of the loads applied to the large scale specimens is given in Fig. 1. The shear plane, located at a crack-initiating groove cast into the specimen, was cracked by tensioning the reinforcing bars embedded in the concrete. The desired initial crack width was obtained by stressing the bars to a stress level determined from an axial stiffness test on the specimen after cracking. The shear stresses acting on the shear plane were reversed by shifting the position of the (+) loads to that indicated by (-) loads. Most specimens were cycled for approximately 25 cycles, of which cycles 1, 15, and 25 were done incrementally for detailed measurements of horizontal slip, crack width, and bar strains. Axial stiffness tests were conducted at the end of each test when possible.

Slip and changes in crack width at the shear plane were measured with dial gages. Axial load in the reinforcement was measured with external strain gages. The large scale specimens also had internal strain gages on the reinforcement, located 1 in. from the shear plane.

Each specimen is assigned an identifying number as well as a code that identifies the major parameters; e.g. (4 #7-48-IST+DA) signifies a specimen with 4 #7 reinforcing bars stressed to 48 ksi tension with shear transferred by both interface shear transfer (IST) and dowel action (DA). Typical results given are shear slip and change in crack width at the shear plane as functions of cycling and shear stress. Failure modes are also presented.

Test Results

Small Scale Specimens

The small scale specimen geometry was a double-H shape (see Fig. 2) with 15 in² on each shear plane. Only #4 and #6 bars were used. Dowel action specimens had thin greased

plates at the shear plane to eliminate IST.

Specimen 1 (1#4-0-DA) had 15 cycles of shear load at +150 psi on the shearing area (+11.25 ksi on the dowel area) and 10 additional cycles at +180 psi (13.5 ksi), with response as given in Fig. 3. The first cycle loading in each direction shows a slightly decreasing stiffness at high load. This must be due to localized concrete failure near the shear plane under a complex state of stress. The peak shear slip stabilized after 10 cycles at +150 psi. The higher load level of +180 psi produced increasing slips that had not stabilized after 10 cycles.

Specimen 2 (1#4-25/50-DA) shows the effects of applied tension on dowel action. The bar was tensioned to $f_t = 25$ ksi prior to applying 15 cycles of shear stress at +150 psi (11.25 ksi in the bar). Slip values were more than double those of Specimen 1 (see Fig. 4), and both the slip and crack width increased by 50% during the 15 loading cycles. The axial stress was then increased to 50 ksi, which again doubled the crack width, and the specimen failed from dowel-induced cracking with a single cycle of +150 psi shear.

A second similar specimen was loaded with one cycle at $f_t = 25$ ksi; it withstood four additional cycles at $f_t = 50$ ksi prior to cracking.

Specimen 3 (1#4-25/50-IST+DA) showed the substantial improvement in performance from combined dowel action and interface shear transfer. The specimen had an applied bar tension of 25 ksi for the first 10 load cycles at +150 psi; slips and crack widths were both extremely small for this combination. The bar tension was then increased to 50 ksi, and 15 load cycles at +150 psi were applied. Results are summarized in Fig. 5. After about 5 cycles (16-20) the slip stopped increasing. The specimen was then subjected to 10 cycles each of +250 psi and +400 psi shear stress. Again the peak slip increased rather sharply during the initial cycles and then tended to stabilize. Even at this high load level, however, the shear slips were small compared to those of dowel action alone specimens. A companion specimen gave similar results except it showed much more distress at +400 psi shear.

Specimen 4 (1#6-0/25-DA) studied the influence of dowel diameter on response. The specimen had 5 load cycles at +150 psi (11.3 ksi) with $f_t = 0$, and 10 cycles at the same stress but with f_t set at 25 ksi. Response is shown in Fig. 6. Slip values continued to increase at each cycle until cycle 15. The shape of the load-slip curve and the shear stiffness after free slip had occurred were essentially unchanged during cycles 6-15. The free slip component increased because of the continuing deterioration of the concrete surfaces adjacent to the bar.

Large Scale Specimens

Interface Shear Transfer Plus Dowel Action - #7, #9 and #14 Bars

Specimen 5 (4#7-48-IST+DA) with an initial crack width of 0.02 in., was subjected to 26 cycles of shear stress at +188 psi. The variation in the average shear slip vs. shear stress for cycles 1 and 15 is given in Fig. 7a. In the first cycle, the relationship between slip and shear stress is almost linear, but as cycling proceeds, it can be characterized as a nonlinear, hardening-type response. The low stiffness observed at low stresses is indicative of the large displacements required to mobilize the interface shear transfer mechanism. Peak slips at cycles 1, 15 and 25 were 0.01, 0.019 and 0.021 in., respectively. The variation in the average slip and crack width with the number of cycles is shown in Fig. 7b. Both the average slip and crack width increased significantly during the first 15 cycles. Thereafter, no appreciable change was observed.

The specimen withstood 26 cycles at +188 psi without any evidence of concrete failure. The same specimen, without tension in the reinforcement, was then subjected to a shear stress of 850 psi, at which failure occurred by yielding of the reinforcement across the crack. No significant cracks were observed at the sides of the specimen.

Specimen 6 (4#9-33-IST+DA) with an initial crack width of 0.02 in. was subjected to 25 cycles of shear stress at +160 psi shear. Shear-slip curves for cycles 1 and 15 are given in Fig. 8a. The relationship between the shear stress and the corresponding slip was similar to the one observed for specimen 5. Peak slips at cycles 1, 15 and 25 were 0.006, 0.008 and 0.008 in., respectively. The variation in average slip and crack width with the number of cycles is shown in Fig. 8b. The slip increased during the first 10 cycles at a decreasing rate, but no significant increase was observed in subsequent cycles. The maximum crack width remained practically constant at 0.021 in. throughout the 25 cycles.

This specimen exhibited a behavior more stable than that of specimen 5 as measured by the variations in the slip and crack width. After the 25 cycles at a shear stress of +160 psi, specimen 6, with the tension load on the reinforcement removed, was tested to determine its ultimate failure load. At a shear stress of about 900 psi, longitudinal cracks initiated at the shear plane and propagated along the reinforcement axis. The shear stress was then reversed and at -900 psi the specimen failed by splitting of the concrete along the reinforcement.

Specimen 7 (4#9-22-IST+DA) was similar to specimen 6 except that the initial crack width was set at 0.01 in. by having a lower tension in the reinforcement. A shear stress of +160 psi was applied to the specimen for 25 cycles. The observed behavior was similar to that of the earlier specimens, but peak slips and average crack widths were smaller. Results are summarized in Figs. 9a and 9b. Maximum slip values for cycles 1, 15 and 25 were 0.006, 0.007 and 0.008 in., respectively. The maximum slip remained approximately constant after the 10th cycle and the maximum crack width, did not change significantly during

cycling.

Specimen 8 (2#14-31-IST+DA) contained 2#14 bars placed in a plane perpendicular to the direction of the applied loads. The initial crack width was 0.02 in. with a bar tension of 31 ksi. The specimen was subjected to the following loading schedule: 9 cycles at +110 psi, 5 cycles at +125 psi, 11 cycles at +202 psi and 17 cycles at +260 psi. At the beginning of the cycle 38, the stress in the reinforcement, ft, was increased to 41 ksi. Slip vs. shear for cycles 1 and 15 is plotted in Fig. 10a. Notice the nonsymmetric response in peak slips for the positive and negative shear stresses. Peak slips and crack widths are given in Fig. 10b as a function of the number of cycles. At the end of cycle 32 the crack width measurements were not considered reliable, due to malfunction of one dial gage.

The magnitude of the slips recorded increased continuously as both the number of cycles and the shear stresses were increased. However, after the tensile stress in the reinforcement was increased to 41 ksi, the increase in the positive load direction for cycles 1, 15 and 25 were 0.006, 0.01 and 0.011 in., respectively. Crack width changes were similar in both the (+) and (-) directions. The crack width tended to decrease during the first 15 cycles, but afterwards an increase at a growing rate with the number of cycles was apparent. The largest rate of increase in crack width was observed after cycle 26, at a maximum shear stress of 260 psi.

The specimen failed in a brittle fashion at a shear stress of approximately 230 psi during load cycle 42. The final cracked configuration is shown in Fig. 14a, where the circled numbers indicate the order in which the cracks were recorded. The first cracks were observed at cycle 38, at a shear stress of 175 psi, on the loaded sides of the specimen. All other cracks were simultaneously observed during cycle 42, and due to the sudden failure of the specimen no precise ordering of crack occurrence was possible.

Specimen 9 (2#14-39-IST+DA) was reinforced with 2#14 bars arranged in a plane parallel to the direction of the applied shear loads. The crack width was at 0.02 in. from an applied bar tension of 39 ksi, and the specimen was cycled according to the following schedule: 10 cycles at +110 psi, 4 cycles at +127 psi, 10 cycles at +202 psi and 1 cycle at +260 psi. Slip vs. shear for cycles 1 and 15, is given in Fig. 11a. The variation in peak slip and crack width with number of cycles is shown in Fig. 11b. The peak slips for cycles 1, 15 and 25 were 0.005, 0.01, 0.014 in., respectively. For the first 15 cycles the peak slip increased continuously with cycling, while the crack width remained approximately constant. After cycle 15, the rate of increase of both displacements are accelerated.

The specimen failed during cycle 26 at a maximum shear stress of -260 psi. Small cracks were first noticed on the loaded faces of the specimen, initiating at the shear plane and at a shear stress of +260 psi. After this load was

reversed, a major crack in the reinforcement plane and joining both bars was observed at the failure load (see Fig. 14b).

Dowel Action Alone - #9 Bars

Specimen 10 (4#9-31-DA) was the first large scale specimen tested to study the behavior of the dowel action mechanism alone. The interface shear transfer mechanism was eliminated by means of thin greased steel plates placed at the shear plane. An initial crack width of 0.015 in. was obtained by tensioning the bars to 31 ksi. The specimen reached failure in the first cycle at a shear stress of +188 psi (10.6 ksi average shear stress in the reinforcement). The cracking pattern for this specimen is shown in Fig. 14c. Cracks initiated at the shear plane and propagated along the reinforcement axis as the shear stress was increased. The cracks on the loaded side of the specimen were increased. The cracks on the loaded side of the specimen were noticed at the occurrence of failure.

Specimen 11 (4#9-0-DA) was similar to specimen 10, but without tension applied to the reinforcement. The specimen failed at the end of the 5th cycle at a shear stress of 188 psi (10.58 ksi on the bars). The shear stress vs. slip plot is given in Fig. 12a. Notice the different variation in stiffness of the specimen, when compared to the interface shear transfer and dowel action specimens. The hysteresis loop encloses a larger area and the magnitude of the slips at maximum load increased considerably with cycling. The cracking pattern for the specimen, as given in Fig. 14d, is very similar to the one discussed for specimen 10.

Specimen 12 (4#9-28-DA) is similar to specimens 10 and 11, but was subjected to the following loading schedule: 35 cycles at ± 80 psi (4.5 ksi in the bars), 10 cycles at +125 psi (7.03 ksi), and 1 cycle at +188 psi (10.58 ksi). In Fig. 13a the shear stress vs. average slip is given for cycles 1, 36 and 46, with peak slip values 0.011, 0.02 and 0.023 in., respectively. The variation of peak slip and crack width with cycling is shown in Fig. 13b. The maximum average slip increased continuously with cycling, but it was further augmented by the presence of higher shearing stresses. The same behavior was observed for the variations in the crack width. The specimen failed at the 46th cycle at a shear stress of -188 psi (10.58 ksi on the dowel area). The failure mode was identical to that for specimens 10 and 11.

Experiments Not Reported Here

Additional experiments were conducted on different specimen geometries that had #11 and #14 bars. These results will be reported in our expanded version of this paper.

Discussion of Test Results

The transfer of shear stresses across a precracked surface by the combined effect of dowel action and interface shear transfer was studied from specimens 3 and 5 to 9. Different bar sizes and levels of cyclic shear were considered in the large scale specimens 5 to 9. Specimen 3 was a small scale specimen with only 1 #4 bar, subjected to a shear stress of 150 psi.

In Fig. 15a the slip at cycle 15 is plotted against the shear stress for specimens 5, 6, 8. These curves exhibit the same shape regardless of the bar size and arrangement. The peak slip decreases and the initial stiffness increases with increasing bar sizes. Specimen 5 required a slip value about twice that of specimens 6 and 8 to mobilize the shear transfer mechanism.

In Fig. 15b and 15c, the crack width and peak slips variations with number of cycles are given for specimens 5, 6, and 8. While specimens 6 (4#9) and 8 (2#14), maintained a constant crack width and slip for the first 15 cycles, specimen 5 (4#7) exhibited a decreasing rate of increase in both displacements.

The behavior of specimen 3 is the same as mentioned for the large scale specimens. A direct comparison between the large and small scale specimens is not made here, however, because of the great differences in size.

The failure modes of the large scale specimens is a function of reinforcement size, shear and axial stress, and concrete cover provided to the reinforcement. Specimens 6, 8 and 9, with larger bars had failure modes caused by concrete splitting along the reinforcement axis, whereas specimen 5 (4#7) exhibited a failure mode caused by yielding of the reinforcement crossing the crack. Thus, the large dowel stiffness provided by the larger bars generated stress distributions around the bar which led to concrete failures, rather than failure by yielding of the reinforcement.

The transfer of shear stresses across a precracked surface by the mechanism of dowel action alone was studied with small scale specimens 1, 2 and 4, and large scale specimens 10 to 12. Different bar sizes and axial tensions were considered in these specimens.

Specimen 1 (1#4) and 4 (1#6), were both initially subjected to a shear stress of 150 psi, without tension in the reinforcement. By comparing Fig. 3 and Fig. 6, it can be seen that the magnitude of the peak slip increases with bar size. Also the rate of increase in peak slip with the number of cycles increases with bar sizes.

The presence of axial stresses in the reinforcement induces larger crack widths and peak slips. The additional bond cracks generated by the tension in the reinforcement further deteriorates the concrete around the bar. Hence a decrease in the shear stiffness of the specimen was observed (compare Figs. 3 and 4).

The large scale specimens also exhibited a reduction in dowel stiffness as the tension in the reinforcement was

increased. For a given tension f_t , the dowel stiffness was reduced as the shear stresses were increased. The large scale specimen behavior was stable at shear stresses below 80 psi (4.5 ksi on the bars).

The behavior of the specimens investigated here may be summarized as follows:

a. the dowel action mechanism resists shear loads by direct shear on the dowel, accompanied by bending stresses. When this mechanism is acting alone, high slips have to be induced in order to fully sustain the applied shear stresses. The initial stiffness of these specimens is lower than that observed for specimens with the interface shear transfer and dowel action mechanisms combined. The shear carried by the dowel quickly deteriorates the concrete surrounding the bar. The presence of reversing cyclic shear stresses accentuates this action. The axial tension in the reinforcement influences strongly the behavior of the specimen.

b. For specimens in which the shear stresses are sustained by both interface shear transfer and dowel action, the shear-induced slips are small and stable behavior is observed after a number of cycles, depending upon the reinforcement ratio. The high axial stiffness of the reinforcement crossing the crack mobilizes the IST contribution and greatly reduces the slips for a given value of shear stress (as compared to dowel action alone or to IST alone with a low value of restraining stiffness across the crack (see Ref. 1). This implies that the major portion of the shear is carried by IST. As the initial crack width is reduced the magnitudes of slip and crack width decrease, for a given shear stress level. The reinforcement ratio provided to the section is critical in determining the failure mode of the specimen.

Conclusions

The conclusions given below are based on results of recent experimental work. Current and planned experiments will provide additional insight into shear transfer and may modify some of the conclusions.

1. For dowel action alone, a rather severe reduction in dowel stiffness and reversing dowel load capacity was evident during cyclic shear loading, particularly when axial tension was applied to the bar.
2. Combined dowel action and interface shear transfer is an efficient mechanism for cyclic shear transfer, with small slips and acceptable degradation rates. In general, 25 cycles of shear load produced crack width increases of less than 0.01 in. Large bars (#11) tended to produce splitting effects in the particular specimen geometry used here.
3. The energy absorption capacity of the specimen decreases with cycling.
4. The unloading stiffness is always higher than the loading stiffness. A residual slip is observed upon unloading for all specimens.

5. The size of reinforcing bar is a major parameter in the shear transfer mechanism, particularly at higher shear stress levels.

Acknowledgements

This research was conducted with the support of the National Science Foundation Program of Research Applied to National Needs (RANN).

References

1. White, R. N., and Holley, M. J., Jr., "Experimental Studies of Membrane Shear Transfer," J. of the Structural Div., ASCE, August 1972, p. 1835.
2. Laible, J. P., White, R. N., and Gergely, P., "An Experimental Investigation of Seismic Shear Transfer Across Cracks in Concrete Nuclear Containment Vessels," to be published in ACI Special Symposium Volume on Shear, 1976.
3. Laible, J. P., and Gergely, P., "Nonlinear Dynamic Analysis of Cracked Reinforced Concrete Nuclear Containment Structures," Nuclear Design and Engineering, 30, Sept. 1974.
4. Gergely, P., Stanton, J. F., and White, R. N., "Behavior of Cracked Concrete Nuclear Containment Vessels During Earthquakes," U. S. National Conference on Earthquake Engineering, University of Michigan, June 1975.
5. Eleiott, A. F., "An Experimental Investigation of Shear Transfer Across Cracks in Reinforced Concrete," M.S. Thesis, Cornell University, June 1974.
6. Stanton, J., "The Dowel Action of Reinforcement and the Nonlinear Dynamic Analysis of Concrete Nuclear Containment Vessels," M.S. Thesis and Departmental Report, Cornell University, Aug. 1976.
7. White, R. N., and Gergely, P., "Shear Transfer in Thick Walled Reinforced Concrete Structures Under Seismic Loading," Final Report, NSF Grant GK-27756, Department of Structural Engineering, Cornell University, Ithaca, N. Y., July 1974.
8. White, R. N., and Gergely, P., "Shear Transfer in Thick Walled Reinforced Concrete Structures Under Seismic Loading," Annual Report for NSF Grant AEN 73-03178 A01, Dept. of Structural Engineering Report No. 75-10, Cornell University, Dec. 1975.

Specimen No.	Shear Area in ²	f _c psi	f _y ksi	Reinforcement	Axial Stress, ksi	Shear Stress psi (ksi)*	No. of Cycles
1	15	2980	40	1#4	0	150(11.25) 180(13.5)	15 10
2	15	3080	75	1#4	25 50	150(11.25) 150(11.25)	15 1
3	15			1#4	25 50 50 50	150 150 250 400	10 10 10 10
4	15	3130	60	1#6	0 25	150(5.1) 150(5.1)	5 10
5	225	2830	64	4#7	48	188 850	26 1
6	225	3150	66	4#9	33 0	160 900	25 1
7	225	3074	66	4#9	22	160	25
8	225	3320	68	2#14	31 31 31 31 41	110 125 202 260 260	9 5 11 13 4
9	225	3450	68	2#14	39	110 127 202 260	10 4 10 1
10	225	3048	66	4#9	31	188(10.6)	1
11	225	3107	66	4#9	0	188(10.56)	5
12	225	3196	64	4#9	28	80(4.5) 125(7.0) 188(10.6)	35 10 1

*for specimens with dowel action alone, the average shear stress on the bar is also given in parentheses.

Table 1 - Definition of Specimens and Loading History

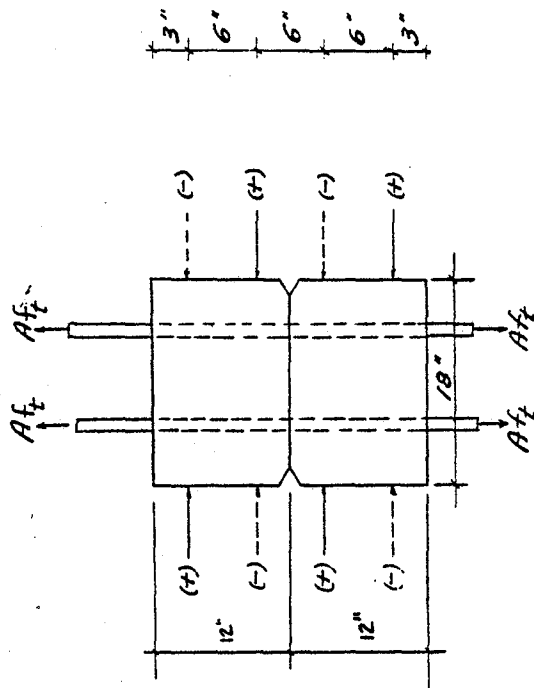


Fig. 1 - Large scale specimen geometry

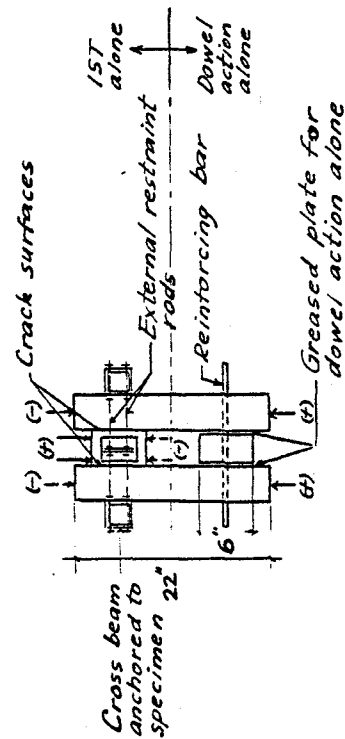


Fig. 2 - Small scale specimen geometry

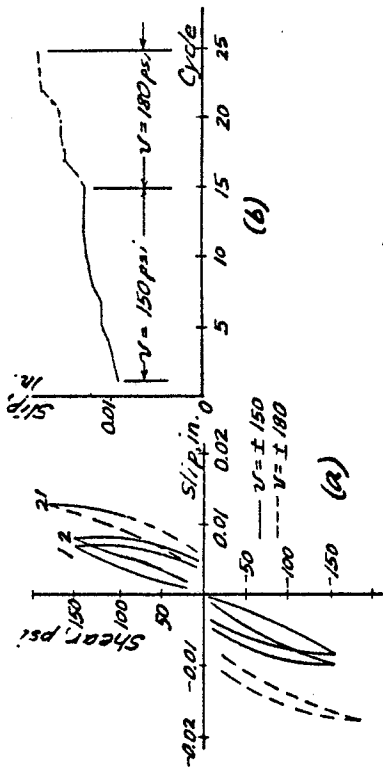


Fig. 3 - Spec. 1 (1#4-0-DA)

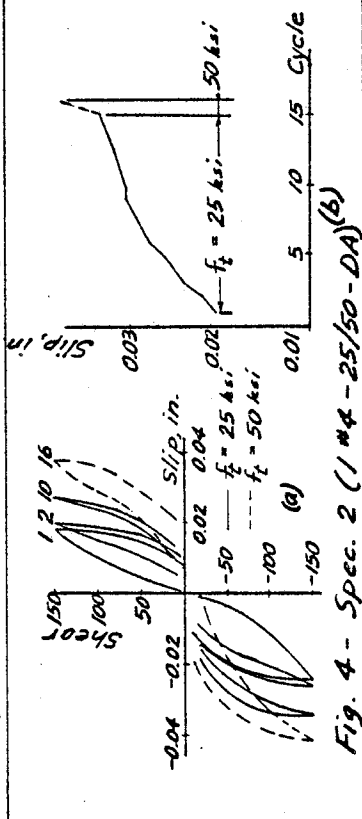


Fig. 4 - Spec. 2 (1#4-25/50-DA)

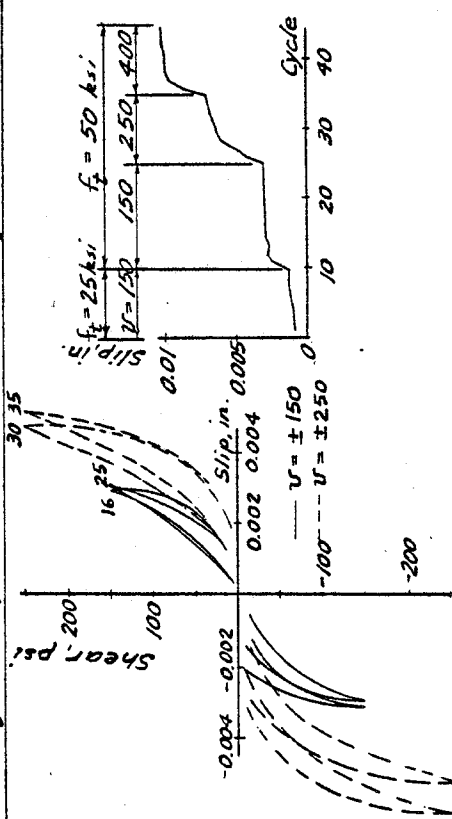


Fig. 5 - Spec. 3 (1#4-25/50-15T+DA)

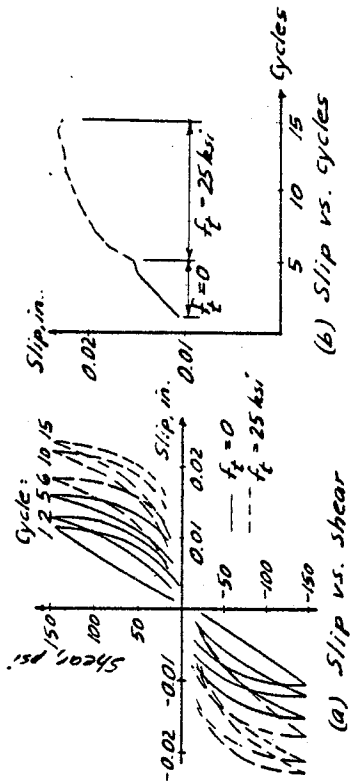


Fig. 6 - Specimen 4 (1#6-0/25-DA)

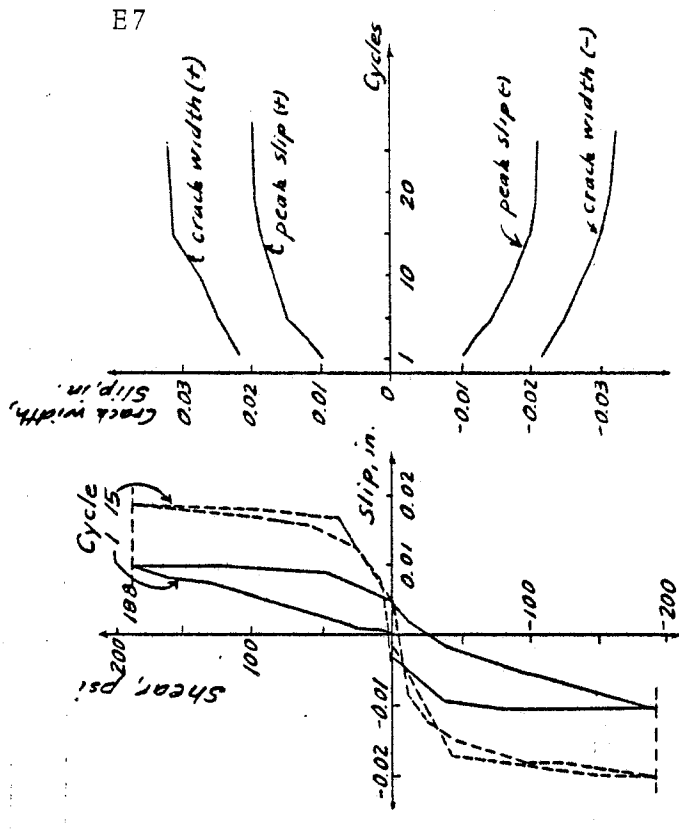


Fig. 7 - Specimen 5 (4#7-48-15T+DA)

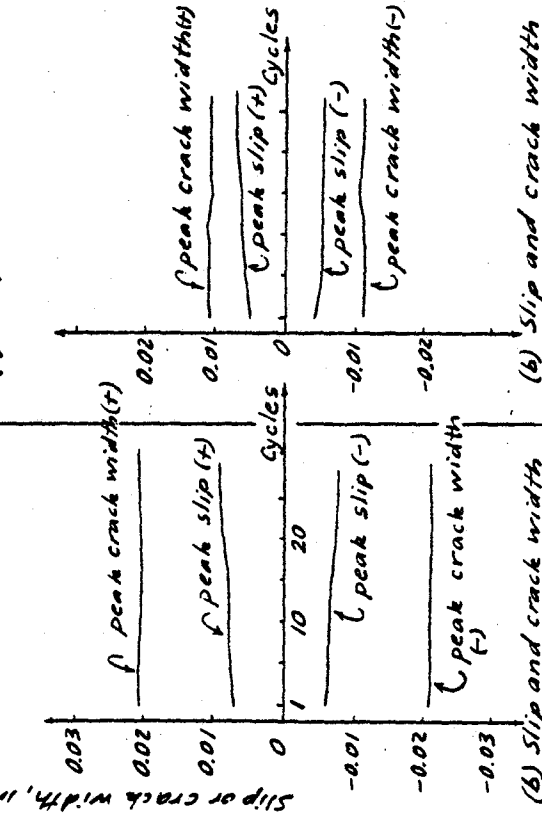
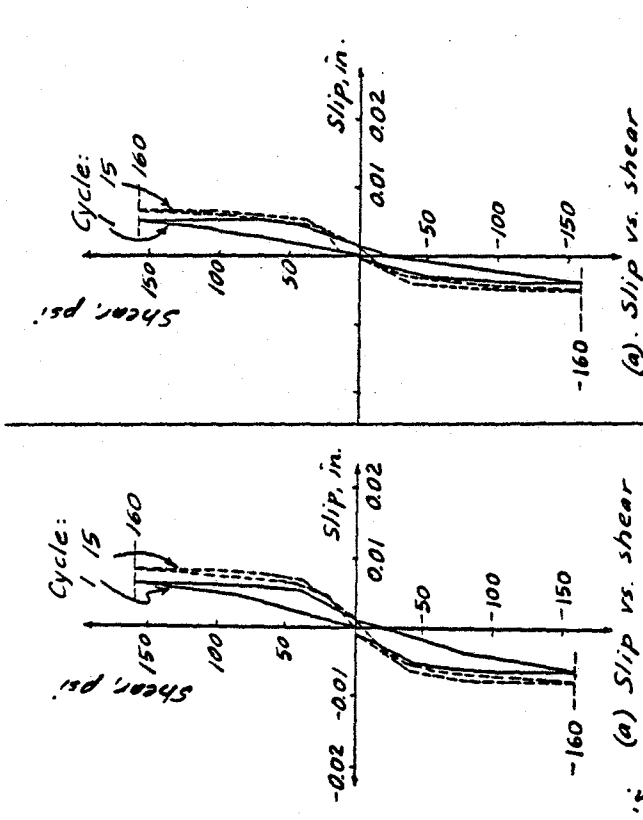


Fig. 8 - Specimen 6 (4#9-33-15T + DA)

Fig. 9 - Specimen 7 (4#9-22-15T + DA)

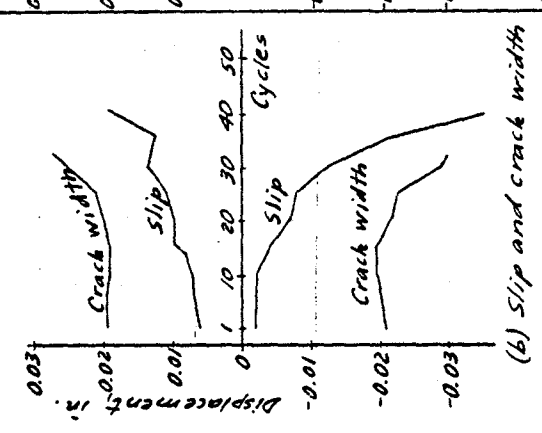
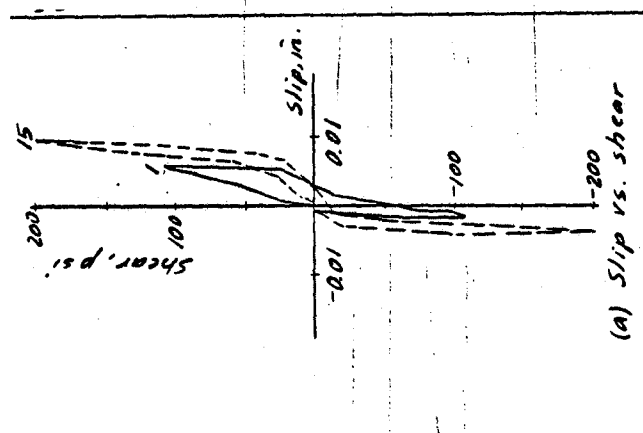


Fig. 10 - Specimen 8 (2#14-31-15T + DA)

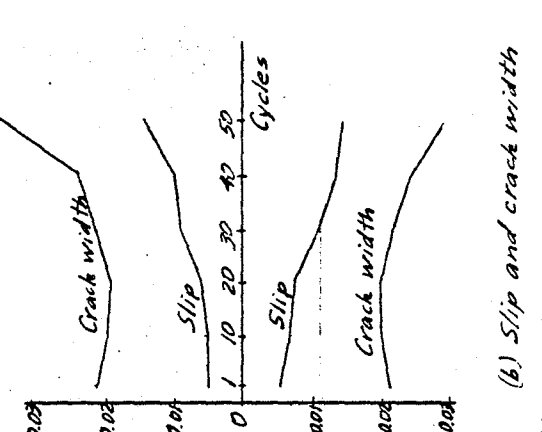
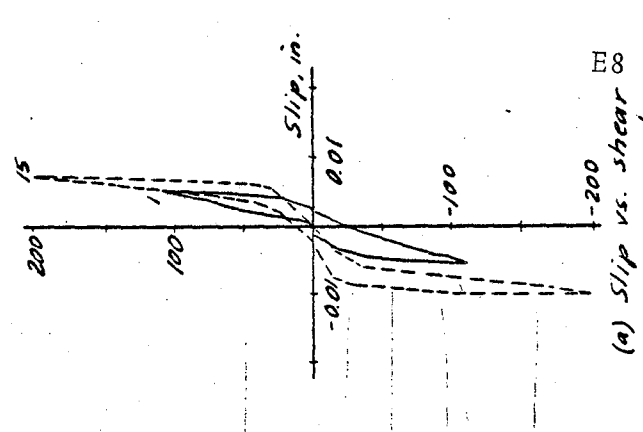


Fig. 11 - Specimen 9 (2#14-39-15T + DA)

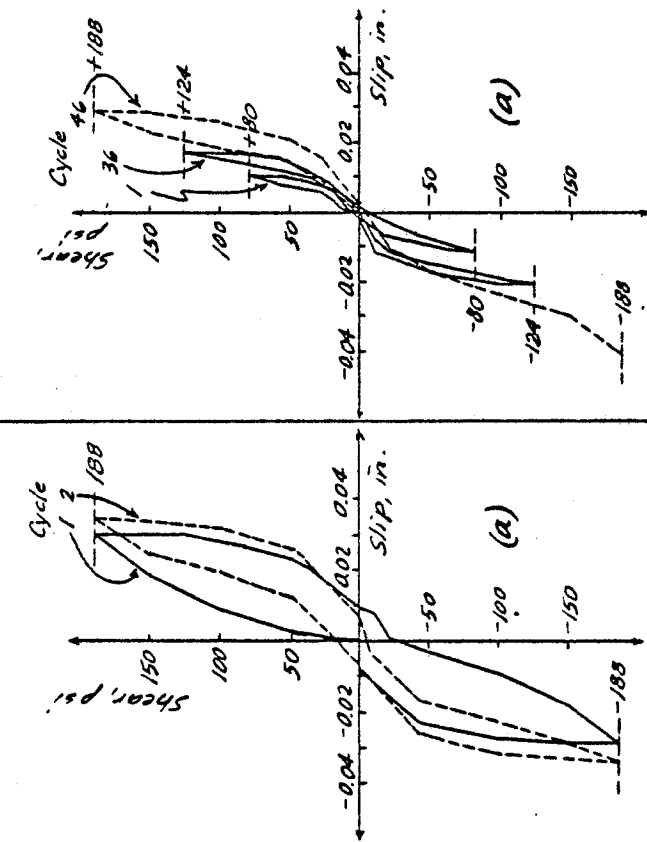
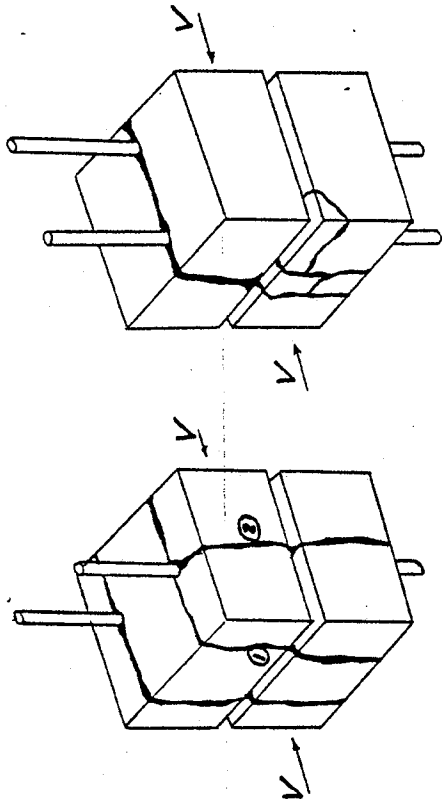
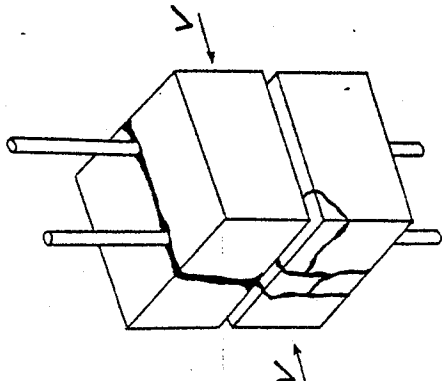


Fig. 12 - Specimen 11 (4#9-0-DA)

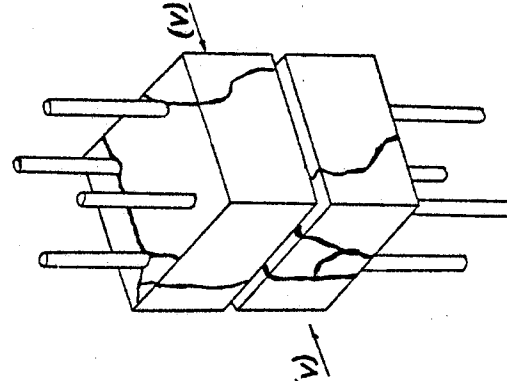
Fig. 13 - Specimen 12 (4#9-28-DA)



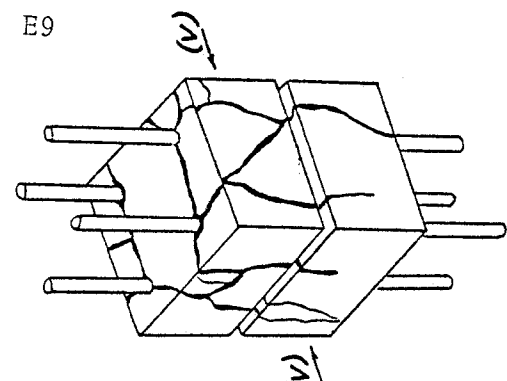
(a) Spec. 8



(b) Spec. 9



(c) Spec. 10



(d) Spec. 11

Fig. 14 - Failure Modes

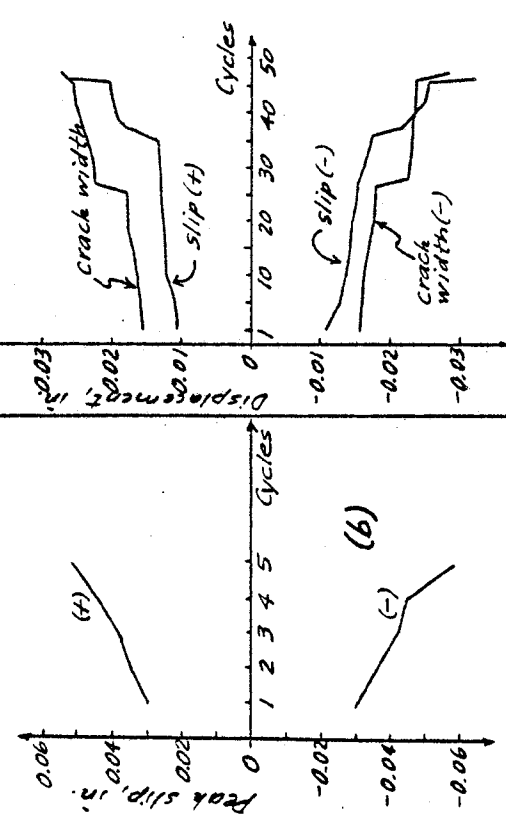
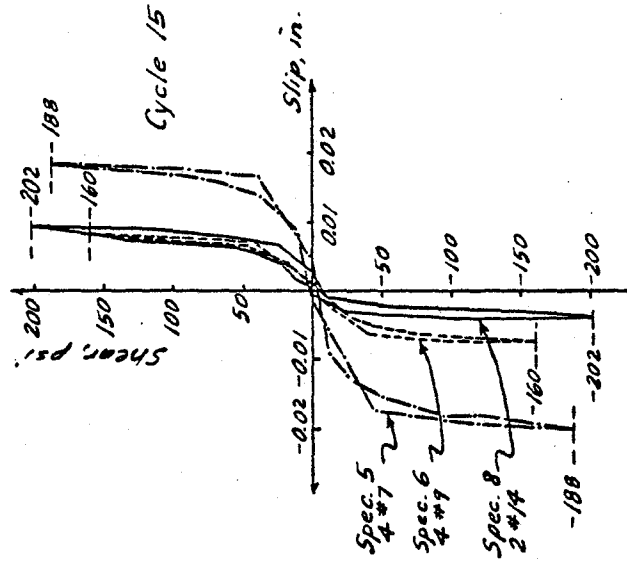
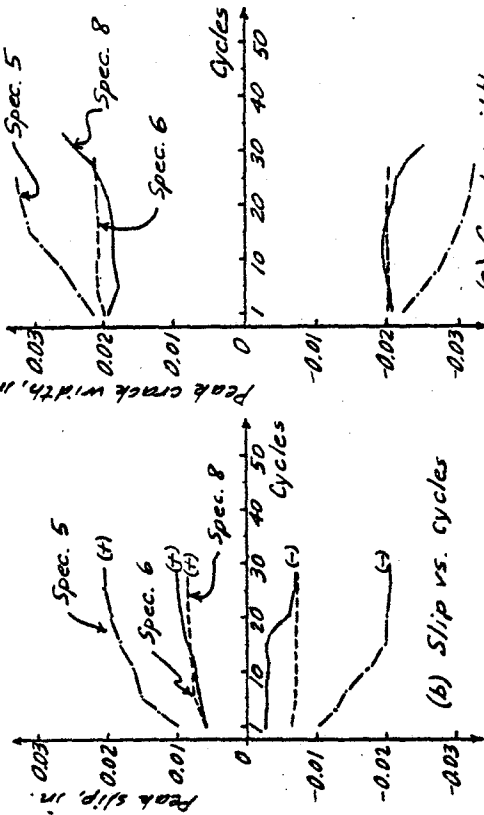


Fig. 12 - Specimen 11 (4#9-0-DA)

Fig. 13 - Specimen 12 (4#9-28-DA)



(a) Peak slip vs. shear, 15th cycle, Spec. 5, 6, 8



(b) Slip vs. cycles

(c) Crack width vs. cycles

Fig. 15- Comparison of Behavior, Spec. 5, 6, 8

REFERENCES

1. Eleiott, Alan F., "An Experimental Investigation of Shear Transfer Across Cracks in Reinforced Concrete," M.S. Thesis, Cornell University, Ithaca, June 1974.
 2. Stanton, John F., "An Investigation of the Dowel Action of the Reinforcement of Nuclear Containment Vessels and their Nonlinear Dynamic Response to Earthquake Loads," M.S. Thesis, Cornell University, January 1977.
 3. Gergely, P., Stanton, J.F. and White, R.N., "Behavior of Cracked Concrete Nuclear Containment Bessels During Earthquakes," U.S. National Conference on Earthquake Engineering, University of Michigan, June 1975, pp. 512-518.
 4. Smith, Jay, "The Effects of Cracks on the Seismic Analysis of Reinforced Concrete Nuclear Containment Vessels," Ph.D. Thesis and Department of Structural Engineering Report No. 368, Cornell University, April 1977.
 5. Jimenez, R., Perdikaris, P., Gergely, P., and White R.N., "Interface Shear Transfer and Dowel Action in Cracked Reinforced Concrete Subject to Cyclic Shear," Methods of Structural Analysis, Proceedings of ASCE Conference, Madison, Wisconsin, August 1976, pp. 457-475.
 6. Jiminez, R., "Shear Transfer Across Cracks in Reinforced Concrete, Ph.D. Thesis, Cornell University, expected date 1978.
- Several papers based on this research are in preparation for presentation at national conferences and publication in journals. Earlier Cornell University publications on shear transfer in cracked concrete include:
7. White, R.N., "Behavior of Pre-Cracked Concrete Subjected to Reversing Shear Stresses," Report SWND-5, Stone and Webster Engineering Corp., Boston, Mass., Nov. 1969.
 8. White, R.N., "Behavior of #18 Reinforcing Bars Under Combined Axial Load and Plastic Bending," Report SWND-5S, Stone and Webster Engineering Corp., Boston, Mass., Dec. 1969.
 9. White, R.N., and Holley, M.J., Jr., "Experimental Studies of Membrane Shear Transfer," J. of the Structural Div., ASCE, August 1972, p. 1835.
 10. White, R.N., Gergely, P., Laible, J., and Fajardo, O., "Shear Transfer in Thick Walled Reinforced Concrete Structures Under Seismic Loading," Progress Report, NSF Grant GK-27756, Department of Structural Engineering, Cornell University, Ithaca, N.Y., Feb. 1973.

11. Laible, J.P., "An Experimental Investigation of Interface Shear Transfer and Applications in the Dynamic Analysis of Nuclear Containment Vessels," Ph.D. Thesis, Cornell University, Aug. 1973.
12. White, R.N., and Gergely, P., "Shear Transfer in Thick Walled Reinforced Concrete Structures Under Seismic Loading," Final Report, NSF Grant GK-27756, Department of Structural Engineering, Cornell University, Ithaca, N.Y., July 1974.
13. Laible, J.P., and Gergely, P., "Nonlinear Dynamic Analysis of Cracked Reinforced Concrete Nuclear Containment Structures," Nuclear Design and Engineering, 30, Sept. 1974.
14. Laible, J.P., White, R.N., and Gergely, P., "Experimental Investigation of Seismic Shear Transfer Across Cracks in Concrete Nuclear Containment Vessels," ACI Special Publication, S'P 53-9, pp. 203-226.

Oral Presentations include:

1. "The Problem of Seismic Shear Transfer in Nuclear Containment Vessels," seminar presented by R. White at the University of Washington (Dec. 1974), University of California (Feb. 1975), and Stanford University (March 1975).
2. "Seismic Shear Transfer Research," seminar presented by R. White at the School of Civil Engineering, National University of Mexico, Mexico D.F., August 1976.
3. "Shear Transfer in Reinforced Concrete Subjected to Biaxial Tension and Cyclic Shear" by R. White, P. Gergely and P. Perdikaris, Research Session at the 1976 ASCE National Convention, Philadelphia, Sept. 1976.
4. "Interface Shear Transfer in Concrete," seminar presented by P. Gergely at the Department of Civil Engineering, University of Toronto, October 1976.
5. "Seismic Design of Nuclear Power Plants," presented by P. Gergely at the Department of Civil Engineering, University of Toronto, November 1976.
6. "Seismic Shear Effects in Reinforced Concrete Containment Vessels," seminar presented by R. White at the State University of New York, Buffalo, November 1976.
7. "Bond and Dowel Capacities of Reinforced Concrete," by R. Jimenez, R. White and P. Gergely, ACI Spring Convention, San Diego, April 1977, to be published in ACI Symposium Volume.